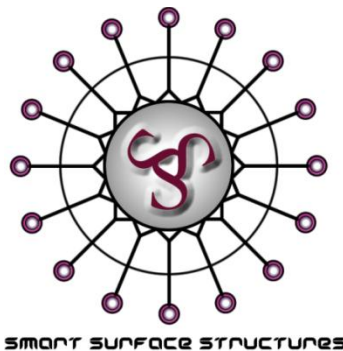


# Carbon Nanotubes for Photovoltaic Devices



**Flinders**  
UNIVERSITY



Thesis submitted to the School of Chemical and Physical Sciences, Faculty of Science  
and Engineering, Flinders University in fulfilment of the requirements for the degree of  
Doctor of Philosophy

**Mark A. Bissett**



# **Declaration**

I certify that this thesis does not incorporate without acknowledgment any material previously submitted for a degree or diploma in any university; and that to the best of my knowledge and belief it does not contain any material previously published or written by another person except where due reference is made in the text.

---

**Mark Alexander Bissett**

# Contents

<b>Declaration</b> .....	<b>i</b>
<b>Contents</b> .....	<b>ii</b>
<b>Acknowledgments</b> .....	<b>vii</b>
<b>Publications From This Thesis</b> .....	<b>viii</b>
<b>Abstract</b> .....	<b>x</b>
<b>Figures &amp; Tables</b> .....	<b>xii</b>
<b>Abbreviations</b> .....	<b>xxv</b>

## **Chapter 1**

<b>1. Introduction</b> .....	<b>1</b>
1.0 Power Generation .....	2
1.1 Photovoltaics .....	3
1.1.1 Silicon Solar Cells .....	4
1.1.2 Dye Sensitised Solar Cells .....	6
1.2 Carbon Nanotubes.....	13
1.2.1 Structure of Carbon Nanotubes.....	14
1.2.2 Methods of Carbon Nanotube Production.....	16
1.3 Integration of Carbon Nanotubes in Light Harvesting Technology.....	19
1.3.1 Chemical Modification of Carbon Nanotubes for Light Harvesting Devices ..	23
1.4 Thesis Outline .....	26

## **Chapter 2**

<b>2. Materials &amp; Methods</b> .....	<b>28</b>
2.0 Experimental Details .....	29

---

2.1 Single-walled Carbon Nanotube Solutions.....	29
2.1.1 SWCNT Arrays on Silicon.....	30
2.1.2 Arrays on Fluorine Doped Tin Oxide Coated Glass.....	31
2.1.3 Carbon Nanotube Electrochemical Solar Cells.....	32
2.1.4 Multi-walled Carbon Nanotube Devices.....	33
2.2 Chemically Functionalised Single-walled Carbon Nanotube Arrays.....	33
2.2.1 Ruthenium Tetraphenyl Porphyrin Functionalised Arrays.....	33
2.2.2 N3 Dye Functionalised Array.....	36
2.2.3 Dendron Functionalised Array.....	38
2.3 Chemical Vapour Deposition Growth of Carbon Nanotubes.....	40
2.3.1 Carbon Nanotube Arrays Grown by Chemical Vapour Deposition.....	40
2.3.2 Carbon Nanotube Arrays Grown by Plasma Enhanced Chemical Vapour Deposition.....	41
2.5 Solar Cell Performance.....	43
2.5.1 Spectral Response.....	44
2.6 Electrochemistry.....	45
2.6.1 Cyclic Voltammetry.....	45
2.6.2 Differential Pulse Voltammetry.....	47
2.6.3 Electrochemical Impedance Spectroscopy.....	49
2.7 Raman Spectroscopy.....	51
2.8 X-Ray Photoelectron Spectroscopy.....	54
2.9 Scanning Electron Microscopy.....	55

### **Chapter 3**

<b>3. Photoresponse of Single-walled Carbon Nanotube Arrays.....</b>	<b>57</b>
3.0 Introduction.....	58

---

3.1 Characterisation of Carbon Nanotube Array on FTO .....	59
3.1.1 Raman Spectroscopy of CNT Arrays on FTO .....	59
3.1.2 XPS Characterisation of SWCNT on FTO .....	63
3.1.3 Electrochemistry of SWCNT Arrays on FTO .....	66
3.2 Photovoltaic Properties of Single-Walled Carbon Nanotube Arrays .....	75
3.2.1 Spectral Response of SWCNT Functionalised FTO.....	83
3.3 Comparison of SWCNT to MWCNT Functionalised FTO.....	85
3.3.1 Raman of MWCNT Functionalised FTO .....	86
3.3.2 Electrochemistry of MWCNT Functionalised FTO .....	88
3.3.3 XPS Characterisation of MWCNT Functionalised FTO .....	91
3.3.4 Photovoltaic Properties of MWCNT Functionalised FTO.....	92
3.4 Chapter Conclusions.....	93

## **Chapter 4**

<b>4. Single-walled Carbon Nanotube Arrays as Scaffolds for Chemical Functionalisation .....</b>	<b>95</b>
4.0 Introduction.....	96
4.1 Dye Functionalisation of SWCNT Arrays .....	96
4.1.1 Electrochemical Characterisation of Dye Functionalised SWCNT Arrays.....	96
4.1.2 Photovoltaic Properties of Dye Functionalised SWCNT Arrays .....	102
4.2 Porphyrin Functionalisation of SWCNT Arrays.....	105
4.2.1 Electrochemical Characterisation of Porphyrin Functionalised SWCNT Arrays.....	106
4.2.2 Photovoltaic Properties of Porphyrin Functionalised SWCNT Arrays .....	108
4.3 Dendron Functionalisation of SWCNT Arrays .....	110
4.3.1 Raman Characterisation of Dendron Functionalised SWCNT Arrays .....	111

---

4.3.2 Electrochemical Characterisation of Dendron Functionalised SWCNT Arrays.....	112
4.3.3 Photovoltaic Properties of Dendron Functionalised SWCNT Arrays .....	116
4.4 Dye Modification of Dendron Functionalised SWCNT Arrays .....	121
4.4.1 Electrochemical Characterisation of Dye Modified Dendron Functionalised SWCNT Arrays.....	123
4.4.2 Photovoltaic Properties of Dye Modified Dendron Functionalised SWCNT Arrays.....	129
4.5 Chapter Conclusions.....	132

## **Chapter 5**

<b>5. Growth of Carbon Nanotubes for Photovoltaic Devices.....</b>	<b>133</b>
5.0 Introduction.....	134
5.1 Thermal Chemical Vapour Deposition Growth of Carbon Nanotube Arrays on Silicon.....	134
5.1.1 Scanning Electron Microscopy of CVD Grown CNT Arrays .....	135
5.1.2 Electrochemical Characterisation of CVD Grown CNT Arrays .....	136
5.1.3 Raman Characterisation of CVD Grown CNT Arrays.....	139
5.1.4 XPS Characterisation of CVD Grown CNT Arrays.....	140
5.1.5 Photovoltaic Properties of CVD Grown CNT Arrays .....	146
5.2 Thermal Chemical Vapour Deposition Growth of CNT Arrays on Indium Tin Oxide Coated Quartz.....	147
5.2.1 Scanning Electron Microscopy of CVD Grown CNT on ITO Coated Quartz ..	147
5.2.2 Raman Characterisation of tCVD Grown CNT On ITO Coated Quartz .....	151
5.3 Plasma Enhanced Chemical Vapour Deposition for Growth of Carbon Nanotube Arrays.....	153
5.3.1 Scanning Electron Microscopy.....	155

---

5.3.2 Electrochemical Characterisation of PECVD Grown CNT Arrays .....	156
5.3.3 Raman Characterisation of PECVD Grown CNT Arrays.....	158
5.3.4 XPS Characterisation of PECVD Grown CNT Arrays .....	164
5.3.5 Photovoltaic Properties of PECVD Grown CNT Arrays .....	166
5.4 Chapter Conclusions.....	167

## **Chapter 6**

<b>6. Conclusion &amp; Future Work .....</b>	<b>168</b>
6.1 Conclusions.....	169
6.2 Future Work .....	171

## **Chapter 7**

<b>7. References.....</b>	<b>173</b>
---------------------------	------------

---

# Acknowledgments

There are many people whose help made this thesis possible and I would like to express my thanks to everyone who has assisted me in this research.

Firstly I should express my thanks and appreciation for my primary supervisor Prof. Joe Shapter, whose ability to reply to questions and queries as well as reading drafts of this thesis in record time has made the process of writing this thesis possible. The wealth of experience you have brought to this project have made it a pleasure to work with you, and I hope that in the future I will be able to continue to collaborate with you as a colleague. I would also like to thank my co-supervisor Assoc. Prof. Jamie Quinton whose insightful input often helped me see what was right in front of me the whole time and whose discussions about PhDs and life in general often helped me put things in perspective.

I especially need to thank the other PhD students within the Smart Surface Structures Group with which I have undertaken this research, both for your professional collaborations and friendship. This includes all members of our research group with specific thanks to Cameron Shearer, Anders Barlow, Adam Blanch, Sam Ogden, Lintern Fairbrother, Leo Velleman, Daniel Tune and Jingxian Yu. I would also like to thank Dr. Ingo Köper for his assistance with the electrochemical analysis and specifically the EIS data interpretation, also Dr. Chris Gibson for his assistance and smooth running of the Raman setup

I would also like to acknowledge the collaboration with the Queensland University of Technology, specifically with Prof. John Bell and his PhD students Paul Moonie and Muthuraaman Achari without whose assistance in establishing our own solar cell testing procedures this work would not have been possible.

I would like to acknowledge the financial support of Flinders University in the form of my Flinders University Research Scholarship and also funding for attending conferences both nationally and internationally.

Lastly, but definitely not least, I would like to thank my whole family for their support throughout this journey. I would especially like to thank my wife Natasha, who has supported and encouraged me throughout this whole process.

---

# Publications From This Thesis

## Journal Publications

1. **Bissett, M. A.**; Shapter, J. G., Photocurrent Response from Vertically Aligned Single-Walled Carbon Nanotube Arrays. *J. Phys. Chem. C* 2010, *114* (14), 6778-6783, DOI: 10.1021/jp1003193
2. **Bissett, M. A.**; Shapter, J. G., Electrochemistry and Photocurrent Response from Vertically-Aligned Chemically-Functionalized Single-Walled Carbon Nanotube Arrays. *J. Electrochem. Soc.* 2011, *158* (3), K53-K57, DOI: 10.1149/1.3527057
3. **Bissett, M. A.**, Köper, I., Quinton, J. S., Shapter, J. G., Dendron Growth from Vertically Aligned Single-Walled Carbon Nanotube Thin Layer Arrays for Photovoltaic Devices. *Phys. Chem. Chem. Phys.* 2011, *13*, 6059-6066, DOI: 10.1039/C0CP02740E.
4. **Bissett, M. A.**, Barlow, A. J., Shapter, J. G., Quinton, J. S., Transition from single to multi-walled carbon nanotubes grown by inductively coupled plasma enhanced chemical vapor deposition. *J. Appl. Phys.* 2011, *110* (13), 34301-34306, DOI:10.1063/1.3615945
5. **Bissett, M. A.**, Köper, I., Quinton, J. S., Shapter, J. G., Dye Functionalisation of PAMAM-type Dendrons Grown from Vertically Aligned Single-Walled Carbon Nanotube Arrays for Light Harvesting Antennae. *J. Mater. Chem.* 2011, DOI: 10.1039/C1JM13957F
6. **Bissett, M. A.**, Barlow, A. J., Shearer, C., Quinton, J. S., Shapter, J. G., Carbon Nanotube Modified Electrodes for Photovoltaic Devices. *Carbon*, In Press

---

## Published Conference Proceedings

1. **Bissett, M. A.**, Köper, I.; Shapter, J.G., Photocurrent Response from Vertically Aligned Single-walled Carbon Nanotube Arrays. *Proceedings of the International Conference on Nanoscience and Nanotechnology (ICONN2010)*
2. Shapter, J.G., **Bissett, M. A.**; Photocurrent Response from Vertically-Aligned Chemically-Functionalised Single-walled Carbon Nanotube Arrays. *Proceedings of the International Conference on Nanotechnology: Fundamentals and Applications (ICNFA2010)*
3. **Bissett, M. A.**, Barlow, A. J., Shapter, J. G, Quinton, J. S.; Raman Characterisation of Carbon Nanotubes Grown by Plasma Enhanced Chemical Vapour Deposition. *Proceedings of the Fifth International Conference on Advanced Materials and Nanotechnology (AMN-5)*

## Conference Presentations

1. “*Photocurrent Response from Vertically Aligned Single-walled Carbon Nanotube Arrays*”, International Conference on Nanoscience and Nanotechnology 2010 (ICONN2010), Sydney, NSW, Australia
2. “*Electrochemical Impedance Spectroscopy of Chemically Modified Single-Walled Carbon Nanotube Arrays*”, ARNAM/ARCNN 2010 Joint Workshop, Adelaide, SA, Australia
3. “*Dendrimer Functionalisation of Single Walled Carbon Nanotube Arrays*”, 23rd International Microprocesses and Nanotechnology Conference (MNC 2010), Kokura, Fukuoka, Japan
4. “*Plasma Enhanced Chemical Vapour Deposition Growth of Single-Walled Carbon Nanotubes*”, Fifth International Conference on Advanced Materials and Nanotechnology (AMN-5), 2011, Wellington, New Zealand

# Abstract

The aim of this work was to investigate how carbon nanotubes can be applied in the development of novel photovoltaic devices. This has been done by taking an existing system of vertically aligning single-walled carbon nanotubes on oxide surfaces and adapting it to solar cell design. Once the ability to construct solar cells from CNT functionalised electrodes was demonstrated, work then focused on improving the performance of these cells. Initially arrays of vertically aligned SWCNT were used as the working electrode in a DSSC type cell architecture. These CNT solar cells were then characterised by photovoltaic testing. The arrays themselves were investigated using electrochemistry and Raman spectroscopy. It was found that the vertically aligned single walled carbon nanotube arrays were capable of producing a prompt, response times less than 200ms, and stable photocurrent of  $\sim 13\mu\text{A}\cdot\text{cm}^{-2}$  and a voltage of 42mV when exposed to  $100\text{mW}\cdot\text{cm}^{-2}$  of light. This photoresponse changed with the number of nanotubes attached to the surface and the treatment time used to process the CNTs before attachment. Multi-walled carbon nanotube arrays were also created and analysed and found to be inferior to the SWCNT arrays due to their metallic band structure.

To improve upon the response of the SWCNT arrays they were then chemically modified to increase the cell's performance. This will be done firstly by further functionalising the CNT arrays with chromophores such N3 dye and ruthenium tetraphenyl porphyrin molecules. Attachment of these redox active molecules was verified by electrochemistry and the surface concentration and electron transfer rates compared to literature and found to be in good agreement. Photovoltaic testing indicated that N3 dye attachment lead to an increased photocurrent density ( $\sim 17\mu\text{A}\cdot\text{cm}^{-2}$ ) but a reduced voltage (26mV) when compared to the unmodified array, in agreement with similar work in the

literature. This response could also be modified by altering the attachment of nanotubes to the surface thus altering the resultant dye concentration, with 2 hours of CNT attachment found to produce the maximum dye concentration. Functionalisation was then progressed from simple molecules to PAMAM-type dendrons that were grown from the SWCNT array acting as a core. These dendrons were analysed using electrochemistry, Raman spectroscopy and photovoltaic testing and found to be able to increase performance over the unmodified array by  $\sim 70\%$  for the 2<sup>nd</sup> generation dendron. The two methods of chemical modification were then combined with the dendrons being grown from the SWCNT array and then N3 dye attached to the amine terminated chains. This produced an increased performance over the unmodified dendron with a current density of  $\sim 15\mu\text{A}\cdot\text{cm}^{-2}$  whilst maintaining a voltage of 45mV.

To further increase the density of carbon nanotubes on the surface growth of CNTs was undertaken using chemical vapour deposition and then the resultant performance compared to the chemically attached arrays. Growth of nanotubes was undertaken using both thermal and plasma-enhanced procedures. Thermal CVD was found to produce predominantly MWCNT whilst PECVD was able to produce SWCNT. It was found upon comparison of the CVD growth procedure to the covalent attachment that the chemical attachment provided for superior electron transfer kinetics despite lower nanotube coverage. This equated into a superior photoresponse. It was also found that the grown SWCNT were superior to the grown MWCNT, in agreement with previous results which suggested that SWCNT are needed to produce photocurrent due to their semi-conducting nature.

# Figures & Tables

## Chapter 1

Figure 1.1: AM1.5 solar spectrum (Inset: air mass schematic showing; AM 0, AM 1.0 and AM 1.5), spectrum reproduced from ASTM G173-03. <sup>6</sup> .....	4
Figure 1.2: A) Intrinsic silicon B) n-Type silicon with phosphorous dopant C) p-Type silicon with boron dopant. From <i>Sze et al.</i> <sup>5</sup> .....	5
Figure 1.3: Energy band diagram of a p-n junction showing photogenerated electron-hole pair. $E_v$ is the valence band energy, $E_f$ the Fermi energy and $E_c$ the conduction band energy. From <i>Sze et al.</i> <sup>5</sup> .....	6
Figure 1.4: Schematic of a dye sensitised solar cell showing electronic energy levels. From <i>Calandra et al.</i> <sup>13</sup> .....	8
Figure 1.5: Structure of N3 dye molecule. ....	8
Figure 1.6: J-V curve of DSSC showing key properties. Modified from <i>Grätzel et al.</i> <sup>12</sup> ....	9
Figure 1.7: Incident photon to current efficiency for unmodified $\text{TiO}_2$ , and $\text{RuL}'(\text{NCS})_3$ or 'black dye' and $\text{RuL}_2(\text{NCS})_2$ or 'N3' Dyes. From <i>Grätzel et al.</i> <sup>14</sup> .....	10
Figure 1.8: Examples of alternative dye molecules; Z907, C102 and N749 (From left to right). From <i>Meyer.</i> <sup>20</sup> .....	11
Figure 1.9: Copper complexes used in DSSC electrolyte. From <i>Hattori et al.</i> <sup>28</sup> .....	11
Figure 1.10: Spray coated MWCNT for DSSC counter electrode. Optical image of coated glass slide (a), SEM image of nanotube layer (b). From <i>Ramasamy et al.</i> <sup>36</sup> .....	12
Figure 1.11: ZnO nanowire array based DSSC. From <i>Law et al.</i> <sup>43</sup> .....	12

Figure 1.12: Integration of SWCNT into existing DSSC. (Left) SEM image showing TiO <sub>2</sub> particles and nanotube composite. (Right) IPCE spectra for TiO <sub>2</sub> and TiO <sub>2</sub> /SWCNT mixture. From <i>Jung et al.</i> <sup>46</sup> .....	13
Figure 1.13: Graphene sheet (A), single-walled nanotube (B), multi-walled nanotube (C) .....	14
Figure 1.14: Transmission electron micrographs of MWCNTS. From <i>Iijima</i> . <sup>62</sup> .....	14
Figure 1.15: Schematic showing vectors that produce different chirality CNTs. The vectors OA and OB define the chiral vector <i>Ch</i> and the translational vector T of the nanotube, respectively. The rectangle OAB'B defines the unit cell for the nanotube. The figure is constructed for an $(n, m) = (4, 2)$ nanotube. From <i>Dresselhaus et al.</i> <sup>69</sup> ....	15
Figure 1.16: Examples of patterned CNT arrays produced by tCVD showing pillars and sheets of dense single-walled carbon nanotubes. From <i>Hata et al.</i> <sup>72</sup> .....	18
Figure 1.17: Example of CNT arrays produced by PECVD. From <i>Meyyappan</i> . <sup>85</sup> .....	19
Figure 1.18: Response of SWCNT bundles to illumination ( $20\text{mW}\cdot\text{cm}^{-2}$ ) in the presence of a 10V bias. From <i>Zhang et al.</i> <sup>87</sup> .....	20
Figure 1.19: SEM image of single nanotube diode (A) Graph of photocurrent produced versus incident light intensity (B). From <i>Freitag et al.</i> <sup>89</sup> .....	21
Figure 1.20: Schematic of a SWCNT diode along with I-V curve showing increasing photovoltaic response with increasing illumination intensity. From <i>Lee</i> . <sup>50</sup> .....	21
Figure 1.21: Photocurrent and photovoltage on-off cycles for SWCNT film (Incident light $\approx 100\text{mW}\cdot\text{cm}^{-2}$ ). From <i>Barazzouk et al.</i> <sup>49</sup> .....	22
Figure 1.22: Schematic of possible solar cell design and benefits of directed electron transport. From <i>Kamat</i> . <sup>52</sup> .....	23
Figure 1.23: Porphyrin molecules used and cell schematic for SWCNT-porphyrin hybrid solar cell. From <i>Hasobe et al.</i> <sup>92</sup> .....	24

Figure 1.24: Synthesis of PAMAM dendrimer to generation 0.5 (G-0.5) and a schematic showing the increasing complexity of dendrimer molecules. From *Frechet et al.*<sup>111</sup> ....25

Figure 1.25: Schematic of PAMAM dendron growth from MWCNT in solution. From *Pan et al.*<sup>98</sup> .....26

## **Chapter 2**

Figure 2.1: Schematic of the hydroxylation of the silicon substrate and subsequent formation of the SWCNT array. ....31

Figure 2.2: Schematic of the hydroxylation of the FTO glass substrate and subsequent formation of the SWCNT array. ....32

Figure 2.3: Schematic of CNT functionalised electrochemical solar cell architecture. (Not to scale).....33

Figure 2.4: Schematic of the functionalisation of SWCNT array with RuTPP on FTO Glass. Modified from *Yu et al.*<sup>94</sup> .....35

Figure 2.5: Schematic of the functionalisation of SWCNT array with N3 dye on FTO....37

Figure 2.6: Functionalisation scheme for modifying SWCNTs attached to FTO glass. Step 1: Attachment of PDA leading to G-0.5; Step 2: attachment of methyl acrylate leading to G-1.0. Step 1 and 2 are then alternated for higher generations. ....39

Figure 2.7: Schematic of thermal chemical vapour deposition growth of CNTs. ....41

Figure 2.8: Reaction chamber used in plasma nanotube growth showing A: top view and B: side view. In B the antenna is shown rotated 90 degrees for clarity. Distance between antenna and sample is 10cm. ....42

Figure 2.9: Schematic of PECVD CNT growth process. ....43

Figure 2.10: Spectrum of LED solar simulator, from supplier.....44

Figure 2.11: Example cyclic voltammogram with peak current $I_p$ and voltage $E_p$ labelled for both the anodic and cathodic peaks. ....	46
Figure 2.12: DPV potential waveform E, with respect to time, t. From Manufacturer (BAS Inc). ....	48
Figure 2.13: Example differential pulse voltammogram with peak current $I_p$ and voltage $E_p$ labelled.....	49
Figure 2.14: Example of EIS spectra, simulated using a Randles type circuit. A) Nyquist Plot. B) Bode Plot. ....	50
Figure 2.15: Example of equivalent circuits and the corresponding Nyquist plot. Modified from <i>Barsoukov et al.</i> <sup>134</sup> .....	50
Figure 2.16: Diagram of Raman spectrometer. Modified from supplier. ....	52
Figure 2.17: Schematic of an X-ray photoelectron spectrometer. ....	54
Figure 2.18: XPS spectrum of platinum. Inset: High resolution XPS of Pt 4f binding region. ....	55
Figure 2.19: Photograph and schematic of a scanning electron microscope. ....	56

### **Chapter 3**

Figure 3.1: Raman spectra for a single semi-conducting and metallic SWCNT. From <i>Dresselhaus et al.</i> <sup>146</sup> .....	59
Figure 3.2: Confocal Raman images showing nanotube coverage. (A and B) Image A is a plot of the intensity of the glass specific peak ( $1030\text{cm}^{-1}$ ). Image B is the G band ( $1570\text{cm}^{-1}$ ) intensity present in the spectra (C) for 24 hours of nanotube attachment, with 8 hours cutting time.....	60
Figure 3.3: Graph of D and $G^+$ band ratio and $G^-$ and $G^+$ ratio versus cutting time. Each point represents the average of several individual spectra taken across a wide area on	

---

the sample, with error bars showing one standard deviation. Dashed line added to guide the eye.....	62
Figure 3.4: Histogram of G-band intensity for differing cutting times (2, 4 and 8 hours as indicated) of CNT attached to FTO glass for 24 hours and identical Raman laser intensity.....	63
Figure 3.5: XPS survey spectra of bare FTO and SWCNT functionalised FTO. ....	64
Figure 3.6: High resolution XPS spectra of; oxygen 1s binding region (A) and carbon 1s binding region (B) for bare FTO, oxygen 1s binding region (C) and carbon 1s binding region (D) for SWCNT functionalised FTO.....	65
Figure 3.7: CV plots for ferrocene in solution with bare FTO working electrode. (A) Graph showing relationship between peak current and square root of scan rate. (B)..	67
Figure 3.8: Plot of anodic and cathodic peak potential ( $E_p$ ) versus the natural logarithm of scan rate ( $v$ ) for the bare FTO working electrode. ....	68
Figure 3.9: CV plots for ferrocene in solution with SWCNT functionalised working electrode. Scan rate: (innermost) $20\text{mV}\cdot\text{s}^{-1}$ , $50\text{mV}\cdot\text{s}^{-1}$ , $100\text{mV}\cdot\text{s}^{-1}$ , $200\text{mV}\cdot\text{s}^{-1}$ , $300\text{mV}\cdot\text{s}^{-1}$ , $400\text{mV}\cdot\text{s}^{-1}$ , $500\text{mV}\cdot\text{s}^{-1}$ (outermost). (A) Graph showing relationship between peak current and square root of scan rate. (B) .....	69
Figure 3.10: Plot of peak anodic and cathodic potential ( $E_p$ ) versus the natural logarithm of scan rate ( $v$ ) for the SWCNT functionalised working electrode.....	69
Figure 3.11: Comparison of CV plots for both the bare FTO working electrode and the SWCNT functionalised working electrode at the same scan rate. (Scan rate = $100\text{mV}\cdot\text{s}^{-1}$ ) .....	70
Figure 3.12: Typical Nyquist plot for a DSSC. Modified From <i>Wang et al.</i> <sup>138</sup> .....	71
Figure 3.13: Nyquist plot (A) and Bode plot (C) (without illumination) for a freshly prepared and aged FTO-SWCNT electrochemical solar cells. (B) Shows the enlarged high frequency area. Cells were stored in the dark between testing.....	72

---

Figure 3.14: Platinum symmetrical cell in dark (A). SWCNT symmetrical cell in light (B). .....	74
Figure 3.15: Equivalent circuits used for electrochemical solar cell modelling.....	74
Figure 3.16: ‘Normal’ cell Nyquist plot (A) and Bode plot (B) for both measured and simulated data using symmetrical cells. ....	75
Figure 3.17: On-Off light response from FTO-CNT cell and blank cell containing no CNT. The arrows indicate the light on and off cycle. (CNT attachment time was 24 hours and cutting time was 8 hours. Points are separated by 200ms. Light intensity $35\text{mW.cm}^{-2}$ ) .....	76
Figure 3.18: Light soaking response of the cell (From Figure 3.17) left under illumination for over 200 minutes. Dashed line added to show gradual increase in current. Light intensity $35\text{mW.cm}^{-2}$ . ....	77
Figure 3.19: J-V curves for FTO-SWCNT solar cell with incident intensity of $35\text{mW.cm}^{-2}$ and $100\text{mW.cm}^{-2}$ . ....	78
Figure 3.20: J-V curves for a FTO-SWCNT cell under illumination ( $100\text{mW.cm}^{-2}$ ) and darkness. ....	79
Figure 3.21: Peak current versus CNT attachment time (A). Peak voltage versus CNT attachment time (B). Light intensity is $35\text{mW.cm}^{-2}$ . ....	80
Figure 3.22: Graph of current versus CNT cutting time (A) and voltage versus CNT cutting time. (B) Light intensity is $35\text{mW.cm}^{-2}$ Error bars show 10% experimental error.. .....	81
Figure 3.23: Wavelength response of FTO-SWCNT solar cell along with UV-Vis absorption spectrum of SWCNT solution.....	84
Figure 3.24: Spectral response of FTO-SWCNT solar cells of different SWCNT cutting times. (A) Photovoltage, (B) photocurrent density and (C) power output.....	85

Figure 3.25: SEM images of CNT modified surfaces. (A-B) MWCNT attached to FTO, (C-D) SWCNT attached to FTO. ....	86
Figure 3.26: Raman spectra comparing SWCNT and MWCNT chemically attached to FTO (A). Enlargement of G band region (B). ....	87
Figure 3.27: CV Plots for ferrocene in solution with MWCNT functionalised working electrode. (A) Graph showing relationship between peak current and square root of scan rate. (B) .....	88
Figure 3.28: Plot of anodic and cathodic peak potential ( $E_p$ ) versus the natural logarithm of scan rate ( $v$ ) for the MWCNT functionalised working electrode. ....	89
Figure 3.29: Comparison of CV plots for bare FTO, SWCNT and MWCNT functionalised FTO, along with a table summarising these values.....	90
Figure 3.30: XPS survey spectra for bare FTO and MWCNT functionalised FTO. ....	91
Figure 3.31: High resolution XPS of O1s (A) and C1s Regions (B) for FTO-MWCNT. ....	92
Figure 3.32: J-V curve comparison for MWCNT and SWCNT solar cells, along with tabulated $J_{sc}$ , $V_{oc}$ and power values. ....	93

## **Chapter 4**

Figure 4.1: DPV of unmodified and N3 modified CNT arrays (24 Hours attachment time). DPV of N3 in solution (Inset).....	97
Figure 4.2: N3 peak current vs. CNT exposure time on silicon. (Dashed line added to guide the eye) .....	98
Figure 4.3: DPV comparison of N3 functionalised SWCNT arrays on both silicon and FTO substrates.....	99
Figure 4.4: Background subtracted cyclic voltammograms of FTO-CNT-EDA-N3 (2hr SWCNT attachment time). (A) Graph of peak current versus scan rate. (B) .....	100

- Figure 4.5: Plot of anodic and cathodic peak potential ( $E_p$ ) versus  $\ln(v)$  for N3 functionalised SWCNT on FTO. .... 102
- Figure 4.6: J-V comparison between SWCNT and N3 functionalised SWCNT cells. (A) J-V comparison of 2 and 24 hour attachment times for N3-SWCNT cells. (B) Light intensity is  $35\text{mW}\cdot\text{cm}^{-2}$ . .... 104
- Figure 4.7: On-Off light response for 24Hr CNT modified with N3. (A) On-Off light response for unmodified 24Hr CNT produced at similar time (B) Light intensity  $35\text{mW}\cdot\text{cm}^{-2}$ . .... 105
- Figure 4.8: Cyclic voltammograms of RuTTP in  $\text{CH}_2\text{Cl}_2$ . Dashed line is the background subtracted trace showing two reversible oxidation peaks. .... 106
- Figure 4.9: Background subtracted DPV of RuTTP functionalised SWCNT array for 2hrs and 24 hrs of SWCNT attachment. .... 108
- Figure 4.10: Comparison of the J-V Curves for RuTTP functionalised cells with 2 and 24 hours of SWCNT attachment. Light intensity  $35\text{mW}\cdot\text{cm}^{-2}$ . .... 109
- Figure 4.11: Comparison of the J-V curves from RuTTP and N3 functionalised cells. (Both cells used 2 hours of SWCNT attachment) .... 110
- Figure 4.12: Normalised Raman spectra for the G-0.5 and G-2.0 modified surface. The graphitic or G band and the disorder or D band are labelled. .... 112
- Figure 4.13: DPV of p-phenylenediamine solution and G-0.5 modified SWCNT. .... 113
- Figure 4.14: Background subtracted DPV for G-0.5 and G-2.0 modified array. Plot of peak voltage and FWHM versus dendron generation. (Inset) .... 114
- Figure 4.15: Bode plots for the different dendron generations. Solid lines correspond to fit using an equivalent circuit. .... 115
- Figure 4.16: (A) Plot comparing DPV peak height and photoresponse. (B) Plot comparing EIS resistance and photoresponse. (C) Plot comparing EIS capacitance and

photoresponse. Error bars are from fitting of equivalent circuit and smoothed line present to guide the eye..... 117

Figure 4.17: J-V curve for the unmodified SWCNT array (G-0.0) and the 2<sup>nd</sup> generation dendron modified array (G-2.0). Light intensity 100mW.cm<sup>-2</sup>. Also included are the dark current curves with no illumination. .... 118

Figure 4.18: Spectral response of unmodified SWCNT cell (G-0.0) as seen in Chapter 3 and UV-Vis of SWCNT in solution. (A) Response of the dendron modified cell (G-2.0 and G-2.5) and the UV-Vis of the dendrimer in solution. (B) ..... 120

Figure 4.19: Schematic of N3 dye modification of successive generations of dendron. .... 122

Figure 4.20: DPV comparison of different generations of N3 modified dendrons. Dashed line is DPV for N3 in solution. .... 124

Figure 4.21: Background subtracted cyclic voltammograms with increasing scan rate for G-1.5-N3 modified substrate. (A) Plot of peak current versus scan rate from CV plots. (B) Plot of peak voltage versus the natural log of scan rate. (C) ..... 125

Figure 4.22: Bode (A) and Nyquist (B) plots for G-1.5 and G-1.5-N3 electrochemical solar cells under illumination. Dashed line represents fit from an equivalent circuit diagram. .... 128

Figure 4.23: Comparison of J-V curves for G-1.5 and G-1.5-N3 modified SWCNT array. (A) J-V curves for successive generations of N3 modified dendrons. (B) Light intensity is 100mW.cm<sup>-2</sup> ..... 130

Figure 4.24: Trend for DPV peak current and photocurrent for N3 modified dendrons. .... 131

## **Chapter 5**

Figure 5.1: SEM images of tCVD grown CNT array on silicon. .... 135

---

Figure 5.2: tCVD CNTs grown with a nickel catalyst. ....	136
Figure 5.3: CV plots for ferrocene in solution with bare silicon working electrode. (A) Graph showing relationship between peak current and square root of scan rate. (B) .....	137
Figure 5.4: CV plots for ferrocene in solution with tCVD functionalised working electrode. (A) Graph showing relationship between peak current and square root of scan rate. (B) .....	137
Figure 5.5: Comparison of CV plots for bare silicon and tCVD grown CNT on silicon at an identical scan rate ( $100\text{mV}\cdot\text{s}^{-1}$ ).....	138
Figure 5.6: Plot of anodic and cathodic peak potential ( $E_p$ ) versus the natural logarithm of scan rate ( $v$ ) for the tCVD functionalised working electrode. ....	139
Figure 5.7: Comparison between tCVD grown SWCNT arrays and purchased MWCNT arrays chemically attached to FTO glass. ....	140
Figure 5.8: XPS survey spectrum of bare silicon. ....	141
Figure 5.9: XPS survey spectrum of silicon after 5nm iron deposition. ....	142
Figure 5.10: High resolution XPS spectrum of oxygen 1s binding region for silicon after iron catalyst layer deposition.....	143
Figure 5.11: Survey XPS spectrum of tCVD MWCNT surface. ....	144
Figure 5.12: High resolution XPS spectra of O1s binding region (A) and C1s binding region (B) for the tCVD MWCNT surface. ....	145
Figure 5.13: XPS spectra comparing each step of tCVD CNT growth.....	146
Figure 5.14: J-V curve for tCVD grown and chemically attached MWCNT. Light intensity $100\text{mW}\cdot\text{cm}^{-2}$ .....	147

---

Figure 5.15: SEM images of ITO coated quartz slides. A) As received and B) after 750°C for 10 mins. ....	148
Figure 5.16: Angled SEM image of tCVD Modified ITO-quartz slide showing iron-no iron interface. (A) Zoom of single sphere on no iron side. (B) Zoom of single sphere on iron side. (C).....	149
Figure 5.17: EDX spectrum of spheres seen on ITO surface. ....	150
Figure 5.18: Side-on view of CNTs grown on ITO-quartz.....	150
Figure 5.19: SEM images of CNTs grown on ITO without hydrogen.....	151
Figure 5.20: Raman image (G-Band) of CNT covered sphere. (A) SEM image of a similar CNT covered sphere. (B) .....	152
Figure 5.21: Raman spectra of the tCVD CNTs grown on ITO-quartz. ....	153
Figure 5.22: Scanning electron microscopy images of the patterned substrate after CNT growth at different magnifications. The scale bars are 500µm (A), 50µm (B), 10µm (C) and 2µm (D). ....	155
Figure 5.23: Comparison of CV plots for bare silicon, tCVD and PECVD grown CNT on silicon at identical scan rates (100mV.s <sup>-1</sup> ).....	156
Figure 5.24: CV plots for ferrocene in solution with PECVD functionalised working electrode. (A) Graph showing relationship between peak current and square root of scan rate. (B) .....	157
Figure 5.25: Plot of anodic and cathodic peak potential (E <sub>p</sub> ) versus the natural logarithm of scan rate (v) for the PECVD functionalised working electrode.....	157
Figure 5.26: Raman spectra corresponding to the patterned area (SWCNT) and unpatterned area (Silicon). Inset is a 100x100µm image plotting the intensity of the G band at 1590cm <sup>-1</sup> showing the boundary between where the masked areas. ....	159

Figure 5.27: Enlargement of Raman G Band region showing $G^-$ peak at $1570\text{cm}^{-1}$ and $G^+$ peak at $1590\text{cm}^{-1}$ , characteristic of semi-conducting SWCNT.....	160
Figure 5.28: Raman spectra with changing growth time (A) and growth temperature (B). .....	162
Figure 5.29: Raman spectra for nickel and iron catalysts showing D and G Bands (A). Spectra for aluminium underlay present and no aluminium layer. (B) .....	163
Figure 5.30: XPS survey spectra for bare silicon, silicon after iron deposition and finally after PECVD growth has occurred.....	164
Figure 5.31: High resolution XPS spectrum of C1s binding region. ....	165
Figure 5.32: J-V curves for PECVD grown SWCNT electrode and chemically attached SWCNT electrode. Light intensity $100\text{mW.cm}^{-2}$ .....	166
Figure 5.33: J-V curves for PECVD grown SWCNT electrode and tCVD MWCNT electrode. Light intensity $100\text{mW.cm}^{-2}$ .....	167

## Tables

### Chapter 1

Table 1.1: Comparison between carbon nanotubes and silicon. Modified from <i>Zhu et al.</i> <sup>59</sup> .....	16
---	----

### Chapter 2

Table 2.1: List of wavelength filters used in this work.....	44
Table 2.2: Raman spectral features of carbon nanotubes with laser energy 2.41eV. Modified from <i>Dresselhaus et al.</i> <sup>69</sup> .....	53

### Chapter 3

---

Table 3.1: Frequency ( $f$ ) and effective electron lifetime ( $\tau_{\text{eff}}$ ) for fresh and aged cells..	73
Table 3.2: Integrated area under histogram peaks from Figure 3.4, and current from Figure 3.22.....	82
Table 3.3: Raman D/G ratio for SWCNT and MWCNT modified FTO.....	88

## **Chapter 4**

Table 4.1: Comparison of redox active molecules chemically attached to SWCNT arrays. .....	101
Table 4.2: Surface concentration and electron transfer coefficients of N3 dye for successive dendron generations.....	127
Table 4.3: Summary of resistance and capacitance values produced by fitting an equivalent circuit model to the data shown in Figure 4.22. ....	129
Table 4.4: Photocurrent, photovoltage and total power for N3 modified surfaces.....	131

## **Chapter 5**

Table 5.1: Methane dissociation reactions. From <i>Mao et al.</i> <sup>83</sup> .....	154
---	-----

# Abbreviations

4-Aminopyridine	4-AP
Air Mass	AM
Acetylene	C <sub>2</sub> H <sub>2</sub>
Counter Electrode	CE
Methane	CH <sub>4</sub>
Carbon Nanotube	CNT
Constant Phase Element	CPE
Cyclic Voltammetry	CV
Chemical Vapour Deposition	CVD
Disorder Raman Band	D-Band
N,N'-Dicyclohexylcarbodiimide	DCC
Dichloromethane	DCM
De-Ionised	DI
4-Dimethylaminopyridine	DMAP
N,N-Dimethylformamide	DMF
Dimethyl Sulfoxide	DMSO
Density of States	DOS
Differential Pulse Voltammetry	DPV
Dye Sensitised Solar Cell	DSSC
Ethylenediamine	EDA
Energy Dispersive X-ray Analysis	EDX
Electrochemical Impedance Spectroscopy	EIS
Peak Potential	E <sub>p</sub>
Fill Factor	<i>ff</i>
Fluorine Doped Tin Oxide	FTO
Full Width Half Maximum	FWHM
Graphitic Raman Band	G-Band
Hydrogen Peroxide	H <sub>2</sub> O <sub>2</sub>
Sulphuric Acid	H <sub>2</sub> SO <sub>4</sub>
Nitric Acid	HNO <sub>3</sub>
Iodide/Tri-iodide	I <sup>-</sup> /I <sub>3</sub> <sup>-</sup>

Inductively Coupled Plasma	ICP
Incident Photon to Current Efficiency	IPCE
Indium Tin Oxide (In <sub>2</sub> O <sub>3</sub> 90% - SnO <sub>2</sub> 10%)	ITO
Current-Voltage	I-V
Short Circuit Current Density	$J_{sc}$
Current Density-Voltage	J-V
Electron Transfer Co-efficient	$k_s$
Multi-Walled Carbon Nanotube	MWCNT
<i>cis</i> -bis(isothiocyanato)bis(2,2'-bipyridyl-4,4'-dicarboxylato)-ruthenium(II)	N3
Poly(amidoamine)	PAMAM
P-Phenylenediamine	PDA
Plasma Enhanced Chemical Vapour Deposition	PECVD
Radial Breathing Mode	RBM
Reference Electrode	RE
Ruthenium Tetrphenyl Porphyrin	RuTPP
Standard Cubic Centimetres per Minute	SCCM
Scanning Electron Microscopy	SEM
Single-Walled Carbon Nanotube	SWCNT
Tetrabutylammonium Hexafluorophosphate	TBAPF <sub>6</sub>
Thermal Chemical Vapour Deposition	tCVD
Transmission Electron Microscopy	TEM
Titanium Dioxide, Titania	TiO <sub>2</sub>
Ultra-Violet-Visible Light Spectroscopy	UV-Vis
Open Circuit Voltage	$V_{oc}$
Working Electrode	WE
X-ray Photoelectron Spectroscopy	XPS
Real Component of Impedance	$Z'$
Imaginary Component of Impedance	$Z''$
Global Efficiency	$\eta$
Scan Rate	$\nu$
Raman Frequency	$\omega$

---

# **1. Introduction**

---

## 1.0 Power Generation

Sustainable energy production is one of the key scientific challenges for humanity and with its realization many of the world's current challenges can be solved. Traditional methods of energy production have included combustion of fossil fuels (e.g. coal, oil and natural gas), nuclear fission and to a much smaller degree renewable energy sources (e.g. solar, wind, hydroelectric, tidal and geothermal). However, the limitations of fossil fuel based energy generation have become more and more prevalent in the past decade. Environmental ramifications and supply limitations continue to be a key area of debate amongst both the scientific community and the general public. Nuclear fission is one alternative method of energy production which although producing almost no carbon dioxide (CO<sub>2</sub>) still has negative connotations within the general public. Recently there has been a significant push towards alternative clean renewable energy sources. Of these solar power provides the highest quantity, most widely available and most stable energy source. By contrast other forms of renewable energy production are limited to specific areas, such as rivers for hydroelectric power, meteorological conditions for wind power and geologically limited areas with active geothermal power. Solar energy allows for decentralised power generation which has significant advantages, the most obvious being no transmission losses over large distances that must occur with centralised power plants.<sup>1</sup> Solar power also has an abundant supply. Every minute the amount of solar energy incident on the Earth is far greater than the energy provided by fossil fuels in an entire year.<sup>2</sup> However, photovoltaics, devices that convert solar radiation to electricity, make up only 0.04% of power generated.<sup>2</sup> This is due to high costs, both financially and energetically, involved due to expensive manufacturing processes and low energy conversion efficiencies.

The photovoltaic effect was first discovered by *Becquerel* in 1839<sup>3</sup> but was not until 1940 that *Ohl* constructed a p-n silicon junction that achieved significant voltage.<sup>4</sup> Since then the photovoltaic effect has been the subject of increased interest with amorphous and crystalline silicon, thin films of semiconductors such as gallium arsenide, cadmium arsenide and more recently polymers, nanocrystals and dye-sensitisation all being investigated. The market for solar cells has remained small

however, with over 80% of those in use being the so called first-generation p-n silicon junctions. Initially there was very low uptake of solar power technology. It wasn't until the use of solar panels in the 1960s and 1970s for space exploration that they had received much interest at all. This was mainly due to the relative abundance and low cost of fossil fuels throughout that time period. However, increasing costs, detrimental environmental effects and geopolitics affecting supply the push for cheaper and more efficient solar cells has been revived.

## 1.1 Photovoltaics

Photovoltaic devices or solar cells convert radiation, usually in the visible wavelength range (400-750nm), into electricity. This can be performed via several different mechanisms. The majority of commercially available solar cells work on what is known as a p-n junction, whereby incident photons create exciton pairs consisting of an electron and a hole. Traditional p-n junction solar cells require doped semiconductor material that can be very expensive to produce in sufficient purity and will be discussed in more detail in section 1.1.1. Another form of solar power production is electrochemical solar cells, which mimic the process of photosynthesis in plants by using a metal based organic molecule to absorb the light and excite an electron, creating an oxidised dye that is then reduced by an electrolyte upon completion of the circuit. To compare and analyse a solar cell's efficiency standard conditions must be chosen, as the intensity of solar radiation fluctuates depending on time of day, latitude and weather. To compensate for the changing angle of the sun a system called air mass values is used. Air mass values (AM) are used to determine the angle the sun is from the Earth's surface and thus the amount of atmosphere that the light has had to traverse, as seen in the Figure 1.1 inset. A thinner atmosphere leads to a higher intensity light due to the decrease in reflection and scattering processes, whilst a thick atmosphere will reduce the incident intensity. AM 0 corresponds to normal incident light with no atmosphere, and is most relevant for use in space (i.e. satellites and space stations). AM 1.0 is light also at normal incidence onto the Earth's surface; this is the least amount of atmosphere for a terrestrial based solar cell. Throughout a normal day the angle of the sun changes and so an average value of AM 1.5 is used, this is the sun at  $48.2^\circ$  from normal incidence and is accepted as the standard conditions to

evaluate a solar cell performance for a real world application. At AM0 the intensity of sun light is on average  $135.3\text{mW}\cdot\text{cm}^{-2}$ , whilst at AM1.0 this value decreases to  $92.5\text{mW}\cdot\text{cm}^{-2}$  and AM1.5 is  $84.4\text{mW}\cdot\text{cm}^{-2}$ .<sup>5</sup> Thus the standard light intensity for solar cell testing is chosen to be  $100\text{mW}\cdot\text{cm}^{-2}$  to make the calculation of efficiency simpler. The choice to focus on visible light over ultra-violet or infrared becomes clear when we look at the solar spectrum, seen in Figure 1.1, where the highest spectral irradiance occurs for visible light between 300-800nm. The sudden drops in spectral irradiance are caused by the infrared absorbance of  $\text{H}_2\text{O}$ ,  $\text{CO}_2$ ,  $\text{O}_2$  and other species present in the atmosphere. The maximum in energy is seen at around 550nm and thus a solar cell should strive to be most sensitive to this wavelength range.

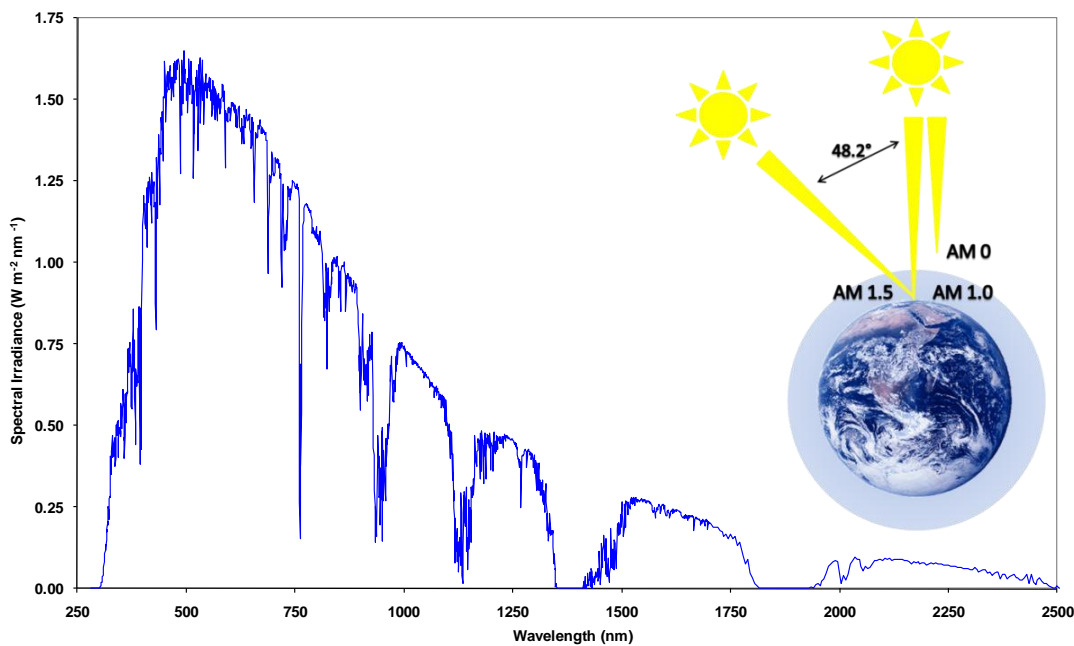
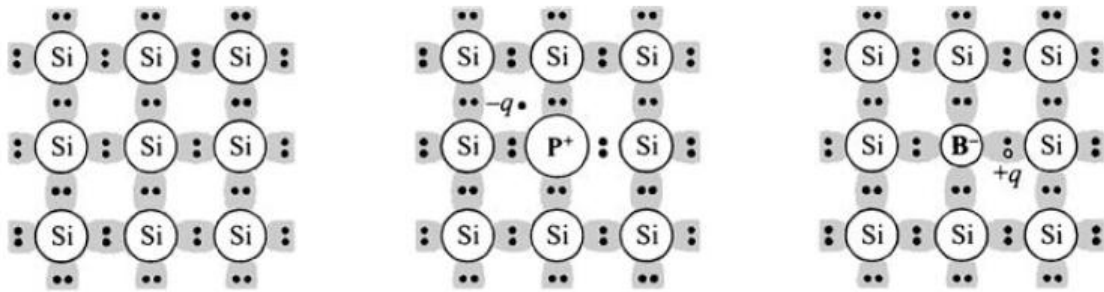


Figure 1.1: AM1.5 solar spectrum (Inset: air mass schematic showing; AM 0, AM 1.0 and AM 1.5), spectrum reproduced from ASTM G173-03.<sup>6</sup>

### 1.1.1 Silicon Solar Cells

When discussing photovoltaics or solar cells most people think of the widely commercially available polycrystalline solar cell, a solid state cell. These solid state silicon based solar cells are referred to as generation one cells. Silicon can exist as an intrinsic semi-conductor due to the relative energy levels of its four outer shell

electrons. At room temperature the intrinsic band gap of silicon is 1.12eV, equivalent to a photon with a wavelength of 1108nm. However, through the process of doping, or the implantation of charge carriers, silicon can have its electronic configuration altered, modifying its band structure.<sup>7-9</sup>. The two types of doping are 'n' (negative) and 'p' (positive). In n-type doping a species, typically a pentavalent or group 5 species such as phosphorous or arsenic is implanted to provide an excess of electrons. As a result of the fact that the dopant has five valence electrons, one is left un-bound to the silicon crystal lattice and is free to move around providing an extra electron energy level within the band gap, lowering the required energy for a transition to the conduction band. In p-type doping a species, typically a trivalent species from group 3 such as boron or gallium, is implanted into the silicon lattice to provide an excess of holes. These holes are caused because the dopant has only three valence electrons and leaves a hole that acts as a positive charge. This can be seen schematically in Figure 1.2.



**Figure 1.2: A) Intrinsic silicon B) n-Type silicon with phosphorous dopant C) p-Type silicon with boron dopant. From Sze *et al.*<sup>5</sup>**

This process of doping determines whether the silicon will have an abundance of electrons or holes and the location of the Fermi level. By constructing a junction consisting of both n and p type silicon in electrical contact with one another an incident photon of light with energy equal to or greater than the band gap means an electron can be excited from its ground state into the conduction band and hence allowed to flow, leading to electricity. Conversely, a hole is created and flows in the opposite direction. Figure 1.3 schematically shows a p-n junction at the interface. When placed in contact with one another and with no external stimuli, such as electric fields, and in thermal equilibrium, the excess electrons from the n-doped side will begin to diffuse into the p-doped side until equilibrium is achieved.<sup>5</sup> By exposing the

interface to light an electron-hole pair is created. Figure 1.3 shows the respective energy levels for the valence and conduction bands for each semi-conductor material, and then the flow of electrons (filled dot) and holes (empty dot) through each material.

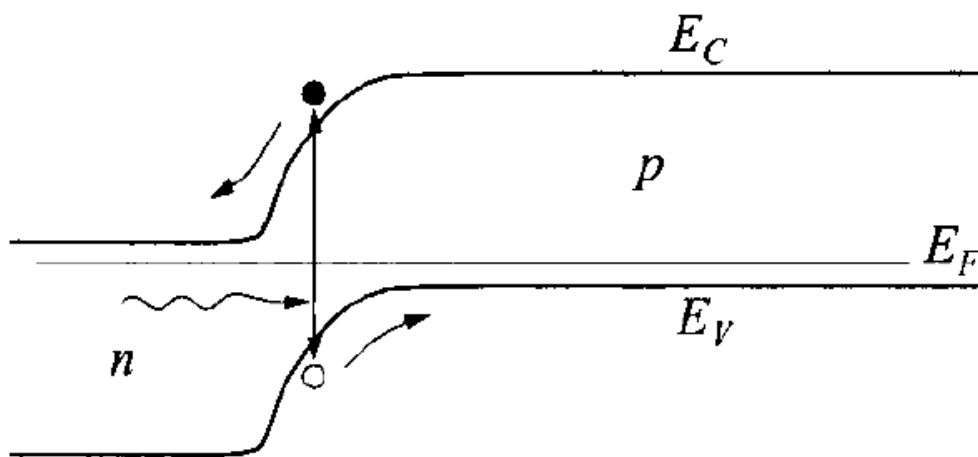


Figure 1.3: Energy band diagram of a p-n junction showing photogenerated electron-hole pair.  $E_V$  is the valence band energy,  $E_F$  the Fermi energy and  $E_C$  the conduction band energy. From Sze *et al.*<sup>5</sup>

However, to produce p-n junctions of sufficient purity and with the required lack of defects expensive purification techniques are required. These first generation solar cells are energetically inefficient, taking between 3 to 5 years running at peak efficiency recoup the energy initially required to produce the cell.<sup>10</sup> A direct band gap means that both the conduction and valence bands are aligned and an exciton can transfer directly between them, an indirect band gap is where there is a mismatch between the two energy levels and a phonon is needed to assist the transition. This indirect band gap means that silicon cells must have a minimum thickness of approximately 125 $\mu\text{m}$  to be efficient, compared to 0.9 $\mu\text{m}$  for a direct band gap material.<sup>11</sup> This leads us to attempt to find superior materials for the construction of photovoltaics.

### 1.1.2 Dye Sensitised Solar Cells

In 1991 Brian O'Regan and Michael Grätzel published a paper entitled "A Low-Cost, High-Efficiency Solar-Cell Based on Dye-Sensitized Colloidal  $\text{TiO}_2$  Films." in the journal *Nature*,<sup>12</sup> and with this an entirely new system for generating electricity from light became highly publicised and created the now termed "Grätzel Cell". The Grätzel

cell or dye sensitised solar cell (DSSC) has since become an area of fervent research over the past two decades. A schematic of this system is shown in Figure 1.4, showing the flow of electrons and the iodide redox couple. The DSSC works on what is sometimes called artificial photosynthesis whereby an organic molecule, a dye, is attached to a film of nanoparticles of the semiconductor titania (titanium dioxide,  $\text{TiO}_2$ ) supported by a transparent conducting layer, often ITO. This ITO layer provides an electrically conductive substrate as well as allowing light through to excite the dye. When an incident photon impacts the dye molecule its energy is absorbed and the dye is excited. The dye then injects an electron into the conduction band of the titania and the electron diffuses through the layer (a distance of typically  $10\mu\text{m}$ ) to the underlying supporting substrate. Once the electron has reached the working electrode it travels through an external circuit, performing work before returning to the cell via a platinum coated counter electrode. The platinum acts as a catalyst in reducing a redox couple used in the liquid electrolyte, typically iodide/triiodide ( $\text{I}^-/\text{I}_3^-$ ). The redox couple acts as an electron shuttle and transports the electron through solution in the form of ions. The iodide then reduces the dye back to its ground state, regenerating the starting position of the system. In Figure 1.4,  $D$  is the dye's ground state energy and upon excitation the electron moves to  $D^*$  the excited state, then into the conduction band of the titania. The total voltage provided by the system, the open circuit voltage  $V_{oc}$ , is the difference in the energy levels from the electrolyte redox potential  $E_r$  and  $E_f$ . The dye used in the initial 1991 paper was known as N3, a ruthenium based molecule with the systematic name of *cis*-bis(isothiocyanato)bis(2,2'-bipyridyl-4,4'-dicarboxylato)-ruthenium(II) (structure seen in Figure 1.5).



of  $J_{sc}$  and  $V_{oc}$  typically a value near 80% is expected for DSSCs. Lower fill factor values can be caused by low shunt resistance, or the unwanted short circuit between the working and counter electrodes, due to back reactions where the flow of electrons is reversed, which lower the cell's performance considerably. Series resistance can also reduce the fill factor of functional devices, and is caused the inherent materials properties such as the sheet resistance of the transparent conductive substrates used for both electrodes as well as the resistance of the electrolyte. By taking the optimal power output of the cell ( $P$ ) and dividing by the incident radiance of light the global efficiency ( $\eta$ ) can be calculated.<sup>13a</sup>

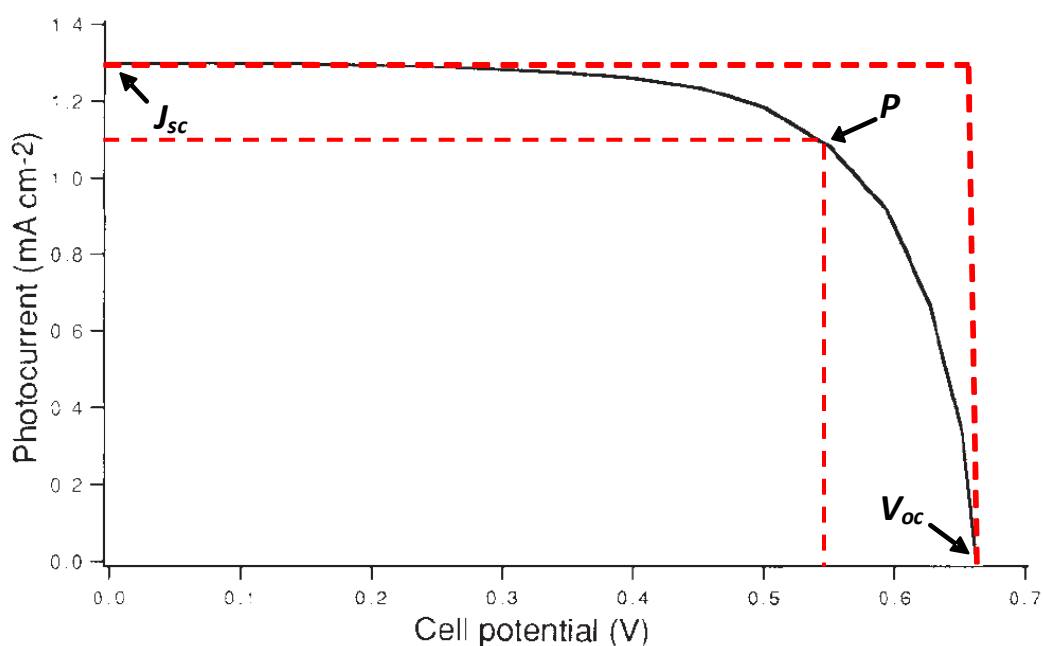
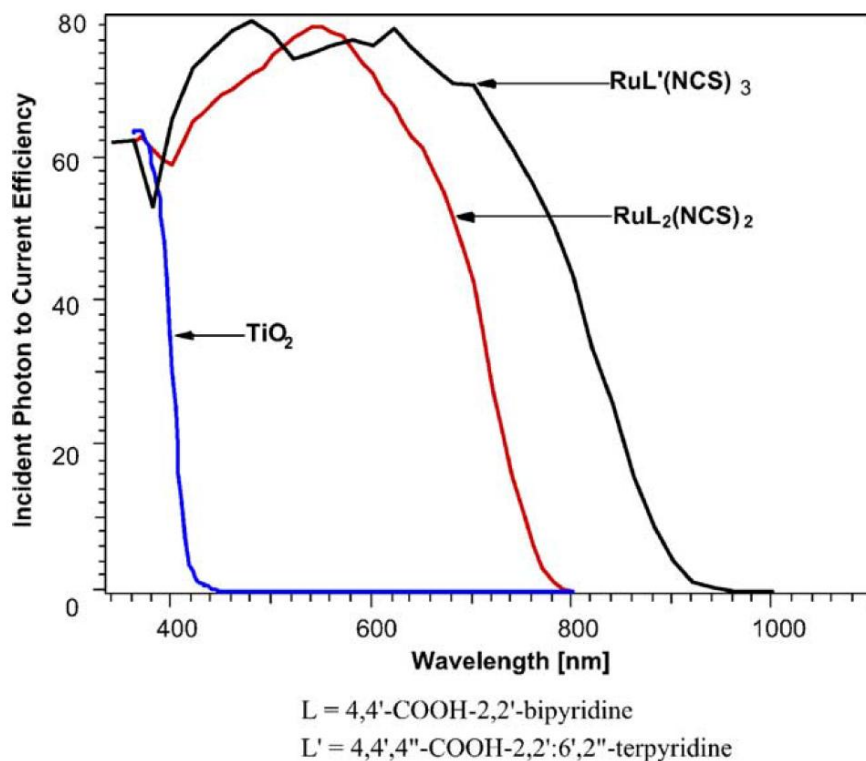


Figure 1.6: J-V curve of DSSC showing key properties. Modified from Grätzel *et al.*<sup>12</sup>

As well as acquiring J-V curves which demonstrate a cell's performance under the full solar spectrum, it is often important to know which wavelengths are producing the greatest response. To measure this, incident photon to current efficiency (IPCE) spectra are taken. In IPCE the cell is exposed to one wavelength at a time and the resultant current response is measured. Figure 1.7 shows the IPCE spectrum for a typical DSSC. The blue line shows the response of unmodified titania, showing negligible response at visible wavelengths until into the UV below 400nm. However, once modified with a dye, either N3 (red line) or N749 (black line), the response drastically changes, forming a peak at  $\approx 600$ nm with an IPCE of  $\sim 80\%$ . The position of

this peak depends on the absorption characteristics of the dye used, whilst the efficiency depends on the photoactive elements ability to create charge carriers. IPCE provides an excellent method to determine if modification has successfully occurred and if so, its influence on overall cell performance.



**Figure 1.7:** Incident photon to current efficiency for unmodified  $\text{TiO}_2$ , and  $\text{RuL}'(\text{NCS})_3$  or 'black dye' and  $\text{RuL}_2(\text{NCS})_2$  or 'N3' Dyes. From Grätzel *et al.*<sup>14</sup>

Since the publication of the initial Grätzel paper in 1991 there have been many attempts to improve the efficiency of DSSCs, with researchers trying to improve the efficiency to close to that of theoretical limits for such a system. This has been attempted using several methods, including changing the dye molecule,<sup>15-21</sup> changing the electrolyte and the redox couple,<sup>22-30</sup> replacing the platinum layer,<sup>31-39</sup> changing the morphology of the titania,<sup>40-43</sup> and recently integrating carbon nanotubes into the DSSCs design.<sup>40, 44-46</sup> Each of these methods will now be reviewed in more detail.

After initial work into photosensitisers by Nazeeruddin *et al.*<sup>15</sup> on what was to become known as N3 and N719, many attempts have been made to improve efficiency. These have included simply modifying the structure of N3 with different ligands, as is the case for the dyes shown in Figure 1.8.<sup>19, 20</sup> Other efforts have focussed on entirely

new organic molecules that replace the ruthenium.<sup>21</sup> However, many of these modifications offer only marginal improvement over the N3 dye, but often have benefits in terms of ease of production or lower cost.

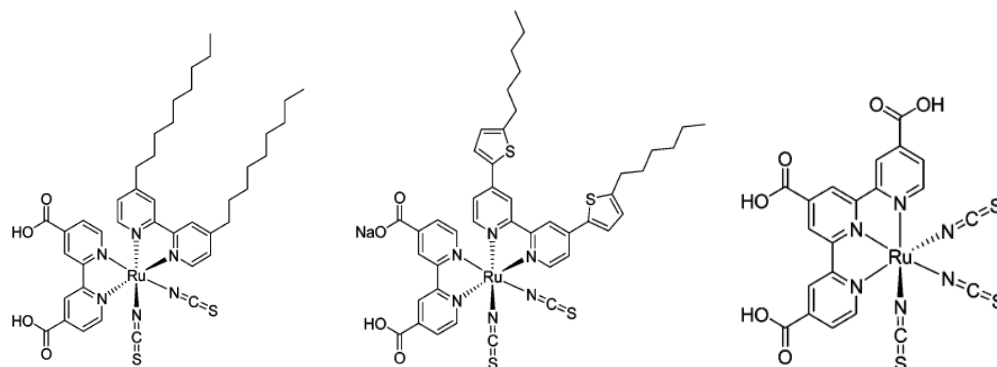


**Figure 1.8: Examples of alternative dye molecules; Z907, C102 and N749 (From left to right). From Meyer.<sup>20</sup>**

As described previously the open circuit voltage of a DSSC depends on the energy difference between the redox potential of the redox couple in the electrolyte and the conduction band of the titania. Thus, there would be an obvious benefit if the redox couple was modified to maximise this difference. This has been achieved with bromine,<sup>47</sup> selenium,<sup>30</sup> cobalt<sup>48</sup> and copper.<sup>28</sup> The chemical structures of frequently used copper complexes are shown in Figure 1.9 and show the increased level of complexity needed when using metal complexes instead of simple diatomic molecules such as bromine or iodine.

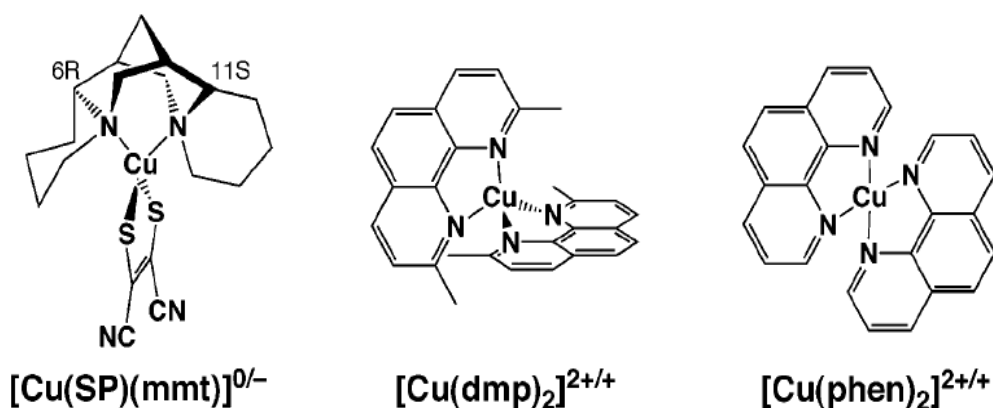


**Figure 1.9: Copper complexes used in DSSC electrolyte. From Hattori *et al.*<sup>28</sup>**

Another approach to decrease cost whilst maintaining efficiency has been the replacement of the platinum catalyst layer with carbon nanotubes. Carbon nanotubes have proven to be an excellent electrode material for the reduction of  $I_3^-$  due to their high conductivity and surface area. An example of this is shown in Figure 1.10 where a layer of multi-walled carbon nanotubes has been spray coated onto glass to act as the catalytic layer.

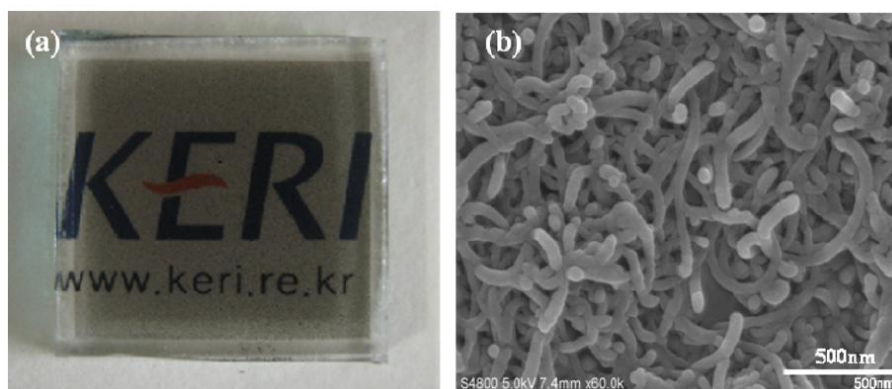


**Figure 1.10: Spray coated MWCNT for DSSC counter electrode. Optical image of coated glass slide (a), SEM image of nanotube layer (b). From Ramasamy *et al.*<sup>36</sup>**

Changing the morphology of the supporting electrode, to increase both the active surface area of the working electrode and the electron diffusion to the supporting electrode by having more directed flow, has also been attempted. To do this, titania can be replaced with zinc oxide (ZnO) which can be grown into nanowires<sup>43</sup> as seen in Figure 1.11. In this case the height of the nanowire array is  $\sim 20\mu\text{m}$ , and the main benefit of this cell architecture is the greatly decreased electron diffusion times.

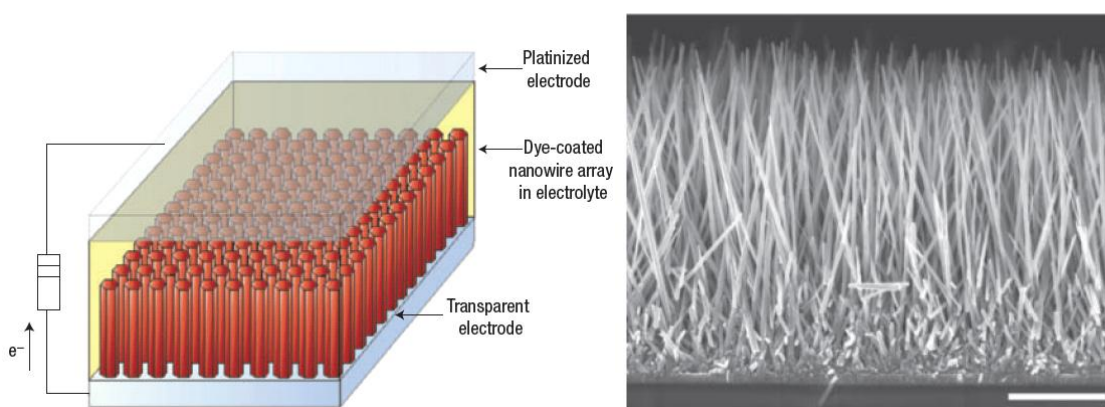


**Figure 1.11: ZnO nanowire array based DSSC. From Law *et al.*<sup>43</sup>**

Rather than only using metal oxides such as  $\text{TiO}_2$  or  $\text{ZnO}$ , the increased conductivity and interconnectivity that CNTs can offer has also been explored in standard DSSC design. By mixing in a dispersion of SWCNTs with the titania before depositing onto the electrode, the presence of a mixture that contains many highly conductive wires decreases the electron diffusion time that is normally needed through many layers of titania. An SEM image of such a dispersion, and the increased cell response are seen in Figure 1.12.

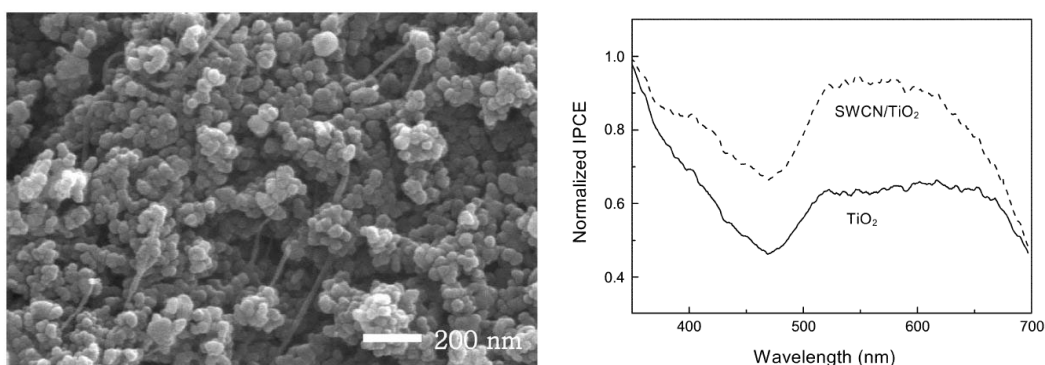


**Figure 1.12: Integration of SWCNT into existing DSSC. (Left) SEM image showing  $\text{TiO}_2$  particles and nanotube composite. (Right) IPCE spectra for  $\text{TiO}_2$  and  $\text{TiO}_2/\text{SWCNT}$  mixture. From Jung *et al.*<sup>46</sup>**

There has also been some work more recently on replacing the titania nanoparticles completely and replacing it with carbon nanostructures as the light harvesting element.<sup>49-61</sup> This in particular offers promise as it allows for modification and optimisation with a higher degree of control over the system.

## 1.2 Carbon Nanotubes

Carbon nanotubes (CNTs) have been the subject of significant research since the initial report of their production in a now famous publication in 1991.<sup>62</sup> CNTs can be thought of as rolled up sheets of graphene, illustrated in Figure 1.13A. Graphene is a one atom thick sheet of  $\text{sp}^2$  hybridised carbon atoms packed in a hexagonal array. Starting with a graphene sheet, this can be rolled up to form a single-walled carbon nanotube (SWCNT) seen in Figure 1.13B or a multi-walled carbon nanotube (MWCNT) seen in Figure 1.13C. MWCNTs exist as either the ‘Russian doll’ model where smaller diameter tubes sit concentrically inside progressively larger ones (pictured), or the ‘parchment’ model where the sheet is rolled in on itself several times, analogous to a rolled up parchment.

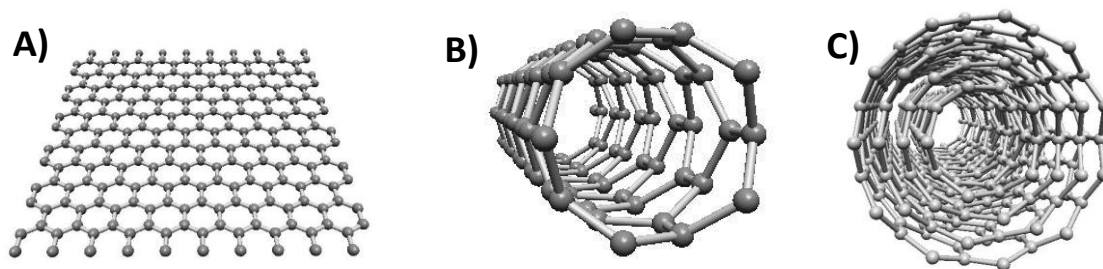


Figure 1.13: Graphene sheet (A), single-walled nanotube (B), multi-walled nanotube (C)

### 1.2.1 Structure of Carbon Nanotubes

One of the most direct methods for determining the structure of a particular CNT is through transmission electron microscopy (TEM). In Figure 1.14, TEM has been used to analyse several different kinds of MWCNTs, showing the core of the tube is hollow and surrounded by several layers of carbon. The number of walls and thickness between them can thus be determined. The number of walls can range from one for SWCNTs, to 2 for double-walled carbon nanotubes (Figure 1.14B) to many walls (Figure 1.14C, which has 7), providing a range of possible thicknesses and different possible applications for CNTs.

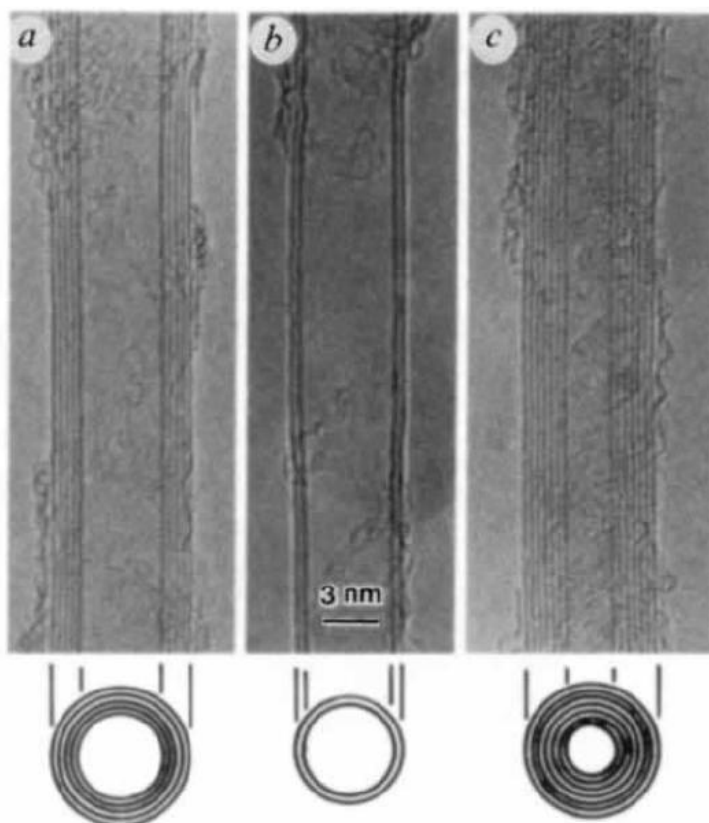
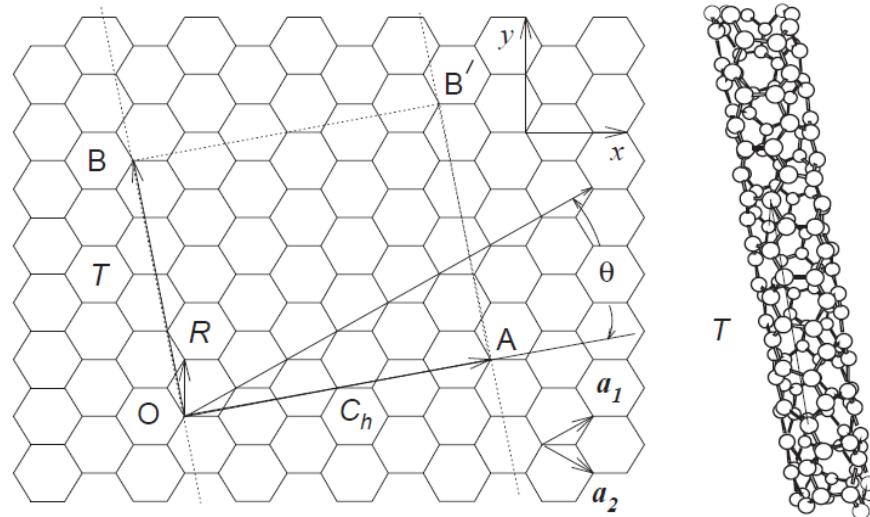


Figure 1.14: Transmission electron micrographs of MWCNTs. From Iijima.<sup>62</sup>

CNTs possess high conductivity, with carrier mobilities typically around  $10,000\text{cm}^2.\text{V}^{-1}.\text{s}^{-1}$ , an order of magnitude higher than silicon and a current density of  $4 \times 10^9\text{A}.\text{cm}^{-2}$ , three orders of magnitude higher than copper.<sup>63</sup> This high conductivity is due to the high amount of  $sp^2$  hybridisation giving rise to a large number of delocalised  $\pi$  electrons, which in turn leads to a complex density of states (DOS). This complex DOS means that both single and multi-walled nanotubes can exist as metallic conductors, but that single-walled can also exist as semiconductors. It is this semiconducting property that makes them of specific interest to the electronics industry.<sup>64-66</sup> Their physical properties such as a high tensile strength and a high strength to weight ratio also make them of great importance, especially to the materials industry.<sup>67</sup> It is their electronic properties that currently hold the most promise for device integration. Behaving as either semi-conducting or metallic has been found to be strongly dependent on both tube chirality and diameter.<sup>68</sup> Generally the larger the diameter of the nanotube, the more metallic characteristics are observed. Figure 1.15 shows how different chiralities of CNTs can be formed depending on the vector along which the tube is rolled, with each chirality possessing a different DOS and thus different electronic properties such as band gap and conductivity.



**Figure 1.15:** Schematic showing vectors that produce different chirality CNTs. The vectors OA and OB define the chiral vector  $Ch$  and the translational vector  $T$  of the nanotube, respectively. The rectangle OAB'B defines the unit cell for the nanotube. The figure is constructed for an  $(n, m) = (4, 2)$  nanotube. From Dresselhaus *et al.*<sup>69</sup>

The electronic properties of carbon nanotubes also make them of interest for application in photovoltaic devices. Table 1.1 summarises some of the key properties of CNTs and compares them to single crystal silicon, a material typically applied in solar cells. Clearly it can be seen that nanotubes present a lower density and more conductive alternative to silicon. This increased conductivity is apparent when we compare the carrier mobility. As mentioned previously, SWCNTs can be either metallic or semi-conducting. When semi-conducting, SWCNTs usually have a band gap between the valence and conduction electron bands that is typically in the range of 0.3-2.0eV, depending on their size and chirality.<sup>59</sup> The band gap is a direct gap and is inversely proportional to the diameter of the tube. Most CNTs are found to be p-type semi-conductors and so have had some applications in p-n junction solar cells.<sup>50, 58</sup> Thus, these properties show that carbon nanotubes would be an ideal material for use in photovoltaics.

**Table 1.1: Comparison between carbon nanotubes and silicon. Modified from Zhu et al.<sup>59</sup>**

Property	CNT	Silicon
Density (g/cm <sup>3</sup> )	0.8-1.2	2.33
Band Gap (eV, 300K)	0.3-2.0	1.12
Resistivity (Ωcm, 300K)	0.1	~1*
Electron Mobility (cm <sup>2</sup> /Vs, 300K)	1x10 <sup>8</sup>	<1400
Hole Mobility (cm <sup>2</sup> /Vs, 300K)	1x10 <sup>3</sup>	<500
Manufacture	Bottom Up	Top Down
Cost	~US\$50/g (SWCNT) ~US\$5/g (MWCNT)	~US\$0.2/g

\* Strongly Dependent on Dopant Concentration

### 1.2.2 Methods of Carbon Nanotube Production

For wide scale application in device integration CNTs need to be synthesised in significant yields and with sufficient control over their structural properties. Currently there are four methods adopted for CNT synthesis. Arc discharge was the first production technique applied to CNT growth, used by Iijima et al.<sup>62</sup> with increased yields demonstrated by Ajayan et al.<sup>70</sup> This technique involves having two graphite rods in close proximity to one another under an inert atmosphere such as argon and

then applying a bias between them. A plasma or arc is formed between the two rods and as the graphite is vapourised CNTs are formed on the surface of the rods. These can then be scraped off, purified by removing amorphous carbon and used. This method allows for large quantities of CNTs to be produced, but offers little control over chirality or number of walls, producing some SWCNTs and predominantly MWCNTs.

The second method of CNT production to be reported was via laser ablation, which was pioneered by Richard E. Smalley's group at Rice University.<sup>71</sup> This method again involved a graphite target in an inert atmosphere such as argon. The chamber was heated to 1200°C and a graphite target radiated with a Nd:YAG laser (1064nm). As the graphite vapourised it was collected on a water cooled copper collector as CNTs. The main advantage of this technique was that the CNTs produced contained a much higher proportion of SWCNTs than those produced with arc discharge. The nanotubes produced during laser ablation were also found to be much cleaner, that is lacking amorphous carbon, than was often found in arc discharge tubes. However, it was considerably more expensive to produce equal yields compared to arc discharge.

Currently the most successful technique, in terms of yield, for producing CNTs is thermal chemical vapour deposition (tCVD), which is the third method for CNT production. In tCVD a catalyst layer, typically a transition metal such as iron or nickel, is deposited on a substrate such as silicon. This substrate is then placed into a furnace and heated under a reducing atmosphere of hydrogen to form nanoparticles. A carbon feedstock gas such as methane or acetylene is then introduced along with an inert gas, hydrogen and an oxidant such as water to produce high quality arrays.<sup>72</sup> This particular method of using water vapour to help reduce amorphous carbon is referred to as water-assisted CVD or the 'super growth' method. Figure 1.16 shows vertically aligned arrays of CNT produced by water-assisted CVD. The yield of these CNTs is extremely high and the largest benefit comes from directed and patterned growth as seen in the image. The ability to grow highly aligned dense arrays of SWCNT in a defined area greatly increases the applicability of CNT to device integration.

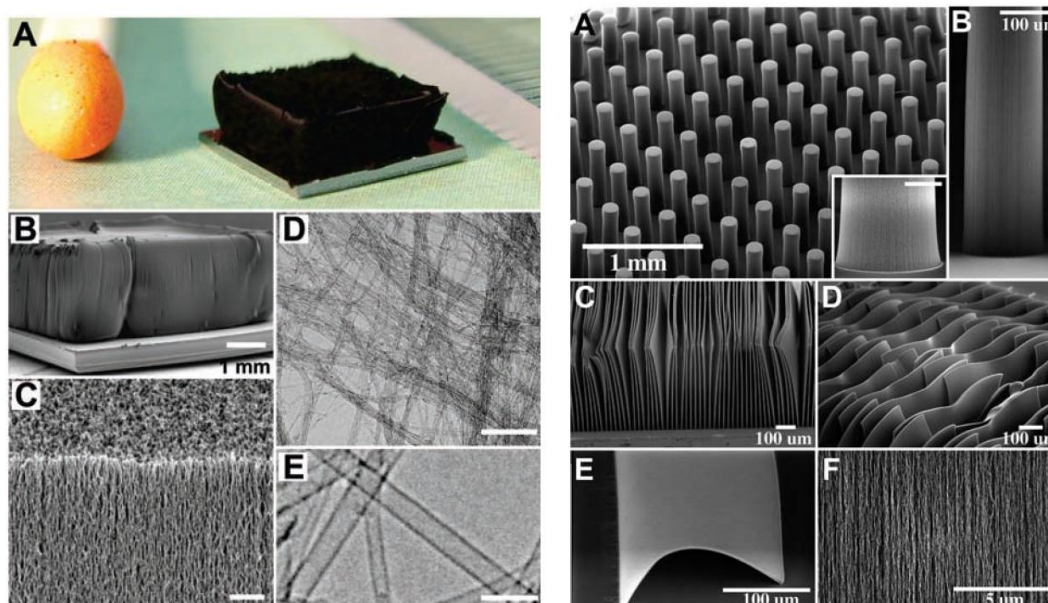


**Figure 1.16: Examples of patterned CNT arrays produced by tCVD showing pillars and sheets of dense single-walled carbon nanotubes. From Hata et al.<sup>72</sup>**

The fourth method of CNT production is plasma enhanced chemical vapour deposition (PECVD), and has several advantages over thermal CVD. The use of plasma to dissociate the carbon feedstock allows for lower growth temperatures, with theory even predicting growth could occur at room temperature.<sup>73</sup> Many kinds of plasma such as microwave,<sup>74, 75</sup> direct current,<sup>76, 77</sup> capacitively coupled<sup>78, 79</sup> and inductively coupled<sup>80-83</sup> have been used for CNT growth. The most frequently used method is inductively coupled plasma (ICP). Conditions for PECVD CNT growth have varied greatly. Plasma powers have ranged from 0-3000W, pressures ranging from 20mTorr to 20Torr, gas mixtures including methane, acetylene, ammonia, argon and hydrogen in varying ratios and temperatures ranging from 27°C to 1000°C.<sup>83</sup> Figure 1.17 shows some typical SEM images of CNT arrays produced by PECVD. When PECVD was first applied for the growth of CNTs there were many unanswered questions and the growth of SWCNT was at first not possible. In a PECVD review in 2003 *M. Meyyappan* made a comprehensive list of important questions aimed at the PECVD community<sup>84</sup> and these indicated that there was much more research needed especially to create SWCNT. Several years later a subsequent review addressed many of these unanswered questions<sup>85</sup> which illustrates the increased focus on PECVD as a technique for the synthesis of CNTs, in particular SWCNT.

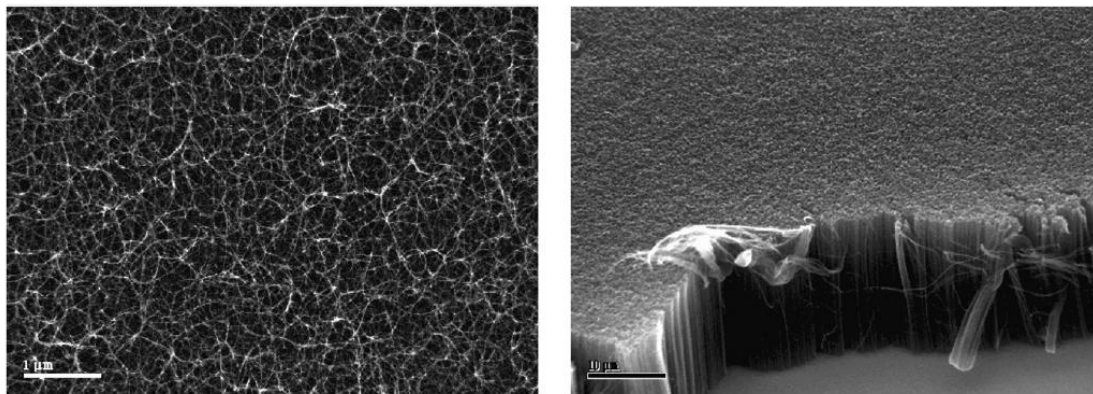


Figure 1.17: Example of CNT arrays produced by PECVD. From *Meyyappan*.<sup>85</sup>

### 1.3 Integration of Carbon Nanotubes in Light Harvesting Technology

There have been several studies on the integration of CNTs into traditional DSSC design. Early work was predominately based on the mixing of CNTs into a mixture of titania to increase interconnectivity and hence conductivity, as seen previously in Figure 1.12.<sup>40, 44, 53, 86</sup> However, the majority of these have focused on the increased conductivity of CNT structures but not their unique ability to act as the light harvesting element themselves. Some researchers then began investigating the fundamental properties and behaviour of nanotubes when exposed to light. The first published result was in 1999 by Zhang and Iijima<sup>87</sup> in which they observed a movement of nanotubes in an electric field when exposed to light. It was suggested that this is due to some form of charging or electrostatic effect when light was shone on the nanotubes, and can be seen in Figure 1.18. This was then supported by theoretical work that was published in 2000.<sup>88</sup>

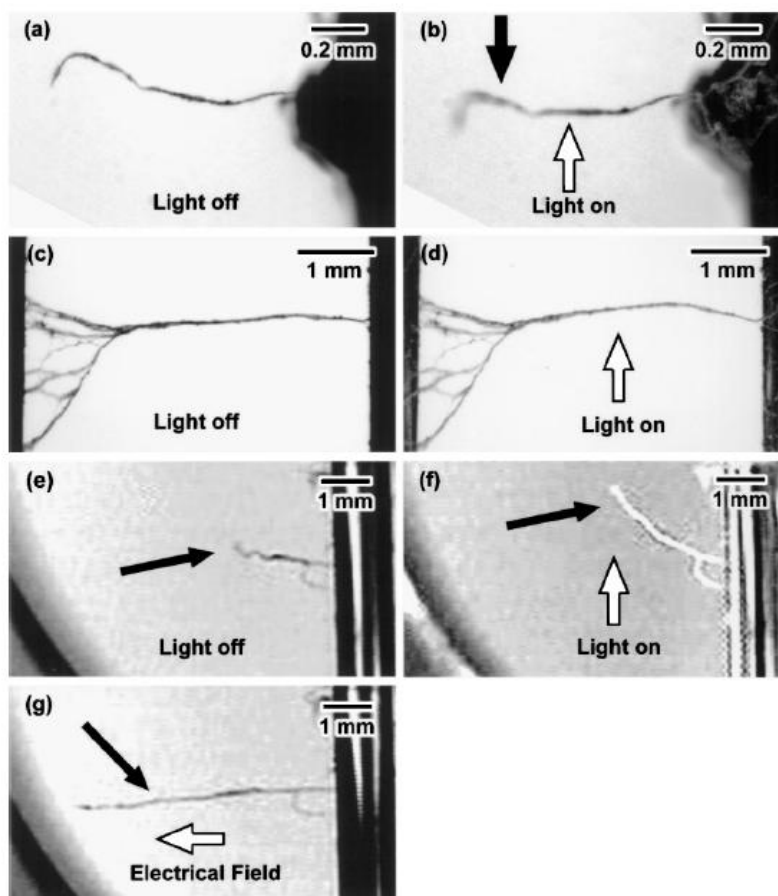


Figure 1.18: Response of SWCNT bundles to illumination ( $20\text{mW}\cdot\text{cm}^{-2}$ ) in the presence of a 10V bias. From Zhang *et al.*<sup>87</sup>

In 2003 *M. Freitag et al.* published an article in which they investigated the photoconductivity of a single carbon nanotube when illuminated with a laser.<sup>89</sup> In this work it was found that upon illumination with an infrared laser a single nanotube across a source-drain diode in a field-effect transistor could produce a photovoltage and current, and suggested that the large bias that was needed on the diode was required to separate the charge carriers. An SEM image of the single nanotube across the source-drain diode is shown in Figure 1.19, with a graph of the generated photocurrent versus incident laser power. Noticeably, the power generated from a single nanotube is in the order of picoamperes even with  $\text{KW}\cdot\text{cm}^{-2}$  incident intensity, which is 3 orders of magnitude greater than the standard intensity used. However, due to the small diameter of SWCNTs it is possible to fit a large number of nanotubes within  $1\text{cm}^2$  which suggests they may be applicable for more significant photocurrent generation.

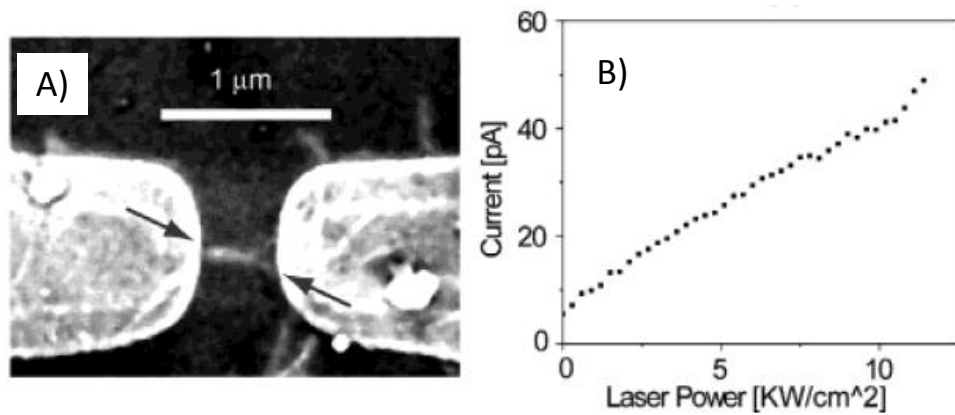


Figure 1.19: SEM image of single nanotube diode (A) Graph of photocurrent produced versus incident light intensity (B). From Freitag *et al.*<sup>89</sup>

This work was then expanded in 2005 by *J. U. Lee* who also worked on SWCNT diodes whilst being illuminated, and again found that individual SWCNTs can produce significant photocurrent.<sup>50</sup> In this work the photon source was an infrared laser (0.8eV, 1550nm), which was chosen to ensure no response was from the underlying silicon substrate. Figure 1.20 shows the schematic of the diode, along with I-V curves for the device under increasing illumination powers into the photovoltaic (PV) quadrant. As before the current is in the picoampere range, but taking into account the illuminated area of the CNT a global efficiency ( $\eta$ ) of 0.2% was achieved, indicating a high sensitivity of SWCNT to illumination and subsequent efficient photocurrent generation.

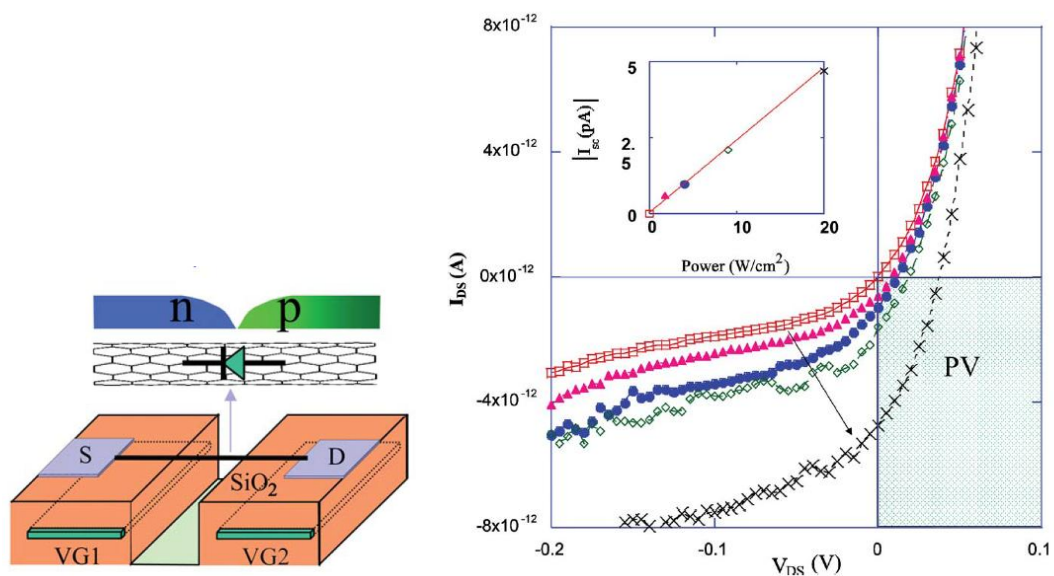


Figure 1.20: Schematic of a SWCNT diode along with I-V curve showing increasing photovoltaic response with increasing illumination intensity. From Lee.<sup>50</sup>

*Barazzouk et al.* demonstrated that films of nanotubes instead of individual tubes could be used and a maximum photocurrent and photovoltage of  $8\mu\text{A}\cdot\text{cm}^{-2}$  and 12mV respectively was achieved, shown in Figure 1.21.<sup>49</sup> SWCNT films were produced by electrophoretic deposition from a suspension of SWCNTs in THF, and an IPCE value of 0.15% suggested that many of the photogenerated charge carriers were lost to recombination processes. This was, however, the first use of SWCNTs as the sole light harvesting element in a DSSC cell architecture.

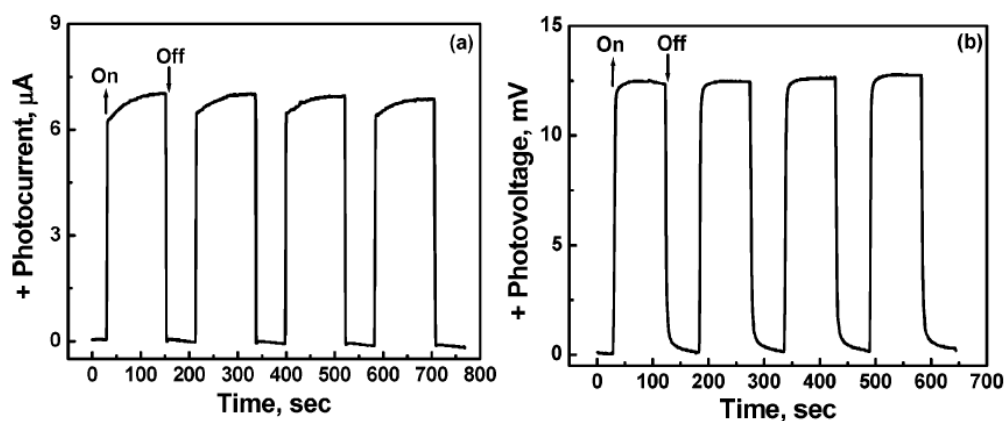


Figure 1.21: Photocurrent and photovoltage on-off cycles for SWCNT film (Incident light  $\approx 100\text{mW}\cdot\text{cm}^{-2}$ ). From *Barazzouk et al.*<sup>49</sup>

The use of CNTs offers a benefit from that of the traditional DSSC design due to the ballistic conduction of electrons and holes within the carbon nanotube structure, as compared to the relatively slow electron diffusion that occurs within the thick titania layer. A schematic of the CNT cell used by *Barazzouk et al.* is shown in Figure 1.22, along with a schematic indicating the increased flow of photogenerated charge carriers when directed along nanotubes. Studies have also been performed to produce MWCNT<sup>51, 90</sup> and double walled CNTs<sup>56</sup> based photovoltaics but the use of SWCNTs has shown the most promise, due to their semi-conducting nature. Recent work has shown that metallic SWCNTs, as well as semi-conducting SWCNTs, can both act as highly efficient hole carriers when used in conjunction with polymers but not when used as the sole light harvesting element.<sup>91</sup>

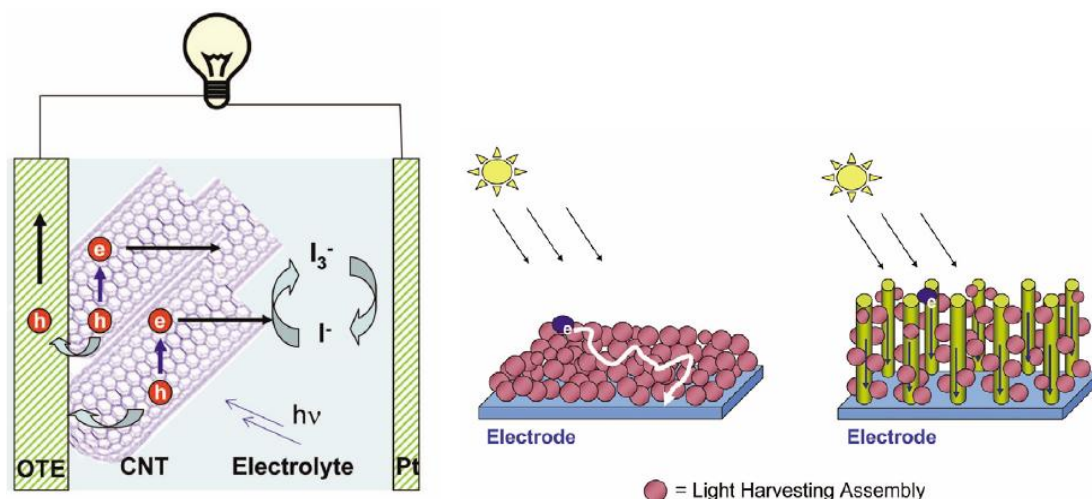
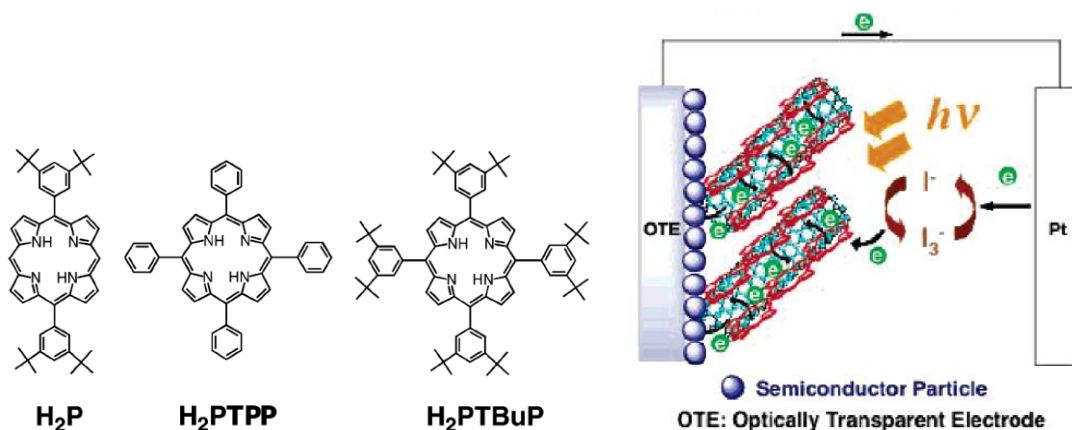


Figure 1.22: Schematic of possible solar cell design and benefits of directed electron transport. From Kamat.<sup>52</sup>

### 1.3.1 Chemical Modification of Carbon Nanotubes for Light Harvesting Devices

As well as acting as the photoactive element themselves there has been extensive work on the use of CNT arrays as scaffold for further functionalisation by chromophores. This has focused primarily on the functionalisation by porphyrins<sup>92-95</sup> but has also included metal based and organic dyes<sup>61, 96</sup> as well as dendrimers.<sup>97-99</sup> Porphyrins are a logical choice due to their presence in natural photosynthesis as chlorophyll. Early work by *Hasobe et al.* involved attaching metal-free porphyrins to SWCNT bundles interdispersed through tin oxide nanoparticles.<sup>92</sup> The porphyrins used and a schematic of the cell are shown in Figure 1.23. By adding porphyrins as charge injectors into the SWCNTs a photocurrent of  $0.1 \text{ mA} \cdot \text{cm}^{-2}$ , photovoltage of 60mV and a *ff* of 0.24 with  $12.4 \text{ mW} \cdot \text{cm}^{-2}$  illumination, giving a  $\eta$  of 0.012%. This is still much lower than traditional DSSC cells but a significant improvement over unmodified SWCNTs. The modification of CNTs with porphyrins was further expanded upon by *Ren et al.* and *Yu et al.* who analysed the covalent attachment of porphyrins to SWCNTs for the possible future application to light harvesting antennae, but did not publish light harvesting results, only characterising the porphyrin modified SWCNTs.<sup>93, 94</sup>



**Figure 1.23: Porphyrin molecules used and cell schematic for SWCNT-porphyrin hybrid solar cell. From Hasobe et al.<sup>92</sup>**

The general characteristics of an optimal light harvesting device include a large photoabsorption cross section, good spatial orientation of harvesters, and efficient charge separation.<sup>100</sup> Organic macromolecules such as dendrimers promise to be an excellent candidate to fulfil these requirements. Dendrimers, or more specifically individual dendrons, provide excellent light harvesting per surface area due to their tree-like structure and can be modified to provide any number of functionalities for further modification. There has been extensive work performed on the production of light harvesting dendrimers.<sup>100-105</sup> However, efforts have so far been limited to the integration of dendrimers and dendrons into traditional DSSC cells, achieved by attaching them to titania particles or dispersing them throughout the electrolyte solution.

There have also been several articles that have reported the attachment of dendrimers or dendrons to CNTs.<sup>106</sup> One of the most studied structures of dendrimer or individual dendrons is the polyamidoamine or PAMAM dendrimer.<sup>107-111</sup> PAMAM consists of alternating reactions between ethylenediamine and methyl acrylate which react with one another through the so-called 'Michael addition' reaction. Michael addition is the nucleophilic addition between a nucleophile, such as a primary amine, and an  $\alpha,\beta$ -unsaturated carbonyl compound, such as methyl acrylate.<sup>112</sup> The synthesis for the first step of a PAMAM dendrimer is shown in Figure 1.24, along with a 3<sup>rd</sup> generation PAMAM dendrimer. Clearly the exponential growth in size can be seen, and the ever growing complexity of the resultant molecule with increasing generations.

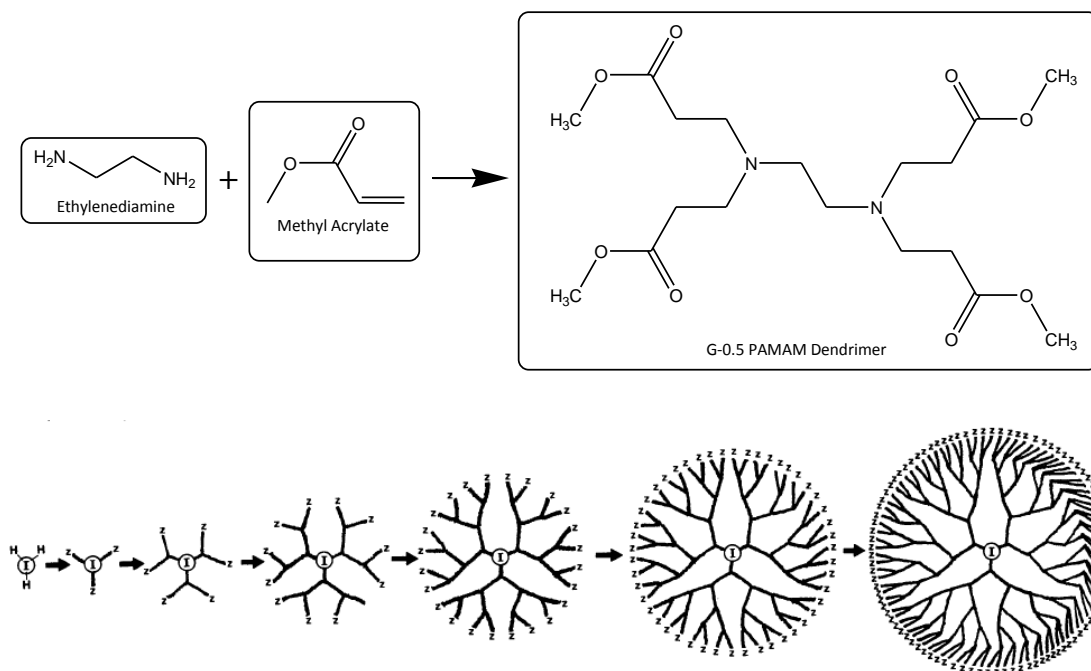


**Figure 1.24: Synthesis of PAMAM dendrimer to generation 0.5 (G-0.5) and a schematic showing the increasing complexity of dendrimer molecules. From Frechet *et al.*<sup>111</sup>**

This growth process can be repeated many times to produce very large dendrimers with an exponential growth of surface attachment points. Thus the use of dendrimers and dendrons for light harvesting would seem logical, as it provides a large surface area connected to a central core and has been investigated in the literature.<sup>100, 101, 104, 105, 113, 114</sup> These have involved a dispersion of SWCNT in with a poly(amidoamine) (PAMAM) type dendrimer that has been modified to be electrically conductive.<sup>97</sup> The conclusions drawn from this work were that covalent functionalisation of SWCNTs with conductive molecules allows for novel applications to device integration. *Pan et al.* demonstrated that dendrons could be grown using the side-wall carboxylic acid groups present on MWCNT as the core. This process is shown schematically in Figure 1.25.<sup>98</sup> These publications demonstrate the first step in creating a functional solar cell design based on chemically functionalised CNT arrays.

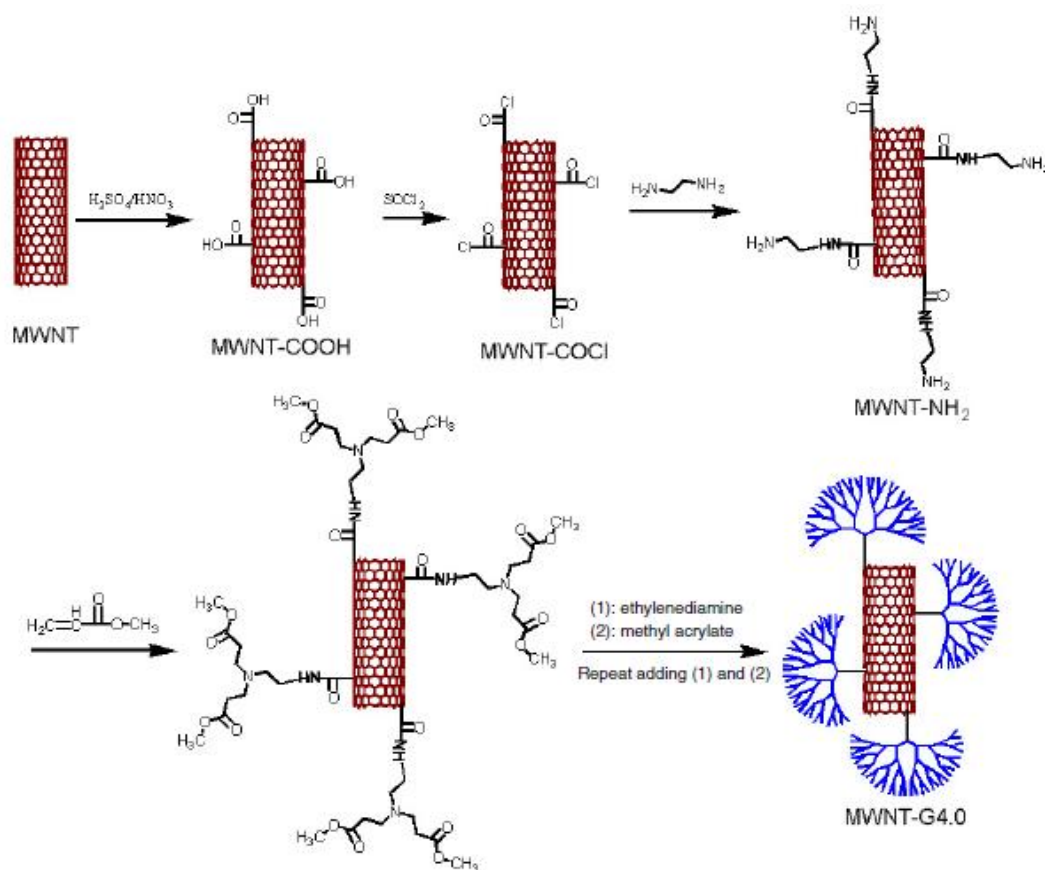


Figure 1.25: Schematic of PAMAM dendron growth from MWCNT in solution. From Pan *et al.*<sup>98</sup>

## 1.4 Thesis Outline

In this thesis the application of carbon nanotubes for photovoltaic devices will be investigated. As has been seen throughout the introduction carbon nanotubes offer many possible advantages for use in solar cells such as excellent conductivity, semi-conducting electronic structure and chemical functionality and it is the aim of this work to more closely investigate the integration and application of carbon nanotubes for use in solar power generation. Firstly, chapter 2 outlines the experimental methods and materials used in this work as well as a brief overview several of the analytical techniques applied. Chapter 3 investigates the use of vertically aligned single-walled carbon nanotube arrays as light harvesters by replacing titania in a DSSC type cell architecture with the aim to create a consistent and reproducible cell output and gain an understanding of the parameters that affect cell performance. The effect of altering the SWCNT treatment time and attachment time and the resulting effect this has on

cell performance will then be investigated. These arrays are analysed using electrochemistry, Raman spectroscopy, X-ray photoelectron spectroscopy and finally photovoltaic efficiency testing. These SWCNT arrays are then compared to MWCNT arrays also chemically attached to a surface. As mentioned previously MWCNTs exist as predominantly metallic conductors and so would be expected to be inferior light harvesters and this work allows for a direct comparison. Chapter 4 explores the ability of the SWCNT arrays to act as scaffolds for further chemical functionalisation. It is the aim of this section to gain a better understanding about the electron transfer properties through the nanotube array and how they relate to photoresponse. As has been discussed there are several classes of molecules that have been found to enhance the photovoltaic properties of cells. In this work this has been done using a dye molecule, N3, which has been proven to be effective in DSSCs. A similar ruthenium based porphyrin will also be investigated and the response compared to that of the dye. As mentioned in the introduction large organic molecules may also prove to be beneficial in light harvesting and with this in mind dendron molecules which are based on PAMAM dendrimers are grown from the SWCNT array and are expected to be beneficial to the overall cell efficiency. A combination of both dendron and dye molecules is also shown which produces an increased efficiency over either of the individual constituents. Finally in chapter 5 the use of chemical vapour deposition and plasma enhanced chemical vapour deposition to grow carbon nanotube arrays directly onto a surface is examined. This allows for the production of both MWCNT and SWCNT arrays directly onto a surface and allows for a direct comparison between them. The growth of material directly onto a substrate allows for comparison between producing the arrays by chemical attachment, where the covalent attachment has previously been hypothesised to have superior electron transfer properties,<sup>154</sup> and this will be verified experimentally. These grown arrays are imaged using scanning electron microscopy as well as characterised by electrochemistry, Raman spectroscopy, XPS and photovoltaic efficiency.

---

## **2. Materials & Methods**

---

## 2.0 Experimental Details

All chemicals, unless otherwise noted, were purchased from Sigma-Aldrich (Sigma-Aldrich, Australia) and used as received without further purification.

### 2.1 Single-walled Carbon Nanotube Solutions

For all work on the chemical attachment of SWCNT to substrates the SWCNT powders used were purchased from Carbon Solutions, Inc. (P2-SWCNT, USA). These are purified (by air oxidation) low functionality carbon nanotubes produced by electric arc discharge with a Ni/Y catalyst, and which according to the supplier have a carbonaceous purity of >90% and a 4-7%wt catalyst content. The average diameter as quoted by the supplier is 1.4nm, with bundle length of 0.5-1.5 $\mu$ m and a bundle diameter of 4-5nm. These as purchased nanotubes are then chemically treated and dispersed in solvent. To purify and chemically modify the pristine tubes a mixed acid bath is used. The carbon nanotube powder is dispersed in a 1:1 ratio (1mg of SWCNT to 1ml of mixed acid) in a 3:1 (v/v) H<sub>2</sub>SO<sub>4</sub> (98%):HNO<sub>3</sub> (70%) bath and sonicated at 0°C for several hours as specified (usually 2,4,6 or 8 hours). This process has been reported on extensively in the literature and is found to introduce carboxylic acid functional groups along the side walls and in higher concentration on the ends of the tubes.<sup>115-119</sup> This introduction of chemical functionality allows for further treatment and reactions to take place. The 'cutting' as it is called, also reduces the average length of the nanotubes to ~360nm.<sup>115</sup> The resulting functionalised nanotube solution was then filtered through a 0.4 $\mu$ m membrane (Isopore HTTP, Millipore) and rinsed with copious de-ionised (DI) water until a neutral pH in the filtrate is reached. The resulting 'bucky paper' as it has been called is then placed in the oven at 80°C for 24 hours to remove any water. The bucky paper is then dispersed in anhydrous dimethyl sulfoxide (DMSO) at a concentration of 0.2mg/ml and sonicated to disperse the nanotubes evenly.

For further use of the carboxylic acid groups on the nanotubes a catalyst is added. N,N'-Dicyclohexylcarbodiimide (DCC) was added at 1:1 (w/w) of cut nanotube and the solution was stored under nitrogen in a glove box. DCC, which acts as a more efficient leaving group in condensation reactions, has been shown to activate the carboxylic acid groups and form an intermediate.<sup>117, 119</sup> This activated CNT solution

remained dispersed in DMSO for several months under a nitrogen atmosphere in a glove box.

### 2.1.1 SWCNT Arrays on Silicon

To prepare vertically aligned carbon nanotube arrays on silicon a well established method, shown in Figure 2.1, was used.<sup>94, 116, 120-125</sup> Firstly a wafer of highly boron doped p-type <100> silicon (Virginia Semiconductor, Inc., USA) was rinsed in acetone then ethanol followed by de-ionised water and dried under a stream of nitrogen. The wafer was then submerged in a 1:1:5 (v/v/v) mixture of  $\text{NH}_4\text{OH}$ (30%),  $\text{H}_2\text{O}_2$ (30%) and de-ionised (DI) water (18M $\Omega$ cm) for 20 min at 80°C then into a 1:1:5 (v/v/v) mixture of 36% HCl, 30%  $\text{H}_2\text{O}_2$  and DI water for 20 min at 80°C. This hydroxylates the native oxide,  $\text{SiO}_2$ , present on the silicon wafers and allows for a condensation reaction to occur between the activated carbon nanotubes and the hydroxyl groups on the surface. This hydroxylated silicon wafer is then submerged in the aforementioned CNT solution and placed in a oven at 80°C for varying lengths of time, up to 24 hours as specified. The wafer is then removed and rinsed with copious quantities of acetone to remove any unattached CNTs and other amorphous forms of carbon and dried under a stream of nitrogen.

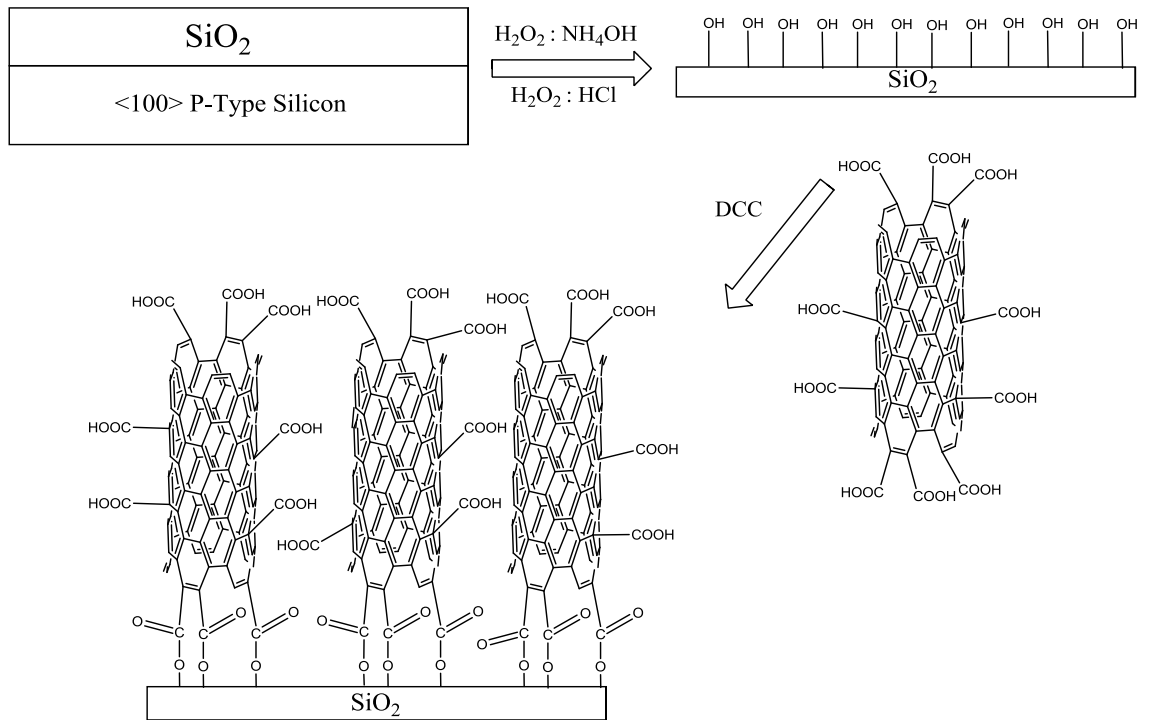


**Figure 2.1: Schematic of the hydroxylation of the silicon substrate and subsequent formation of the SWCNT array.**

### 2.1.2 Arrays on Fluorine Doped Tin Oxide Coated Glass

To create CNT arrays on fluorine doped tin oxide (FTO) glass the same procedure used in 2.1.1 for creating arrays on silicon is adapted. In this case the silicon wafer is simply replaced by the FTO glass slide, shown schematically in Figure 2.2. As the surface is still an oxide the same hydroxylation method was used and the same incubation in CNT solution resulted in excellent CNT coverage. FTO coated glass was purchased (TCO22-15, Solaronix, Switzerland,  $15 \Omega/\text{square}$ ) and hydroxylated by first treating with  $\text{H}_2\text{O}_2$  and  $\text{NH}_4\text{OH}$  and then with  $\text{H}_2\text{O}_2$  and  $\text{HCl}$  as described in 2.1.1. The hydroxylated FTO glass substrates were then submerged in the SWCNT solution and stored at  $80^\circ\text{C}$  for 2, 4, 6, 18 and 24 hours as specified. The aligned nanotube arrays were rinsed with acetone and dried with nitrogen before being used.

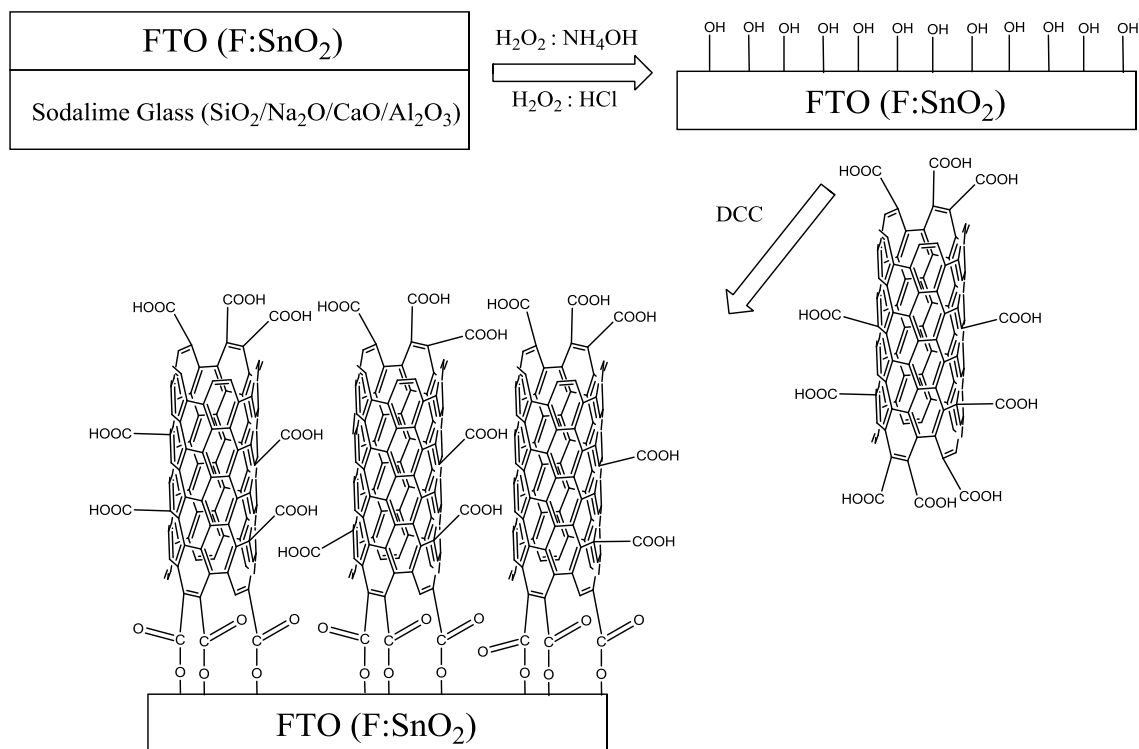


**Figure 2.2:** Schematic of the hydroxylation of the FTO glass substrate and subsequent formation of the SWCNT array.

### 2.1.3 Carbon Nanotube Electrochemical Solar Cells

Electrochemical solar cells were constructed by using the CNT modified FTO glass as the working electrode while counter electrodes were produced by taking FTO glass with fill holes already in place and sputtering a 10nm platinum coating to act as a catalyst. A schematic of the cell architecture can be seen in Figure 2.3. Gaskets were made from 60 $\mu$ m thick Surlyn (SX1170-60, Solaronix, Switzerland) and this was sandwiched between the counter and working electrodes and heated to 100 $^{\circ}$ C in an oven for 10 minutes. The cell was then filled with a solution of 0.8M 1-methyl-3-propylimidazolium iodide, 0.1M iodine and 0.3M benzimidazole in 3-methoxypropylamine, to make an iodide/tri-iodide ( $I^-/I_3^-$ ) redox couple. The benzimidazole is present to suppress back reactions within the electrolyte<sup>22</sup> and will be discussed in more detail later. The fill hole was then sealed with Bynel (SX1162-60, Solaronix, Switzerland) and a glass microscope cover slip. All cells had an active area of 1cm<sup>2</sup>.

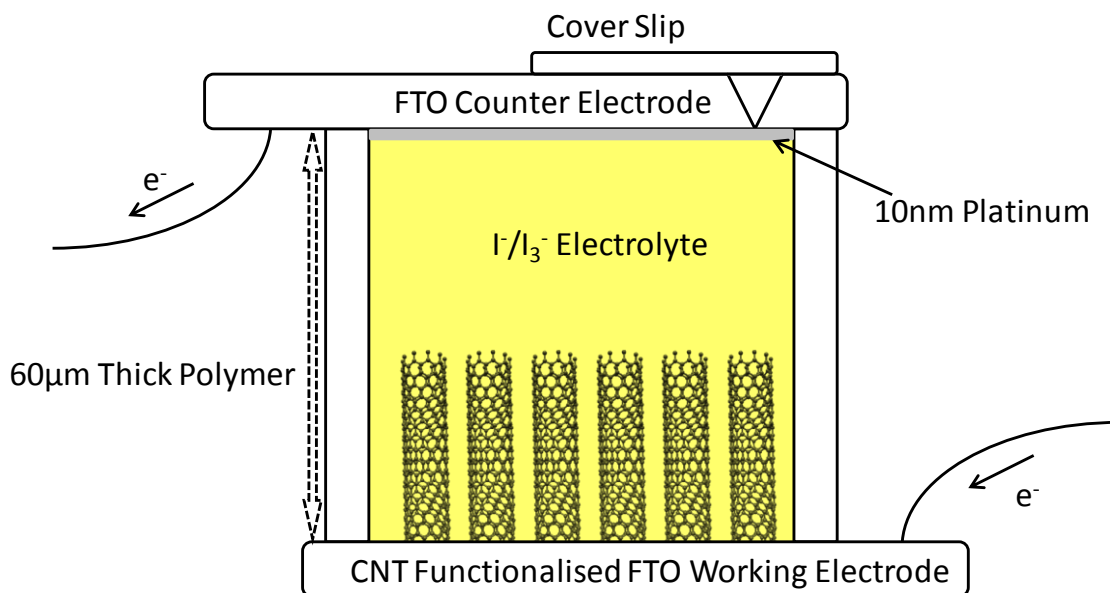


Figure 2.3: Schematic of CNT functionalised electrochemical solar cell architecture. (Not to scale)

### 2.1.4 Multi-walled Carbon Nanotube Devices

To produce MWCNT arrays, MWCNTs (Shenzhen Nanotech Port Co. Ltd, China) were refluxed in 3M nitric acid for 3 hours. They were then sonicated in the  $\text{H}_2\text{SO}_4$  (98%): $\text{HNO}_3$  (70%) mixed acid, as was done for SWCNTs, for 3 hours at room temperature. The resultant MWCNT solution was then filtered and dispersed in DMSO as was performed for the SWCNT. Attachment to the hydroxylated surface was also done using the same method as outlined for the SWCNT.

## 2.2 Chemically Functionalised Single-walled Carbon Nanotube Arrays

To modify the performance of the SWCNT arrays further chemical modification of the CNT array was performed with two different chromophores. This was performed firstly with the well established ruthenium based dye N3 (shown earlier in Figure 1.4). To provide a comparison, porphyrin modified arrays were also created using a ruthenium based molecule (RuTPP) that is analogous to the N3 dye due to the presence of the similar ruthenium metal centre.

### 2.2.1 Ruthenium Tetraphenyl Porphyrin Functionalised Arrays

Ruthenium tetraphenyl porphyrin (5,10,15,20-tetraphenyl-21H,23H-porphine ruthenium(II) carbonyl, RuTPP) modified arrays were created by adapting a method

that was published by *Yu et al.*<sup>94</sup> The technique was modified for the work presented here by simply replacing the silicon wafer used by *Yu et al.* previously with the optically transparent FTO glass in this work, and can be seen schematically in Figure 2.4. Briefly, CNT modified arrays were prepared as described in 2.1.2 and submerged in a solution of 4-aminopyridine (0.01M) in *N,N'*-dimethylformamide (DMF), also containing 0.5mg.ml<sup>-1</sup> of DCC and 0.05mg.ml<sup>-1</sup> of DMAP (4-dimethylaminopyridine). DCC, as mentioned previously, is essential in creating a favourable reaction with the carboxylic acid groups on the CNT surface by the production of an activated intermediate. The presence of DMAP, which acts as a nucleophilic catalyst, allows for the easy formation of amide bonds between the aminopyridine and the nanotubes at room temperature. The FTO-CNT modified surface was left submerged for 24hrs at room temperature in the dark. The substrate was removed and rinsed with DMF and dried with nitrogen before being resubmerged in a solution of 0.5mg.ml<sup>-1</sup> RuTPP in chloroform, again for 24 hours at room temperature in the dark. This allows for the coordination of the ruthenium metal atom at the centre of the porphyrin to the lone pair of electrons on the free amine of the aminopyridine. The substrate was then removed and rinsed with chloroform before being dried with nitrogen.

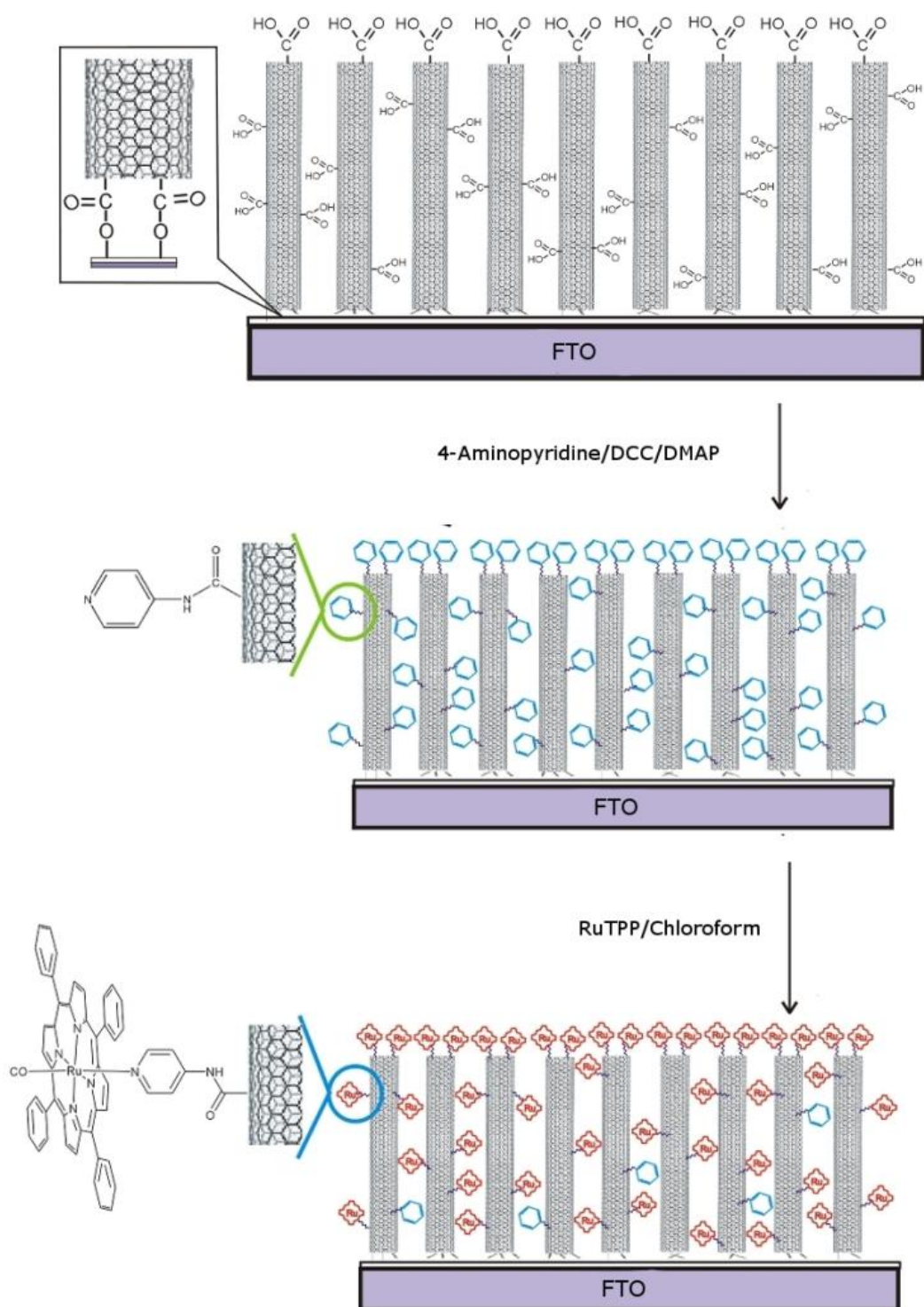


Figure 2.4: Schematic of the functionalisation of SWCNT array with RuTPP on FTO Glass. Modified from Yu *et al.*<sup>94</sup>

### 2.2.2 N3 Dye Functionalised Array

*cis*-bis(isothiocyanato)bis(2,2'-bipyridyl-4,4'-dicarboxylato)-ruthenium(II) (N3 dye) (Ruthenium 535, Solaronix, Switzerland) modified arrays were prepared by taking aligned SWCNT substrates prepared as described in 2.1.2 and submerging them in a neat solution of EDA (ethylenediamine) with  $0.5\text{mg}\cdot\text{ml}^{-1}$  DCC and  $0.05\text{mg}\cdot\text{ml}^{-1}$  DMAP (4-Dimethylaminopyridine) for 24 hours at room temperature and stored in the dark. This attachment method is shown schematically in Figure 2.5 These CNT arrays were then removed and rinsed with copious acetone and dried under a stream of nitrogen. This process produced EDA functionalised SWCNTs, via an amide bond. These EDA modified arrays were then submerged in  $1\text{mM}$  N3 dye in DMSO, with  $0.5\text{mg}\cdot\text{mL}^{-1}$  DCC and  $0.05\text{mg}\cdot\text{mL}^{-1}$  DMAP for 24 hours at room temperature and stored in the dark. These were again then rinsed with copious DMSO and acetone and dried under a stream of nitrogen.

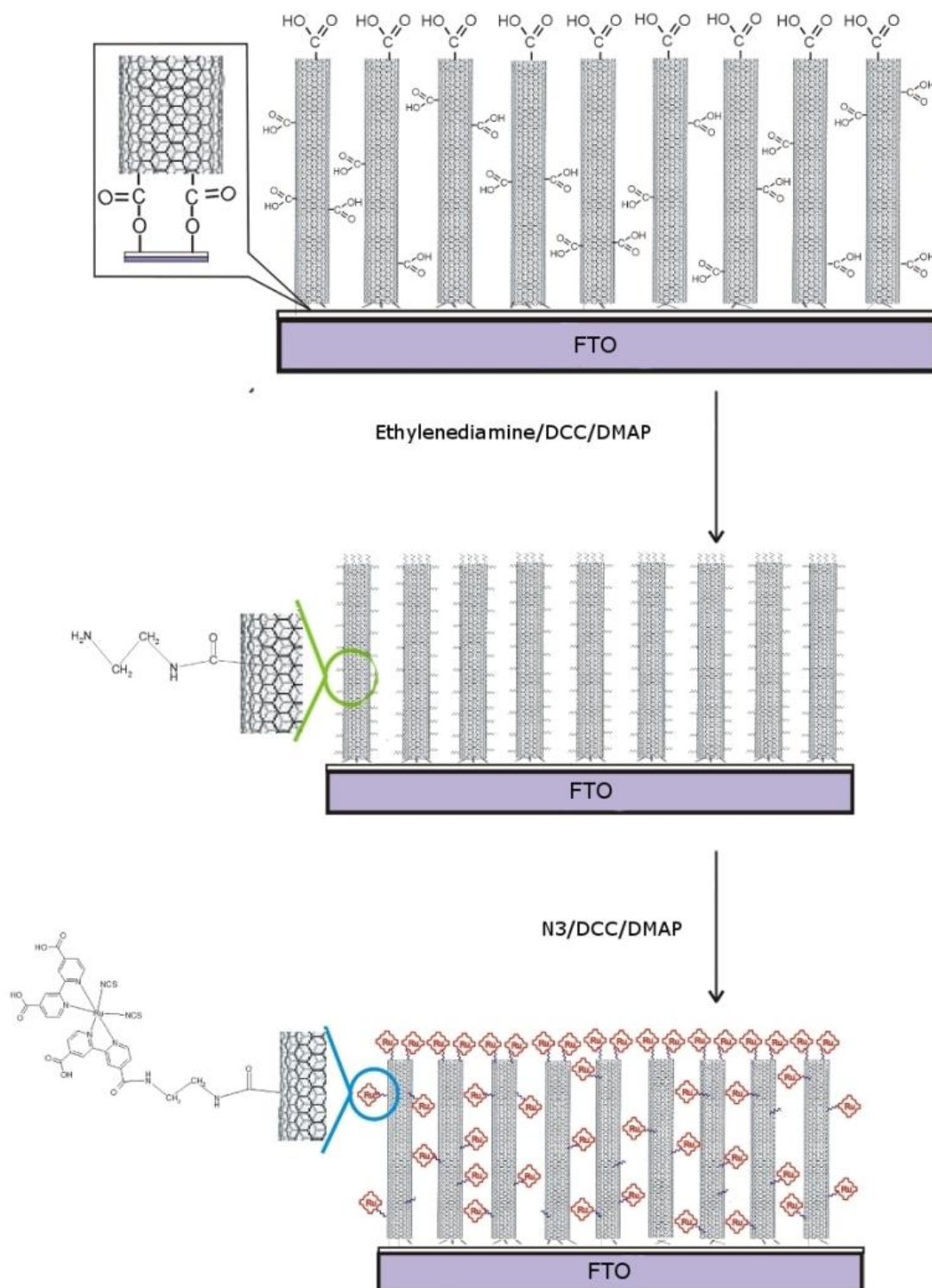
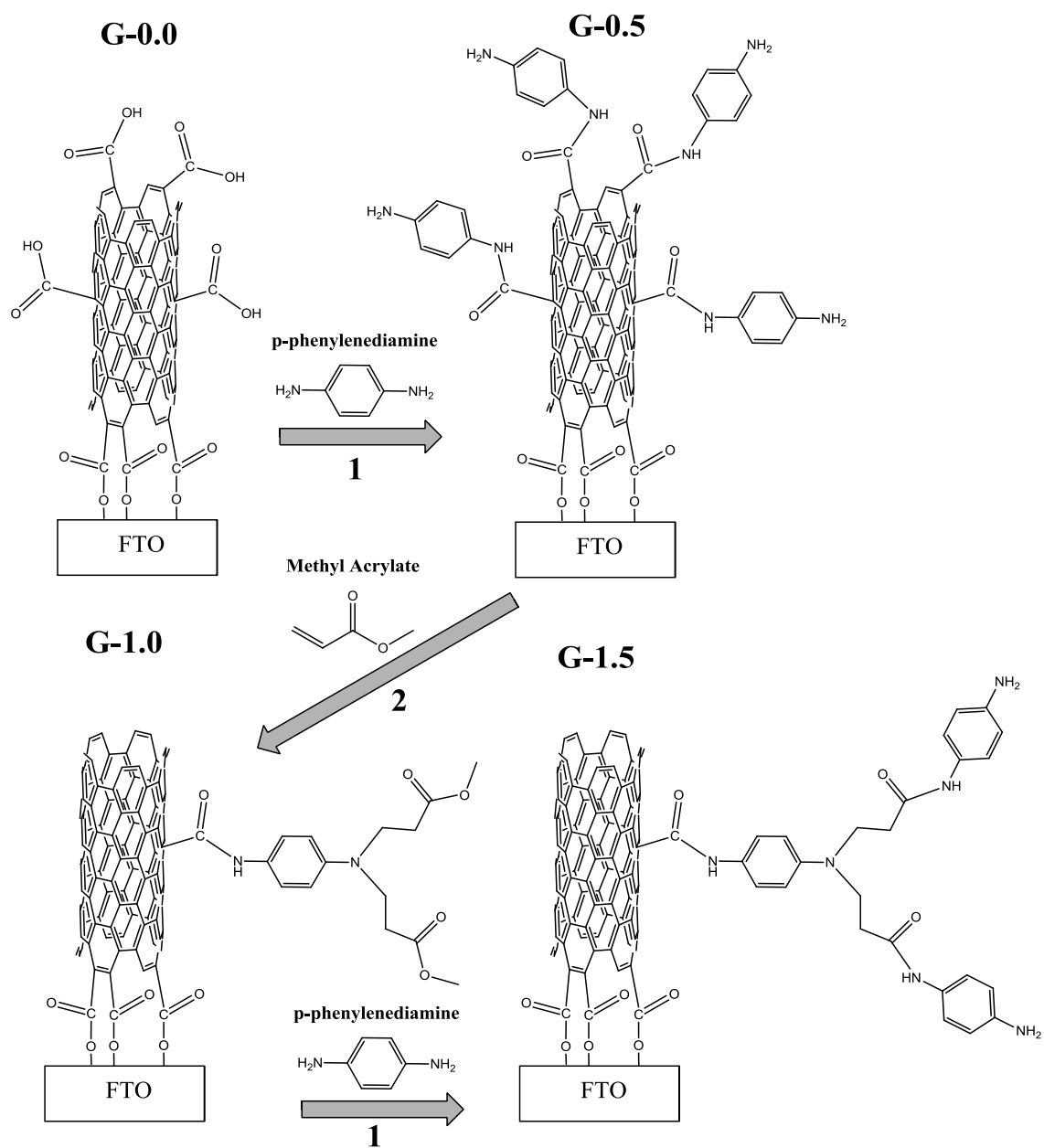


Figure 2.5: Schematic of the functionalisation of SWCNT array with N3 dye on FTO.

### 2.2.3 Dendron Functionalised Array

To produce dendron modified CNT arrays the carboxyl groups on the nanotube sidewalls and ends were used as the core of a PAMAM-type dendron. Here PDA was used in place of EDA as it has been shown to have higher conductivity, but should retain the chemical properties needed.<sup>126</sup> This process, up to generation-1.5 (G-1.5), is shown schematically in Figure 2.6. To create the dendron modified SWCNT array, firstly the SWCNT array was created on FTO glass as outlined in 2.1.2. The nanotube modified substrate is submerged in a solution of p-phenylenediamine (PDA, 0.1M) in methanol for 24 hours to produce the generation-0.5 substrate. The substrate is then removed and rinsed with copious methanol and dried in a stream of nitrogen. The G-0.5 modified substrate is then in turn submerged in a 1:1 (v/v) methyl acrylate and methanol solution and again left for 24 hours to produce the G-1.0 substrate. Repeating the steps in turn, up to G-3.5 substrates were produced.



**Figure 2.6: Functionalisation scheme for modifying SWCNTs attached to FTO glass. Step 1: Attachment of PDA leading to G-0.5; Step 2: attachment of methyl acrylate leading to G-1.0. Step 1 and 2 are then alternated for higher generations.**

## 2.3 Chemical Vapour Deposition Growth of Carbon Nanotubes

### 2.3.1 Carbon Nanotube Arrays Grown by Chemical Vapour Deposition

CNT arrays were grown on two different substrates. Nanotubes were first grown on boron doped p-type silicon wafers (<100>, 0.0008-0.0012Ωcm, Siltronic, France). A schematic of the growth process is shown in Figure 2.7. The chemical vapour deposition process used is known as the water assisted growth technique first published by *Hata et al.*<sup>72, 127</sup> A piece of silicon was rinsed in acetone and dried under nitrogen, this was repeated with ethanol followed by water. Once cleaned the silicon substrate was placed in a sputter coater with a film thickness monitor (K575X, Quorum Technologies, UK). A 5nm layer of iron was sputtered onto the surface. The sample was then placed in a quartz tube inside a tube furnace (Thermolyne 21100, Thermo Scientific, USA) which was flushed with high purity argon whilst heating to 750°C. Once at the required temperature a hydrogen/argon mix (0.5/1.5 sccm) was flushed over the surface for 10 minutes. This hydrogen atmosphere reduces the thin iron film into iron nanoparticles. The carbon feedstock used was acetylene (C<sub>2</sub>H<sub>2</sub>) and was delivered as a mixture of acetylene/hydrogen/argon (0.2/0.5/1.5 sccm), water vapour was also provided into the system by bubbling argon (2.8 sccm) through water. The water is present to remove amorphous carbon. This amorphous carbon reduces the catalytic activity of the iron nanoparticles, preventing further growth.<sup>128</sup> Growth was carried out for 10 minutes, after which time the sample was left to cool under a flow of argon (1.5 sccm).

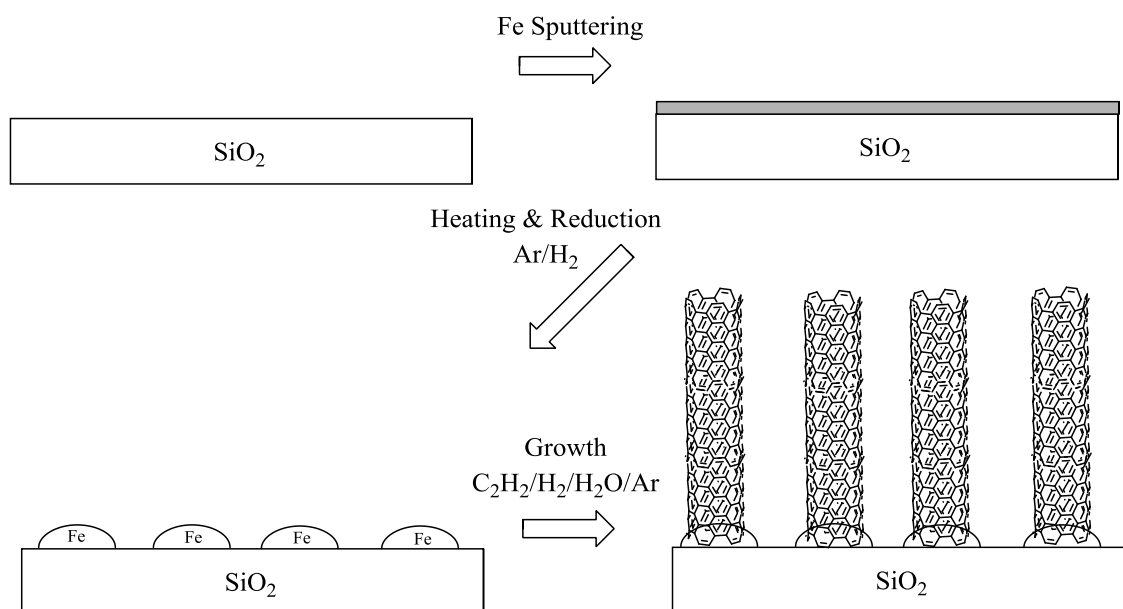


**Figure 2.7: Schematic of thermal chemical vapour deposition growth of CNTs.**

This process was also undertaken on indium tin oxide (ITO) coated quartz slides as the FTO slides used previously are on soda lime glass, and thus is not thermally stable at the temperatures required. ITO coated fused quartz slides with a thickness of 1.1mm, a size of 25mm x 25mm, and a resistance of 8-12 $\Omega$ /square were purchased from SPI Supplies (06453-CF, SPI Supplies, USA). These were then coated with the iron catalyst and CNT growth undertaken in an identical fashion as described for the silicon substrates.

### 2.3.2 Carbon Nanotube Arrays Grown by Plasma Enhanced Chemical Vapour Deposition

The reaction vessel used for PECVD CNT growth in this work is shown in Figure 2.8. It is a stainless steel cylindrical chamber 40cm in diameter with a base pressure of 1x10<sup>-6</sup> Torr. The plasma is inductively coupled via an internal single loop antenna driven by a function generator at 13.56MHz. Samples are mounted on a stainless steel table that is resistively heated via a tungsten filament within the table. Temperature was monitored with a K-type thermocouple attached to the table. Gas pressure is controlled by an automatic servo valve and a manual leak valve.

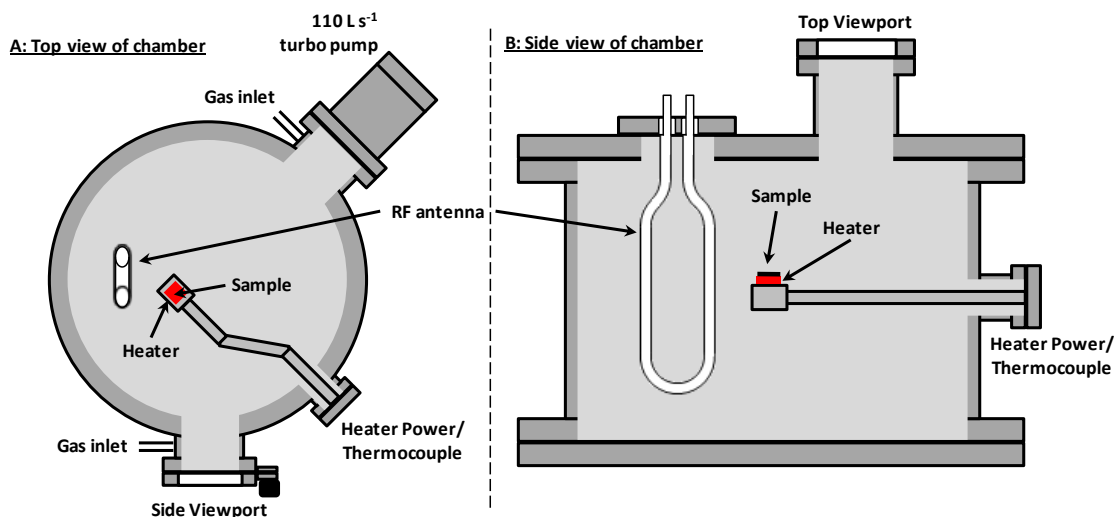


**Figure 2.8:** Reaction chamber used in plasma nanotube growth showing A: top view and B: side view. In B the antenna is shown rotated 90 degrees for clarity. Distance between antenna and sample is 10cm.

The substrate for growth was boron doped p-type silicon wafers (<100>, 0.0008-0.0012 $\Omega$ cm, Siltronic, France). A schematic of the PECVD growth process is shown in Figure 2.9. The catalyst layer was deposited in the same method as for the thermal CVD, described in 2.3.1. The substrates were mounted inside the chamber which was then evacuated to base pressure,  $1 \times 10^{-6}$  Torr, and the sample heated to between 450-650°C as specified and left for 10 minutes to reach thermal equilibrium. The carbon feedstock for this work was high purity methane (CH<sub>4</sub>) and this was diluted with high purity argon. Growth was typically performed at a pressure of 100mTorr with the gases in a 1:4 ratio (20:80mTorr, CH<sub>4</sub>:Ar) and growth was undertaken for 10-30 minutes. The plasma power used was 10W and after the growth the sample was left to cool in the vacuum until <100°C.

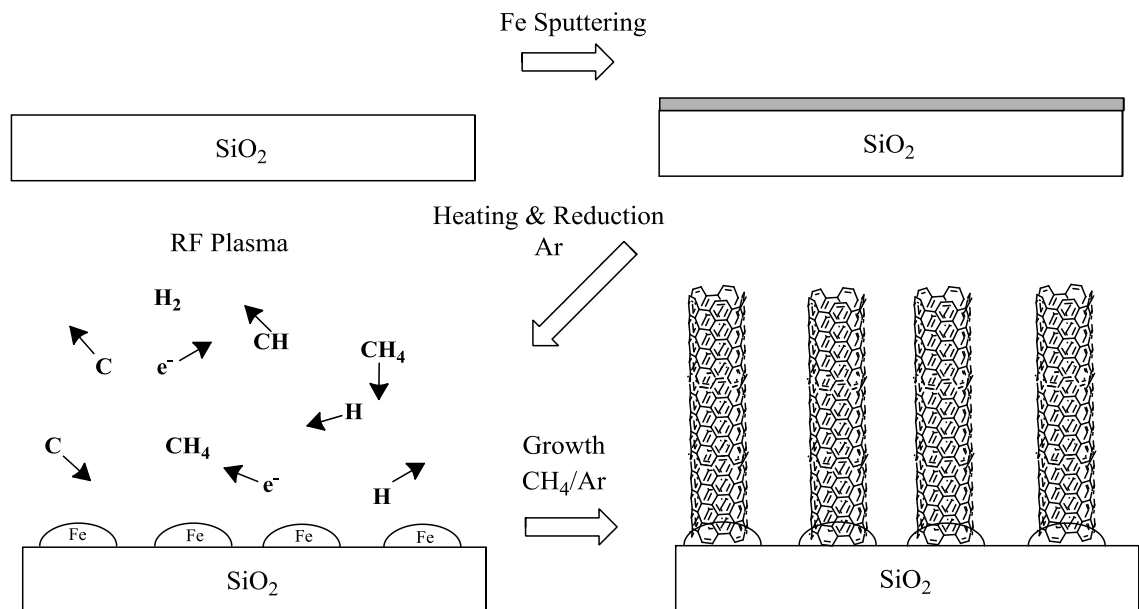


Figure 2.9: Schematic of PECVD CNT growth process.

## 2.5 Solar Cell Performance

Light response measurements were measured using a Keithley 2400 Source-Measure unit (Keithley, USA) interfaced with Labview based software written in-house. This supplied the cells with a known voltage and measured the resultant current output, presented in the form of an I-V curve.

During the course of this work two different light sources were used. The first was a quartz halogen lamp attached to an optic fibre light guide (Dolan-Jenner Fiber-Lite 190-1) with a power of  $\sim 35\text{mW}\cdot\text{cm}^{-2}$ , measured with a light meter (Newport Power Meter, Model 1815-C). The second light source was a white light LED solar simulator built in house, which provided an incident irradiance of  $100\text{mW}\cdot\text{cm}^{-2}$ . The work presented here specifies in each case the incident power for the results shown. The LED light source consisted of 7 LEDs in a single unit and was used as purchased (NT-52D0-0429 Daylight White, Element14, Australia). The spectrum, provided by the supplier, produced by this light source is shown in Figure 2.10. When we compare this to the AM1.5 spectrum, shown previously in Figure 1.1, we see that there is some mismatch. However, the broad peak centred around 570nm closely matches the maximum power (approximately 600nm) of natural sunlight.

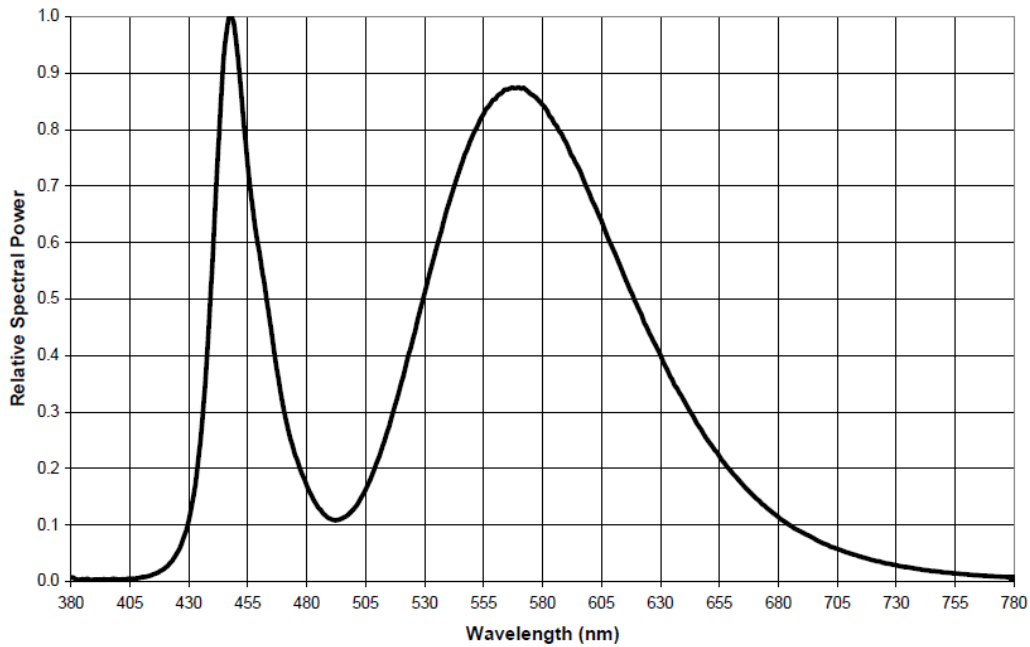


Figure 2.10: Spectrum of LED solar simulator, from supplier.

### 2.5.1 Spectral Response

For spectral response of the cells the LED solar simulator was used with a set of different interference filters. These filters block all but a specific narrow wavelength range allowing for the cell's response to certain wavelengths as opposed to white light to be determined. The filters were purchased from Oriel (LOT Oriel, Germany) and the wavelength centres and supplier codes are listed in Table 2.1. The FWHM of each spectral centre was 10nm. To compensate for the differing spectral power across the wavelengths, when using the filters the radiance of the light source was adjusted by altering the current applied to the light source to produce a normalised output.

Table 2.1: List of wavelength filters used in this work.

Wavelength Centre (nm)	Supplier Part No.
420	53810
450	53830
460	53840
480	53850
500	53860
520	53870
540	53880
550	53890
560	53900
580	53910
600	53920

## 2.6 Electrochemistry

To analyse the conductivity and electron transfer properties of the arrays produced electrochemistry was used. Electrochemistry is a powerful technique that allows for the electronic properties of a sample to be investigated, such as electron transfer rates and conductivity. Electrochemistry is also powerful in verifying the attachment of redox active species to these CNT arrays.

Two different systems were used to perform electrochemistry in this work. Electrochemical measurements (Cyclic voltammetry (CV) and differential pulse voltammetry (DPV)) were done on a BAS100W/B electrochemical analyser. The un-/modified CNT array acted as the working electrode, a platinum mesh was used as the counter and a saturated Ag/AgCl electrode was used as a reference electrode. The electrolyte used was 0.1M tetrabutylammonium hexafluorophosphate (TBAPF<sub>6</sub>) in dichloromethane (DCM). A Teflon cell built in-house was used to hold the electrolyte solution and the electrodes.

CV, DPV and electrochemical impedance spectroscopy (EIS) were also performed on a microAutolab Type III/FRA2 (Eco Chemie, Utrecht, Netherlands) using the modified SWCNT array as the working electrode, a platinum mesh as the counter and a saturated Ag/AgCl reference electrode. The electrolyte used was 0.1M TBAPF<sub>6</sub> in DCM, a Teflon cell was used to hold the electrolyte solution and the electrodes.

### 2.6.1 Cyclic Voltammetry

Cyclic voltammetry (CV) is an electrochemical technique that uses the three electrode system; working electrode (WE), counter electrode (CE) and a reference electrode (RE). The working electrode is swept versus time between one potential and another and then back again completing one cycle. As the WE cycles its potential the resultant current is measured at the counter electrode. This is then plotted as current versus potential (Amperes vs. Volts). A typical CV plot is shown in Figure 2.11. As the potential is swept the current will increase until the potential is equal to the oxidation or reduction potential of the analyte, leading to two peaks, an anodic and a cathodic

peak. These then have a potential  $E_{pc}$  for the cathodic and  $E_{pa}$  for the anodic as well as a corresponding current  $I_{pc}$  and  $I_{pa}$  respectively, shown in Figure 2.11. The separation between the peaks is dependent on the number of electrons,  $n$ , involved in the process. The ideal equation is shown in Equation 2.1.

$$\text{Equation 2.1: } |E_{pc} - E_{pa}| = \frac{57mV}{n}$$

Equation 2.1 shows that in an ideal one electron process the peak separation should be 57mV. The current  $I_p$  is also proportional to the scan rate. A linear relationship between  $I_p$  and scan rate ( $v$ ) indicates that the analyte is bound to the working electrode surface. A diffusion based system will have the scan rate proportional to the square root of the scan rate.<sup>129</sup>

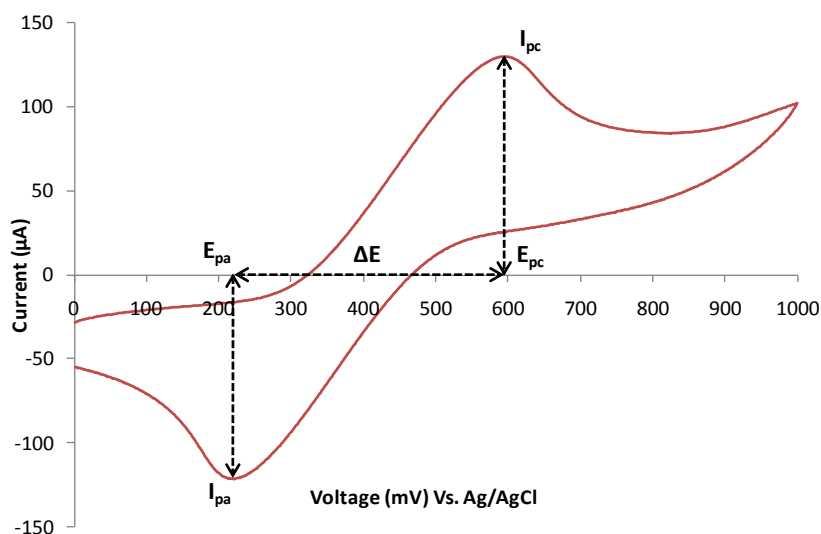


**Figure 2.11:** Example cyclic voltammogram with peak current  $I_p$  and voltage  $E_p$  labelled for both the anodic and cathodic peaks.

Due to the dependence of  $I_p$  and  $E_p$  on scan rate the electron transfer rate coefficient ( $k_s$ ) and the surface concentration can be determined by taking CV plots for several different scan rates, using equations first shown by *Laviron*.<sup>129-131</sup> The Randles-Sevcik equation, shown in Equation 2.2, allows for the diffusion coefficient of ions in solution to be determined. The peak current is shown to be dependent on the number of electrons  $n$ , Faraday's constant  $F$ , electrode area  $A$ , the concentration of analyte  $C$ , and the diffusion co-efficient  $D$ .

$$\text{Equation 2.2: } I_p = 0.4463 nFAC \left( \frac{nFvD}{RT} \right)^{1/2}$$

Equation 2.3 expresses the relationship between peak current  $I_p$  and  $\Gamma$ , the surface concentration in  $\text{mol.cm}^{-2}$ , where  $n$  is the number of electrons involved in the process,  $F$  is the Faraday constant,  $Q$  is the integrated peak area,  $v$  is the scan rate,  $R$  the gas constant and  $T$  the temperature and  $A$  is the electrode area.

$$\text{Equation 2.3: } I_p = \frac{n^2 F^2 A \Gamma v}{4RT} = \frac{nFQv}{4RT}$$

Using the relationship between peak potential ( $E_p$ ) and scan rate ( $v$ ) we can then use Equation 2.4 to calculate  $k_s$ , the electron transfer constant,<sup>129, 131-133</sup> where  $E_p$  is the peak potential,  $E^0$  is the formal redox potential,  $\alpha$  is the transfer coefficient and  $R$ ,  $T$ ,  $F$ ,  $n$  and  $v$  are as previously defined.

$$\text{Equation 2.4: } E_p = E^0 + \frac{RT}{\alpha nF} \ln \frac{RTk_s}{\alpha nF} - \frac{RT}{\alpha nF} \ln v$$

### 2.6.2 Differential Pulse Voltammetry

Differential pulse voltammetry (DPV) is an electrochemical technique closely related to CV. It too uses the same three electrode system, however, instead of simply a linear sweep of potential it has superimposed over it a series of pulses with the current being measured immediately before each voltage change. This waveform is shown in Figure 2.12. The resultant plot is the change in current versus potential.

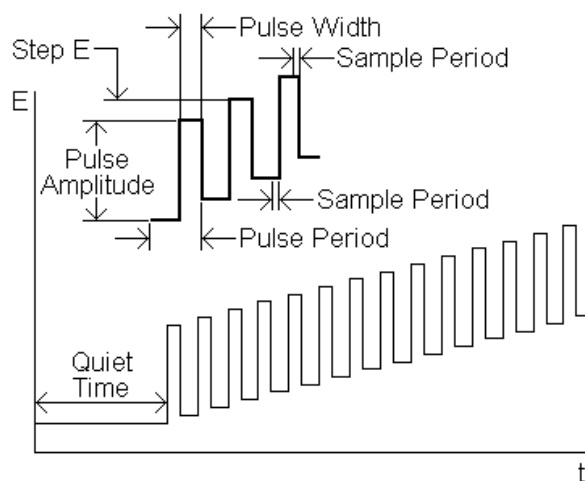


**Figure 2.12: DPV potential waveform E, with respect to time, t. From Manufacturer (BAS Inc).**

Due to the current being read before the potential change there is less background signal. At a potential above or below the redox potential there is no Faradaic current response and as the bias approaches the redox potential a maximum in current is formed followed by a decrease as the current becomes diffusion limited, leading to a symmetrical peak. This also leads to a much lower detection limit than CV. Typically  $10^{-8}\text{M}$  can be detected. Figure 2.13 depicts a standard DPV plot, showing the peak potential  $E_p$  and peak magnitude  $I_p$ . The peak height,  $I_p$ , is directly proportional to the concentration of the analyte and can be used to determine how the concentration may be changing between samples.

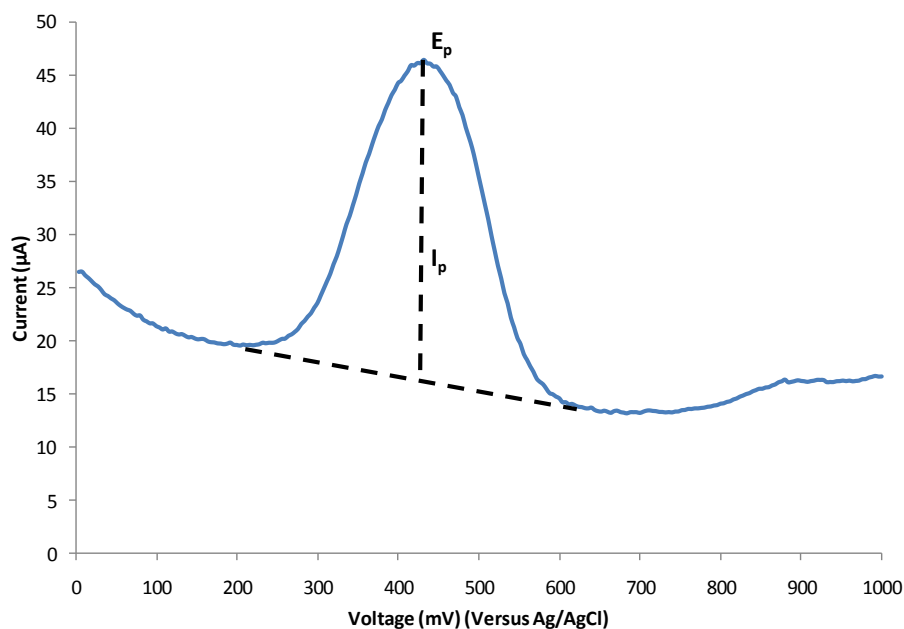


Figure 2.13: Example differential pulse voltammogram with peak current  $I_p$  and voltage  $E_p$  labelled.

### 2.6.3 Electrochemical Impedance Spectroscopy

Electrochemical impedance spectroscopy (EIS) is an electrochemical technique that measures the impedance of a cell as a function of frequency. This means that unlike CV and DPV which use a direct voltage to produce a current, alternating voltage is used to produce a resulting AC current. Impedance is the resistance to AC current in a complex system, meaning there is a real and imaginary component. To measure an EIS spectrum a small AC perturbation signal is applied to the cell, usually on the order of 10mV, whilst the frequency of this signal is ramped. This allows for the dynamic response of the cell to be determined. This data is then typically plotted as a Bode plot and a Nyquist plot. An example of a Bode and Nyquist plot is shown in Figure 2.14. A Bode plot is the phase difference from the applied and measured signal versus the applied frequency ( $^\circ$  vs.  $f$ ), whilst a Nyquist plot shows the planar vector with the complex or imaginary impedance ( $Z''$ ) versus the real impedance ( $Z'$ ).

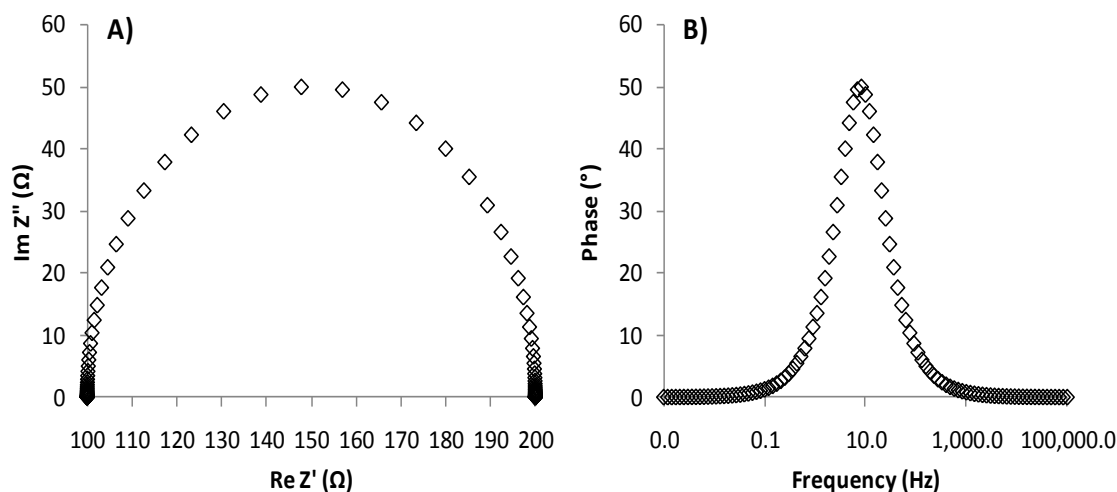


Figure 2.14: Example of EIS spectra, simulated using a Randles type circuit.  
A) Nyquist Plot. B) Bode Plot.

After the experimental data has been acquired from EIS an equivalent circuit can be modelled to determine the cell behaviour. For example an electrode-electrolyte interface has both capacitive and resistive elements due to the electrochemical double layer. An example of this is shown in Figure 2.15 where a simple equivalent circuit and the corresponding Nyquist plot are shown.

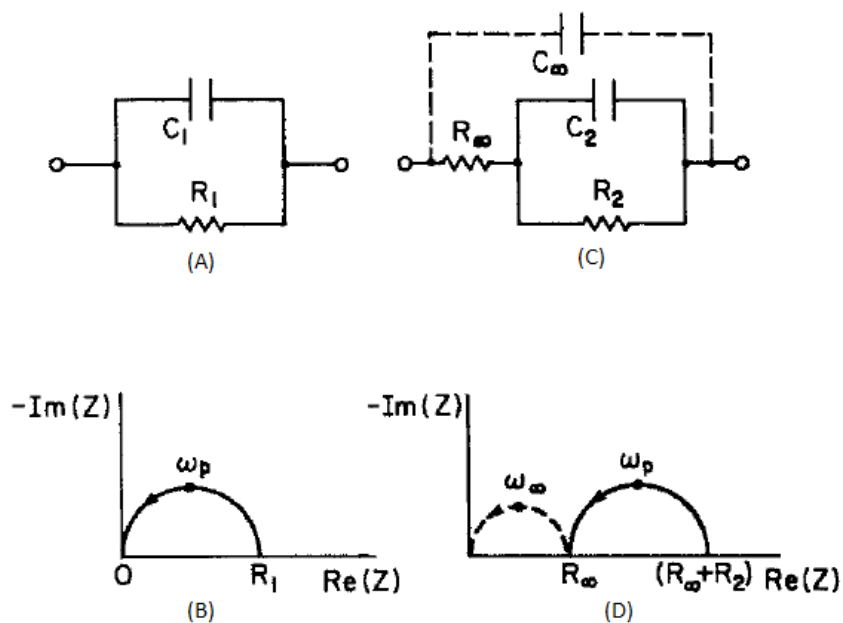


Figure 2.15: Example of equivalent circuits and the corresponding Nyquist plot.  
Modified from Barsoukov et al.<sup>134</sup>

Such an interface is often modelled by a capacitor and resistor in parallel ( $C_1$  and  $R_1$ ), however most real world interfaces do not have ideal capacitive behaviour and as such are modelled using a constant phase element (CPE). A CPE element is given a value of  $n$ , when  $n=0$  would be an ideal resistor, whilst  $n=1$  describes an ideal capacitor. EIS has become particularly useful for investigating electrochemical solar cells because it allows the interface between the electrodes and electrolyte to be studied in detail.<sup>24, 135-140</sup> From EIS the resistance of electrodes can be determined as well as the rates of diffusion of the ions within the electrolyte.

In this work EIS was performed using a microAutolab Type III/FRA2 (Eco Chemie, Utrecht, Netherlands) whilst in the dark with 0mV bias. The amplitude of the perturbation signal was 10mV and the frequency range was logarithmically distributed from 0.02-10000Hz.

## 2.7 Raman Spectroscopy

Since its discovery in 1928<sup>141</sup> Raman spectroscopy has been used extensively for the identification and characterisation of materials. Raman spectroscopy works on the principles of Raman scattering in which samples are irradiated with light and the scattered light is measured. Most of the light photons elastically scatter, retaining all of their incident energy with no change in frequency; this is called Rayleigh scattering. However, a small fraction ( $1$  in  $10^7$ ) of the photons experience inelastic scattering due to an interaction with the substrate or adsorbed material. This loss of energy on interaction with a sample, caused by the interaction with the vibrational states of the sample, leads to a frequency shift of the scattered photon, which is then detected by a spectrometer. A schematic of the confocal Raman microscope used in this work is shown in Figure 2.16, showing light from a laser that is focused onto a sample and the scattered light detected by a spectrometer.

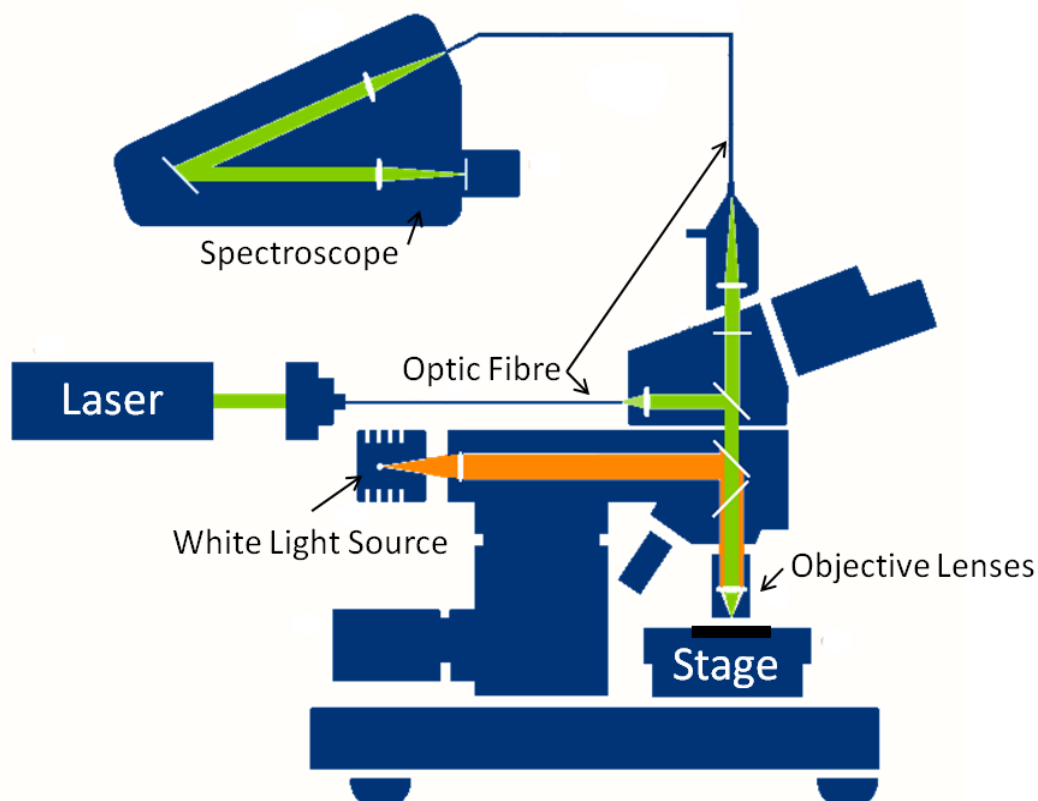


**Figure 2.16: Diagram of Raman spectrometer. Modified from supplier.**

Because of the complex electronic structure of CNTs and large Raman absorption cross-section (as discussed in 1.2.1) Raman spectroscopy is an ideal technique for investigating and identifying sample properties. CNTs have been extensively examined using Raman spectroscopy throughout the past decade.<sup>66, 69, 142-147</sup> The unique density of states that are characteristic of SWCNTs means that the resultant spectrum can provide a large amount of information about the nature of the nanotubes. A table of the Raman peaks seen from CNTs from literature is seen in Table 2.2. The characteristic peaks of interest (shaded) are the radial breathing mode (RBM) peak, which is caused by circumferential phonon interaction. The position of this peak is directly proportional to the diameter of the nanotubes under investigation. The G band or graphitic band is caused by  $sp^2$  hybridised carbon present in graphite and CNTs. The D or 'disorder' band is caused by disruptions to the DOS of the  $sp^2$  carbon of the nanotube, usually by the presence of amorphous or  $sp^3$  carbon. The ratio of disorder to graphitic carbon (D/G ratio) can be used as a measure of CNT purity, pristine

nanotubes should have very little to no D band, whereas highly functionalised or multi-walled CNT will have very high D band intensity.

**Table 2.2: Raman spectral features of carbon nanotubes with laser energy 2.41eV.**  
Modified from *Dresselhaus et al.*<sup>69</sup>

Name	Frequency $\omega$ (cm <sup>-1</sup> )	Notes
iTA	288	Intravalley Scattering
LA	453	Intravalley Scattering
RBM	248 / $d_t$	Radial Breathing Mode, Nanotube Only
IFM <sup>-</sup>	750	Combination Mode oTO-LA
oTO	860	IR-active mode of graphite
IFM <sup>+</sup>	960	Combination Mode oTO+LA
D	1350	Longitudinal Optic (Intervalley Scattering)
LO	1450	Longitudinal Optic (Intervalley Scattering)
BWF	1550	Plasmon Mode (Metallic Carbon)
G	1582	Raman active mode of graphite
SWCNT Specific	1570	$G^-$ feature for in-plane vibrations along the circumferential direction
	1590	$G^+$ feature due to in-plane vibrations along the tube axis
M <sup>-</sup>	1732	Overtone of oTO
M <sup>+</sup>	1755	Overtone of oTO
iTOLA	1950	Combination mode of iTO and LA
G'	2700	Overtone of D mode
2LO	2900	Overtone of LO mode
2G	3180	Overtone of G mode

Raman measurements in this work were taken on an alpha300R microscopy/spectroscopy setup (Witec, Germany). 20x, 40x and 100x objective lenses were used with a 532 nm laser (2.33eV), with a maximum power of 65mW. Both single spectra from a single location and image spectra made up of a large number of spectra over a large area were taken. For each single spectrum an integration time of 6 seconds was used with 10 iterations. For image spectra, where the size is mentioned next to the appropriate figure, 2500 spectra with an integration time of 0.5 seconds

and 50x50 points per image was used. The spectra had their fluorescence background subtracted using the Witec packaged software.

## 2.8 X-Ray Photoelectron Spectroscopy

X-ray photoelectron spectroscopy (XPS) is a technique that is based on the principle of the photoelectric effect. X-rays are produced and directed towards the sample to be analysed. Electrons in the sample material are excited and many have sufficient energy to leave the sample and are channelled into an analyser where their kinetic energy is measured. A simple XPS schematic is shown in Figure 2.17. The kinetic energy of the analysed electron is dependent on the orbital shell that it came from and thus can be used to determine the elemental composition of the sample and each individual element's chemical binding environment. Although the X-rays penetrate several microns into the substrate and excite electrons at this depth, emitted electrons are usually reabsorbed by neighbouring atoms or lose enough kinetic energy to become trapped in the material. Therefore the effective escape depth of electrons through the sample is limited to several nm, making XPS a surface sensitive technique.

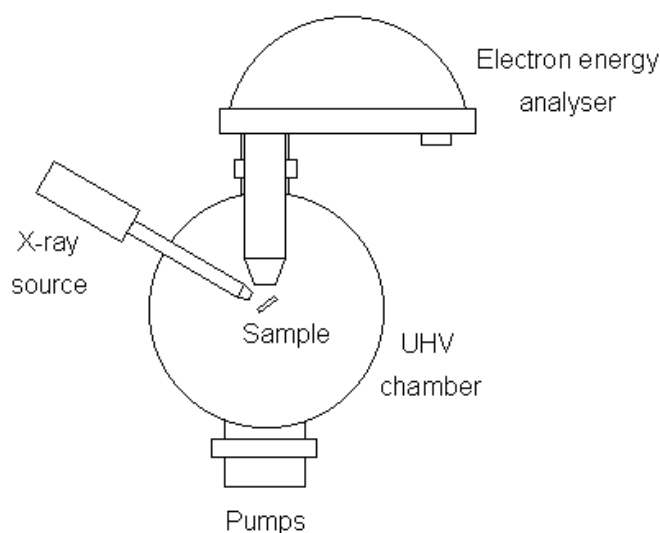


**Figure 2.17: Schematic of an X-ray photoelectron spectrometer.**

The XPS setup used in this work was a Leybold-Heraeus LHS-10, in a chamber with a base pressure of  $10^{-9}$  Torr and an operating pressure of  $10^{-8}$  Torr. The source was a dual anode X-ray source (Specs, Germany) and the energy used was Al K $\alpha$  (1486.6eV) with a 20eV pass energy. Survey spectra were taken in constant retarding ratio mode,

whilst high resolution spectra were an average of 5 spectra taken in fixed analyser transmission mode. An example spectrum of platinum is shown in Figure 2.18, where the survey spectrum and high resolution spectrum (inset) are both shown. In the survey spectrum the Pt 4f peak has little discernable structure; however, by taking a high resolution spectrum of that range of binding energies the doublet can be resolved. The position of these peaks can also be compared to literature values and used for calibration.

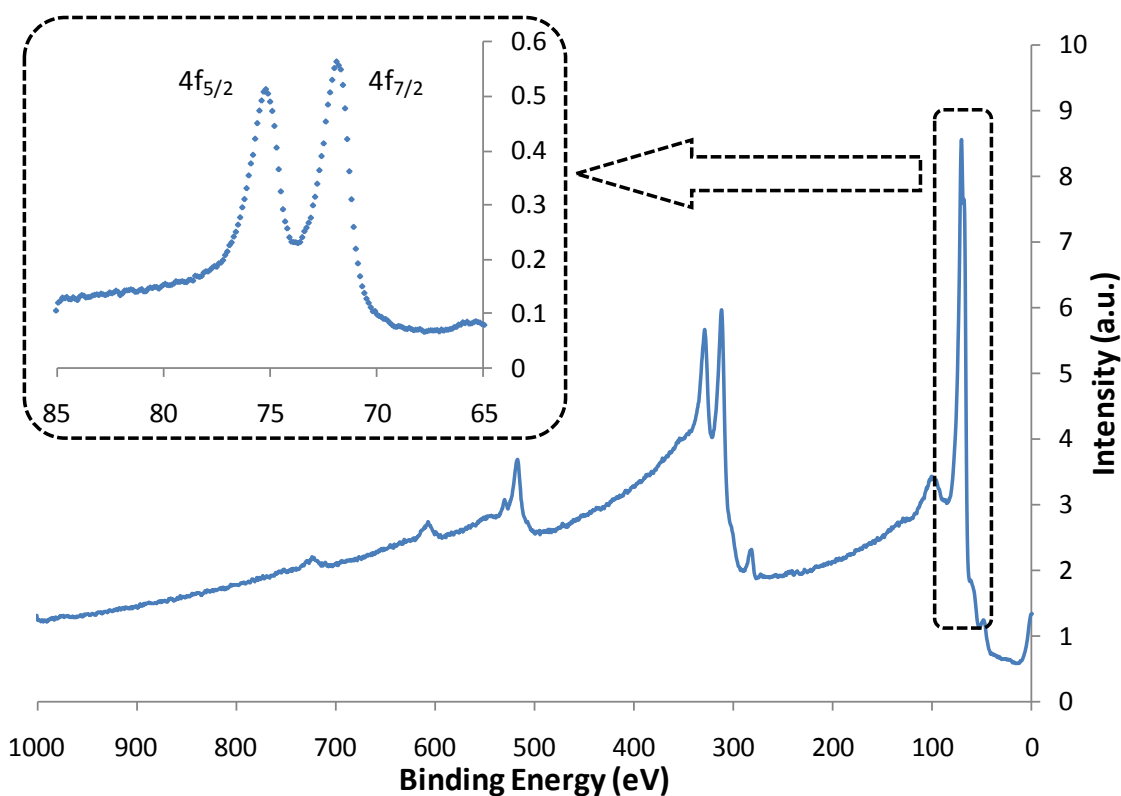
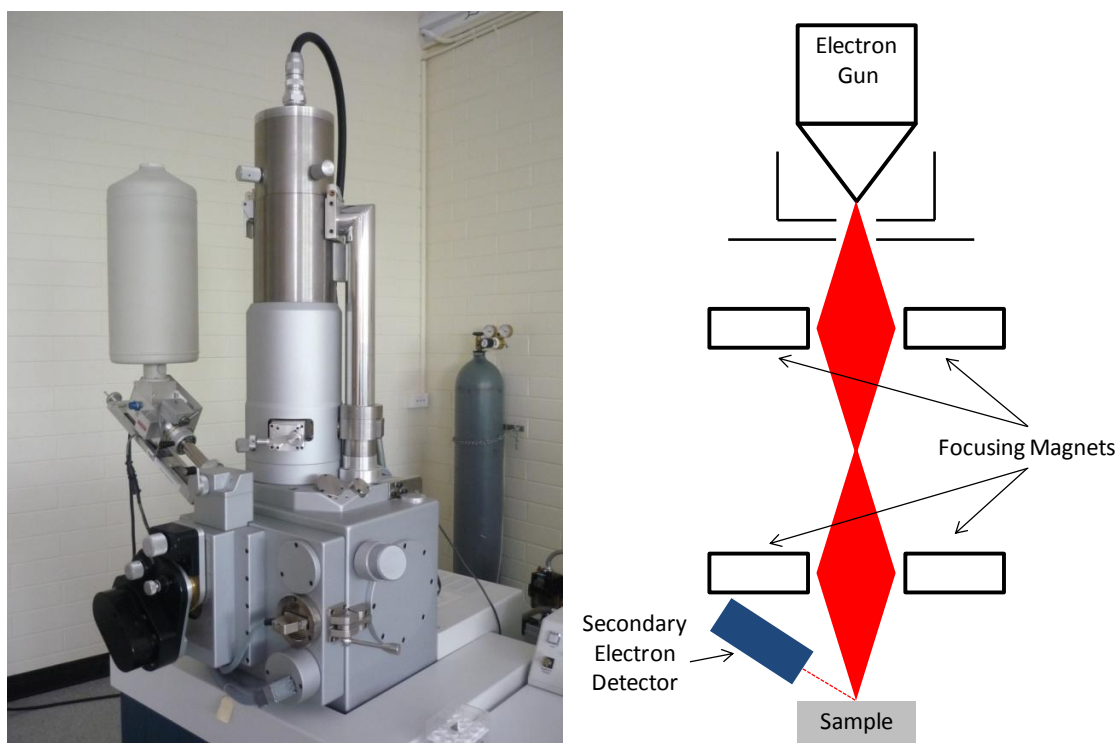


Figure 2.18: XPS spectrum of platinum. Inset: High resolution XPS of Pt 4f binding region.

## 2.9 Scanning Electron Microscopy

Scanning electron microscopy (SEM) is an imaging technique that allows for higher resolution than would normally be possible in a light microscope by using a much smaller wavelength. Normal light microscopes operate in the visible wavelength range, 400-700nm, and thus are limited in resolution to a theoretical feature size of  $\lambda/2$  or 200nm. Even reaching this theoretical limit is very difficult due to problems with optics long before the wavelength becomes a factor. However, in SEM instead of

visible light photons the imaging is performed using high energy electrons. Electrons are produced, usually by thermal filament or field emission source, and are accelerated and focused with several magnetic coils along a vacuum chamber. A schematic of such a chamber is shown in Figure 2.19, where the electron beam is produced, accelerated and focused before hitting the sample. Upon hitting the sample several processes occur; firstly some electrons are elastically rebounded in what is called backscattering, some electrons are absorbed into the sample and cause the excitation and emission of secondary electrons and lastly during the secondary electron process X-rays are produced. The first two procedures, backscattering and secondary electron can be used for imaging, whilst the X-rays emitted can be used for energy dispersive X-ray analysis (EDX).



**Figure 2.19: Photograph and schematic of a scanning electron microscope.**

The SEM images presented in this work were taken on a Camscan MX2500 SEM fitted with an EDX detector (CamScan Electron Optics Limited, UK) using the secondary electron detector. The electron source was a tungsten filament and the accelerating voltage used was 10kV. Prior to imaging each sample was sputter coated with 10nm of platinum using a Quorumtech K575X (Quorum Technologies, UK).

---

### **3. Photoresponse of Single-walled Carbon Nanotube Arrays**

---

### 3.0 Introduction

Work on the photoresponse of CNTs, as discussed in section 1.3, has used various methods for producing the CNT working electrodes. These include growing of CNT arrays by chemical vapour deposition,<sup>51</sup> deposition from solution,<sup>57, 148</sup> and deposition by electrophoresis,<sup>49, 53, 55, 149</sup> even including the use of individual nanotubes.<sup>50, 89, 91, 150</sup> Previously, it has been shown that chemical attachment of CNTs to surfaces provides enhanced electron transport when used in electrochemistry as compared to an unmodified electrode surfaces.<sup>94, 116, 121, 123, 124, 151, 152</sup> This enhanced electron transfer has also been shown to be dependent on orientation of the CNTs used, either vertically or horizontally aligned.<sup>153</sup> Thus, the use of chemical attachment to create CNT arrays is expected to be advantageous for applications in electronic devices due to the increased electron transfer rates and increased conductivity provided by a direct covalent bond, as opposed to a physisorption process present in grown CNT arrays. One method that has been investigated for the integration of CNTs into electronic devices is the use of an electrochemical cell, similar to the DSSC architecture. A layer of carbon nanotubes acts as the working electrode whilst an electrolyte solution containing a iodide/tri-iodide redox couple acts as an electron shuttle to a counter electrode, where a platinum catalyst is present.<sup>49, 52</sup> Previous studies have shown that it is possible to create vertically aligned single-walled carbon nanotube arrays on silicon and utilize the nanotubes as wires allowing conduction into the surface.<sup>154</sup> The vertical alignment is caused by the interaction between the hydrophobic side-walls and the hydrophilic substrate. As bundles of carbon nanotubes approach the hydrophilic surface the functionalised carboxylic acids on the ends covalently attach and the largely hydrophobic sidewalls repel the surface; leading to vertical alignment.

### 3.1 Characterisation of Carbon Nanotube Array on FTO

#### 3.1.1 Raman Spectroscopy of CNT Arrays on FTO

Confocal Raman spectroscopy can be applied to ascertain the presence and properties of SWCNT attached to a surface. The shape and ratio of the  $G^{+/-}$  peaks can be used to determine the metallic or semi-conducting nature of the nanotubes present. In Figure 3.1 the Raman spectra from literature for a single semi-conducting SWCNT (S-SWCNT) and for a metallic SWCNT (M-SWCNT) are shown. The  $G^-/G^+$  ratio for the M-SWCNT is seen to be close to 1 with both peaks around the same intensity. However, for the S-SWCNT the  $G^+$  peak is seen to be much larger giving a  $G^-/G^+$  ratio of around 0.4. Thus, this ratio of  $G^-/G^+$  can be applied to give a measure of semi-conducting nature of SWCNTs.

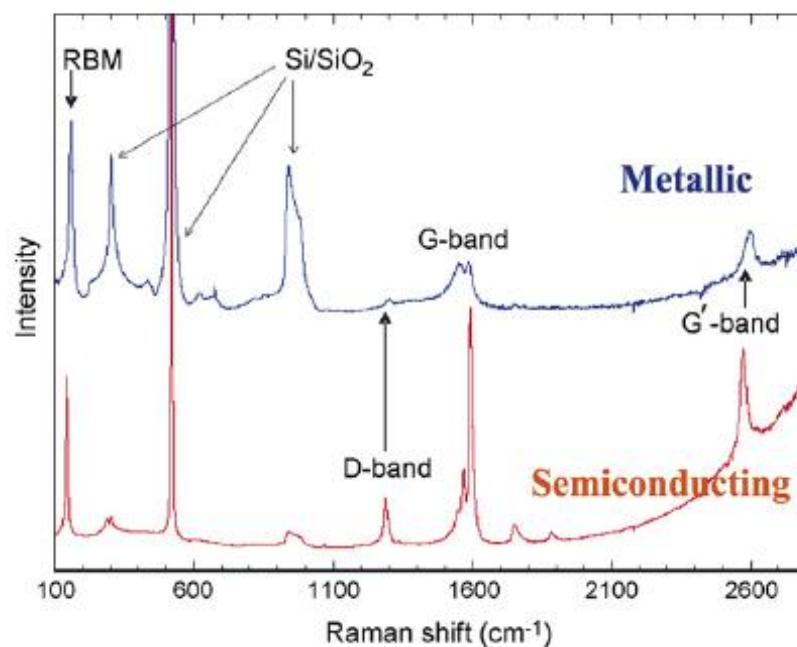
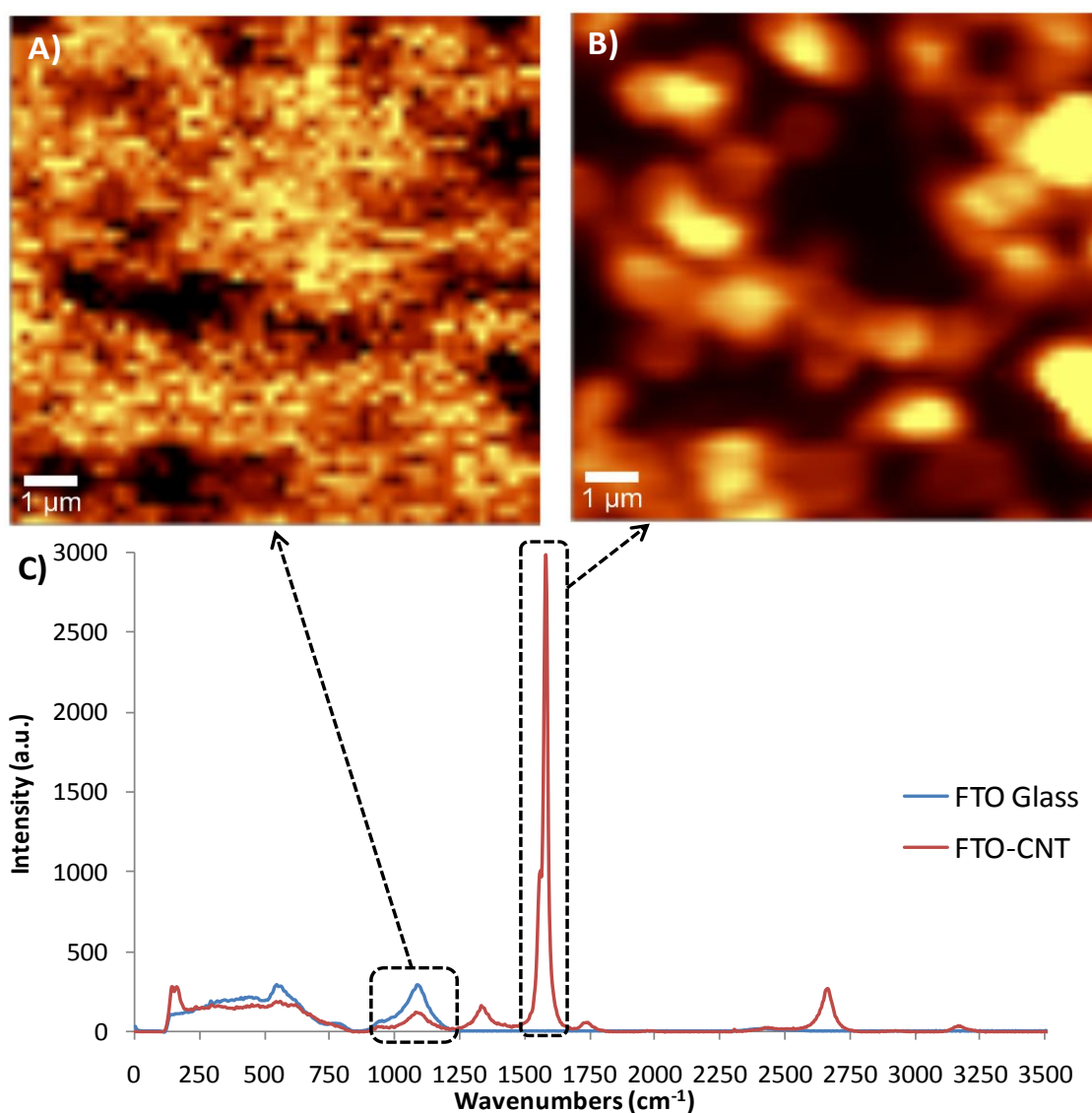


Figure 3.1: Raman spectra for a single semi-conducting and metallic SWCNT. From Dresselhaus *et al.*<sup>146</sup>

To ascertain if nanotubes have been successfully attached to FTO glass substrates and to gather information on the electronic state of the aligned nanotube bundles confocal Raman images and spectra were taken and are shown in Figure 3.2. From the spectra taken, it is clear that the nanotubes have successfully been attached to the FTO glass as nanotube specific peaks, such as the RBM (148cm<sup>-1</sup>) and G band (1580cm<sup>-1</sup>) can be seen.<sup>69</sup> We also see that the G peak is present as a doublet, with

both a  $G^-$  ( $1570\text{ cm}^{-1}$ ) and  $G^+$  ( $1590\text{ cm}^{-1}$ ) peaks. The FTO glass spectrum, shown in Figure 3.2, has only a single peak at  $\sim 1030\text{ cm}^{-1}$  and a region of increased intensity between  $250$  and  $750\text{ cm}^{-1}$ . These FTO features are seen in the FTO-CNT sample as well but with lower intensity due to the nanotubes blocking some of the signal. This is seen in the images in Figure 3.2B where high CNT intensity is represented as lighter areas and these same areas appear as black when we plot the glass peak intensity (Figure 3.2A).



**Figure 3.2: Confocal Raman images showing nanotube coverage. (A and B) Image A is a plot of the intensity of the glass specific peak ( $1030\text{ cm}^{-1}$ ). Image B is the G band ( $1570\text{ cm}^{-1}$ ) intensity present in the spectra (C) for 24 hours of nanotube attachment, with 8 hours cutting time.**

The reaction with the acid mixture during the attachment procedure produces defect sites along the tube's length and this disrupts the electronic structure of the

tubes either altering their band gap or converting metallic tubes to semi-conducting.<sup>66</sup> This modification of the band structure should also be present as changes in both the Raman spectra and the photoresponse of the array. In a typical Raman SWCNT spectrum there are several peaks, listed previously in Table 2.2, which can tell us very specific information. The 'D' band disorder peak provides information about defects along the tube walls which in turn defines the band gap. As defects along the side walls disrupt the electronic state of the tube, the band gap increases making the nanotube semi-conducting with differing band gap energies depending on the number of defects introduced.<sup>145</sup> By taking the ratio of the D band to the  $G^+$  band the level of disorder or number of defects present on the CNTs can be analysed. A ratio is used and not the absolute value to compensate for differing laser energies which will affect peak intensities. Also the ratio of the  $G^-$  to the  $G^+$  peak can be compared. Normally the presence of both peaks alone tells us the sample consists of SWCNTs and not multi-walled tubes. However, by analysing the line shape and intensity the percentage of semi-conducting tubes in the sample can be determined.<sup>145</sup> Extended cutting times should lead to an increased number of semi-conducting tubes and with an increasing band gap. Figure 3.3 shows the graph of  $D/G^+$  ratio as well as the  $G^-/G^+$  ratio, the  $D/G^+$  is seen to be increasing with cutting time up until 4 hours and then the slope decreases levelling out to 8 hours, indicating that the number of defect sites is increasing and then remaining constant. The  $G^-/G^+$  ratio is seen to be decreasing to 4 hours and then plateauing also. This indicates that the percentage of semi-conducting tubes is increasing to a point and then remaining constant. This plateau effect seen after 4 hours of cutting time is thought to be due to the consumption of amorphous carbon and catalyst particles early on leading to a greater change in disorder, which then becomes a more gradual change after 4 hours treatment time.

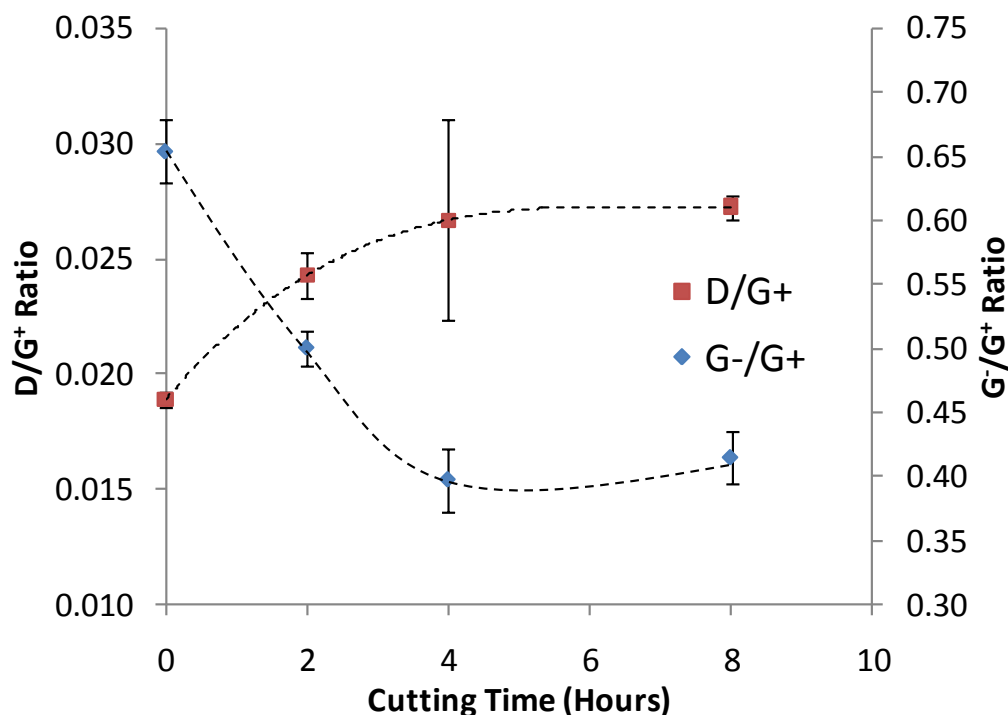


**Figure 3.3:** Graph of D and G<sup>+</sup> band ratio and G<sup>-</sup> and G<sup>+</sup> ratio versus cutting time. Each point represents the average of several individual spectra taken across a wide area on the sample, with error bars showing one standard deviation. Dashed line added to guide the eye.

Confocal Raman images were also obtained from a 5x5 $\mu\text{m}$  area for CNT with differing cutting times attached to FTO glass. These scans were made up of 50x50 individual spectra with an integration time of 0.5 seconds at identical laser power. The spot size of each individual scan, using the 100x objective, is 300nm. Hence this is the resolution of each image. A histogram was then generated by taking the intensity of the G-band from 1485-1685 $\text{cm}^{-1}$  (X-axis, counts) and the number of pixels with that intensity (Y-axis, pixels). The graph in Figure 3.4 shows the histogram for the differing cutting times. The 2 hour cutting time has the lowest intensity with its centre at 2500 counts and then the 4 hour cutting time is centred at 13000 and the 8 hour cutting time at 24000. This increase with cutting time is an indication of the amount of CNT attached to the surface, as an average over the 5 $\mu\text{m}$  square. The distribution also tells us about the bundle size present on the surface. The 2 hour sample has a much narrower distribution indicating that it consists of a lower amount of graphitic carbon on the surface, and in thinner bundles. This can be ascertained because larger bundle sizes would produce a larger number of pixels with high counts, leading to a broadening of the peak. The distribution then widens for the 4 and 8 Hr samples,

indicating an increasing bundle size distribution and increasing surface coverage due to an increased number of pixels with a high count from the G band. A similar trend in surface coverage has been seen before for SWCNT bundles chemically attached to silicon and determined by AFM.<sup>120</sup>

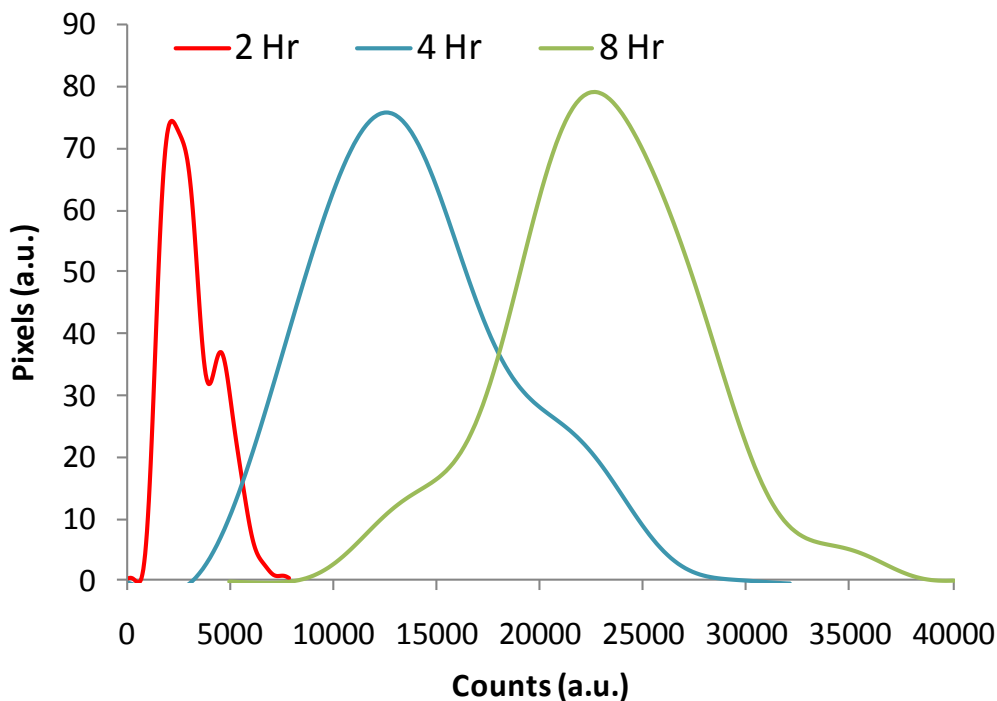


**Figure 3.4:** Histogram of G-band intensity for differing cutting times (2, 4 and 8 hours as indicated) of CNT attached to FTO glass for 24 hours and identical Raman laser intensity.

### 3.1.2 XPS Characterisation of SWCNT on FTO

Figure 3.5 compares the XPS survey spectra for the bare FTO before and then after the SWCNT array has been successfully attached. The main peaks of interest have been labelled, and as would be expected the bare FTO spectrum contains mainly tin and oxygen peaks. The fluorine dopant is in too low a surface concentration to be detected. Of note is the presence of a small carbon 1s peak (C1s). This is caused by exposure to atmospheric conditions and is termed adventitious carbon. Often this adventitious carbon, as it is always present on samples exposed to atmosphere, is used to calibrate XPS spectra because it occurs at a well defined binding energy. After the formation of the SWCNT array the carbon signal intensity increases and the tin signal decreases, this is indicative of the presence of a SWCNT layer which is now attenuating the tin photoemitted electrons from leaving the surface.

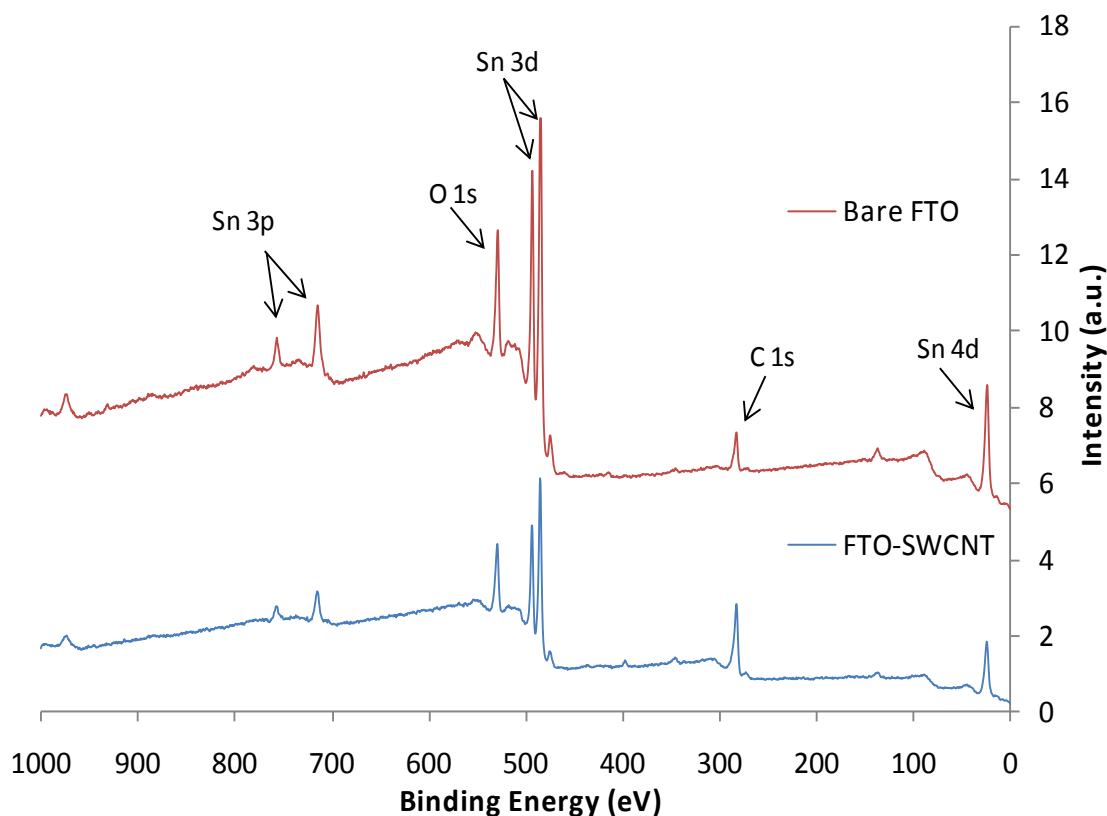


**Figure 3.5: XPS survey spectra of bare FTO and SWCNT functionalised FTO.**

To better understand the chemical environment of the untreated and functionalised FTO, high resolution spectra were taken for the oxygen 1s (O1s) and C1s binding regions. These high resolution XPS spectra are shown in Figure 3.6, with the bare FTO in A and B whilst the functionalised FTO in C and D. Upon comparison of the O1s region for both substrates (Figure 3.6A/C) we see that the predominant peak occurs at 530.3eV for both samples. This is attributed to the tin oxide ( $\text{SnO}_2$ ) on the substrates.<sup>155</sup> There is also a smaller peak occurring at 531.5eV attributed to carbonyl groups (C=O) within the adventitious carbon compounds. The SWCNT oxygen peak is slightly different, apart from the tin oxide peak it has two smaller contributions, one at 532.5eV and another at 534eV (C=O and C-O respectively), both of these correspond well with the literature values for nanotube oxygen bonds.<sup>156</sup> This is to be expected as the treatment to the SWCNTs before attachment involves the introduction of carboxylic acid groups. The C1s binding region for the bare FTO substrate (Figure 3.6B) shows a single peak located at 285eV, in close agreement with literature which state that the generally accepted value for adventitious carbon is at 284.8eV.<sup>155</sup> Figure 3.6D

is the C1s binding region after SWCNT have been attached and shows a distinct difference from the bare FTO. Now the spectrum consists of three main contributions, the first at 284.2eV from  $sp^2$  hybridised carbon, the second at 285.9eV attributed to  $sp^3$  hybridised carbon and finally a broad low intensity peak around 287.2eV caused by carbonyl and carboxylic acid groups (C=O,C-O). Again these peaks match what would be expected as the SWCNT are predominantly graphitic or  $sp^2$  carbon, the  $sp^3$  carbon is present from defect sites and in the adventitious carbon and finally the acid treatment has introduced carboxylic acid groups giving rise to the carbon-oxygen binding. The use of a surface sensitive technique such as XPS allows us to confirm that SWCNTs are present on the surface and to investigate the chemical environment of the surface elements.

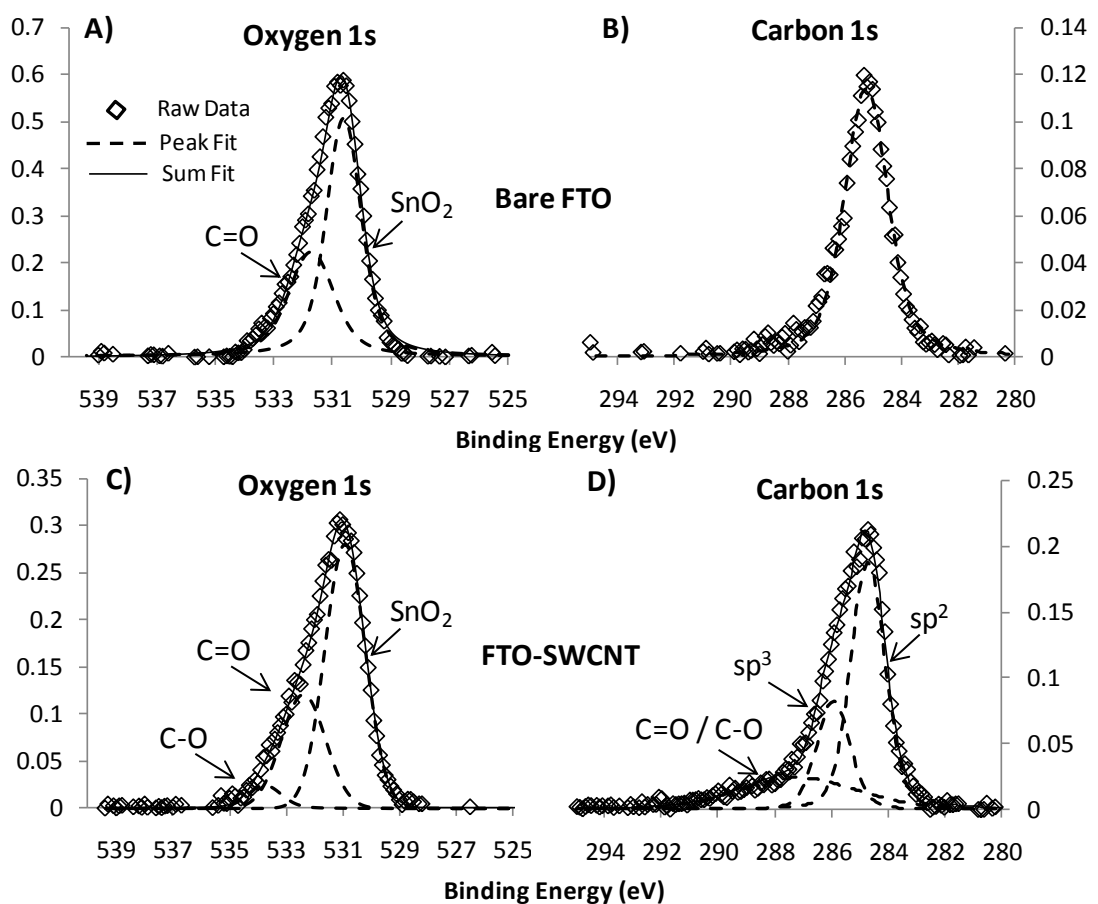


**Figure 3.6:** High resolution XPS spectra of; oxygen 1s binding region (A) and carbon 1s binding region (B) for bare FTO, oxygen 1s binding region (C) and carbon 1s binding region (D) for SWCNT functionalised FTO.

### 3.1.3 Electrochemistry of SWCNT Arrays on FTO

Once the chemical attachment of the SWCNT onto the glass substrates had been verified and investigated with Raman spectroscopy and XPS the electron transport properties of the electrodes were analysed. One method for determining the electron transfer properties of an electrode is through the use of electrochemistry. By using a standardised redox couple such as ferrocene/ferrocenium ( $\text{Fc}/\text{Fc}^+$ ) direct comparisons between the conductivity and electron transfer kinetics of each CNT modified electrode can be made. To act as a benchmark the unmodified FTO surface was investigated first. Figure 3.7A shows the CV at scan rates ranging from  $20\text{mV}\cdot\text{s}^{-1}$  to  $300\text{mV}\cdot\text{s}^{-1}$  of the ferrocene solution with the bare FTO surface acting as the working electrode. The expected peak separation for an ideal one electron redox couple, such as  $\text{Fe}/\text{Fe}^+$ , is 57mV. The peak separation can thus be used as a good measure of ideality, the larger the peak separation the slower the electron transfer kinetics. In Figure 3.7A the peak separation at a scan rate of  $100\text{mV}\cdot\text{s}^{-1}$  is 831mV indicating that the unmodified surface is quite insulating. Figure 3.7B is the plot of peak height versus the square root of scan rate. The data is seen to follow a linear trend, with an  $R^2$  value of 0.99, and this can be used to identify the reaction kinetics taking place. *Laviron*<sup>129</sup> demonstrated that a linear trend between peak height and scan rate indicates that the redox molecule in question is adsorbed to the electrode surface, however, if the peak height is linearly related to the square of the scan rate, as is the case in Figure 3.7B, then the redox species is in solution.

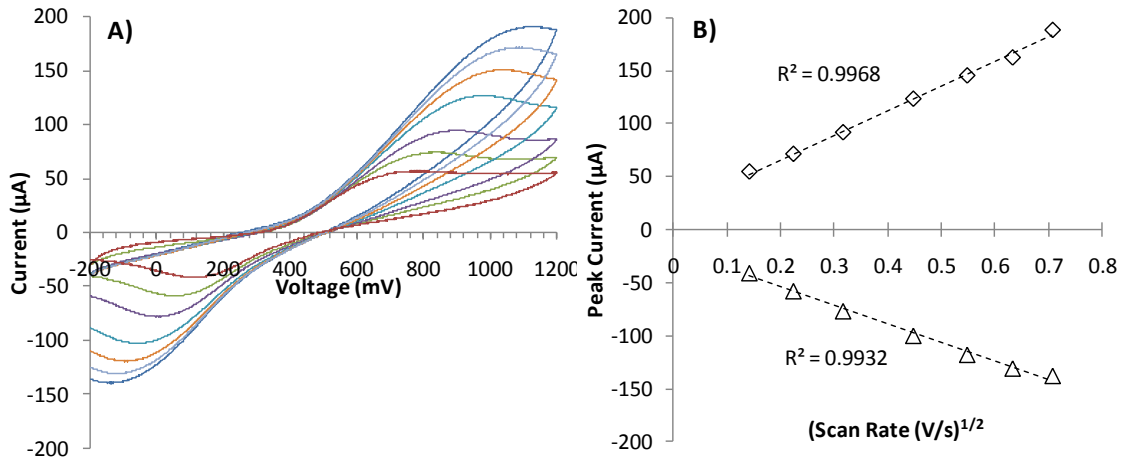


**Figure 3.7: CV plots for ferrocene in solution with bare FTO working electrode. (A) Graph showing relationship between peak current and square root of scan rate. (B)**

As a quantitative measure of electrode performance the electron transfer co-efficient ( $k_s$ ) can be determined using Equation 2.4 as shown in Chapter 2.6.1.

$$\text{Equation 2.4: } E_p = E^0 + \frac{RT}{\alpha nF} \ln \frac{RTk_s}{\alpha nF} - \frac{RT}{\alpha nF} \ln v$$

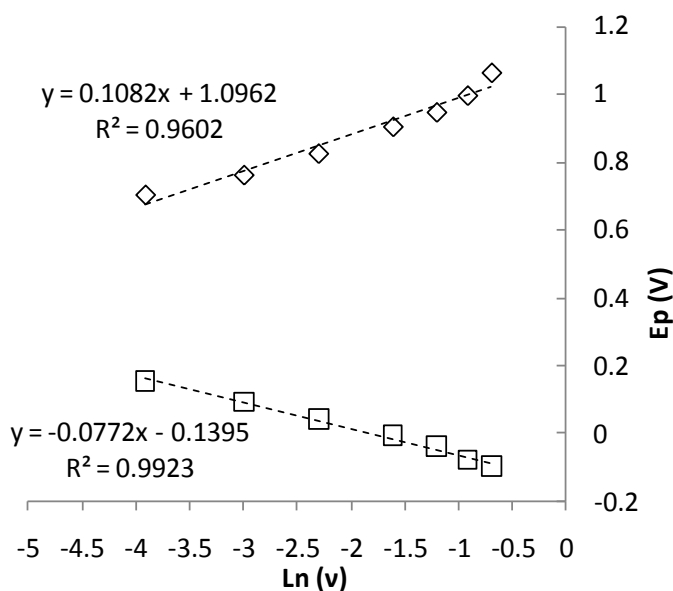
By plotting peak position ( $E_p$ ) versus the natural logarithm of the scan rate the slope of the resultant linear fit can be used to determine  $\alpha$ .

$$\text{Slope} = \frac{-RT}{\alpha nF} \therefore \alpha = \frac{-RT}{\text{Slope} \times nF}$$

The intercept can then be used, along with  $\alpha$ , to calculate  $k_s$ .

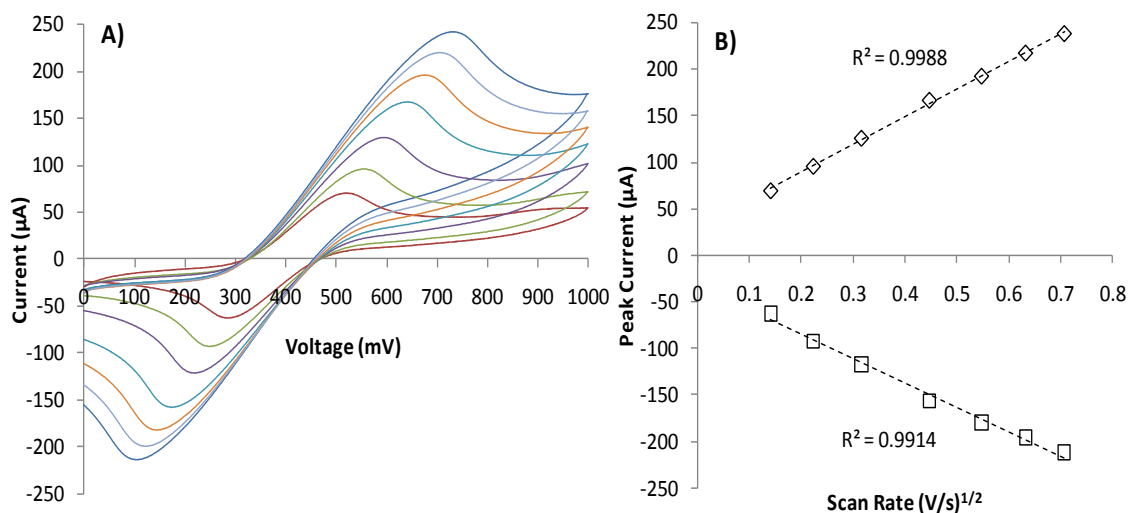
$$k_s = \frac{e^{\left(\frac{\text{intercept} - E_0}{\left(\frac{RT}{\alpha nF}\right)}\right)} \times \alpha nF}{RT}$$

Figure 3.8 is the plot of  $E_p$  versus  $\ln(v)$  for the bare FTO substrate. By taking the slope and intercept and then applying Equation 2.4 and rearranging an electron transfer co-efficient of  $0.015 \pm 0.012 \text{ cm.s}^{-1}$  was determined. This is low when compared to a metallic surface, indicating that the bare metal oxide surface is an inefficient electrode.



**Figure 3.8:** Plot of anodic and cathodic peak potentials ( $E_p$ ) versus the natural logarithm of scan rate ( $v$ ) for the bare FTO working electrode.

The performance of the bare FTO surface can be compared to the SWCNT functionalised FTO surface. Figure 3.9A again shows the CV for ferrocene in solution but now with the FTO-SWCNT substrate, created by cutting the raw CNTs for 8 hours and attaching to the FTO for 24 hours, as the working electrode for varying scan rates. Immediately clear is that the peak separation has decreased significantly over the unmodified surface, with a peak separation of 339mV for the FTO-SWCNT compared to 831mV for the unmodified FTO. Again the peak height increases with increasing scan rate and from Figure 3.9B it is seen to be linearly related to the square root of scan rate. This again indicates that the redox species is in solution as we expect.



**Figure 3.9:** CV plots for ferrocene in solution with SWCNT functionalised working electrode. Scan rate: (innermost)  $20\text{mV}\cdot\text{s}^{-1}$ ,  $50\text{mV}\cdot\text{s}^{-1}$ ,  $100\text{mV}\cdot\text{s}^{-1}$ ,  $200\text{mV}\cdot\text{s}^{-1}$ ,  $300\text{mV}\cdot\text{s}^{-1}$ ,  $400\text{mV}\cdot\text{s}^{-1}$ ,  $500\text{mV}\cdot\text{s}^{-1}$  (outermost). (A) Graph showing relationship between peak current and square root of scan rate. (B)

Figure 3.10 shows the plot of peak position versus scan rate which, after the application of the previously described equations, gives an electron transfer coefficient value of  $0.071 \pm 0.014\text{cm}\cdot\text{s}^{-1}$ . This is a factor of 4.7 higher than the unmodified surface, indicating the functionalisation has greatly improved the electrode performance.

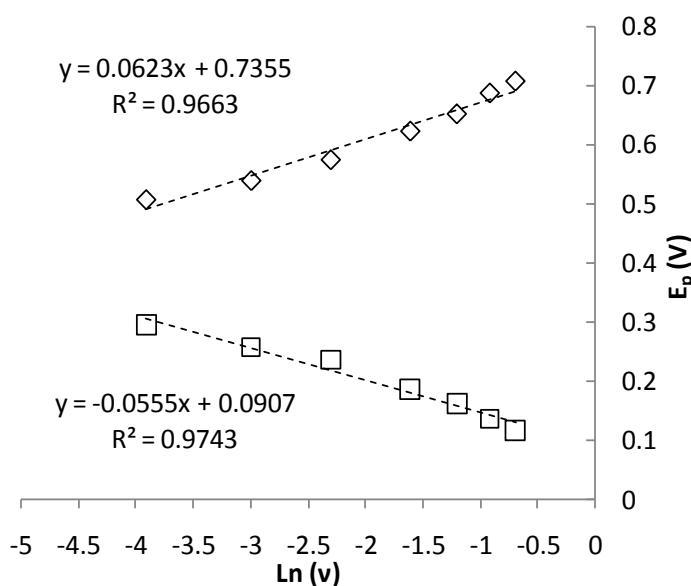


**Figure 3.10:** Plot of anodic and cathodic peak potential ( $E_p$ ) versus the natural logarithm of scan rate ( $v$ ) for the SWCNT functionalised working electrode.

Figure 3.11 shows the direct comparison between the FTO and FTO-SWCNT substrates for identical concentrations of ferrocene and scan rates. The FTO-SWCNT

electrode has increased peak height, indicating an increased conductivity, and a decreased peak separation, indicating superior electrode kinetics. This superior electrode performance is caused by the effective increase in electrode surface area from SWCNT array formation and the excellent electron transport properties through the SWCNT-FTO surface covalent ester bond.

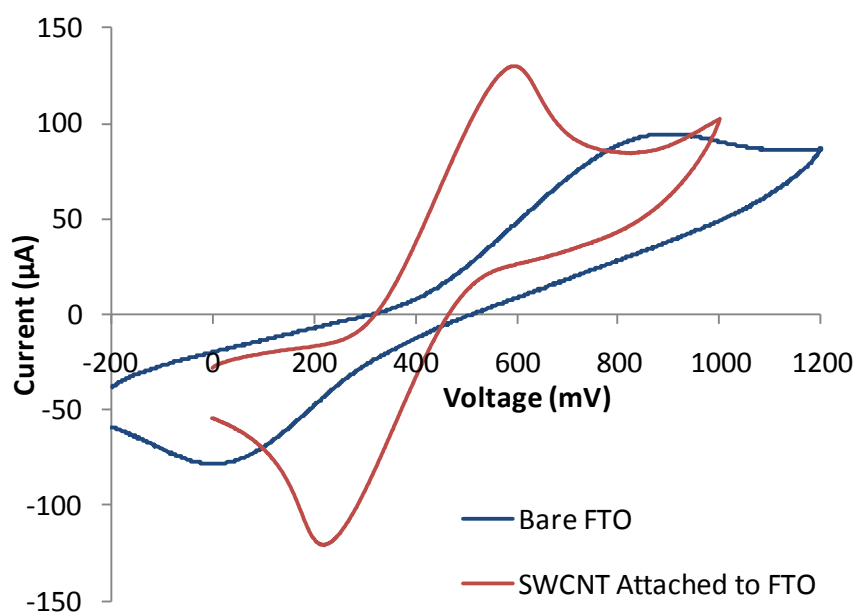


**Figure 3.11: Comparison of CV plots for both the bare FTO working electrode and the SWCNT functionalised working electrode at the same scan rate. (Scan rate =  $100\text{mV}\cdot\text{s}^{-1}$ )**

As well as electrochemistry being performed on the working electrodes to ascertain their performance, impedance spectroscopy can be used on the constructed electrochemical solar cells to understand the performance and behaviour of the cell. Typically the Nyquist plot of a  $\text{TiO}_2$  based DSSC shows three semi-circles, shown in Figure 3.12. The first, in order of increasing impedance, is due to the Pt-FTO interface, the second the  $\text{TiO}_2$ -electrolyte interface and lastly the Nernst diffusion of the ions in the electrolyte.<sup>136, 138</sup>

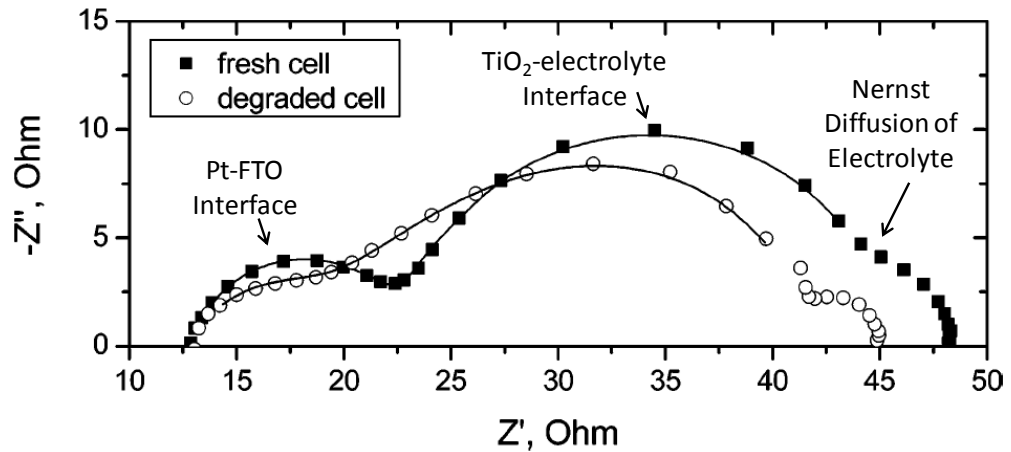
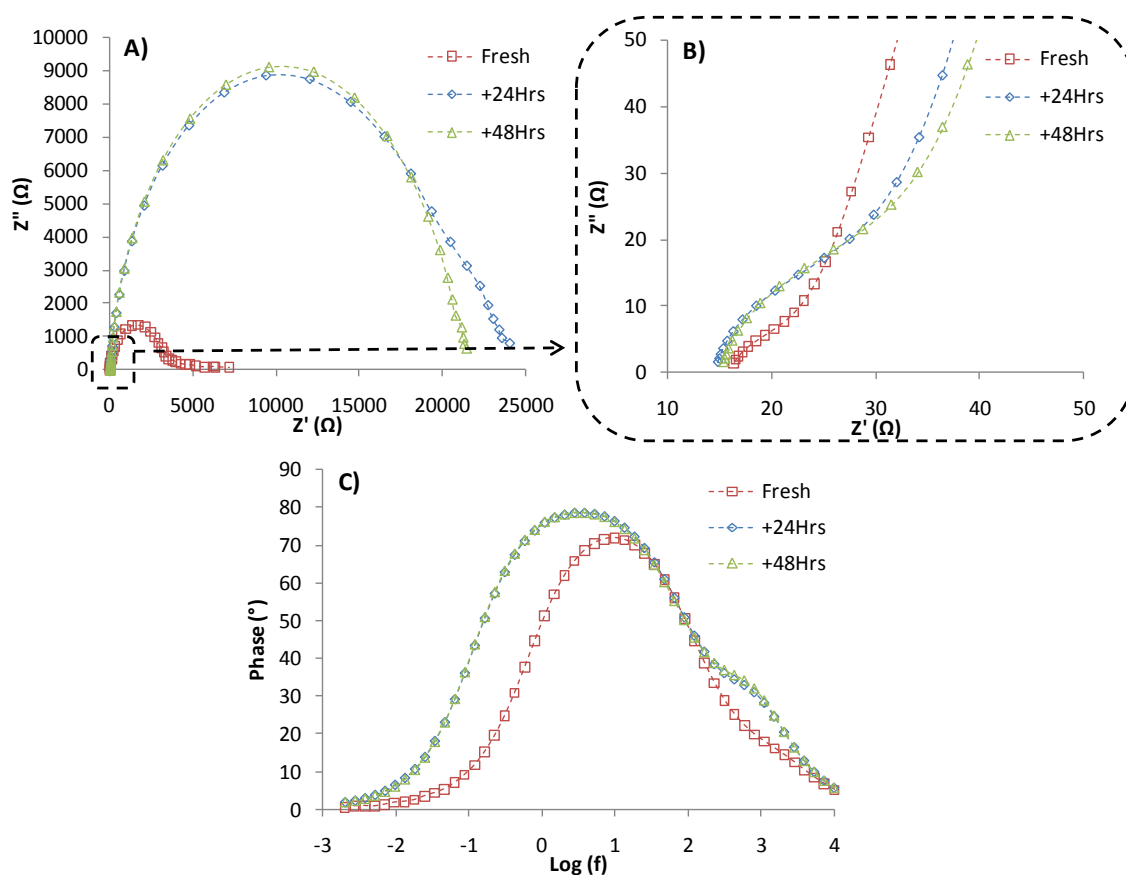


Figure 3.12: Typical Nyquist plot for a DSSC. Modified From Wang *et al.*<sup>138</sup>

The Nyquist and Bode plots of the FTO-SWCNT-cell after being freshly prepared and also aged by 24 and 48 hours in the dark are shown in Figure 3.13. Instead of the three semi-circles typically seen, the spectra in Figure 3.13A appear to be dominated by a single element. However, when the high frequency area is enlarged, seen in Figure 3.13B, the Pt-FTO interface does possess a semi-circle for the catalytic reduction of the iodide/tri-iodide electrolyte. The impedance of this interface is simply much lower than the SWCNT-electrolyte interface and so it cannot be seen on the same scale. The third semi-circle, from the Nernst diffusion within the electrolyte, at the low frequency end of the spectrum does not show a clear semi-circle but the formation of some structure is present at the low frequency end. Likewise the Bode plot, in Figure 3.13C, initially has a single large peak but after the cell has aged a second peak become apparent at 1000Hz ( $\text{Log}(1000) = 3$ ). This is caused by the diffusion at the electrode becoming more significant.



**Figure 3.13: Nyquist plot (A) and Bode plot (C) (without illumination) for a freshly prepared and aged FTO-SWCNT electrochemical solar cells. (B) Shows the enlarged high frequency area. Cells were stored in the dark between testing.**

Clearly there is a definite change in the cell behaviour over the first 24 hours that then remains constant. This change is seen to cause the impedance of the SWCNT-electrolyte interface to increase. To better understand this phenomenon we must look at the Bode plot in Figure 3.13C. When we compare the peak shift after ageing the central peak has shifted to a lower frequency, see Table 3.1. We can convert these frequencies ( $f$ ) into the effective electron lifetime ( $\tau_{\text{eff}}$ ) by using the equation given in Kern *et al.*<sup>136</sup>

$$\text{Equation 3.1: } \tau_{\text{eff}} \approx \frac{1}{\omega} = \frac{1}{2\pi f}$$

The much longer electron lifetime in the aged cell indicates that the recombination process that can occur between the SWCNT-electrolyte interfaces has been suppressed. This reduced recombination is also the reason for the increase in photocurrent and voltage seen in the I-V curves to be discussed in Chapter 3.2. The

physical process behind this “ageing” effect is believed to be related to the formation of the electric double layer in the electrolyte. Interestingly this increase in  $\tau_{\text{eff}}$  is the opposite effect seen in  $\text{TiO}_2$  cells which see a shift to higher frequency caused by degradation of the mesoporous layer, suggesting that the nanotube array possesses an excellent stability.<sup>136</sup>

**Table 3.1: Frequency ( $f$ ) and effective electron lifetime ( $\tau_{\text{eff}}$ ) for fresh and aged cells.**

Cell type	$f$ (Hz)	$\tau_{\text{eff}}$ (ms)
Fresh	9.824	16.20
Aged +24Hrs	3.821	41.65
Aged +48Hrs	3.821	41.65

To help analyse the EIS spectra symmetrical cells were created from both the counter electrode (FTO-Pt—FTO-Pt) and working electrode (FTO-SWCNT—FTO-SWCNT). This allows exclusion of the effect of one electrode and simplifies the impedance spectrum for fitting of equivalent circuits. In a platinum symmetrical cell two peaks are expected, the first is attributed to charge transfer at the Pt/electrolyte interface whilst the second is ionic diffusion in the electrolyte.<sup>140</sup> This is observed in the measured data of Figure 3.14A. The second semi-circle attributed to ionic diffusion will be excluded from fitting, due to its minor influence, to simplify the equivalent cell. In the working electrode (FTO-SWCNT) symmetrical cell again two semi-circles are expected; the first is now attributed to effective electron lifetime in the nanotubes and the second, again the ionic diffusion. In the case of the measured data in Figure 3.14B we see the first semicircle but the low frequency Nernst diffusion is obstructed by noise and thus again will be excluded from fitting. The equivalent circuit for the normal cell to be used is simply a series resistance connected to two Randles type circuits, which consist of a resistor in series with a parallel mesh of a second resistor and a constant phase element, and is shown in Figure 3.15. When fitting a symmetrical cell we can take  $R_2=R_3$  and  $CPE_1=CPE_2$  and simplify to a single Randles type circuit and a series resistance.

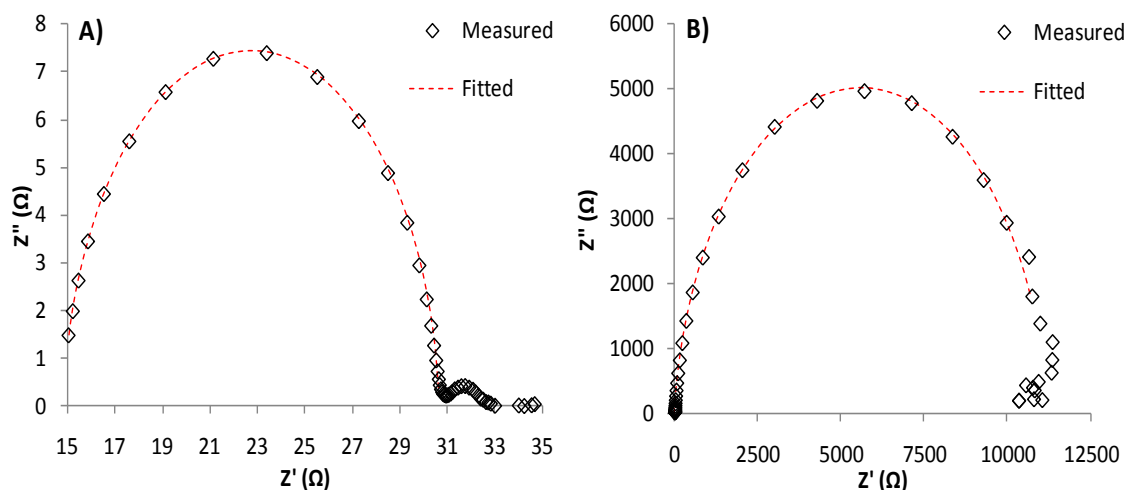


Figure 3.14: Platinum symmetrical cell in dark (A). SWCNT symmetrical cell in light (B).

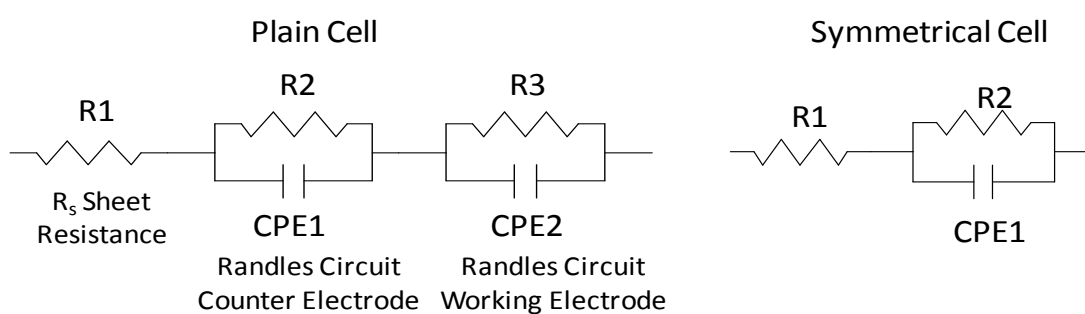
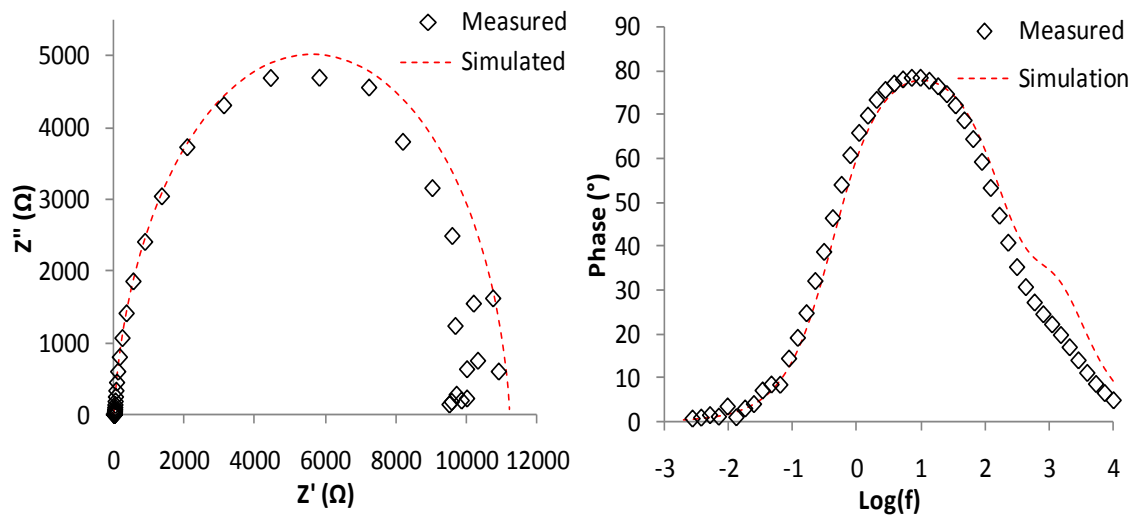


Figure 3.15: Equivalent circuits used for electrochemical solar cell modelling.

By fitting the equivalent circuit (shown in Figure 3.15) to the data from the symmetrical cells it is possible to then combine the two together into the normal cell, which is a combination of a single working and counter electrode, and predict its behaviour. That simulation and the comparison to the measured normal cell are shown in Figure 3.16. It can be seen that the data matches quite closely to that of the simulation indicating that the equivalent circuit proposed does indeed match, and that the technique of using the counter and working electrode symmetrical cells can be used to predict behaviour in normal cells. The difference between the two is due to the simplicity of the model used, which excludes the Nernst diffusion of ions within the electrolyte.



**Figure 3.16: Normal cell Nyquist plot (A) and Bode plot (B) for both measured and simulated data using symmetrical cells.**

This shows that electrochemistry can be used to analyse the performance of a SWCNT modified electrode and predict how it may perform in photovoltaic testing.

### 3.2 Photovoltaic Properties of Single-Walled Carbon Nanotube Arrays

Following characterisation of the SWCNT modified electrodes complete electrochemical solar cells were produced to test the photoresponse of the arrays. Figure 3.17 shows the photocurrent produced when the light source was switched on and off. The data points shown are separated by 200ms. Clearly the array produced a noticeable increase in current, approx  $4.5\mu\text{A}\cdot\text{cm}^{-2}$ , when exposed to light of  $35\text{mW}\cdot\text{cm}^{-2}$ . Of note is that the response time both to the on and off cycle was  $\leq 200\text{ms}$  indicating that it is not a gradual response but a very quick and well defined increase. Also once exposed to light the current appears to be constant and reproducible.

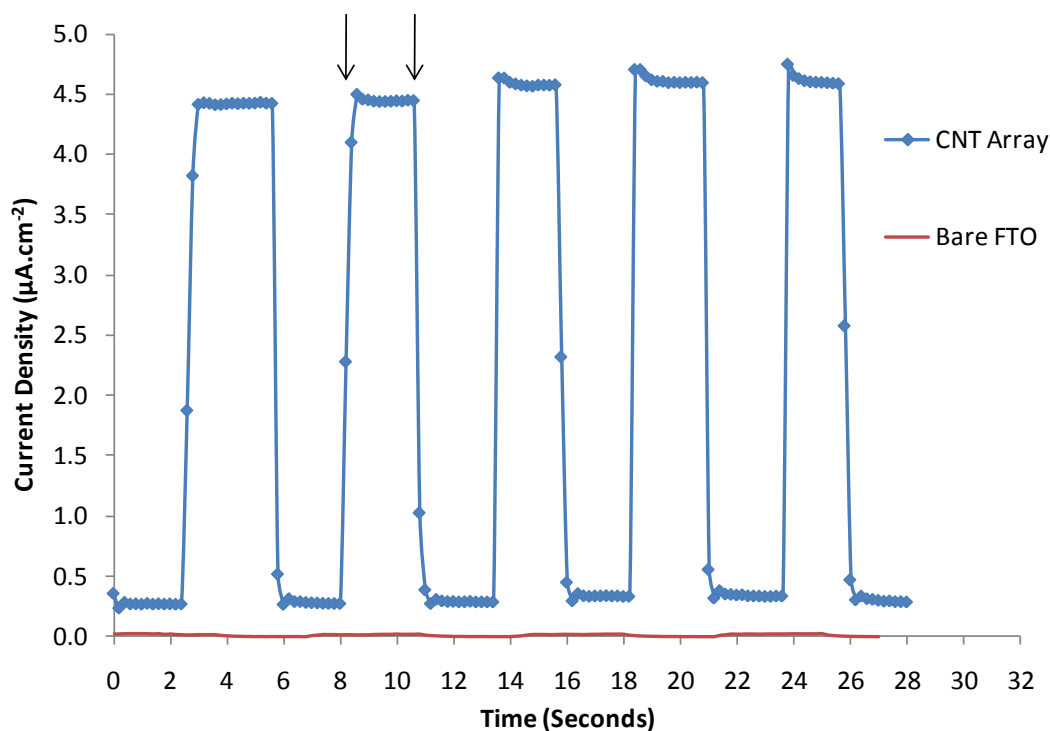


**Figure 3.17: On-Off light response from FTO-CNT cell and blank cell containing no CNT. The arrows indicate the light on and off cycle. (CNT attachment time was 24 hours and cutting time was 8 hours. Points are separated by 200ms. Light intensity  $35\text{mW}\cdot\text{cm}^{-2}$ )**

To verify the stability of the current with respect to time, light soaking experiments were conducted on the array to monitor the affect of constant cycling, and can be seen in Figure 3.18. These results show that over an extended period there is a consistent current output by the cell. There appears to be a slight increase in current over time and this is likely a thermodynamic effect of the cell becoming heated by the light source, and thus increasing the diffusion rate within the electrolyte.

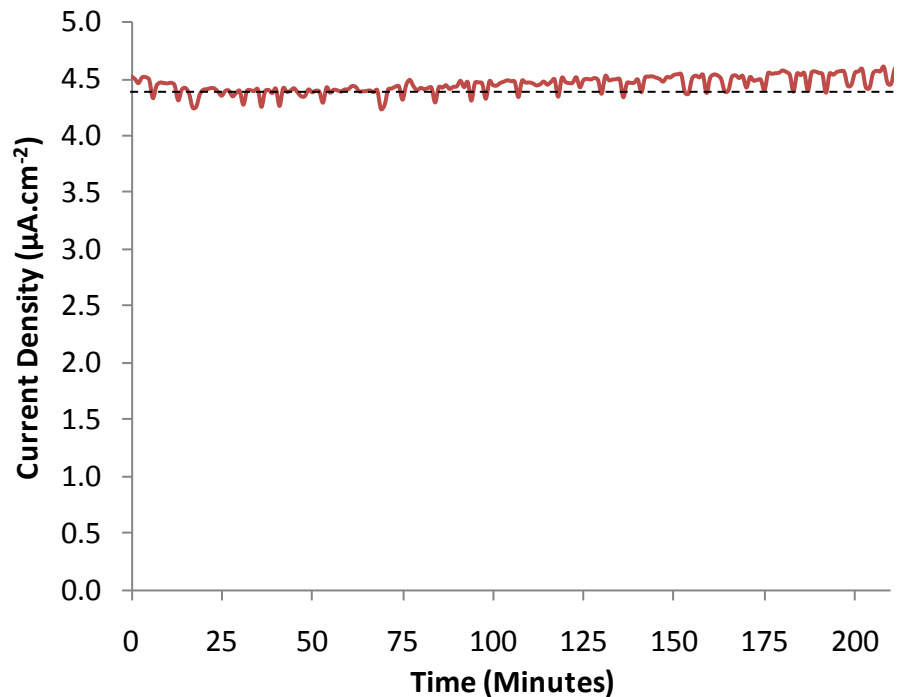


**Figure 3.18:** Light soaking response of the cell (From Figure 3.17) left under illumination for over 200 minutes. Dashed line added to show gradual increase in current. Light intensity  $35\text{mW.cm}^{-2}$ .

To measure the response of the FTO-SWCNT cell over a range of bias voltages J-V curves were taken. Figure 3.19 shows the J-V curves for the FTO-SWCNT cell with two different light sources one with an incident intensity of  $35\text{mW.cm}^{-2}$  and the other with  $100\text{mW.cm}^{-2}$ . As is expected the photovoltage does not change with incident light intensity and both curves have a  $V_{oc}$  of approximately 40mV. The produced photocurrent density however, is directly proportional to incident light intensity and this is seen in the  $J_{sc}$  values of  $4.81\mu\text{A.cm}^{-2}$  and  $13.13\mu\text{A.cm}^{-2}$  for the  $35\text{mW.cm}^{-2}$  and  $100\text{mW.cm}^{-2}$  intensities respectively. As mentioned the photocurrent should be directly proportional to incident light intensity and thus we can say that the  $35\text{mW.cm}^{-2}$  should be 2.86 times less than the  $100\text{mW.cm}^{-2}$ . The ratio between the experimentally observed photocurrent at differing light intensity is 2.73, thus within experimental error the linear trend of photocurrent to light intensity is supported. The data shown in Figure 3.19 allows for a direct comparison between differing incident light intensities and allows for the extrapolation of other light powers. The fact that only  $J_{sc}$  and not  $V_{oc}$  shifted also confirms that it is a photovoltaic effect taking place.

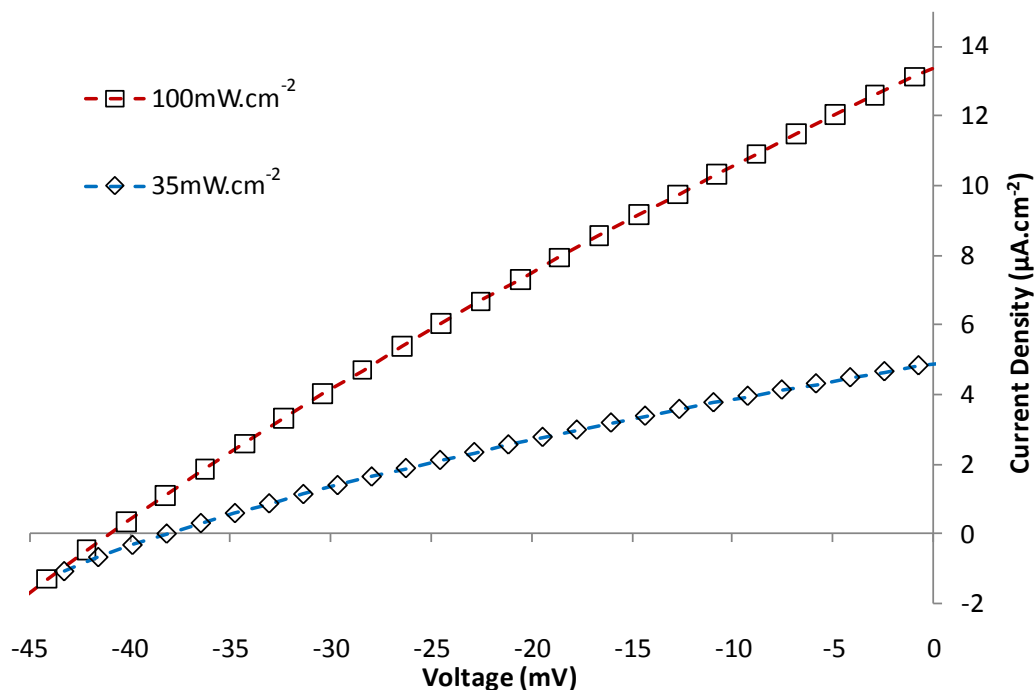


**Figure 3.19:** J-V curves for FTO-SWCNT solar cell with incident intensity of  $35\text{mW}\cdot\text{cm}^{-2}$  and  $100\text{mW}\cdot\text{cm}^{-2}$ .

To better understand the photovoltaic properties of these CNT based electrochemical solar cells, the behaviour of such cells to both illumination and in darkness is needed. Figure 3.20 demonstrates the response of the FTO-SWCNT cell under illumination ( $100\text{mW}\cdot\text{cm}^{-2}$ ) and in near complete darkness. As would be expected with no illumination the cell produces only a negative or dark current when biased, as opposed to exposure to light which causes the graph to shift into the so called 'photovoltaic quadrant'. The dark current is produced by the reduction of the  $\text{I}_3^-$  in the electrolyte by electrons from the CNT conduction band. Typically in a titania based DSSC there is a specific turn on voltage for this to occur. However, in Figure 3.20 the dark current begins to increase almost immediately indicating that the CNT array is particularly good at reducing the triiodide. This effect has been investigated previously and CNT arrays have been used as the counter electrode material, replacing platinum.<sup>13, 31-39, 157-159</sup> It is this dark current that causes the low fill factor seen in the J-V curves, which can be expressed as the low shunt resistance of the nanotube array/electrolyte interface. The fill factor is an average of 30% from several cells, considerably lower than the 70% achieved in most  $\text{TiO}_2$  based cells. Typically shunt resistance is kept as high as possible by applying a 'blocking' insulating layer onto the

titania nanoparticles. This prevents excited electrons from reducing the dye once it has been oxidised before travelling through the circuit, effectively creating a one-way pathway for the electrons. *Nazeeruddin et al.* found that applying a layer of 4-tertiary butyl pyridine (4-TBP) could increase the shunt resistance and lower the dark current by 2-3 orders of magnitude.<sup>15</sup> However, in the case of the SWCNT cells this blocking layer application would be significantly more complex as the attachment of any insulating molecules may in fact have a diminishing effect on the nanotube conductivity and alter its band structure.<sup>144</sup> It is not well understood how the electron-hole generation of large bundles of tubes each with slightly differing density of states, and band gaps will affect recombination within the bundles themselves and this may also lead to significant back reactions. It has also been established that the presence of metallic nanotubes can create short circuits within the array lowering its performance.<sup>160</sup>

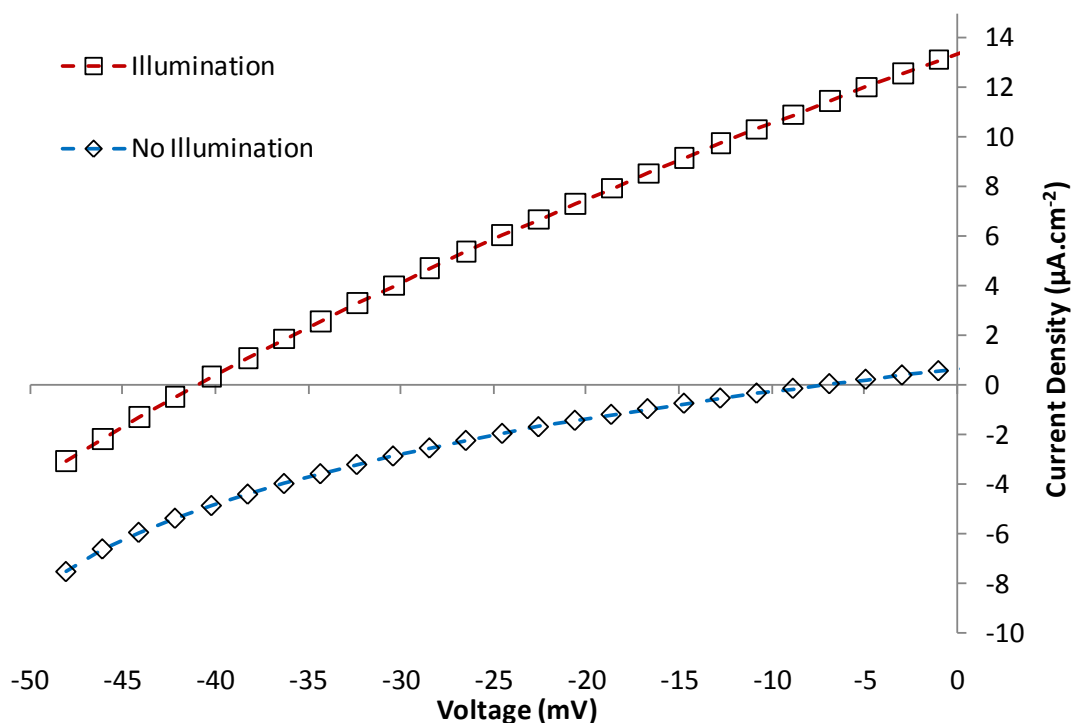


Figure 3.20: J-V curves for a FTO-SWCNT cell under illumination ( $100\text{mW}\cdot\text{cm}^{-2}$ ) and darkness.

By modifying the attachment time of the functionalised nanotubes to the FTO glass the amount of nanotube present in the array can be modified which should have a correlation with photocurrent produced as the number of photoactive elements

changes. Figure 3.21A shows the trend in peak photocurrent with nanotube attachment time for both freshly prepared cells and 24 hour aged cells. Of note is the marked increase of both current and voltage produced from the aged cells. This has been attributed to the slow diffusion of the electrolyte into the carbon nanotube bundles, effectively increasing the active surface area or electrical contact. Clearly there is an increase in photocurrent produced as attachment time increases from 2 to 8 hours, and the slope decreases levelling out after 18 hours. This is expected as the surface coverage is approaching saturation. A similar trend in nanotube coverage has also been seen in AFM images of the surfaces after varying attachment time.<sup>120</sup> The peak current seen from the 18 hour cell is  $\sim 4.7\mu\text{A}\cdot\text{cm}^{-2}$  for  $35\text{mW}\cdot\text{cm}^{-2}$  light. Figure 3.21B also shows the open circuit voltage produced by the cells. Interestingly there is a decrease with attachment time. This is due to the well established ability of the SWCNTs to also act as a catalyst in reducing the tri-iodide present in the electrolyte.<sup>31, 32, 35-38</sup> In the cell architecture used in this work the SWCNTs are acting as the electron-hole generators, however, they can also reduce the tri-iodide causing an increase in back reaction leading to a decrease in effective charge separation. This means that as the number of nanotubes on the surface increases the photocurrent will also increase but will lower the  $V_{oc}$  of the cell by increasing the number of sites for back reaction to occur.

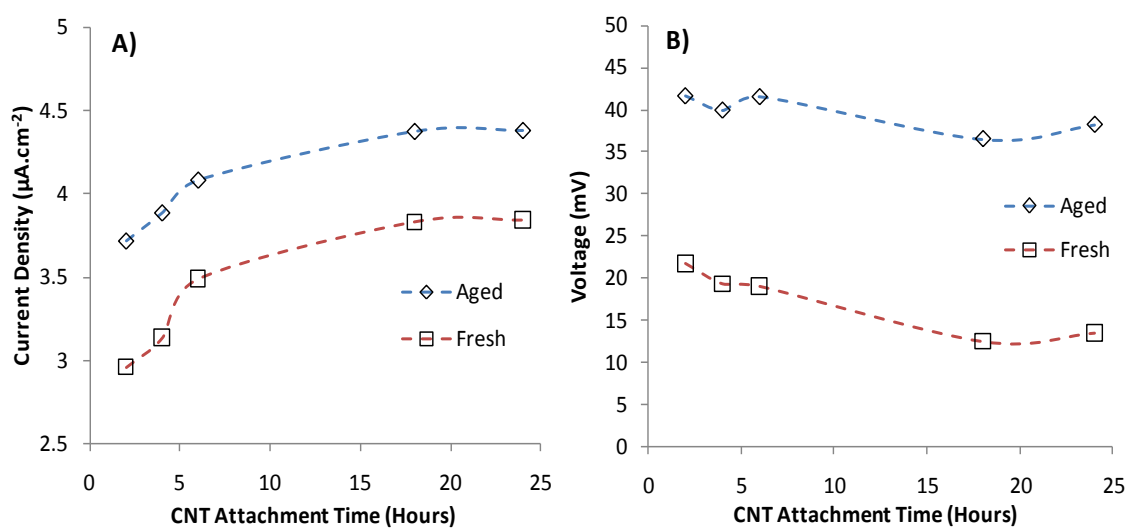
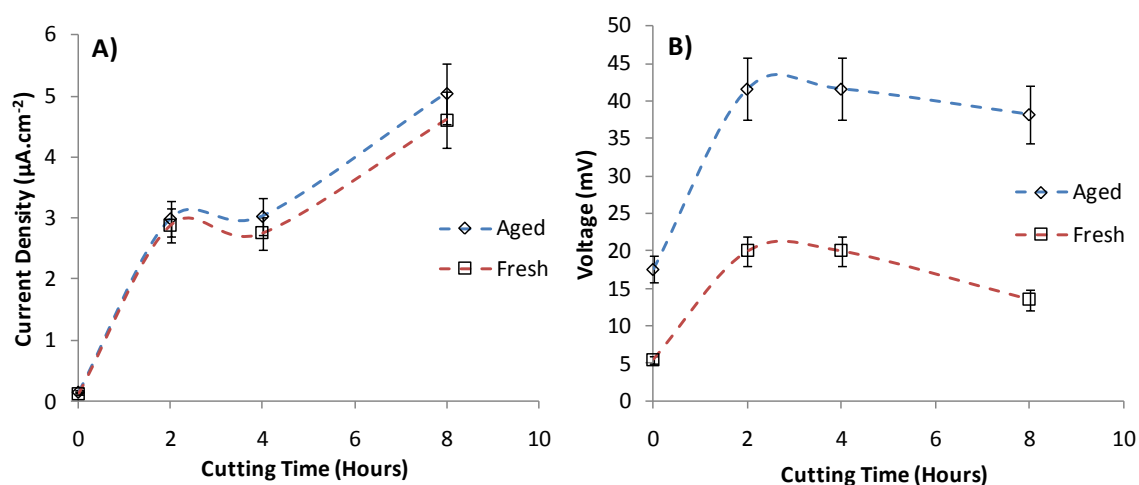


Figure 3.21: Peak current versus CNT attachment time (A). Peak voltage versus CNT attachment time (B). Light intensity is  $35\text{mW}\cdot\text{cm}^{-2}$ .

Different cutting times and the resultant differing band gap energies present in the tubes would be expected to give differing photoresponse properties. Cells were constructed out of arrays containing SWCNT of differing cutting times, with identical attachment times of 24 hours, and the photo response versus cutting time is shown in Figure 3.22. Devices made with uncut nanotubes produced the lowest short-circuit current. This is expected not only because of the more metallic nature of the pristine tubes which will decrease the electron-hole generation but also the low functionality will mean a minimum attachment to the FTO surface, leading to much fewer photoactive elements on the surface. Thus it is hard to discern the contribution of changing the electronic state of the tube because the increased functionality will increase the nanotube density on the surface and lead to an increased photo response. Unlike the attachment time graph (Figure 3.21) that displayed a gradual increase and then levelled out, the current as a function of cutting time appears to increase greatly to  $3\mu\text{A}\cdot\text{cm}^{-2}$  at 2 hours cutting time and then stays at that level before rising to  $5\mu\text{A}\cdot\text{cm}^{-2}$  at the 8 hour cutting time. Part of this increased photo current will be caused by the increased density of SWCNT on the surface as seen in the Raman data but also the increasing semi-conducting nature of the tubes should increase the chance of charge separation and an increase in photocurrent. As well as changing the coverage of nanotubes, the band gap present in the nanotubes would be expected to be altered by the cutting process, as was discussed previously in Chapter 3.1.1.



**Figure 3.22:** Graph of current versus CNT cutting time (A) and voltage versus CNT cutting time. (B) Light intensity is  $35\text{mW}\cdot\text{cm}^{-2}$ . Error bars show 10% experimental error.

By integrating the area under the peak in the Raman histogram (shown previously in Figure 3.4) the relative amount of nanotubes on the surface can be ascertained. In Table 3.2 we can see that the ratio of current per integrated peak area, which is proportional to amount of nanotubes on the surface, is highest for the 2 hour cutting time, followed by the 8 hour and then lastly the 4 hour cutting time. This is because at the shorter cutting time the CNTs have enough semi-conducting nature to be photoresponsive but are also spread out thinly enough to minimise recombination effects and not lower the shunt resistance. The 8 hour sample has a greatly increased percentage of semi-conducting tubes and this gives the increased current, but the detrimental recombination effects mean that even with 4 times the amount of CNT on the surface the current is only 1.7 times higher. Thus, the 2 hour cutting time is the most efficient converter of light to current for this given system.

**Table 3.2: Integrated area under histogram peaks from Figure 3.4, and current from Figure 3.22.**

Cutting Time (Hours)	Max Current ( $\mu\text{A}\cdot\text{cm}^{-2}$ )	Integrated Peak Area (a.u./ $1\times 10^5$ )	Ratio of Current / Peak Area
2	$2.99 \pm 0.022$	$2.23 \pm 0.11$	1.34
4	$3.03 \pm 0.025$	$8.73 \pm 0.44$	0.347
8	$5.04 \pm 0.11$	$8.91 \pm 0.45$	0.566

Although the cells described produce relatively low currents and voltages ( $4.7\mu\text{A}\cdot\text{cm}^{-2}$  and 40mV), one must take into account the low amount of material present on the working electrode. Traditional  $\text{TiO}_2$  cells use a layer thickness of 10-15 $\mu\text{m}$ <sup>12</sup> whilst the nanotube thickness here is only several hundred nanometres thick. Taking this into account, aligned SWCNT arrays do present a viable method for producing a quick and steady photocurrent response, along with the opportunity to produce transparent photovoltaics based on thin layers of SWCNTs. These transparent layers would have a tinting effect, reducing the amount of transmitted light by absorption. However, the absolute power produced by these devices still remains low when compared to similar electrochemical devices such as the DSSC and require further optimisation to be truly competitive.

### 3.2.1 Spectral Response of SWCNT Functionalised FTO

Of interest for the application of these SWCNT modified electrodes for solar cells is their photocurrent response at each specific wavelength of the ultraviolet-visible spectrum. Typically, the wavelength that is most absorbed by a surface produces the highest photocurrent, as more light absorbed will lead to higher chance of electron-hole excitation. To determine the absorbance of the SWCNTs used in this work, UV-Vis absorption spectroscopy was performed on a solution of the cut SWCNTs dispersed in DMSO. Figure 3.23 shows the absorption spectrum for the SWCNT solution (solid line). As is usually seen for CNT dispersions in solution the spectrum has no peaks within the visible region (400-700nm). Instead there is a gradual increase in absorbance at lower wavelengths approaching the UV region. This is caused by the  $sp^2$  hybridised carbon which has high UV absorption. Figure 3.23 also shows the spectral response of the plain SWCNT solar cell (dashed line). The overall power produced by the cell, shown on the Y-axis, is much lower than shown previously as the filters now significantly reduce the incident power, approximately  $10\text{mW}\cdot\text{cm}^{-2}$  or  $1/10^{\text{th}}$  of the previous intensity. However, the incident power has been calibrated to be equal for each wavelength. The cell's response is seen to follow a similar trend to that of the absorption spectrum, showing no specific peaks but instead a gradual increase in power towards the UV region. The increase seen at  $\sim 500\text{nm}$  (2.48eV) indicates a minimum onset energy, wavelengths above this produce minimal current, and then once the wavelength decreases below this the array produces significantly more power. This is in agreement with previous band gap energies stated for SWCNT. Also this indicates that changing the band gap of the SWCNT array will cause this increase in photoresponse to shift to different wavelengths.

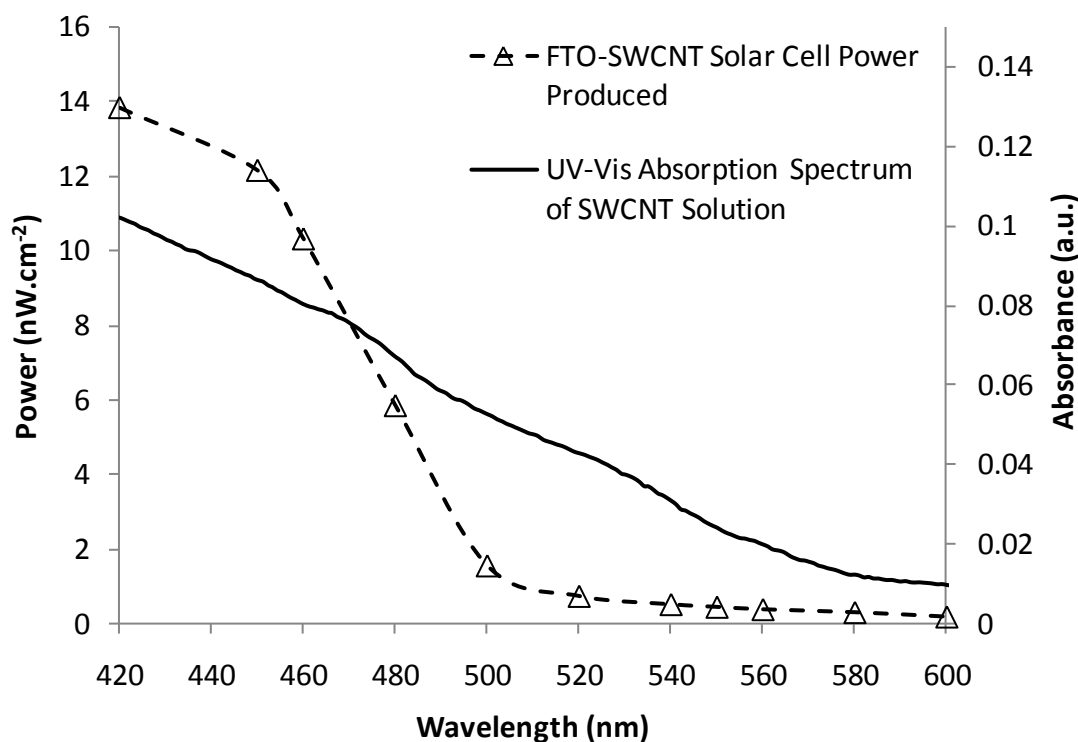


**Figure 3.23: Wavelength response of FTO-SWCNT solar cell along with UV-Vis absorption spectrum of SWCNT solution.**

To investigate the effect of cutting time on spectral response, cells with differing SWCNT cutting times of 2, 4 and 8 hours were produced and analysed. Figure 3.24 shows the respective spectral response curves for each cutting time. Figure 3.24A is the produced photovoltage for each cell whilst Figure 3.24B is the photocurrent produced, these are then combined with the experimentally calculated fill factor of 30% to produce Figure 3.24C, the overall power produced. The overall power, shown in Figure 3.24C, indicates that the 2 hour cutting time generates the most power per unit area for wavelengths below 500nm. This is in agreement with the results discussed previously that indicate that the 2 hour cutting time was the most efficient at photovoltaic conversion.

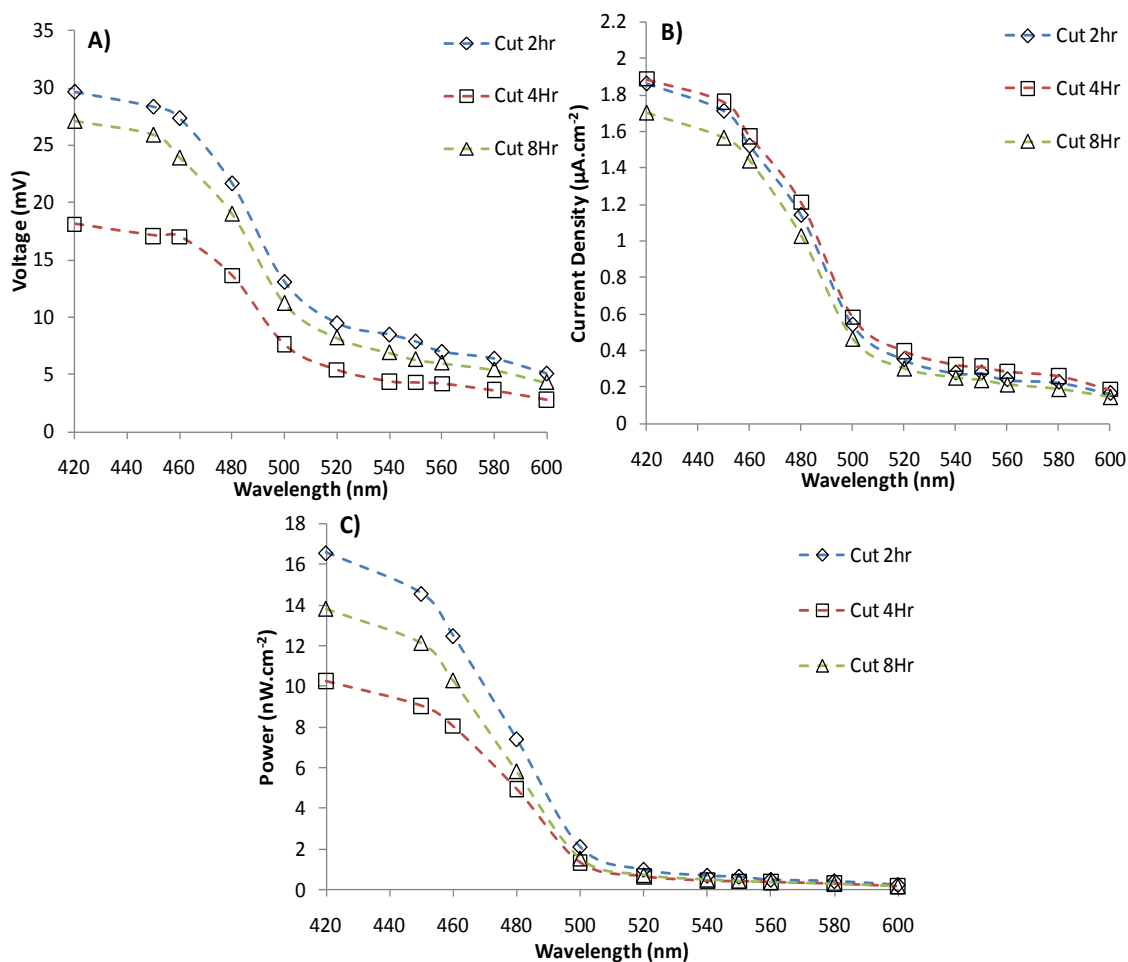
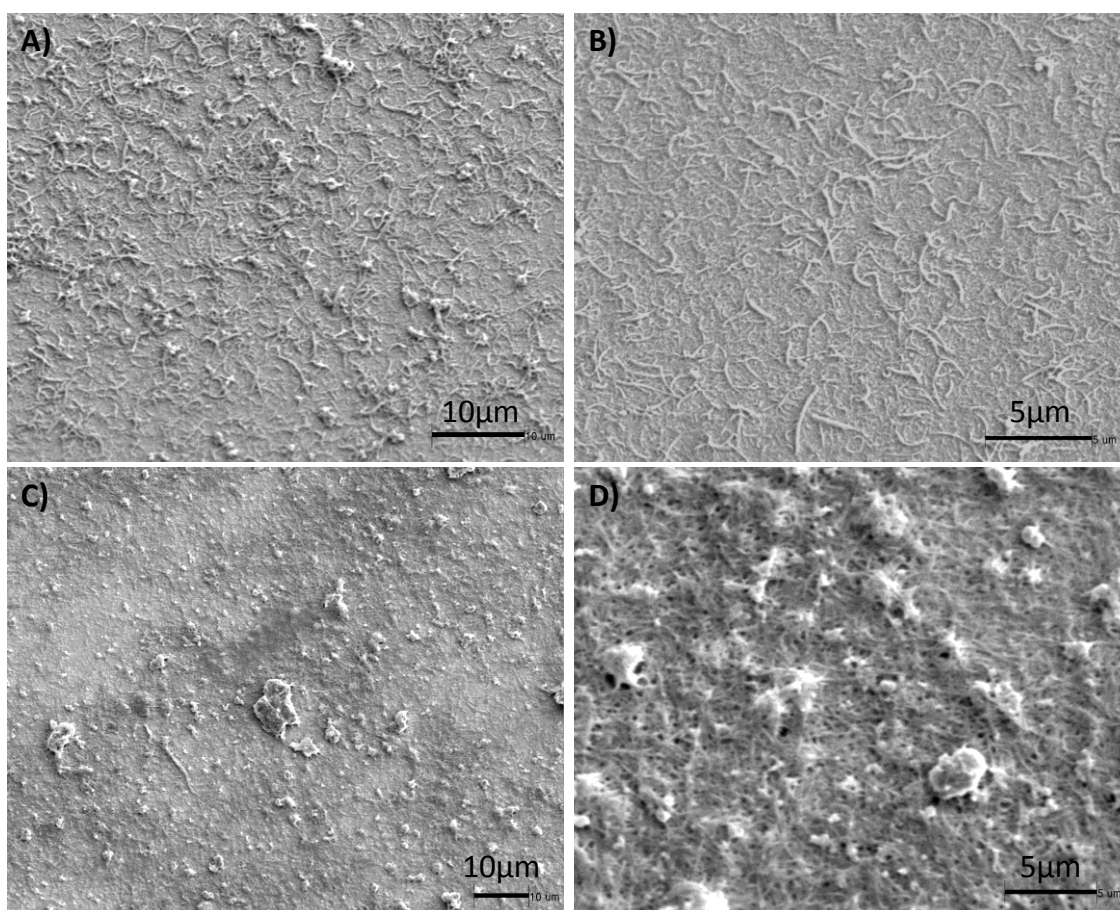


Figure 3.24: Spectral response of FTO-SWCNT solar cells of different SWCNT cutting times. (A) Photovoltage, (B) photocurrent density and (C) power output.

### 3.3 Comparison of SWCNT to MWCNT Functionalised FTO

SWCNTs have been shown to be applicable as light harvesting antennae. However, there remains some doubt as to whether or not MWCNTs could be applied in the same fashion. To address this and allow for a direct comparison MWCNT based solar cells were constructed in a similar fashion as was done for SWCNTs. These MWCNT arrays were also analysed using SEM, electrochemistry, Raman spectroscopy, XPS and solar efficiency testing to compare their performance to SWCNT based devices. Figure 3.25 shows the SEM images of the CNT modified FTO glass substrates, with Figure 3.25A/B showing the MWCNTs and Figure 3.25C/D showing the SWCNTs. Upon comparison of these images it is clear that the MWCNT have a larger bundle diameter and length as they can be much more readily seen at similar scales. The MWCNT also

have a higher degree of functionalisation when acid treated, arising from an increased number of defect sites to begin with as seen in the Raman D/G ratio.<sup>69</sup> This leads to an increase in attachment and thus increased CNT density. It can be seen that there are bundles of CNTs lying flat on the surface and AFM work done previously also suggests that there are small bundles of CNTs that are vertically aligned, with heights of several hundred nanometres, which are harder to resolve using SEM. This increased MWCNT density is important when comparing both SWCNT and MWCNTs to provide an accurate comparison.



**Figure 3.25: SEM images of CNT modified surfaces. (A-B) MWCNT attached to FTO, (C-D) SWCNT attached to FTO.**

### 3.3.1 Raman of MWCNT Functionalised FTO

Raman spectroscopy can be easily used to differentiate between SWCNT and MWCNT. As seen previously in Table 2.2, there are peaks that are specific to SWCNTs (RBM and  $G^{+/-}$ ) and these can be used to differentiate from MWCNTs. Another large difference is the D/G ratio, in SWCNT we have seen that the ratio is typically  $\approx 0.1$ ,

whilst for MWCNT it is typically  $\approx 1$ . This can be seen clearly in Figure 3.26 where the Raman spectra from both the FTO-SWCNT and MWCNT substrates can be compared. In Figure 3.26A the difference in D/G ratio is immediately clear, with the D band for the MWCNT having a much larger intensity, the RBM is also not present in the MWCNT spectrum and there is no splitting of the G band, which can be more clearly observed in Figure 3.26B. Figure 3.26B shows the enlarged G band region showing the difference in peak shape. The SWCNT sample has two peaks,  $G^-$  at  $1562\text{cm}^{-1}$  and  $G^+$  at  $1582\text{cm}^{-1}$ , whilst the MWCNT has a main peak at  $1570\text{cm}^{-1}$  which is the G peak when found in graphite and the difference is caused by the interaction between the many successive layers of graphene. The MWCNT exhibits a second peak at  $1602\text{cm}^{-1}$  and this is attributed to multi-walled carbon nanofibres (MWCNFs), MWCNFs possess this extra shoulder at  $\approx 1612\text{cm}^{-1}$  from the imperfect stacking of successive tubes.<sup>80</sup>

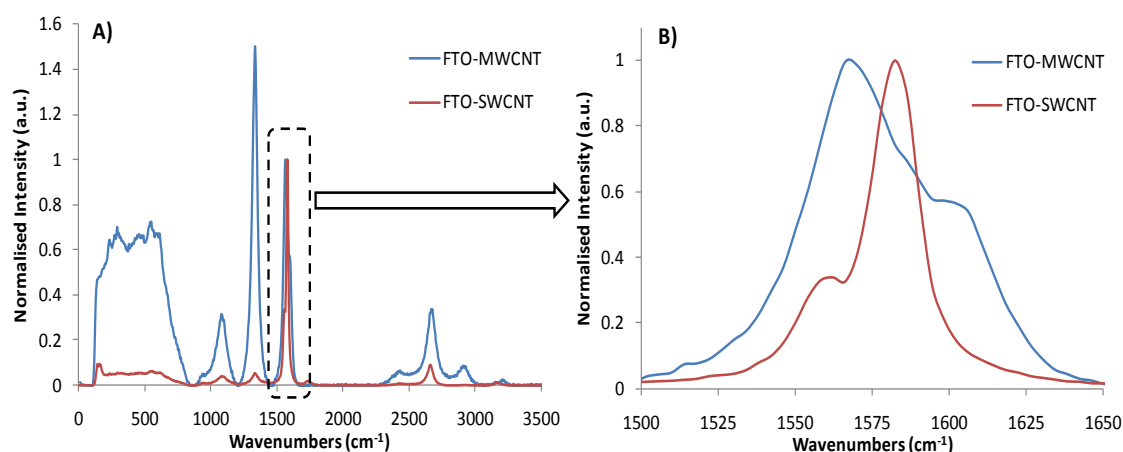


**Figure 3.26: Raman spectra comparing SWCNT and MWCNT chemically attached to FTO (A). Enlargement of G band region (B).**

The D/G ratio between the SWCNT and MWCNT is also clearly different and this can be seen quantitatively in Table 3.3, where the respective D/G ratios are shown along with the standard deviation. As seen previously SWCNT have a low D/G ratio whilst MWCNT possess a much larger ratio. The use of the D/G ratio along with the presence of characteristic peaks such as the RBM and the  $G^{+/-}$  allows for a definitive differentiation between the two substrates.

Table 3.3: Raman D/G ratio for SWCNT and MWCNT modified FTO.

Sample	D/G Ratio
FTO-SWCNT	$0.02 \pm 0.0039$
FTO-MWCNT	$1.19 \pm 0.026$

### 3.3.2 Electrochemistry of MWCNT Functionalised FTO

Cyclic voltammetry was also used on the MWCNT electrodes to provide a comparison to SWCNT modified electrodes. The CV plots of ferrocene with changing scan rates is shown in Figure 3.27A with the trend of peak current with the square root of scan rate is shown in Figure 3.27B. As with the SWCNT modified electrodes there is the same linear increase in peak current and also a shift in peak position indicating a quasi-reversible redox reaction, as was seen for the SWCNT electrode.

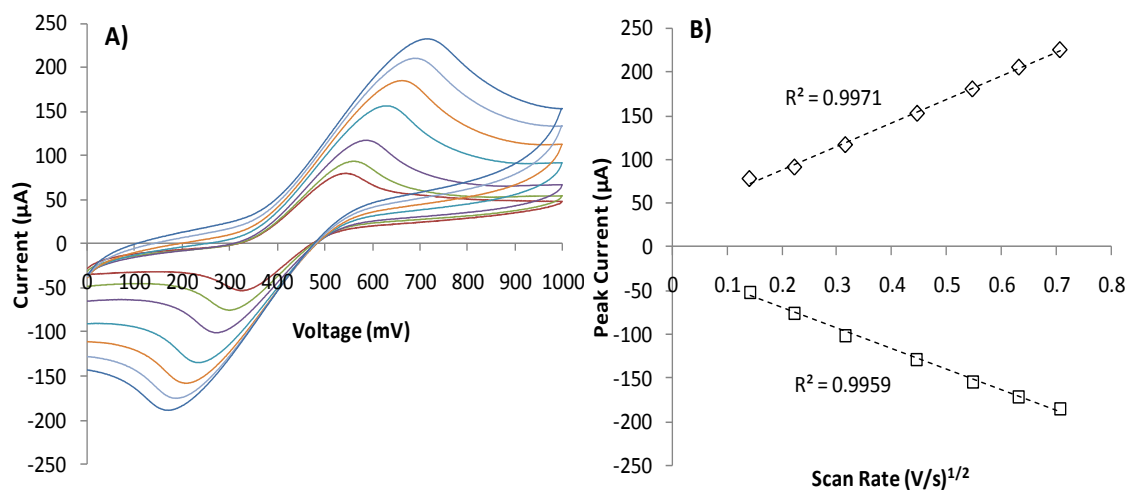
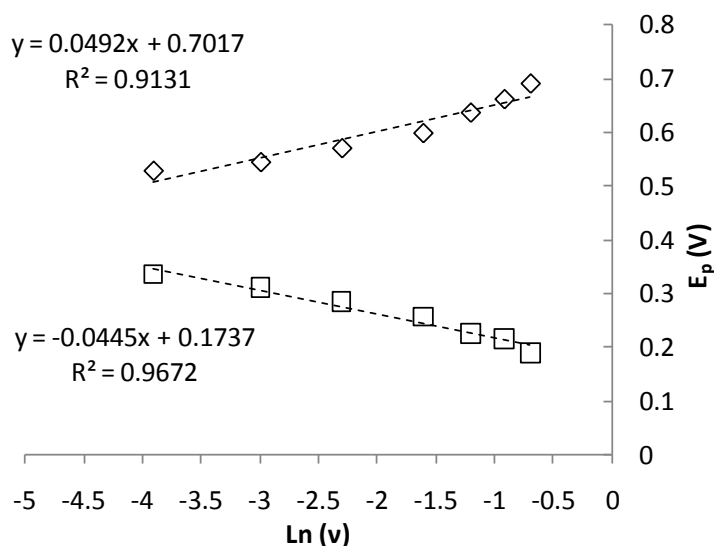


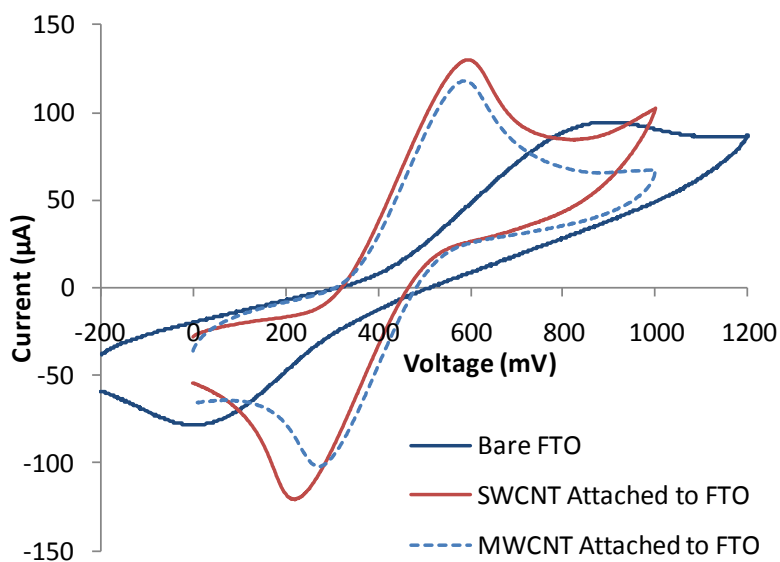
Figure 3.27: CV Plots for ferrocene in solution with MWCNT functionalised working electrode. (A) Graph showing relationship between peak current and square root of scan rate. (B) Graph showing relationship between peak current and square root of scan rate.

Figure 3.28 shows the trend in peak position versus the natural logarithm of scan rate, again following a linear trend. This was used along with Equation 2.4, as for the SWCNT surface, to determine  $k_s$ , which was found to be  $0.076 \pm 0.014 \text{ cm} \cdot \text{s}^{-1}$  which is within experimental error, for the  $0.071 \pm 0.014 \text{ cm} \cdot \text{s}^{-1}$  observed for the SWCNT electrode. Any difference may be attributed to the increased electrode surface area of the MWCNT electrode, caused by larger bundles and nanotube lengths which were observed in the SEM (Figure 3.25).



**Figure 3.28:** Plot of anodic and cathodic peak potential ( $E_p$ ) versus the natural logarithm of scan rate ( $v$ ) for the MWCNT functionalised working electrode.

When we directly compare the unmodified FTO, SWCNT and MWCNT modified FTO, seen graphically and tabulated in Figure 3.29, we can see that both forms of nanotube modification greatly increase electrode performance. The peak separation for the MWCNT case, with a value of 277mV, is lower than that of the SWCNT with 339mV and this is related to the electrode surface area. As discussed previously the increased CNT density from the MWCNT electrode provides a slightly superior electron transfer rate. However, when we compare the peak magnitude ( $I_p$ ) we see that the FTO-SWCNT has a value of 129 $\mu$ A whilst the FTO-MWCNT is lower with 117 $\mu$ A, this indicates that the SWCNT electrode provides increased conductivity despite the lower electrode surface area. Thus, if we take into account the different nanotube densities present on the surface the SWCNT modified electrode is superior to the MWCNT for solar cell applications which require high electron conductivity.



Substrate	Electron Transfer Co-efficient ( $\text{cm.s}^{-1}$ )	Peak Current ( $\mu\text{A}$ )	Peak Separation (mV)
Bare FTO	$0.015 \pm 0.012$	93	831
FTO-SWCNT	$0.071 \pm 0.014$	129	339
FTO-MWCNT	$0.076 \pm 0.014$	117	277

Figure 3.29: Comparison of CV plots for bare FTO, SWCNT and MWCNT functionalised FTO, along with a table summarising these values.

### 3.3.3 XPS Characterisation of MWCNT Functionalised FTO

As was done for the SWCNT functionalised FTO XPS was used to investigate the surface chemistry of the MWCNT functionalised FTO. Figure 3.30 compares the survey spectra for both the bare FTO and after MWCNT functionalisation has been undertaken. Many of the peaks are similar, but the C1s peak is seen to increase in intensity and there is a corresponding drop in intensity for the tin peaks, similar to what was observed for the SWCNT surfaces. This increased carbon signal and decreased tin signal is as expected for the presence of a carbon nanotube array.

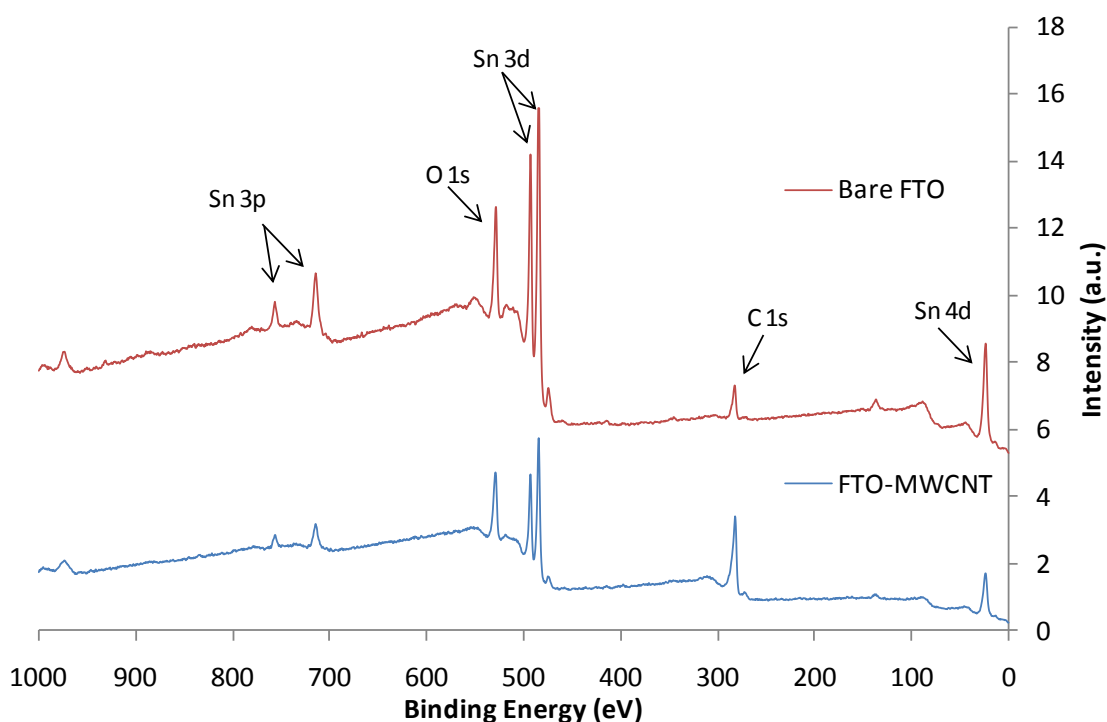


Figure 3.30: XPS survey spectra for bare FTO and MWCNT functionalised FTO.

High resolution spectra were taken of the oxygen and carbon binding regions, and these are shown in Figure 3.31. In Figure 3.31A, the O1s binding region, there are 3 peaks that are contributing to the overall signal. The most intense is, as expected, the tin oxide peak at 530.8eV followed by the carbonyl peak at 532.2eV and finally the C-O peak at 533.3eV. These correspond to the presence of carboxylic acid groups present on the MWCNT surface.<sup>156</sup> Figure 3.31B is the deconvolution of the C1s region, again with three constituent peaks; the most intense at 284.3eV from  $sp^2$  carbon, 284.9eV from  $sp^3$  and adventitious carbon and finally a broad peak at 287.7eV from

the presence of C-O and C=O bonds. These again are as expected from the presence of carboxylic acid functionalised MWCNTs.

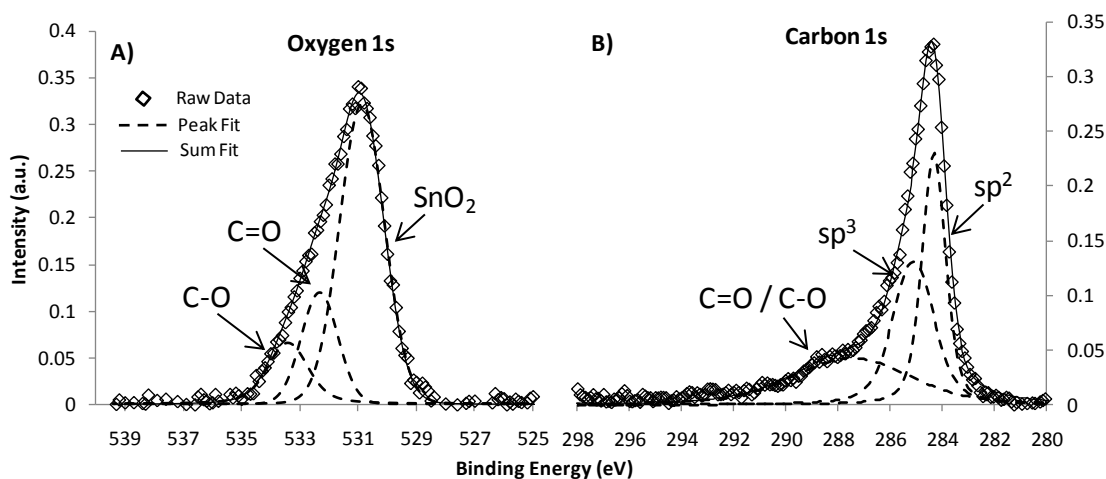
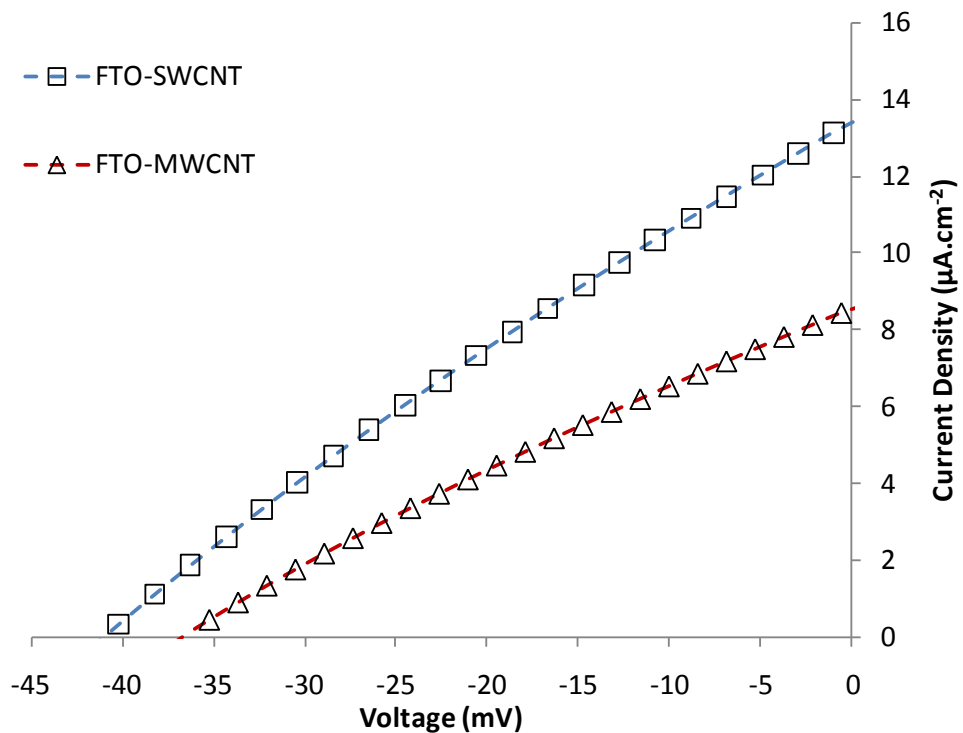


Figure 3.31: High resolution XPS of O1s (A) and C1s Regions (B) for FTO-MWCNT.

### 3.3.4 Photovoltaic Properties of MWCNT Functionalised FTO

Once the MWCNT functionalised electrodes had been characterised complete electrochemical solar cells were constructed and solar cell efficiency measurements were performed to compare the cell efficiency to SWCNT modified cells. Figure 3.32 shows graphically the J-V curve for both the SWCNT modified cell, as seen previously in Chapter 3.2, and the MWCNT cell. As mentioned previously it has also been shown that MWCNT are not ideal for photovoltaics as they exist predominantly as metallic conductors. However, the cutting in mixed acid used to attach the MWCNT to the FTO substrate introduces defects into the density-of-states of the nanotubes converting some MWCNTs into semi-conducting tubes. Clearly in Figure 3.32 the SWCNT cell possesses superior performance compared to the MWCNT cell, with a photocurrent  $\approx 50\%$  higher. The SWCNT cell also generated a larger photovoltage which was  $\approx 15\%$  greater than generated by the MWCNT cell. This trend also supports what was observed in the electrochemical experiments that showed that the SWCNT electrode provided a superior conductivity. From these results it can be concluded that SWCNTs are a superior light harvesting material to MWCNTs.



Substrate	Photoresponse		
	$J_{sc}$ ( $\mu\text{A}\cdot\text{cm}^{-2}$ )	$V_{oc}$ (mV)	$P$ ( $\text{nW}\cdot\text{cm}^{-2}$ )
FTO-SWCNT	13.13	42.16	166.03
FTO-MWCNT	8.42	36.8	92.96

Figure 3.32: J-V curve comparison for MWCNT and SWCNT solar cells, along with tabulated  $J_{sc}$ ,  $V_{oc}$  and power values.

### 3.4 Chapter Conclusions

In this chapter it has been shown that arrays of SWCNT can be used in photovoltaic devices. These arrays are capable of producing a photocurrent when exposed to visible light with response times of  $\leq 200\text{ms}$  indicating that the electron-hole pair generation and separation occurs rapidly in the nanotubes. The current produced,  $\sim 13\mu\text{A}\cdot\text{cm}^{-2}$  with  $100\text{mW}\cdot\text{cm}^{-2}$  incident light intensity, was seen to be stable over extended periods with little or no degradation. The ageing affect seen in each of the constructed cells is attributed to the diffusion of the electrolyte solution into the attached bundles of nanotubes on the surface increasing the contact with the working

electrode. The most efficient conditions for converting light to current on a per nanotube basis are seen to be a cutting time of 2 hours with an attachment time of 24 hours. The trend of increasing photocurrent with attachment time matches the results seen in AFM of nanotube coverage using a similar attachment technique,<sup>120</sup> indicating a direct correlation between current and number of nanotubes on the surface. Variation of nanotube cutting time allows modification of both nanotube functionality and degree of semiconducting nature. This is seen both in the Raman data and photoresponse of the cells. The increasing nanotube coverage and bundle size shows an increase in photocurrent, whilst showing a decrease in voltage. It is also shown that MWCNT have an inferior photovoltaic performance when compared to SWCNT due to the lack of semi-conducting band structure. However, electrochemistry indicates that the electron transfer kinetics is superior in the MWCNT array due in part to the increased surface coverage.

---

**4. Single-walled Carbon  
Nanotube Arrays as Scaffolds  
for Chemical  
Functionalisation**

---

## 4.0 Introduction

As we have seen from Chapter 3 SWCNT arrays can be used to generate photocurrent by themselves, however, it may be possible to increase their performance with the addition of light harvesting molecules. These vertically aligned nanotube covered substrates provide a large surface area and an array of highly conductive wires which are themselves photoactive. Thus, the attachment of photosensitive redox molecules to these arrays would appear to be a beneficial step toward producing a high efficiency solar cell. As the SWCNT solar cells have been based on the DSSC design it would seem logical to first attach a dye molecule to the nanotube array which can then be verified using electrochemistry to investigate the electron transfer properties and surface bound concentration followed by photovoltaic testing. Porphyrin molecules are used in nature for the conversion of light to chemical energy in the form of photosynthesis, thus analogous ruthenium based porphyrins may also be possible to provide an improved response over the unmodified nanotube array. It will also allow direct comparison between metal based dyes and porphyrins in terms of photovoltaic performance. As was discussed in Chapter 1.3 the growth of dendrimers and dendrons from the nanotube array may provide an increased active area to improve photoresponse and an increased surface area for attachment of dye molecules. The chemical modification of the SWCNT arrays will now be investigated using a combination of electrochemistry and photovoltaic testing.

### 4.1 Dye Functionalisation of SWCNT Arrays

#### 4.1.1 Electrochemical Characterisation of Dye Functionalised SWCNT Arrays

As a proof of principle that SWCNT arrays could be chemically modified with organic photosensitisers such as dyes, samples were made on silicon wafers to test the modification technique before progressing to transparent FTO substrates. The details of the modification technique used, which involves the initial attachment of a diamine linker molecule, were shown in section 2.2.2. Detection and verification that the dye had been attached was performed by differential pulse voltammetry (DPV). DPV results for the N3 modified array are shown in Figure 4.1, with the DPV of N3 in solution inset. To help identify the redox peak the background signal present in the

unmodified array can then be subtracted showing only the signal present due to the presence of the dye. The clear presence of the peak at  $\sim 910\text{mV}$  correlates well with the peak position in solution of  $\sim 950\text{mV}$ , and with literature.<sup>15</sup> The difference in peak position is thought to occur because of covalent attachment of the dye to the nanotube which shifts the redox potential of the molecule. The full width at half maximum (fwhm) is  $240\text{ mV}$  which is greater than the theoretical value of  $90.6/n\text{ mV}$  where  $n$  is the stoichiometric number of electrons in the reaction for an ideal reversible bound species,<sup>130</sup> implying that there are a variety of interaction environments for the attached dye molecules on the carbon nanotube array. The presence of this peak indicates that indeed N3 dye is attached to the CNT array.

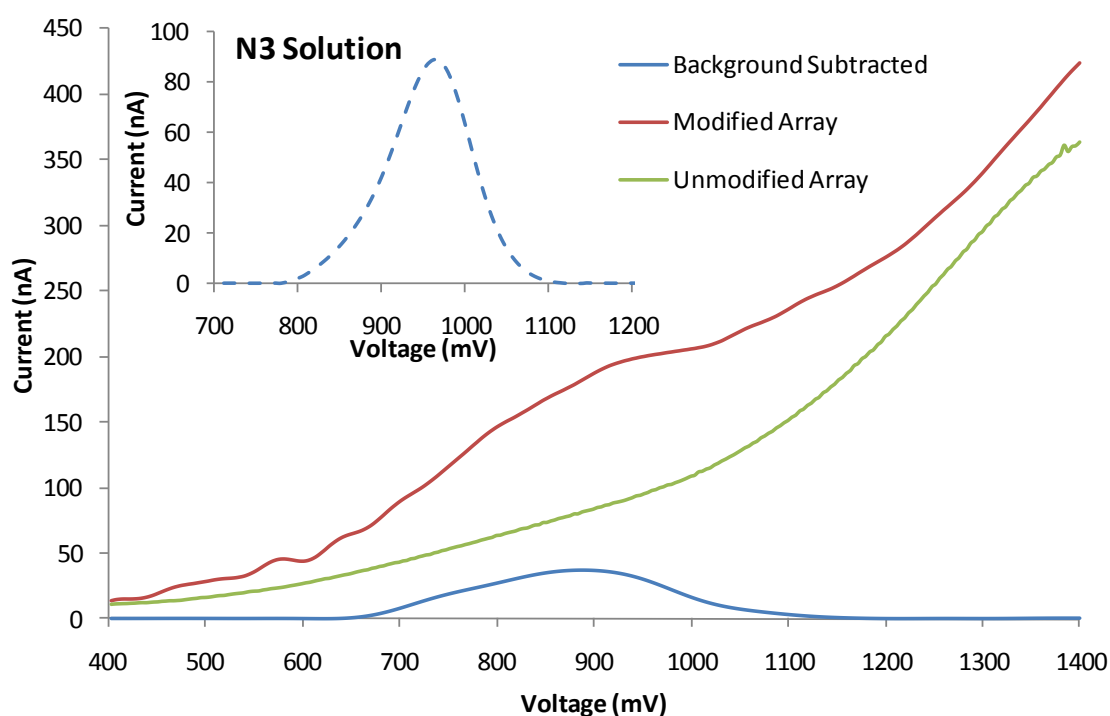


**Figure 4.1: DPV of unmodified and N3 modified CNT arrays (24 Hours attachment time). DPV of N3 in solution (Inset).**

Altering the CNT attachment time during array production (see Figure 2.5) will affect the concentration of dye attached to the surface by altering the number of attachment sites available for the dye. Low attachment times will create bundles of nanotubes that remain small and are sparsely spread over the surface. As attachment time increases the nanotube coverage initially increases but then drops somewhat at long times, this trend has been observed previously.<sup>120</sup> This indicates that there may

be an optimal nanotube coverage which maximises surface area leading to maximum amount of dye attached to the surface. To discover the optimal coverage differing attachment times were used whilst maintaining the cross linker and dye attachment times. To determine the concentration of dye attached the magnitude of the peak current from DPV is used as a measure of dye concentration. Figure 4.2 shows a graph of background subtracted peak current from DPV versus attachment time on silicon. A peak in current occurs at the 2 hour attachment time. This is believed to be caused by steric hindrance of the dye molecule, as the bundles of nanotubes become too large they actually prevent further dye molecules from attaching effectively lowering the active surface area available.

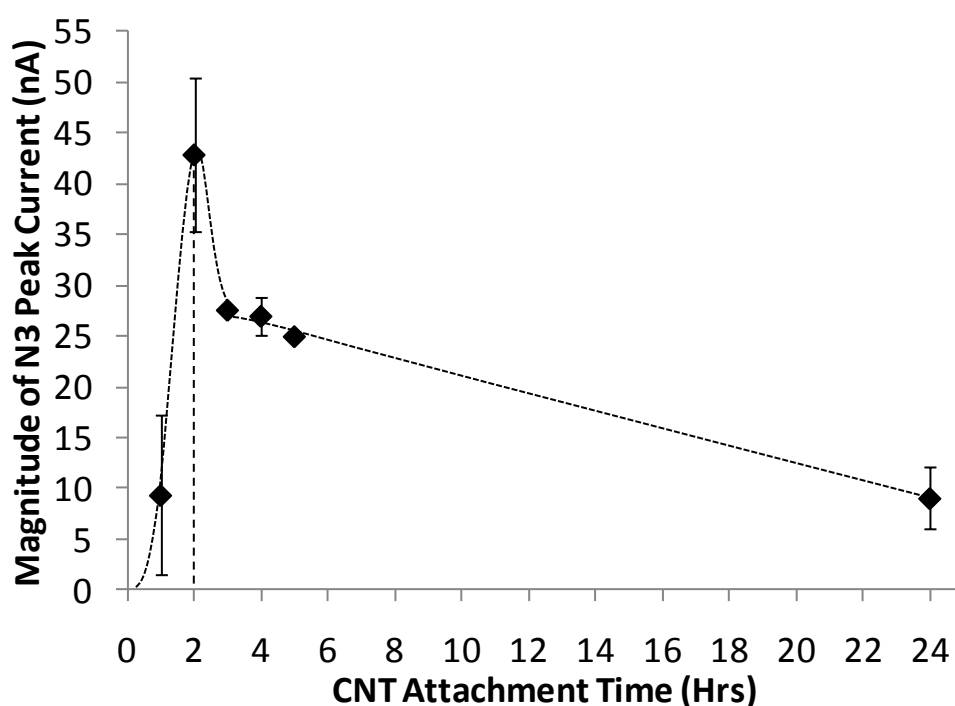
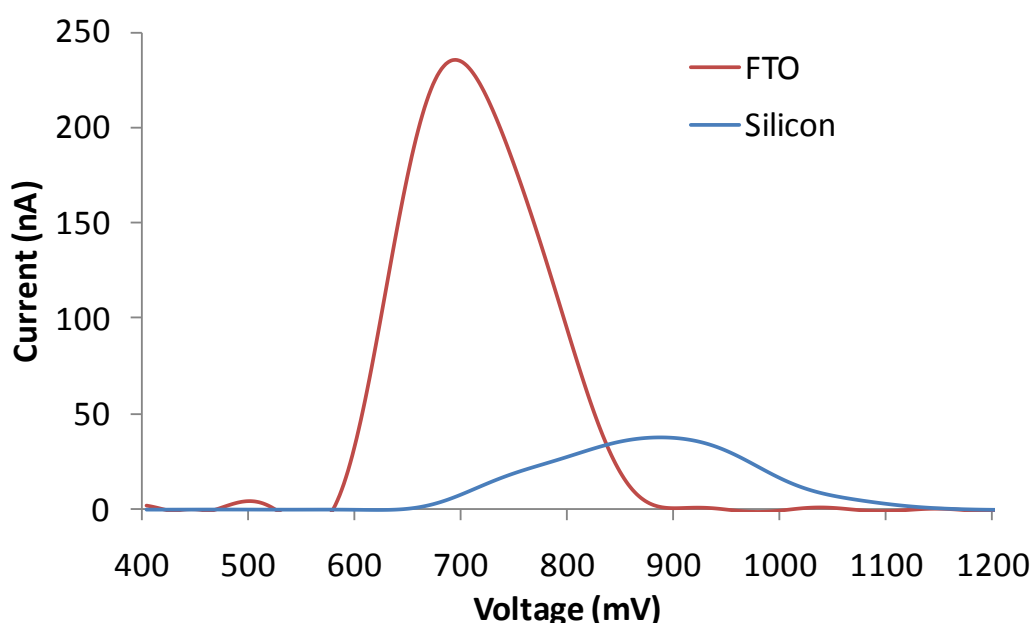


Figure 4.2: N3 peak current vs. CNT exposure time on silicon. (Dashed line added to guide the eye)

Once this trend had been established using silicon as the substrate a transparent conductive substrate, FTO coated glass, was used to form the arrays for photovoltaic performance testing. The use of the transparent substrate is of obvious benefit for any applications in light harvesting as it allows for a larger number of cell orientations. Figure 4.3 compares the DPV curves of both the N3 modified SWCNT arrays on silicon and FTO substrates. The increased magnitude of the current observed on the FTO substrate is due to increased nanotube coverage on the surface compared

to the silicon substrates. This larger coverage is likely due to more complete initial hydroxylation of the FTO surface compared to the relatively unreactive silicon surface, leading to a higher subsequent SWCNT coverage. The shift in peak potential from 950mV on silicon to 700mV on FTO could be caused by the increased dye concentration present on the surface. This higher dye concentration will increase the chance of forming dimers of the N3 dye molecules which would be expected to shift the redox potential.<sup>160a</sup> The results in the rest of the chapter were obtained using FTO coated glass as the substrate.



**Figure 4.3: DPV comparison of N3 functionalised SWCNT arrays on both silicon and FTO substrates.**

To further investigate the attachment of N3 dye to the array cyclic voltammetry experiments were carried out to investigate the nature and efficiency of the electron transfer. The CVs obtained show a large background current as expected due to the rough surface obtained from the deposition of the nanotubes. This increased surface roughness leads to capacitance, which causes the increased background current.<sup>151</sup> Figure 4.4 shows the background subtracted cyclic voltammograms at varying scan rates with the inset showing the linear dependence on scan rate indicating a surface bound redox species. This differs from the linear dependence on the square root of scan rate seen when the redox active molecule is in solution.<sup>129</sup> This supports the idea that the N3 is attached to the SWNT array on the surface. The peak position is also

linearly related to scan rate. This indicates that it is a quasi-reversible reaction, due to non-ideality of the electrode surfaces.<sup>129, 131, 133, 161</sup>

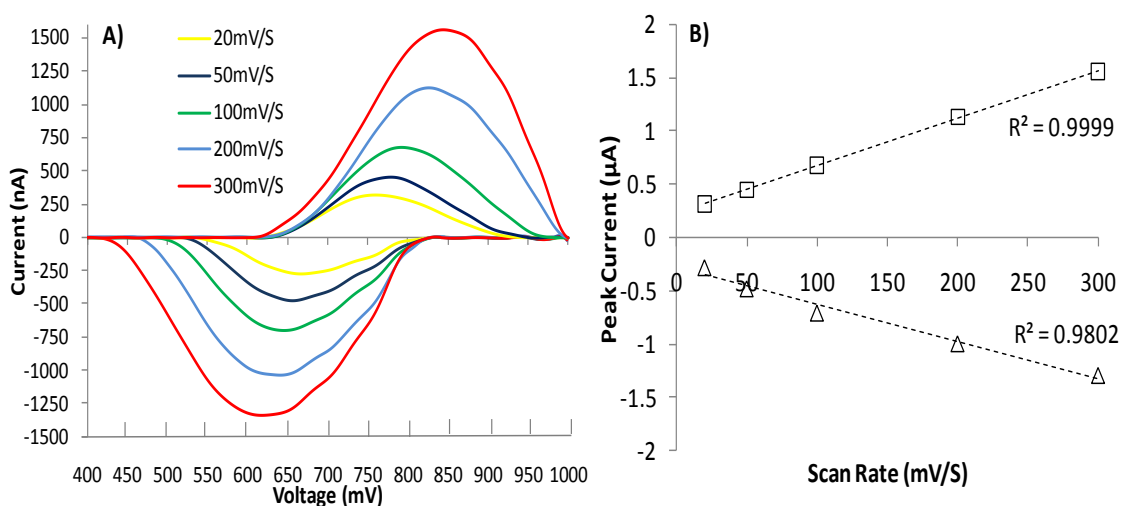


**Figure 4.4:** Background subtracted cyclic voltammograms of FTO-CNT-EDA-N3 (2hr SWCNT attachment time). (A) Graph of peak current versus scan rate. (B)

The linear dependence between peak height and scan rate means that the surface concentration can be calculated using the previously discussed Equation 2.3.

$$\text{Equation 2.3: } I_p = \frac{n^2 F^2 A \Gamma v}{4RT} = \frac{nFQv}{4RT}$$

Where  $I_p$  is the peak current,  $n$  is the number of electrons involved in the process (one for N3 dye),  $F$  is Faraday constant,  $Q$  is the integrated peak area,  $v$  is the scan rate,  $R$  the gas constant and  $T$  the temperature (298K for this work),  $A$  is the electrode area ( $\sim 0.05\text{cm}^2$ ) and  $\Gamma$  is the surface bound concentration in  $\text{mol}\cdot\text{cm}^{-2}$ . By applying Equation 2.3 this gives a value of  $4.2 \times 10^{-8} \text{ moles}\cdot\text{cm}^{-2}$  ( $2.0 \times 10^{16} \text{ molecules}\cdot\text{cm}^{-2}$ ) for 2 hours of SWCNT attachment time which is comparable to work in the literature attaching molecules to similar CNT arrays.<sup>120, 122, 132</sup> It is however, approximately 5 times lower than the  $1.3 \times 10^{-7} \text{ mol}\cdot\text{cm}^{-2}$  (found using optical absorbance) stated in Grätzel cells.<sup>12</sup> This is to be expected as the titania layer used traditionally is approximately 10-15 $\mu\text{m}$  thick with high porosity leading to an increased surface area, whilst the nanotube layer thickness is found to be several hundred nanometres (0.1-0.5 $\mu\text{m}$ ). Table 4.1 compares several previously published methods for preparing SWCNT modified electrodes and attaching redox active molecules. Noticeably the gold and graphite based electrode systems have a significantly higher electron transfer rate due to the increased

conductivity and the use of a metallic conductor. The most similar system in terms of attached molecule is the work by *Yu et al.* in attaching the ruthenium porphyrin (RuTPP) as it will have a similar size to the N3 molecule used and a similar coverage is observed. Using the relationship between peak potential and scan rate we can then use the previously defined Equation 2.4 to calculate  $k_s$ , the electron transfer constant.<sup>129, 131-133</sup> The plot of peak potential,  $E_p$ , versus the natural log of scan rate,  $\ln(v)$ , is shown in Figure 4.5. By taking both the intercept and the slope,  $k_s$  was calculated to be  $1.48\text{s}^{-1}$ . This is substantially faster than the electron transfer rate observed for redox species in solution, seen in chapter 3 where ferrocene in solution had a transfer rate of  $0.071 \pm 0.014\text{cm}\cdot\text{s}^{-2}$ , as there is no diffusion to the working electrode.

**Table 4.1: Comparison of redox active molecules chemically attached to SWCNT arrays.**

Author	Electrode Description	Attached Molecule	Surface Concentration (molecules.cm <sup>-2</sup> )	Electron Transfer Rate, $k_s$ (s <sup>-1</sup> )
Yu et al. <sup>123</sup>	Vertically aligned SWCNT attached to P-type silicon	Ferrocene	$5.57 \times 10^{16}$	21
Yu et al. <sup>94</sup>	Vertically aligned SWCNT attached to P-type silicon	RuTPP	$2.07 \times 10^{16}$	--
Flavel et al. <sup>132</sup>	Vertically aligned SWCNT attached to thiol modified gold	Ferrocene - methanol	$9.06 \times 10^{13}$	36.95
Gooding et al. <sup>153</sup>	Vertically aligned SWCNT attached to thiol modified gold	Ferrocene - methylamine	$1.51 \times 10^{14}$	459
Tu et al. <sup>162</sup>	Vertically aligned SWCNT attached to Graphite	FeTMPyP	$4.02 \times 10^{15}$	6.68
This Work	Vertically aligned SWCNT attached to FTO glass	N3 Dye	$2.00 \times 10^{16}$	1.48

The electron transfer co-efficient of  $1.48\text{s}^{-1}$  is however quite low compared to some of the other systems shown in Table 4.1 and this is likely to be caused by the slow transfer of the electrons through the covalent amide bond formed between the

EDA and N3 molecules, as it is the ruthenium metal centre that experiences oxidation and this electron must then transfer through its ligands.

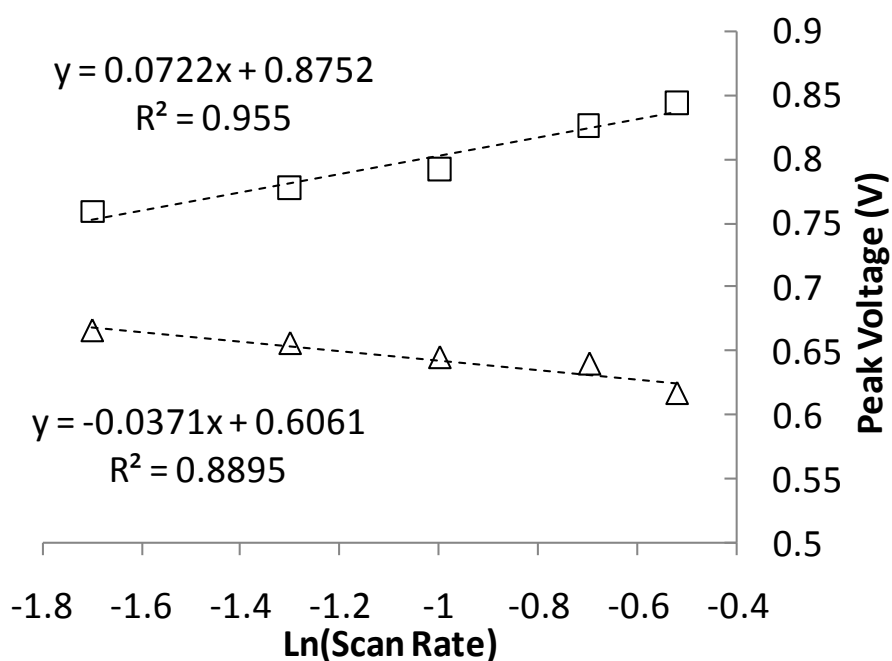
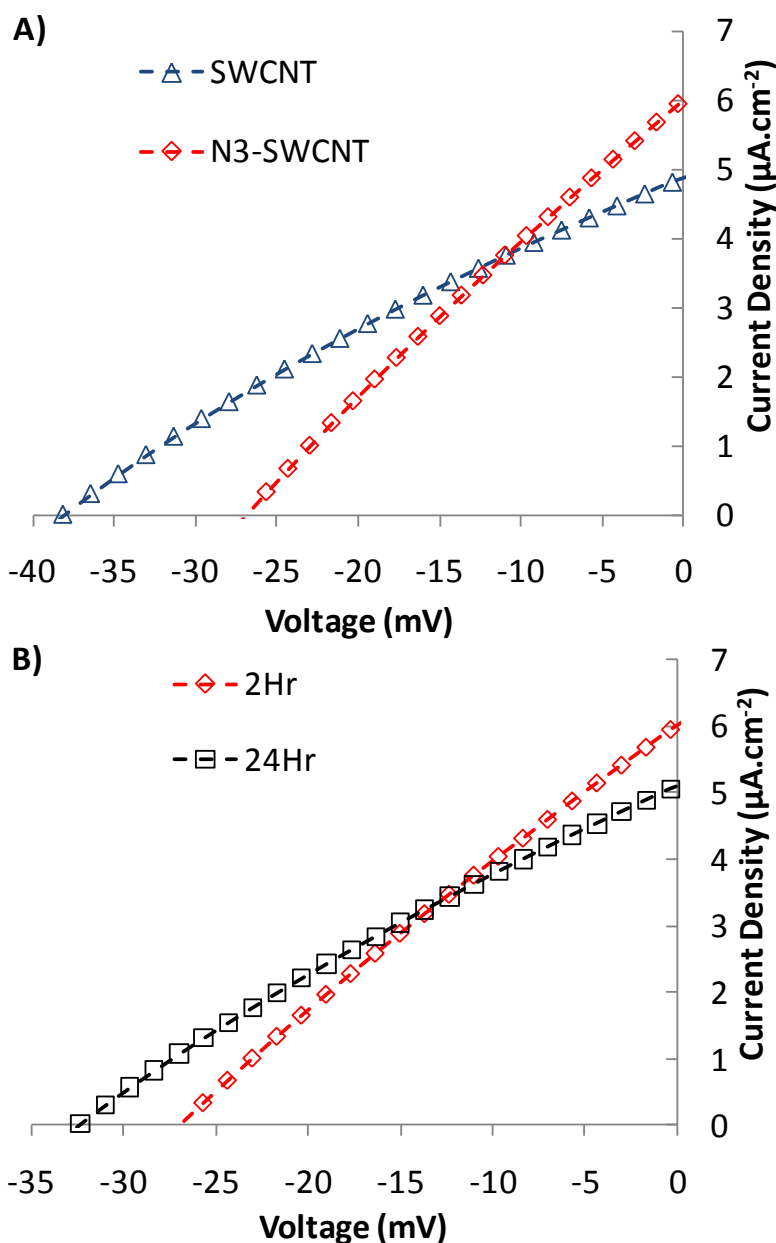


Figure 4.5: Plot of anodic and cathodic peak potential ( $E_p$ ) versus  $\ln(v)$  for N3 functionalised SWCNT on FTO.

#### 4.1.2 Photovoltaic Properties of Dye Functionalised SWCNT Arrays

Having established that CNT arrays have been modified with N3 by electrochemistry, J-V curves on complete cells whilst illuminated were taken to analyse cell efficiency. Figure 4.6A compares the J-V curves for the unmodified SWCNT array, as discussed in Chapter 3, and the N3 modified array. When compared to the unmodified CNT array the N3 modification has caused a decrease in photovoltage and an increase in photocurrent. The  $V_{OC}$  value is decreased to 27mV and the  $J_{SC}$  increases to  $6\mu A.cm^{-2}$ . The decrease in voltage indicates that the presence of the dye has altered the energy gap between the Fermi level of the nanotubes and the redox potential of the electrolyte. Whilst the increased photocurrent indicates that the N3 molecules are injecting electrons into the CNT array to increase the current. The presence of the dye provides a second route for electron-hole generation, in the form of the excited dye, as

well as what can be created by the SWCNT array by itself. This increase in current and decrease in voltage has been seen previously<sup>61, 163, 164</sup> and has been attributed the introduction of new energy levels causing a shift in the Fermi level whilst increasing the electron injection efficiency into the electrode. Figure 4.6B compares the J-V curves for 2 hours of SWCNT attachment, discussed in section 4.1.1 to have the highest concentration of N3 dye, and 24 hours of SWCNT after N3 functionalisation. The higher dye concentration (2hr sample) shows an increased photocurrent and decreased photovoltage when compared to the 24hr sample. This strongly supports, firstly; that the 2hr attachment time has higher dye surface concentration and consequently that the presence of dye molecules increases photocurrent produced whilst shifting the Fermi level leading to a lower cell voltage being produced.



**Figure 4.6:** J-V comparison between SWCNT and N3 functionalised SWCNT cells. (A) J-V comparison of 2 and 24 hour attachment times for N3-SWCNT cells. (B) Light intensity is  $35\text{mW}\cdot\text{cm}^{-2}$ . SWCNT cutting time was 8 hours.

Figure 4.7A shows the photocurrent produced by the 24hr SWCNT-N3 cell when the light source was switched on and off. As for the unmodified SWCNT cells the data points shown are separated by 200ms. Clearly the array produced a noticeable increase in current, approx  $\sim 5\mu\text{A}\cdot\text{cm}^{-2}$ , when exposed to light. Of note is that this is approximately the same as the response seen previously in Figure 3.18 for the

unmodified SWCNT array, however, this particular experiment was performed chronologically before the data shown in Chapter 3 and the processes involved in producing the cells became much improved over time. Thus to provide a fair comparison this response can then be compared to Figure 4.7B of the unmodified CNT cell produced at a similar time. Figure 4.7B shows a photocurrent response of just  $\sim 2\mu\text{A}\cdot\text{cm}^{-2}$  considerably lower than for the N3 modified array.

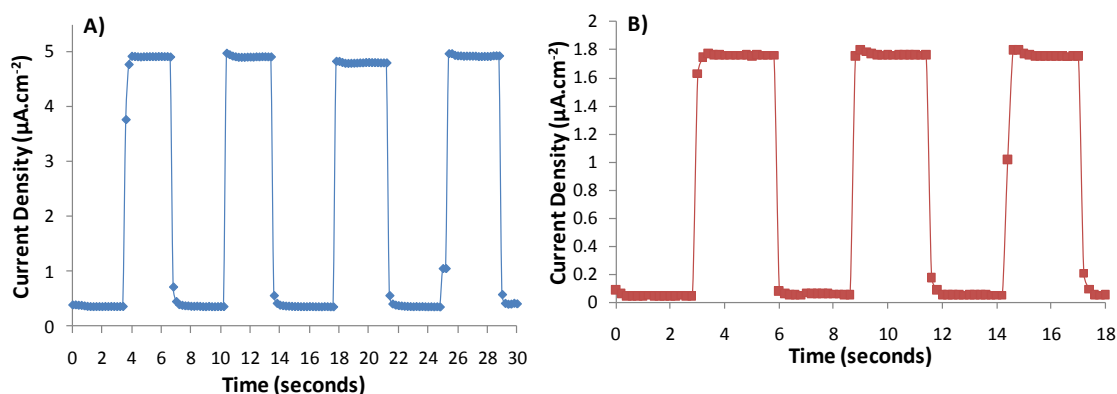


Figure 4.7: On-Off light response for 24Hr CNT modified with N3. (A) On-Off light response for unmodified 24Hr CNT produced at similar time (B) Light intensity  $35\text{mW}\cdot\text{cm}^{-2}$ .

## 4.2 Porphyrin Functionalisation of SWCNT Arrays

After establishing that N3 dye could be successfully attached to the SWCNT arrays and provide an increased photocurrent an analogous porphyrin was chosen to also attach and act as a comparison. N3 dye, as shown previously, is a ruthenium based molecule thus to compare a ruthenium based porphyrin was chosen, ruthenium tetraphenyl porphyrin. This should allow a comparison between porphyrin-type molecules and traditional dyes and a determination of which has the superior photovoltaic performance. The use of porphyrins in photovoltaics would seem logical due to their role in photosynthesis, but so far have lacked the wide range visible light absorbance needed for efficient light harvesting.

### 4.2.1 Electrochemical Characterisation of Porphyrin Functionalised SWCNT Arrays

To verify the modification of the SWCNT arrays with porphyrin, electrochemical measurements were taken as with the N3 Arrays. The electrochemical oxidation/reduction of ruthenium porphyrins has been reported previously in non-

aqueous media such as DCM,<sup>165</sup> THF,<sup>166</sup> acetonitrile,<sup>167</sup> and others.<sup>168</sup> RuTPP(CO) can be oxidised in CH<sub>2</sub>Cl<sub>2</sub> by two successive one-electron oxidations which occur on a platinum electrode at 825mV and 1098mV (vs. Ag/AgCl).<sup>168-170</sup> The first oxidation corresponds to the formation of [Ru(II)TPP(CO)]<sup>+</sup>, then the product of [Ru(II)TPP(CO)]<sup>+</sup> oxidation is assigned to an abstraction of an electron from the metal centre at the second oxidation.<sup>171, 172</sup> The CV for RuTPP solution in CH<sub>2</sub>Cl<sub>2</sub> is shown in Figure 4.8, where the working electrode was HOPG, the counter a platinum mesh and a saturated Ag/AgCl reference electrode was used and the scan rate was 100mV.s<sup>-1</sup>. The large background current comes from using a low concentration of RuTPP. The dashed line in Figure 4.8 is the background subtracted spectra more clearly showing two reversible peaks, the first centred around 710mV and the second centred at 1088mV. These are in close agreement with the previously observed literature values.<sup>94</sup>

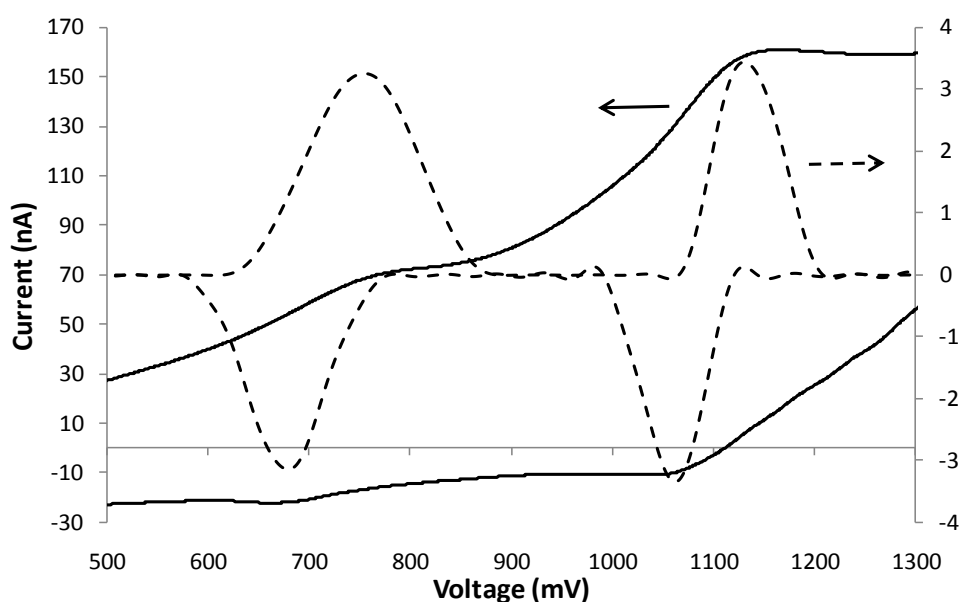


**Figure 4.8:** Cyclic voltammograms of RuTPP in CH<sub>2</sub>Cl<sub>2</sub>. Dashed line is the background subtracted trace showing two reversible oxidation peaks.

The DPV of the RuTPP modified SWCNT array is shown in Figure 4.9. There are two clear peaks seen in the DPV; one at ~675mV and the other at ~1100mV. These peak positions are close to those observed in solution although the first is shifted to a lower potential. This shift is likely due to the co-ordination of the porphyrin metal centre to the electron withdrawing character of the 4-aminopyridine, causing a shift in the oxidation potential. The connection to the RuTPP is through the metal centre via

the aminopyridine linker, so the peak position, at 1100mV, attributed to the abstraction from the metal centre is unchanged. The presence of these peaks on the SWCNT array is strong evidence that the co-ordination of the RuTPP to the aminopyridine has occurred successfully. To determine if a similar trend as was observed for N3 attachment exists, namely that 2 hours of SWCNT attachment led to an increased surface concentration, both 2 and 24 hour SWCNT arrays were constructed and functionalised with RuTPP. The magnitude of current in the 24hr sample is ~2.6nA increasing to ~14nA in the 2hr case, both seen in Figure 4.9. In the 2hr CNT attachment the first oxidation peak has shifted from 675 to 540 mV while the position of the second peak remains unchanged. The 2hr array has nanotubes which are more sparsely spaced than the 24hr attachment case. This will mean there are more nanotube sidewalls available for interaction with the organic portion of the porphyrin and this will further affect the redox potential for the first step, the formation of  $[\text{Ru(II)TPP(CO)}]^+$ , moving it to a lower potential. In both arrays the connection to the metal of the RuTPP is through the aminopyridine, so the peak position attributed to the abstraction from the metal centre is unchanged. As the current is directly proportional to amount of porphyrin attached the increased current indicates increased concentration of attached porphyrin, similar to the trend seen for N3 attachment.

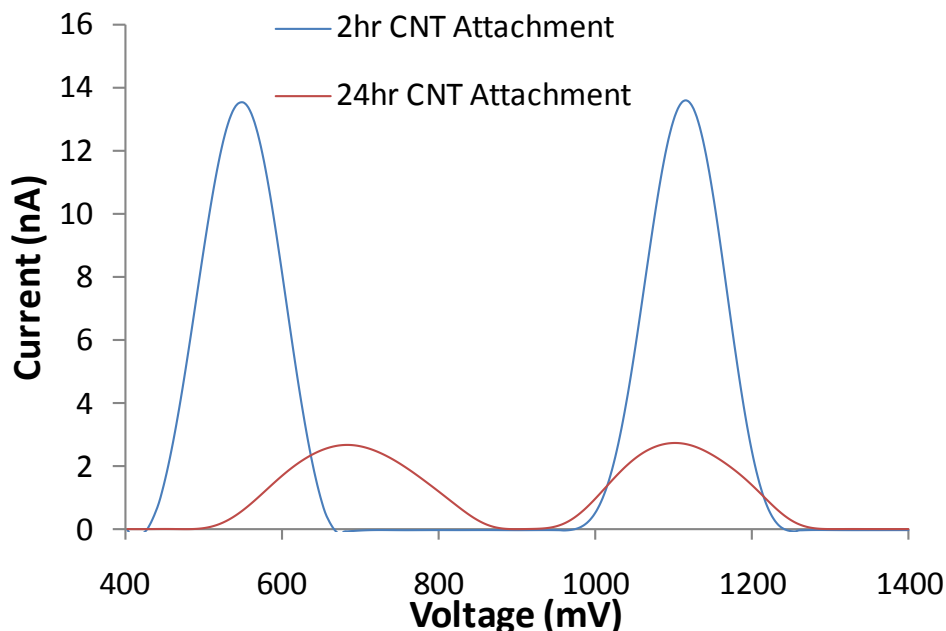


Figure 4.9: Background subtracted DPV of RuTTP functionalised SWCNT array for 2hrs and 24 hrs of SWCNT attachment.

#### 4.2.2 Photovoltaic Properties of Porphyrin Functionalised SWCNT Arrays

After verification that the SWCNT arrays had been modified with RuTPP porphyrin by electrochemistry, complete cells were constructed as for the N3 and unmodified arrays. Figure 4.10 compares the J-V curves for the porphyrin modified 2 and 24 hour CNT attachment times arrays. As was suggested by the electrochemistry results the lower SWCNT coverage, 2 hours of attachment time, allowed for the maximum photocurrent and voltage to be generated. However, both samples have low photoresponse with the 2 hour sample only producing  $2.7\mu\text{A}\cdot\text{cm}^{-2}$  and 27mV, this is significantly lower than the unmodified SWCNT electrode as well as the N3 modified arrays. This suggests that the presence of either the 4-aminopyridine cross-linker or the RuTPP itself is detrimental to the photoresponse.

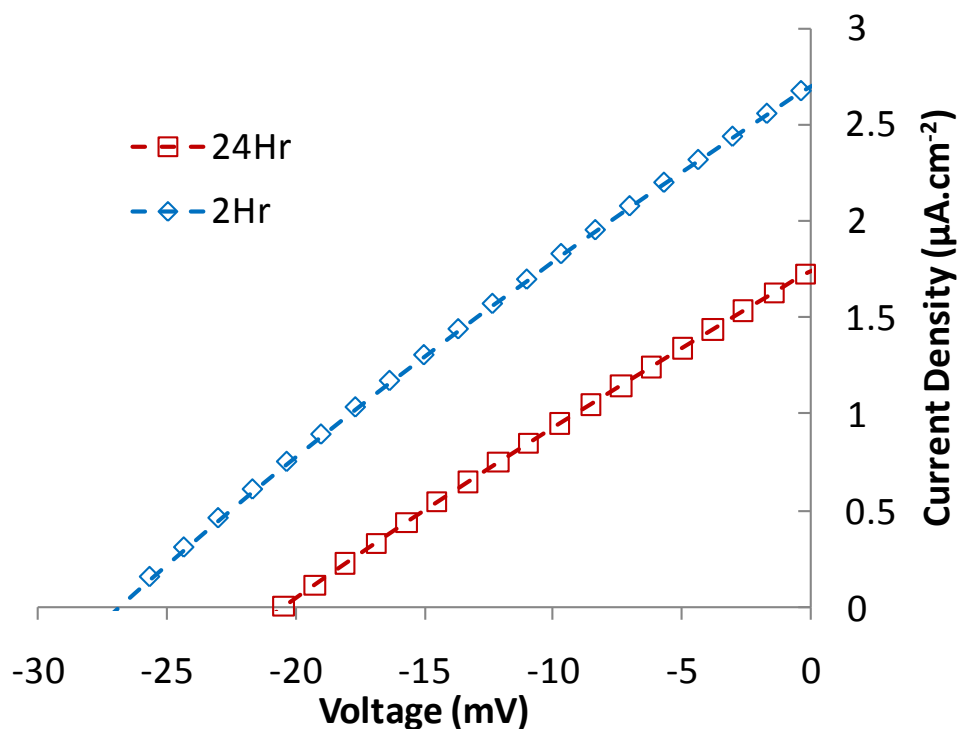


Figure 4.10: Comparison of the J-V Curves for RuTPP functionalised cells with 2 and 24 hours of SWCNT attachment. Light intensity  $35\text{mW.cm}^{-2}$ .

A comparison of photovoltaic characteristics for the N3 and RuTPP modified arrays is shown in Figure 4.11. The N3 I-V curve has a greater current compared to that of the porphyrin, with the same voltage. Electron transfer rates have been measured between porphyrins and single-walled nanotubes<sup>162</sup> and are very similar to that measured in this work for the N3 dye. It should be pointed out that while the functionalisation approaches in *Tu et al.'s* work<sup>162</sup> and that reported in this work is quite different, it is likely that the electron transfer rates would be similar. This means the difference in photovoltaic performance is not likely traceable to electron transfer differences. The observed differences in the J-V curves are most probably due in part to the energy levels of the electrolyte used, as  $\text{I}^-/\text{I}_3^-$  is chosen as it is a good match to N3 dye which has different energy levels to that of the RuTPP.

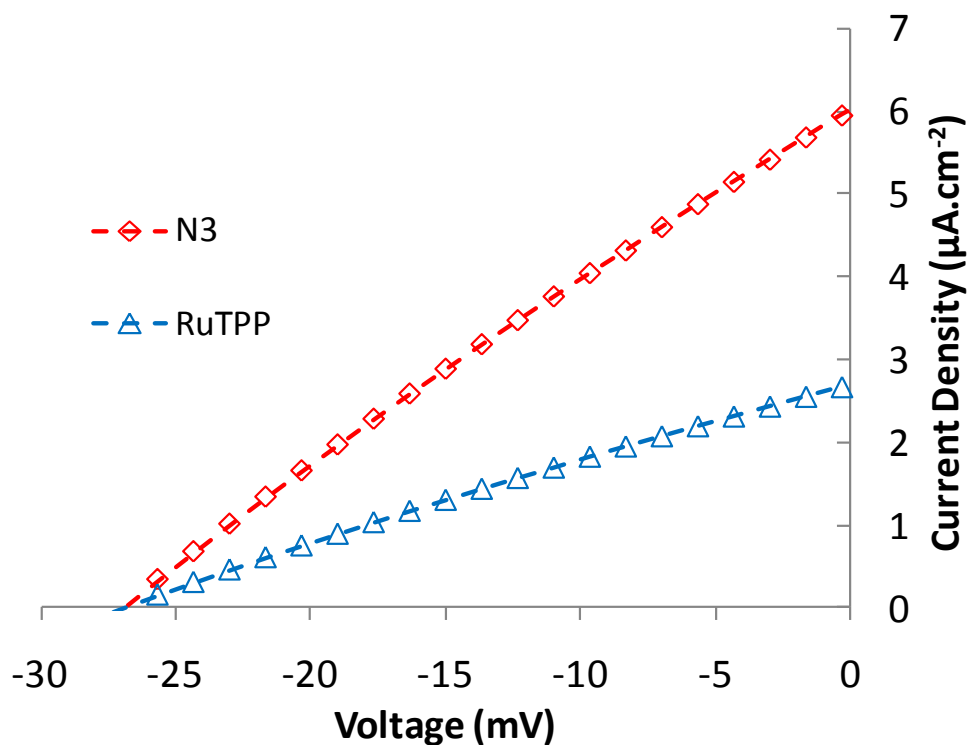


Figure 4.11: Comparison of the J-V curves from RuTPP and N3 functionalised cells. (Both cells used 2 hours of SWCNT attachment)

### 4.3 Dendron Functionalisation of SWCNT Arrays

As has been discussed in Chapters 3 and 4 SWCNT have been able to produce a photoresponse that could be modified by further chemical functionalisation. This was then further expanded by the use of SWCNT arrays as a scaffold for the growth of light harvesting dendrons. One of the most commonly studied dendrimers is PAMAM (polyamidoamine). It consists of successive alternating generations of ethylenediamine and methyl acrylate, which are coupled by Michael addition.<sup>107-109, 173-175</sup> p-Phenylenediamine (PDA) has been previously shown to have superior conductivity compared to ethylenediamine for use as a molecular wire.<sup>126</sup> Thus, in this study a system where the ethylenediamine is replaced with p-phenylenediamine was used. This modification should also transform the dendrons themselves into the photosensitiser of the solar cell due to the visible light absorption of PDA, thus increasing the expected power output over that of the unmodified array. Furthermore, the attachment of the macromolecule is also expected to affect the electron transfer

at the working electrode interface. The use of PAMAM type dendrimers allows for control of the surface functionality, by either leaving the surface amine or acrylate terminated, which could allow for further functionalisation by other chromophores.

#### 4.3.1 Raman Characterisation of Dendron Functionalised SWCNT Arrays

Confocal Raman spectroscopy has been established as a technique to probe the presence of SWCNTs attached to FTO electrodes previously.<sup>18</sup> Here we use the well established technique of comparing the relative ratio of the 'D' or disorder band to the 'G' or graphitic band to determine the level of relative disorder, which in turn indicates the level of functionalisation present in the SWCNT. In Figure 4.12 the normalised spectra for the G-0.0 and G-0.5 modified surfaces are shown, both have been normalised to the intensity of the G band at  $1570\text{cm}^{-1}$ . Firstly the presence of the characteristic nanotube peaks indicates that the SWCNT array has successfully been formed. Secondly, noticeably the D band intensity from the normalised spectra is much higher for the G-0.5 surface (0.36) compared to the G-0.0 (0.15). This more than double increase occurs because the chemical functionalisation of SWCNT is known to increase disorder, due to the disturbance in the density of states.<sup>23,41,42</sup> Here the attachment of the PDA molecules to the SWCNT has increased the disorder of the array. This provides a good measure that the initial functionalisation has occurred successfully.

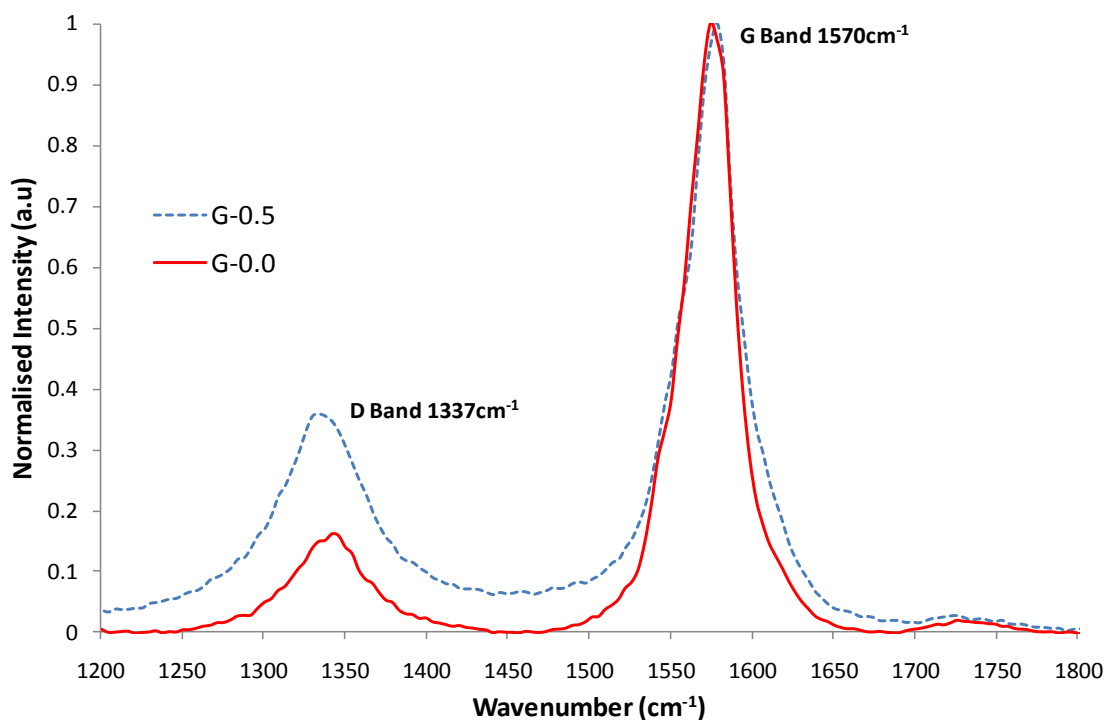


Figure 4.12: Normalised Raman spectra for the G-0.5 and G-2.0 modified surface. The graphitic or G band and the disorder or D band are labelled.

### 4.3.2 Electrochemical Characterisation of Dendron Functionalised SWCNT Arrays

To confirm that the functionalisation seen in the Raman data is in fact due to dendron growth, differential pulse voltammetry (DPV) was performed using the modified nanotube array as the working electrode. Data was recorded for G-0.5 through to G-3.5, with the G-0.0 being used for background subtraction. The redox peak attributed to the dendron occurs at about 480mV and is due to the presence of the p-phenylenediamine, confirmed by its appearance in solution, as seen in Figure 4.13, and as reported in the literature.<sup>176</sup> In solution the peak occurs at a different voltage (377mV) due to the electron withdrawing nature of the free amine groups, which are converted to amides once attached to the CNTs shifting the redox potential (480mV).

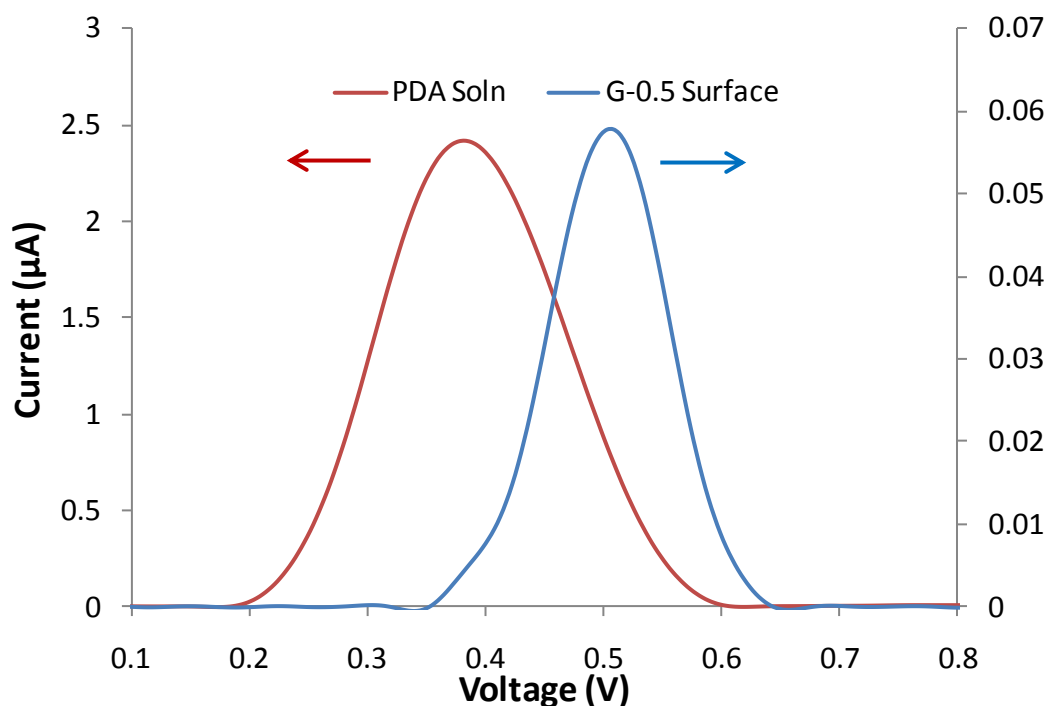


Figure 4.13: DPV of p-phenylenediamine solution and G-0.5 modified SWCNT.

The position of this peak shifted to lower potentials with increasing dendron generation (Figure 4.14 Inset). A similar effect has been observed in the literature, where in organic solvents oxidation becomes easier with increasing generation.<sup>175, 177-179</sup> This is believed to be due to the increased dendron size leading to an increased active surface area, thus facilitating oxidation. In DPV, the magnitude of the peak current is proportional to the concentration and can therefore be used to determine the amounts of PDA, and thus be used to monitor the propagating dendron growth. With increasing dendron generation, a clear DPV signal could be detected, indicating the successful modification of the nanotube array (Figure 4.14). The magnitude of the signal increased up to generation 2.0 by ~350%, before decreasing again (Figure 4.16). This increase is expected as mentioned previously as the number of PDA molecules is increasing. Additionally, the increased size of the dendron will cause greater electron transfer rates, leading to an increased peak height for the methyl acrylate terminated surface as well as the increased amounts of PDA. The decrease after G-2.0 is thought to be caused by steric effects between dendrons of neighbouring SWCNTs, whereby they begin to come into contact and possibly even chemically react with each other. This would lead to an effective 'short circuiting' effect that prevents the electrons from

interacting with the PDA molecules. This would decrease the overall efficiency of a device. The peak FWHM, shown in the Figure 4.14 inset, of the DPV signal increased also with increasing dendron generation, indicating that the redox of the PDA has become less reversible.

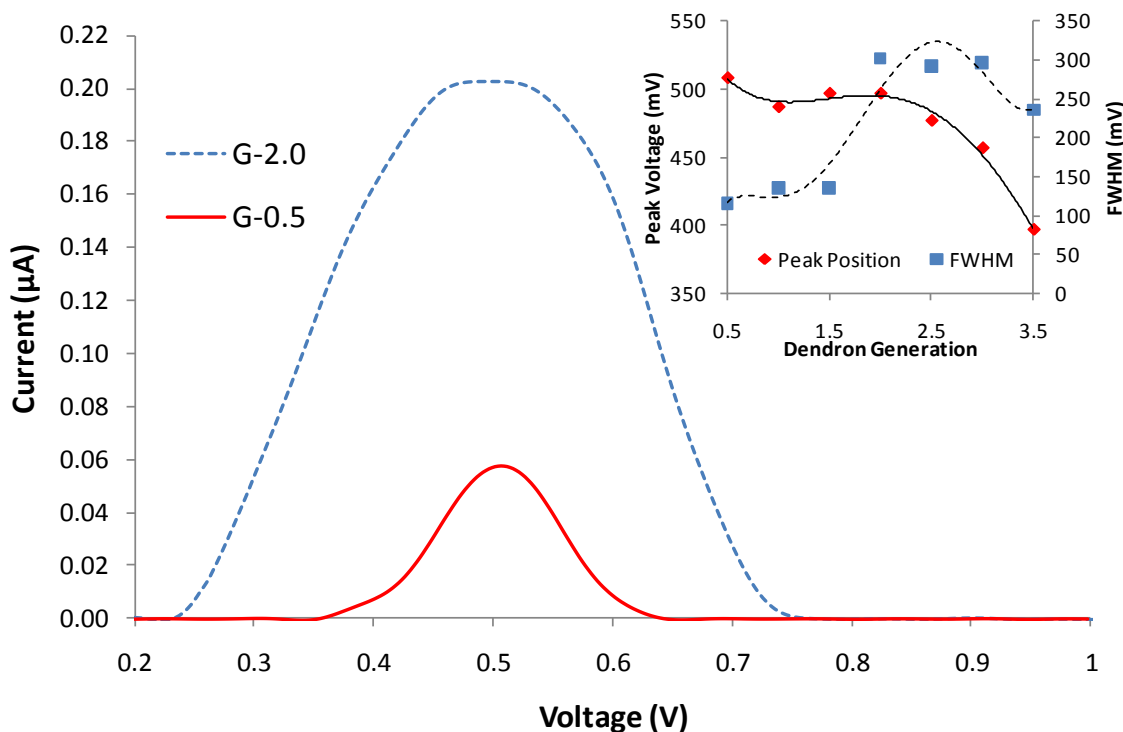


Figure 4.14: Background subtracted DPV for G-0.5 and G-2.0 modified array. Plot of peak voltage and FWHM versus dendron generation. (Inset)

To test the electrical properties of complete electrochemical solar cells, cells were then constructed as outlined in the experimental section. The electrical properties of these assembled solar cells were analysed using electrochemical impedance spectroscopy (EIS). EIS is a popular technique for investigating electrochemical solar cells as it provides information about the behaviour at the electrode interfaces.<sup>140, 180</sup> EIS spectra were taken for all cells ranging from the unmodified G-0.0 surface through to the G-3.5 modified electrodes. The cell's response was then plotted as Bode plots (Phase shift versus frequency) shown in Figure 4.15. This allowed the cell's response to be analysed in terms of an equivalent circuit that modelled the SWCNT interface as a resistor-capacitor (RC) element, a parallel mesh of a resistor and a capacitor. In order to take into account heterogeneities at the interface, a constant phase element (CPE) was used instead of a pure capacitor. The RC

element corresponds to the working electrode interface as the predominant element, since the counter electrode has much lower impedance. A typical DSSC consists of three separate elements; one for each electrode interface and one for the diffusion of the electrolyte. However, in the present case the large impedance of the working electrode dominated the spectrum. The data could be fitted using a parameter  $\alpha = 0.92$  to fit the EIS data for all generations. This parameter,  $\alpha$ , corresponds to the broadness of the distribution of capacitive elements. A value of about 0.9 corresponds to a relatively narrow distribution,<sup>134</sup> indicating a relatively homogeneous coverage of the nanotubes. The resistance and capacitance values varied with the dendron generation and are shown in Figure 4.16B and C respectively. A maximum in resistance was observed for generation 1.0, where the capacitance showed a minimum. The latter showed a maximum value for generation 2.0, corresponding to the maximum in both DPV signal and photoresponse as discussed later.

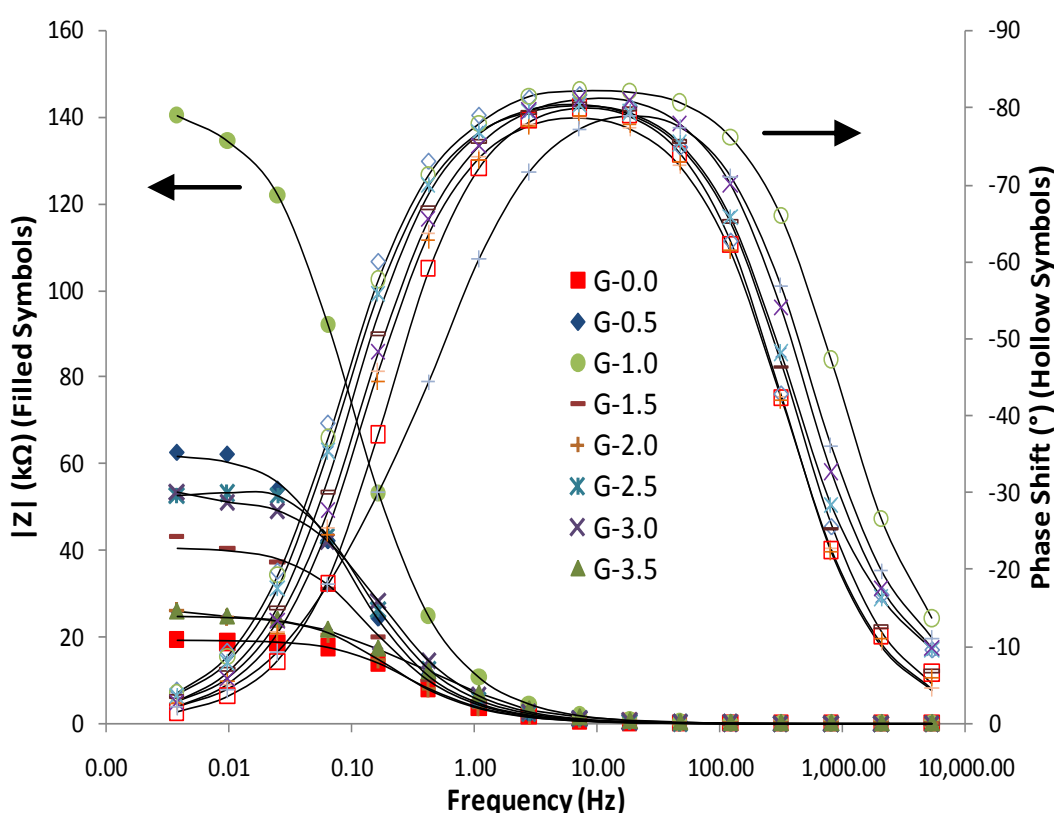


Figure 4.15: Bode plots for the different dendron generations. Solid lines correspond to fit using an equivalent circuit.

### 4.3.3 Photovoltaic Properties of Dendron Functionalised SWCNT Arrays

Dendron modified electrodes were manufactured into electrochemical solar cells and were then analysed using a solar simulator to measure the photoresponse. As the photoresponse curves have previously been shown with photocurrent and photovoltage, the overall cell power will be plotted for clarity. The power of each cell was calculated by taking the maximum current, voltage and fill factor. The photoresponse power varied with dendron generation. This trend can be compared to the generation dependence of the electrical parameters of the cell, i.e. the DPV response and the electrochemical impedance data (Figure 4.16). The photoresponse shows a minimum for generation 1.0 and a maximum for generation 2.0. This is in good agreement with the results obtained by DPV and with the capacitive behaviour of the cell. Additionally, the minimum in power corresponds to a maximum in resistance. These complete characteristics of the cell show that generation 2.0 seems to be the optimal configuration for the cell. In this configuration, the structure of the dendron layer allows for an optimal electron transfer as seen in the DPV and impedance data. At the same time, the high capacitance indicates a good charge separation, leading to a high power output. For larger dendron generations, the electrical properties of the organic layer decrease, leading to a lower cell output. The high resistance of generation 1.0 also decreases the power of this configuration.

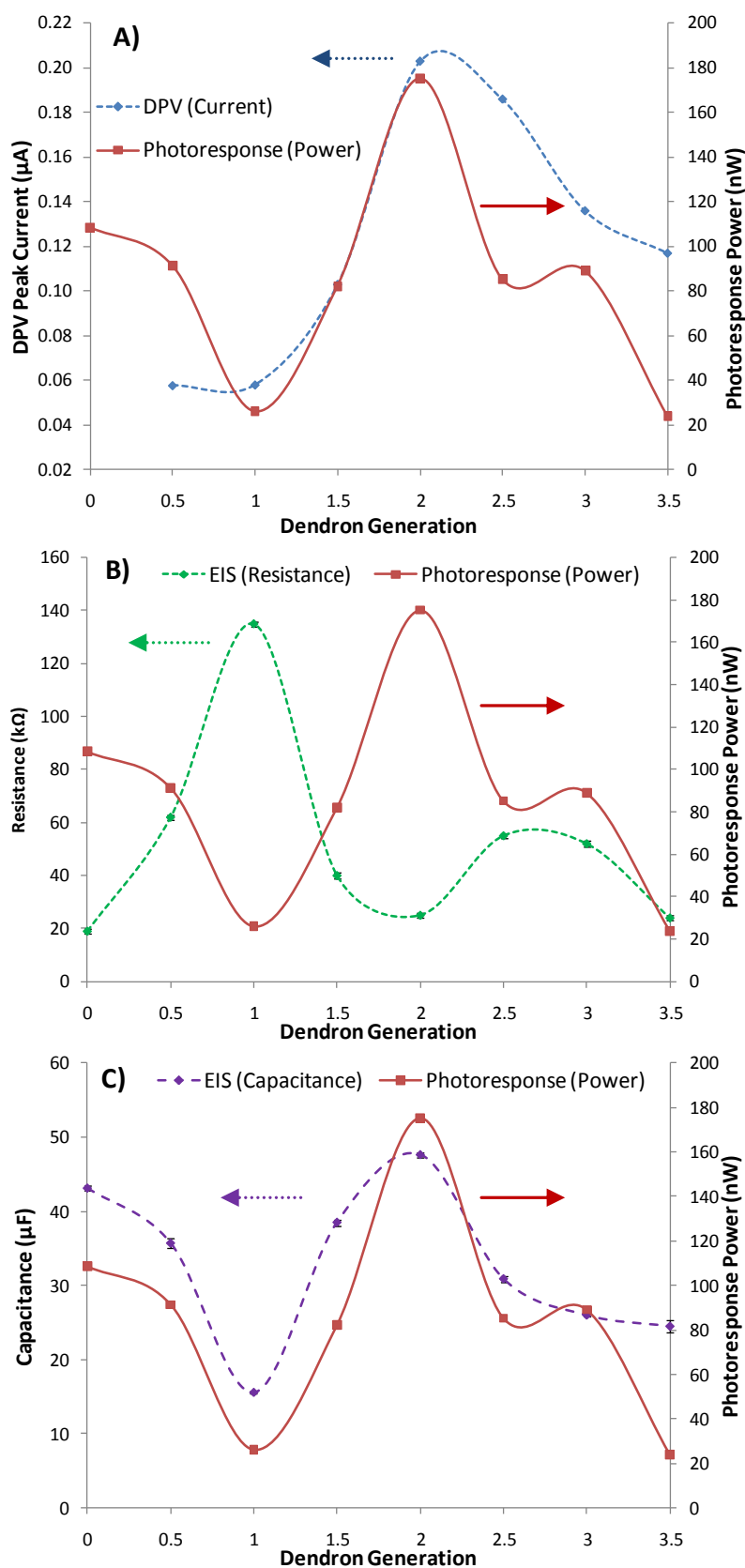


Figure 4.16: (A) Plot comparing DPV peak height and photoresponse. (B) Plot comparing EIS resistance and photoresponse. (C) Plot comparing EIS capacitance and photoresponse. Error bars are from fitting of equivalent circuit and smoothed line present to guide the eye.

Compared to the unmodified cell, the G-2.0 modification led to a 60% increase in power. Figure 4.17 shows the current density-voltage (J-V) characteristic behaviour of the respective cells. Such J-V curves show the short circuit current density  $J_{sc}$  and open circuit voltage  $V_{oc}$  that a cell produces when exposed to light, they also allow for the fill factor, the ratio of maximum power over  $J_{sc}$  and  $V_{oc}$ , to be determined. Previously, it has been shown that unmodified arrays produce an almost linear curve with a very low fill factor ( $\sim 28\%$ ) due to a low shunt resistance caused by recombination effects at the nanotube-electrolyte interface.<sup>60</sup> A similar behaviour has been seen for the G-0.0 surface. However, the G-2.0 has a slightly increased fill factor, going from 28.5% to 30.5%. The dark current is also seen to decrease, indicating that the recombination has been affected by the increased electrode conductivity after the addition of large macromolecules at the electrolyte interface.

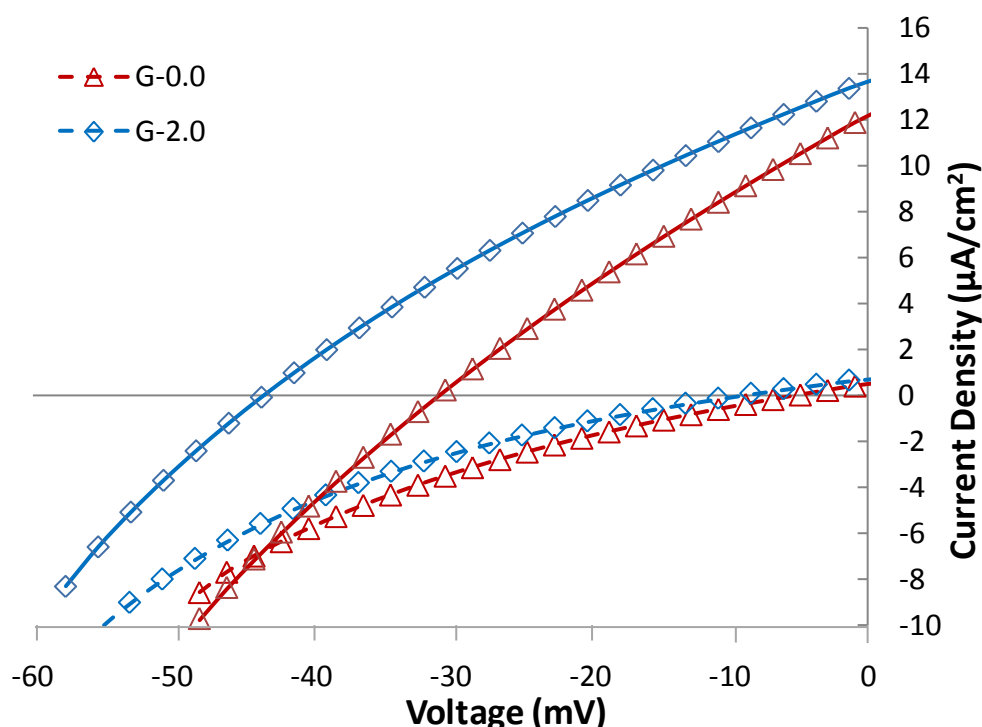
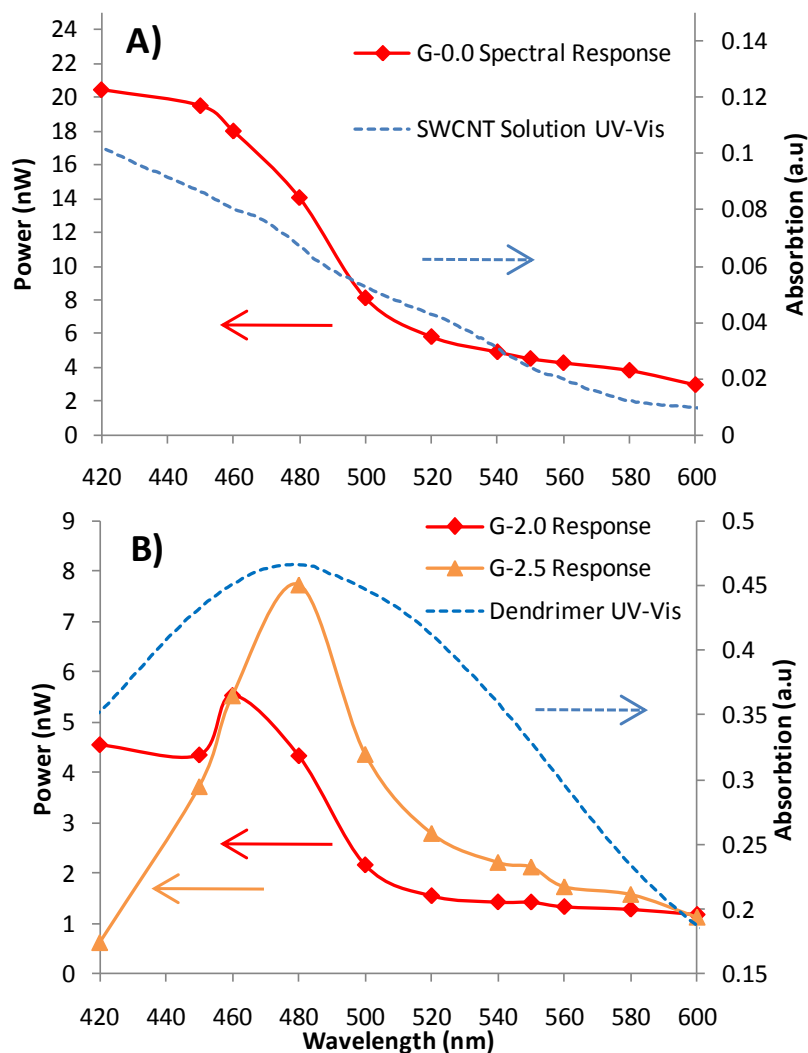


Figure 4.17: J-V curve for the unmodified SWCNT array (G-0.0) and the 2<sup>nd</sup> generation dendron modified array (G-2.0). Light intensity  $100\text{mW}\cdot\text{cm}^{-2}$ . Also included are the dark current curves with no illumination.

The 60% increase in light-harvesting performance from G-0.0 to G-2.0 is substantial and to further verify that this is due to the presence of the dendrons, the spectral response of the cells was measured. The dependence of output power on the

wavelength of the incident light of the unmodified cell is shown in Figure 4.18. The power produced closely matched the UV-Vis absorption spectrum of nanotubes when dispersed in a solution of DMSO before attachment to the surface, with the largest contribution from the blue end of the visible spectrum. However, Figure 4.18 shows the spectral response of the G-2.0 and the G-2.5 modified cell with the contribution of the nanotubes removed through subtraction of the unmodified G-0.0 spectrum, to highlight the influence of the dendrons on the spectral response. In this case, a distinct peak in the spectral response curve is evident and centred around 480nm when the dendrons are present. This closely matches the UV-Vis absorption of the dendrimer in solution (Figure 4.18B Dashed Line); further verifying that dendron functionalisation was successful and a contributing factor to the cell power.



**Figure 4.18: Spectral response of unmodified SWCNT cell (G-0.0) as seen in Chapter 3 and UV-Vis of SWCNT in solution. (A) Response of the dendron modified cell (G-2.0 and G-2.5) and the UV-Vis of the dendrimer in solution. (B)**

PAMAM-like dendrons have been grown from surface mounted single-walled carbon nanotube (SWCNT) arrays and investigated for solar cell applications. Raman spectroscopy also verified that chemical functionalisation had taken place through an evident change in the D/G band ratio. The presence of the dendron was confirmed by differential pulse voltammetry and spectral response of solar cells fabricated from such architectures. These cells were analysed with impedance spectroscopy and the maximum in resistance corresponded to a minimum in output power, whilst the maximum in capacitance corresponds to the maximum power. These dendron modified arrays were found to increase the photoresponse of the unmodified SWCNT array by a maximum of 60% for the G-2.0 modified array. The apparent decrease in

power after G-2.0 is attributed to the interaction of dendrons from neighbouring bundles of SWCNTs as their size increases.

#### 4.4 Dye Modification of Dendron Functionalised SWCNT Arrays

Due to the increased performance of both dendron modifying the CNT arrays and the functionalisation with N3 dye the logical subsequent procedure is to combine the two methods. This involves first dendron modifying the CNT arrays and leaving them amine terminated, which occurs at every half generation (e.g. G-0.5, G-1.5, G-2.5). With an amine terminated dendron N3 dye can easily be covalently bound via an amide bond by one of the four carboxylic acid groups on each N3 dye molecule. Once these dye modified arrays have been produced they are named in a similar fashion to the dendrons (e.g. G-0.5-N3, G-1.5-N3, G-2.5-N3) and these can be seen schematically in Figure 4.19. Due to the increased flexibility and mobility of the terminally attached dye molecules at longer chain lengths the higher generations are shown with multiple attachments to the dye molecules. This is believed to be a more realistic depiction of the chemical environment of each dye molecule and is supported by electrochemical results as will be discussed shortly. These dye modified dendron arrays are then characterised with electrochemistry to determine the surface concentration and electron transfer rates. The electrochemical data will then be used to help explain their respective photovoltaic performance.

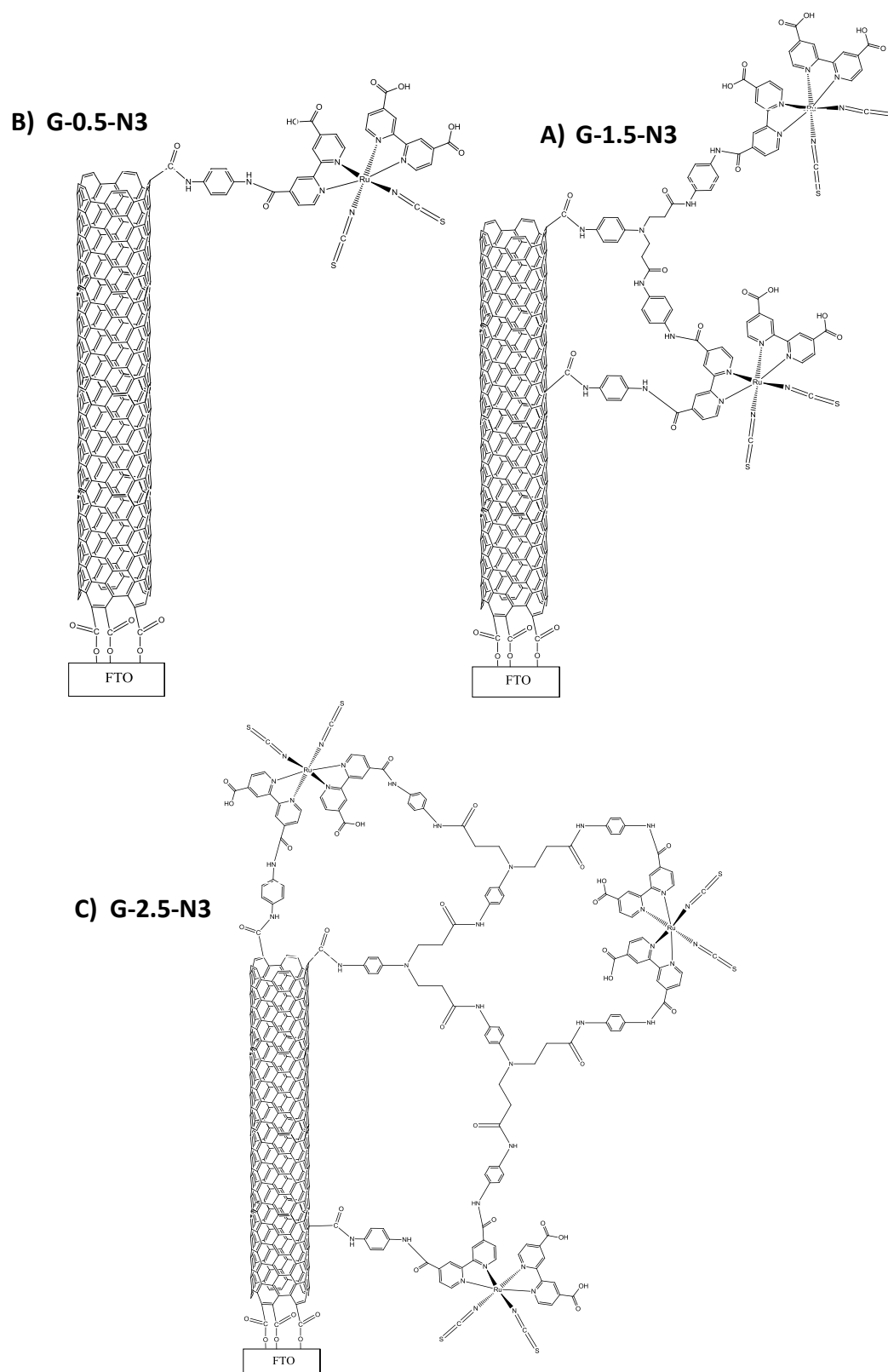


Figure 4.19: Schematic of N3 dye modification of successive generations of dendron.

#### 4.4.1 Electrochemical Characterisation of Dye Modified Dendron Functionalised SWCNT Arrays

Figure 4.20 compares the DPVs of the successive generations of dye modified dendron. As previously discussed the magnitude of the peak height is directly proportional to the concentration of the redox active species. In Figure 4.20 firstly we see that the potential of the peaks is close to that of the N3 in solution, but shifted to a slightly lower potential. This is expected as the attachment to a surface has been shown to shift the redox potential. The trend in peak current matches that of the dendron by itself, with G-0.5-N3 having  $\sim 30\text{nA}$  and then increasing to  $\sim 65\text{nA}$  for G-1.5-N3 followed by a large drop to G-2.5-N3. The initial increase when going from G-0.5 to G-1.5 is expected when looking at the schematic in Figure 4.19, which shows that the number of dye attachment points has doubled. The decrease following the initial increase is believed to be due to the size and steric hindrance of the G-2.5-N3 system leading to collisions between neighbouring dendrons. This combined with the increased flexibility of the longer dendron generations may indeed lead to multiple attachments to each dye molecule, instead of an increased concentration of the dye. This is supported by the trend in electron transfer rate as discussed later. Also in Figure 4.20 we see that the G-0.5-N3 has a second peak present at approximately 500mV, this corresponds to the PDA. This peak at 500mV is not seen in the later generations (G-1.5-N3 and G-2.5-N3) and this is because as the unreacted amine groups are reacted with the carboxylic acid on the dye and form amide bonds this peak disappears. This indicates that for the G-0.5-N3 sample that there is an incomplete dye attachment as there is signal from the unreacted amine groups still present, however when progressing to G-1.5-N3 the dye signal increases and no signal is detected from the amine, indicating complete dye coverage.

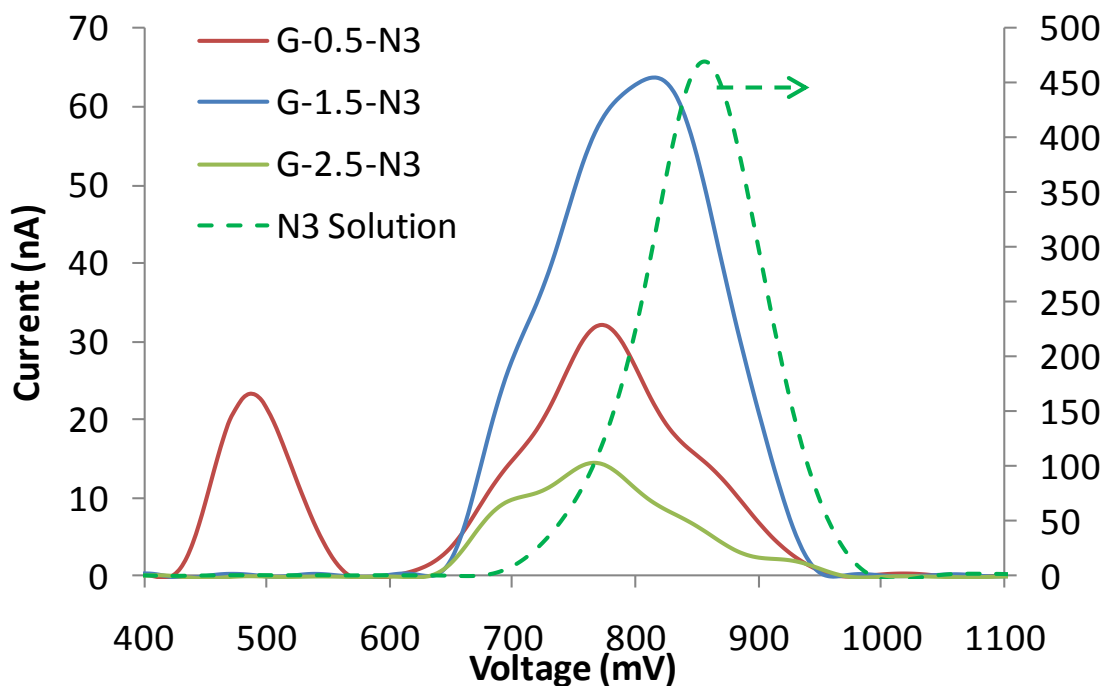
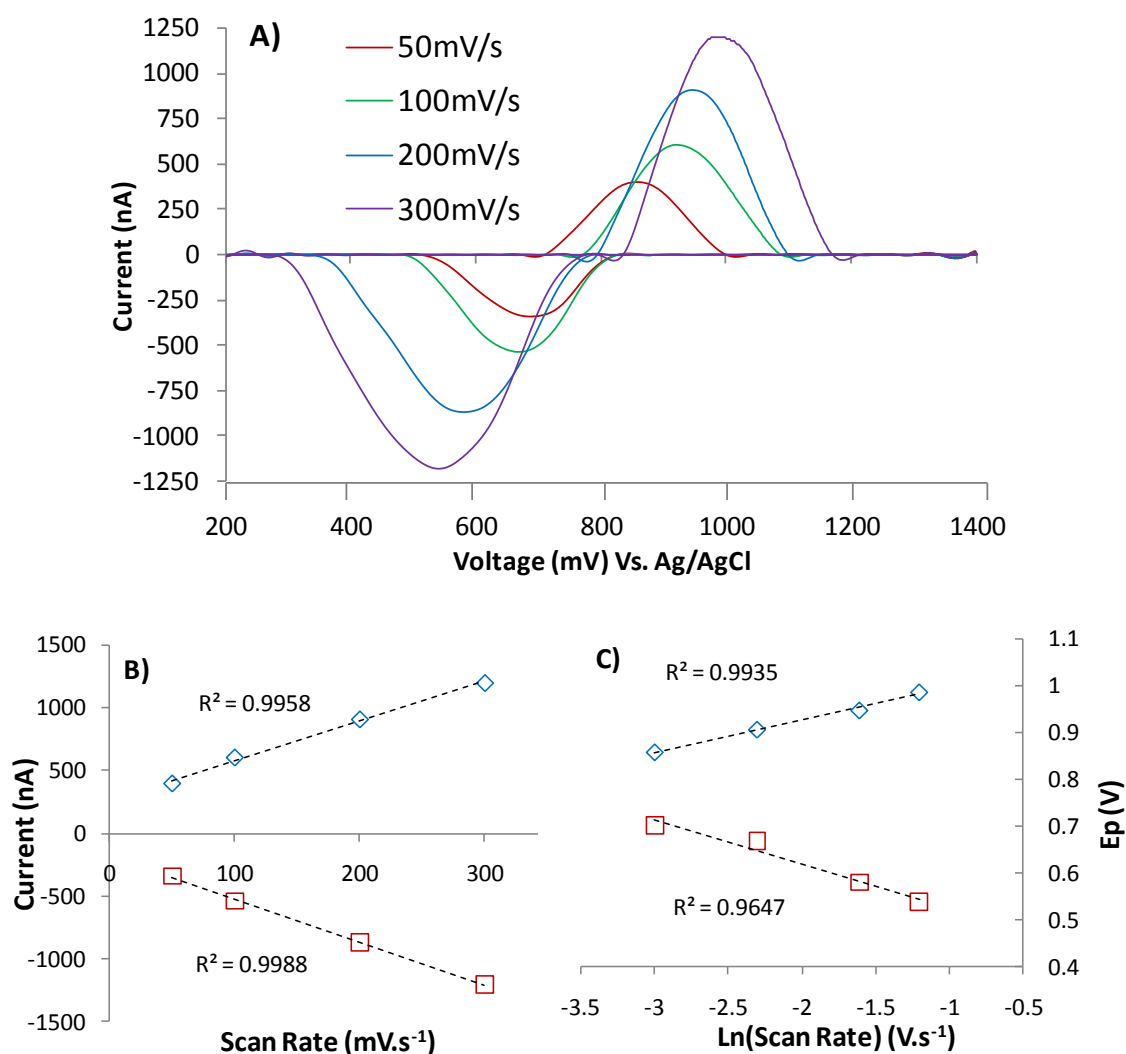


Figure 4.20: DPV comparison of different generations of N3 modified dendrons. Dashed line is DPV for N3 in solution.

Cyclic voltammetry was also used to analyse the dye modified dendron arrays and the successive voltammograms with increasing scan rate can be seen in Figure 4.21A. As was carried out previously, CV can be used to verify that the redox active species is surface bound by fitting a linear trend line to the plot of peak current versus scan rate, and this can be seen in Figure 4.21B for the G-1.5-N3 modified surface. The linear relationship between peak voltage and the natural log of scan rate, seen in Figure 4.21C, can then be used to determine the electron transfer coefficient of  $0.257s^{-1}$ . To support this method of calculating the  $k_s$  value the built-in modelling and simulation package from the Autolab software was also used on the DPV data by fitting a model to the raw data. To verify the validity of this method the same model was also applied to the G-0.5-N3 and G-1.5-N3 samples and this produced identical numbers as was calculated from the CV data. This indicates that the number produced by the simulation can be justifiably compared to the value calculated from the CV data.



**Figure 4.21: Background subtracted cyclic voltammograms with increasing scan rate for G-1.5-N3 modified substrate. (A) Plot of peak current versus scan rate from CV plots. (B) Plot of peak voltage versus the natural log of scan rate. (C)**

Electron transfer properties were then calculated for each of the modification schemes and the resultant dye concentration and transfer coefficients are shown in Table 4.2. The concentration and  $k_s$  values for the EDA bound N3, from Chapter 4.1.1 are also provided for comparison. The higher concentration N3 dye in the EDA-N3 system compared to the PDA-N3 (G-0.5-N3) is attributed to the initial cross linker functionalisation. The EDA functionalised SWCNT array was created by submerging the SWCNT array into a neat solution of EDA whilst the PDA-N3 array was created by submerging the SWCNT array into 0.1M PDA in methanol. These much more dilute conditions combined with the decreased reactivity of the amine when attached to the phenyl ring will cause less of the PDA to attach to the SWCNT. This lower number of

amine cross-linker attachments will decrease the available attachment points for the N3 dye in the successive functionalisation and cause a lower surface concentration of N3 dye. Interestingly, the  $k_s$  value for the EDA linked N3 is  $1.48\text{s}^{-1}$  whilst for the  $\pi$ -substituted PDA attached N3 it is only  $0.199\text{s}^{-1}$ , a factor of 7.5 lower. The large difference in transfer rate is attributed to the increased concentration of EDA cross linkers on the surface, which will increase the chances of multiple attachments to individual dye molecules. These multiple attachment sites will then increase the rate at which electrons can be moved from the dye to the substrate.

Progressing from the G-0.5-N3 to the G-1.5-N3 surfaces there is an increase in dye concentration, this is as expected when looking at the schematic in Figure 4.19 which shows that as the dendron increases in size the number of dye attachment sites is increasing. This is followed by a decrease for the G-2.5-N3 surface and this trend matches very closely that seen in the DPV data in Figure 4.20. The decrease is due to the increasing steric bulk of the dendron, upon reaching G-2.5 there are reactions between neighbouring dendrons and bundles of SWCNT that reduce the available attachment sites. In either case, the net effect is a reduction in the available amine sites for reaction with the N3 dye. Also, as a dye molecule attaches there is an increased chance of multiple cross-linker attachments to a single dye molecule, effectively reducing the available sites for other molecules but also increasing the transfer rate. This increase in transfer rate is exactly what is observed. Despite the decreasing concentration, the transfer rate is increasing for successive generations, due to the increasing number of attachments to each dye molecule. As the concentration of the N3 dye on the G-2.5-N3 was below the detection limits for CV no concentration can be obtained and the DPV results were used to calculate the electron transfer rate.

**Table 4.2: Surface concentration and electron transfer coefficients of N3 dye for successive dendron generations.**

Sample	Surface Concentration (molecules.cm <sup>-2</sup> )	Electron Transfer Coefficient (s <sup>-1</sup> )
SWCNT-EDA-N3	2.00 x 10 <sup>16</sup>	1.48
G-0.5-N3	6.86 x 10 <sup>12</sup>	0.199
G-1.5-N3	1.98 x 10 <sup>13</sup>	0.257
G-2.5-N3	Below Detection Limits for CV	0.316*

\* This value was calculated using the Autolab fitting and simulation software

EIS was also used to investigate and compare the behaviour of the unmodified and dye functionalised dendrons once constructed into complete electrochemical solar cells. Figure 4.22 shows both the Bode and Nyquist plots for the unmodified G-1.5 and the dye functionalised G-1.5-N3 cells. In the Bode plot there a distinct change in the N3 modified sample when compared to the unmodified G-1.5 for the phase observed at ~1000Hz (Log (1000) = 3). The Nyquist plot shows a significant reduction, approximately 50%, in impedance for the dye modified dendron. This decreased impedance is the reason for the increased power output seen later and indicates that the resistance at the electrolyte-nanotube interface has decreased significantly with dye attachment. This is because under illumination the flow of electrons and holes has become easier due to an increased tendency for charge separation, caused by the dye functionalisation.

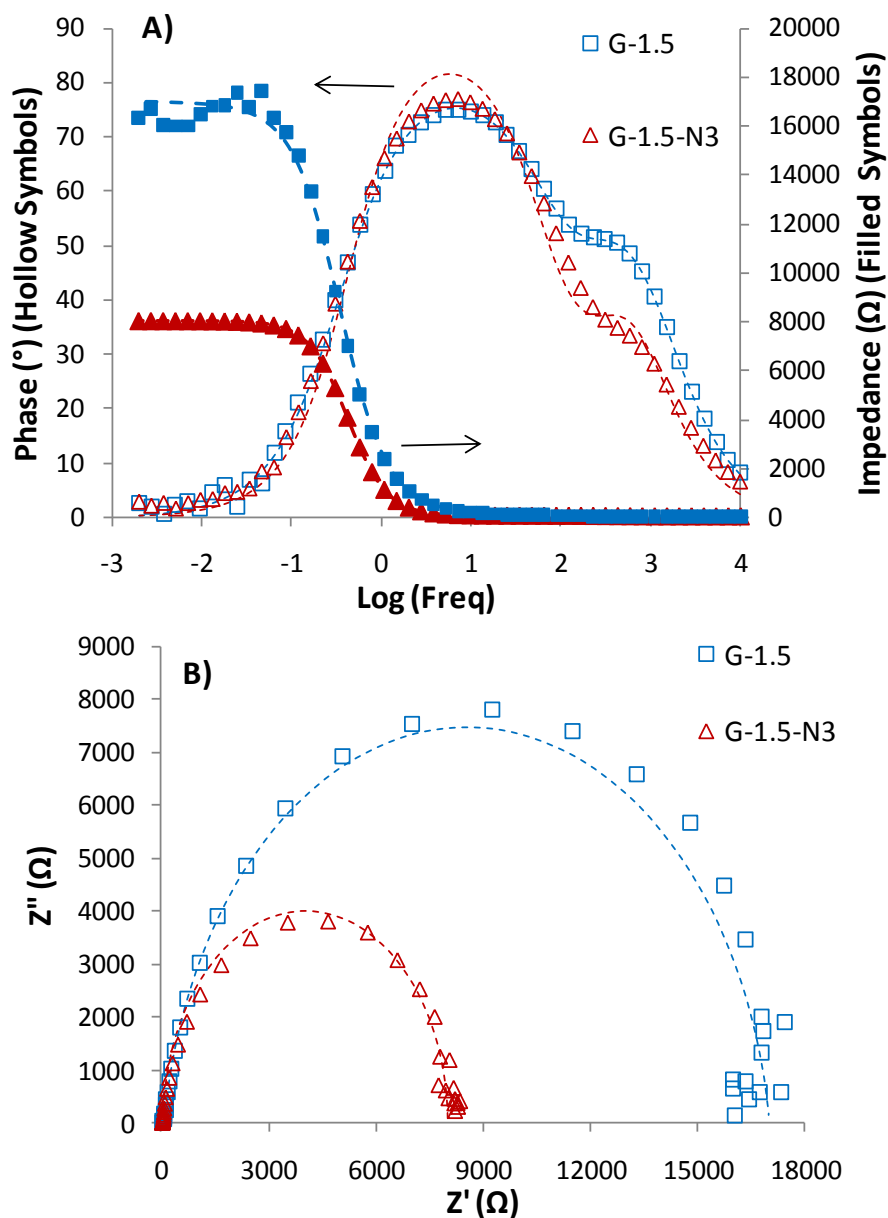


**Figure 4.22: Bode (A) and Nyquist (B) plots for G-1.5 and G-1.5-N3 electrochemical solar cells under illumination. Dashed line represents fit from an equivalent circuit diagram.**

After fitting of the equivalent circuit the respective resistances and capacitances of each of the electrode interfaces can be analysed individually and this is shown in Table 4.3. R1 represents the sheet resistance of the FTO glass so we would expect this value to be similar for each sample. R2 and R3 represent the interface between active elements of the cell, the dendrons and nanotubes, and the iodide/tri-iodide electrolyte. In the case of the dye modified dendron both of these resistance values are approximately 50% of the unmodified value, indicating a significant increase in flow of current. CPE1 represents the capacitance within the FTO-nanotube interface

and this is seen to have similar values for both samples again as would be expected, CPE2 however is 60% larger for the dye modified system again this is due to the increased charge separation properties of the dye in conjunction with the dendrons. This trend of decreased resistance and increased capacitance would be expected to produce significant overall efficiency increases for the dye modified system over the unmodified system, and indeed this is realised in the photoresponse data.

**Table 4.3: Summary of resistance and capacitance values produced by fitting an equivalent circuit model to the data shown in Figure 4.22.**

Sample	R1 ( $\Omega$ )	R2 ( $\Omega$ )	CPE1 ( $\mu\text{F}$ )	R3 ( $\text{k}\Omega$ )	CPE2 ( $\mu\text{F}$ )
G-1.5	$20.44 \pm 0.33$	$53.7 \pm 4.01$	$18.6 \pm 4.05$	$16.96 \pm 0.13$	$28.75 \pm 0.44$
G-1.5-N3	$17.05 \pm 0.52$	$26.36 \pm 1.87$	$17.35 \pm 1.54$	$7.98 \pm 0.15$	$46.9 \pm 0.96$

#### 4.4.2 Photovoltaic Properties of Dye Modified Dendron Functionalised SWCNT Arrays

Upon construction into complete electrochemical solar cells photovoltaic testing was undertaken on the dendron-N3 modified electrodes. Figure 4.23A shows the comparison of the photoresponse between the unmodified G-1.5 dendron and the G-1.5-N3 sample, which from electrochemistry was shown to have the highest concentration of N3 dye. Clearly the attachment of the dye has markedly increased the photocurrent, by ~50%, with little difference in voltage. This differs from the dye attached directly to the SWCNT seen in section 4.1.2 which showed an increase in photocurrent coupled with a decrease in voltage. In the case of the dendron-N3 modified samples the increased photocurrent is attributed to the presence of the dye whilst the superior charge separating abilities of the PAMAM-like dendron can maintain the voltage produced. Figure 4.23B compares the J-V curves for successive N3 modified dendrons showing an initial increase in both current and voltage when progressing from G-0.5 to G-1.5 followed by a large decrease for G-2.5-N3. The G-1.5-N3 also has the highest fill factor, or curved trace, indicating that the back reaction resistance has increased. A similar effect was observed for the unmodified dendrons,

whereby there is an initial increase in performance followed by a decrease. This was also seen in the previous section where the electrochemistry showed that the dye concentration was at a maximum at G-1.5-N3. The decrease after G-1.5 is attributed to steric hindrance of the large dendron molecule lowering the number of attachment sites and the collision of neighbouring dendrons.

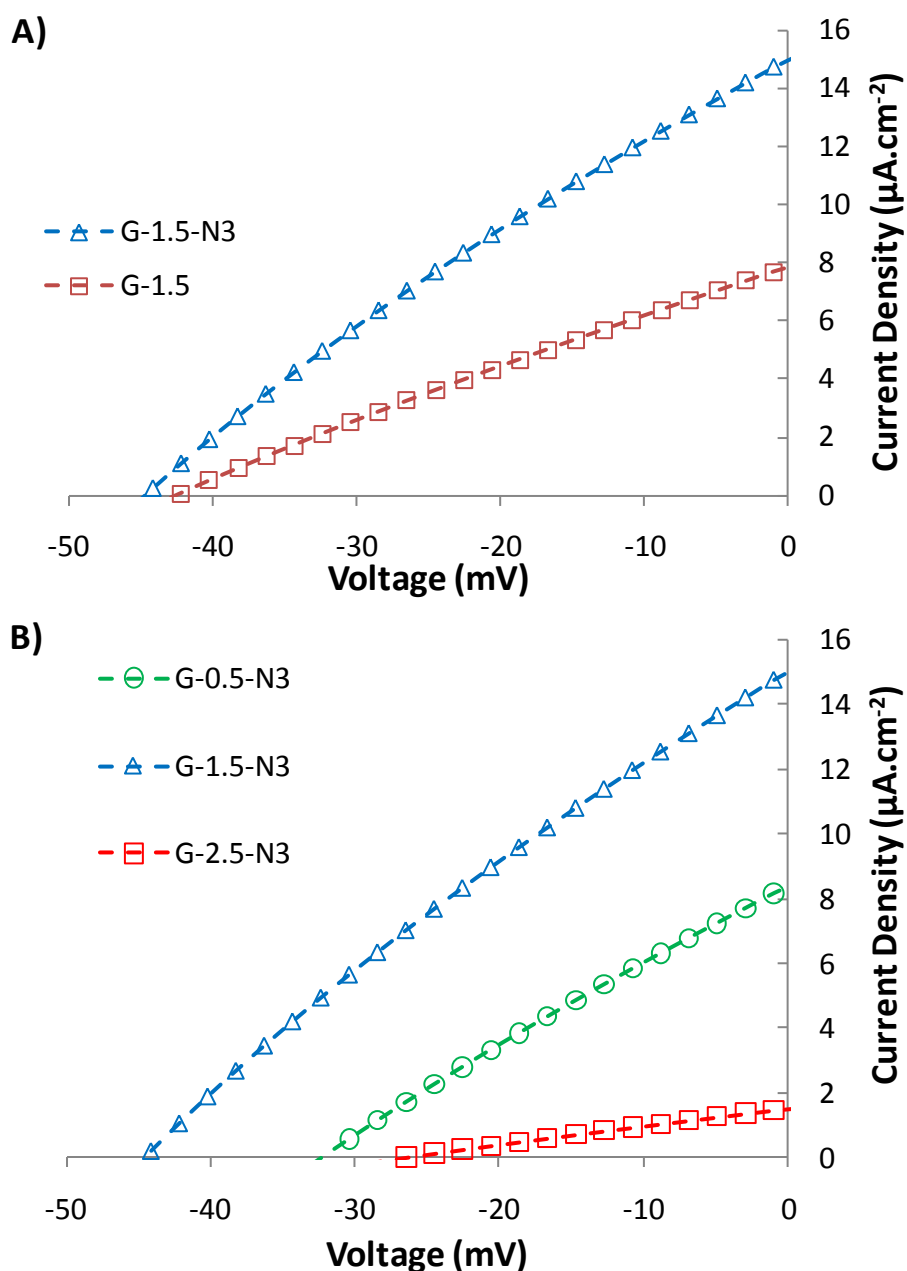


**Figure 4.23:** Comparison of J-V curves for G-1.5 and G-1.5-N3 modified SWCNT array. (A) J-V curves for successive generations of N3 modified dendrons. (B) Light intensity is  $100\text{mW}\cdot\text{cm}^{-2}$ .

Figure 4.24 compares the trend between the DPV responses of the dendron-N3 functionalisation, where DPV is directly proportional to the dye concentration, and the

produced photocurrent when constructed into a final operational device. There is a clear correlation between the two, as would be expected. When the dye surface concentration is at its maximum at G-1.5-N3 the photocurrent is also at its maximum. This trend matches what was observed for the unmodified dendrons, where a maximum occurred at G-2.0 followed by a decrease.

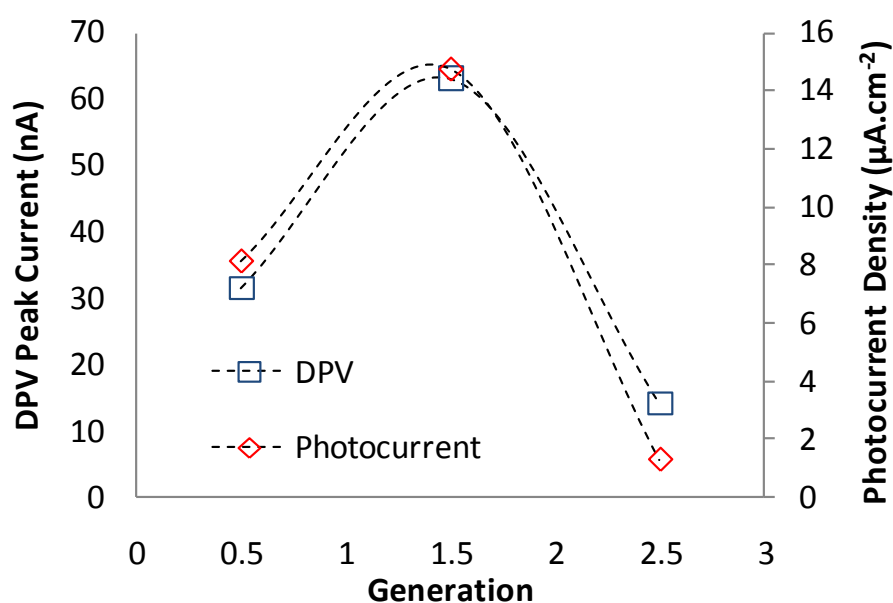


Figure 4.24: Trend for DPV peak current and photocurrent for N3 modified dendrons.

Table 4.4 summarises the photoresponse of each of the N3 modified dendron surfaces as well as the EDA-N3 surface for comparison. Although the current is higher for the EDA-N3 sample the resultant drop in voltage lowers the overall power output, whilst the G-1.5-N3 system has an increased photocurrent as well as high voltage, providing the overall highest output power of  $195\text{nW}\cdot\text{cm}^{-2}$ .

Table 4.4: Photocurrent, photovoltage and total power for N3 modified surfaces.

Sample	Photocurrent ( $\mu\text{A}\cdot\text{cm}^{-2}$ )	Photovoltage (mV)	Power ( $\text{nW}\cdot\text{cm}^{-2}$ )
SWCNT-EDA-N3	16.5	25.7	127.22
G-0.5-N3	8.12	34.31	83.58
G-1.5-N3	14.75	44.12	195.23
G-2.5-N3	1.27	30.39	11.58

## 4.5 Chapter Conclusions

In this chapter it has been shown how arrays of SWCNTs can be chemically modified with redox active molecules. The attached molecules have applications in electrochemical sensors due to the rapid transfer of electrons through the nanotubes and the increased surface areas provided by the vertically aligned arrays. These redox active molecules can also be photoresponsive and this provides applications in photovoltaics. The presence of a ruthenium based dye, N3, was verified by electrochemistry and the surface concentration was found to be at a maximum ( $2 \times 10^{16}$  molecules.cm<sup>-2</sup>) for 2 hours of SWCNT attachment. The covalent attachment of this N3 dye to the nanotube array was shown to provide an increased photocurrent density over the unmodified SWCNT array, but this was accompanied by a decrease in voltage. The attachment of the analogous porphyrin, RuTPP, which was also verified by electrochemistry and produced both a decreased photocurrent and voltage due to the mismatch in energy levels with the electrolyte used. The growth of PAMAM-type dendrons from the sidewalls and end groups of the SWCNTs was found to produce an increased photoresponse of ~60% for the 2<sup>nd</sup> generation dendron. These dendrons were then modified with the N3 dye and it was found that this provided an increased photocurrent but maintained a high voltage. The maximum dye concentration occurred at generation 1.5. This work shows how versatile SWCNT arrays can be as scaffold for further chemical modification, be it for photovoltaic or any range of electrochemical application.

---

# **5. Growth of Carbon Nanotubes for Photovoltaic Devices**

---

## 5.0 Introduction

The results presented in this thesis so far have been solely based on the use of purchased carbon nanotubes which were then chemically attached to surfaces and modified. However, as was discussed in Chapter 3, CNTs are able to produce a photocurrent that is dependent on the number of CNTs on the surface. Thus, increasing the number of nanotubes on the surface should be able to increase the efficiency of the fabricated devices. By growing CNT arrays directly onto a substrate a much higher nanotube density can be achieved, providing an obvious improvement to the established cell design. However, the chemical attachment of CNTs is believed to be a vital element of the solar performance as it allows for a much more efficient electron transport through the covalent bond as opposed to the physisorbed carbon to catalyst particle present in grown arrays. Arrays of carbon nanotubes were produced by both thermal and plasma-enhanced chemical vapour deposition and then characterised using XPS, Raman, electrochemistry and finally photovoltaic performance and the results compared to their chemically attached counterparts.

### 5.1 Thermal Chemical Vapour Deposition Growth of Carbon Nanotube Arrays on Silicon

A simple and easily up-scalable technique for producing a dense and highly aligned array of carbon nanotubes is thermal chemical vapour deposition (tCVD). tCVD has the ability to produce large amounts of CNTs with a high degree of control over their final properties by modification of experimental variables during their growth. As was discussed in section 1.2.2 the advantages of CVD over other nanotube production methods include its relative ease and low cost to produce nanotubes directly onto a substrate with a high degree of control over their properties. In this work arrays were produced on silicon wafers as they provide excellent thermal stability at the temperature required for growth as well as being chemically inert and electrically conductive.

### 5.1.1 Scanning Electron Microscopy of CVD Grown CNT Arrays

After tCVD was used to produce CNT arrays they were analysed using scanning electron microscopy (SEM). This allows for information about the alignment and density of the nanotubes as well as some insight into their nanostructure. Figure 5.1 shows the SEM images for several different magnifications and angles of the tCVD grown nanotube array. Figure 5.1A shows that there are large sections of high density CNTs that appear to be falling over in some sections, Figure 5.1B shows that the CNT is made up of a vertically aligned tangled web like structure with a height of approximately 20 $\mu\text{m}$ . Figure 5.1D shows the interface between where the iron catalyst particles have been deposited and areas of no catalyst, clearly there is a well defined interface showing a thick mat of CNTs on one side and none on the bare silicon. Also from the SEM we can see that the nanotubes are most likely multi-walled due to the apparent diameter of approximately 50nm, much thicker than the 1-2nm seen in single-walled tubes.

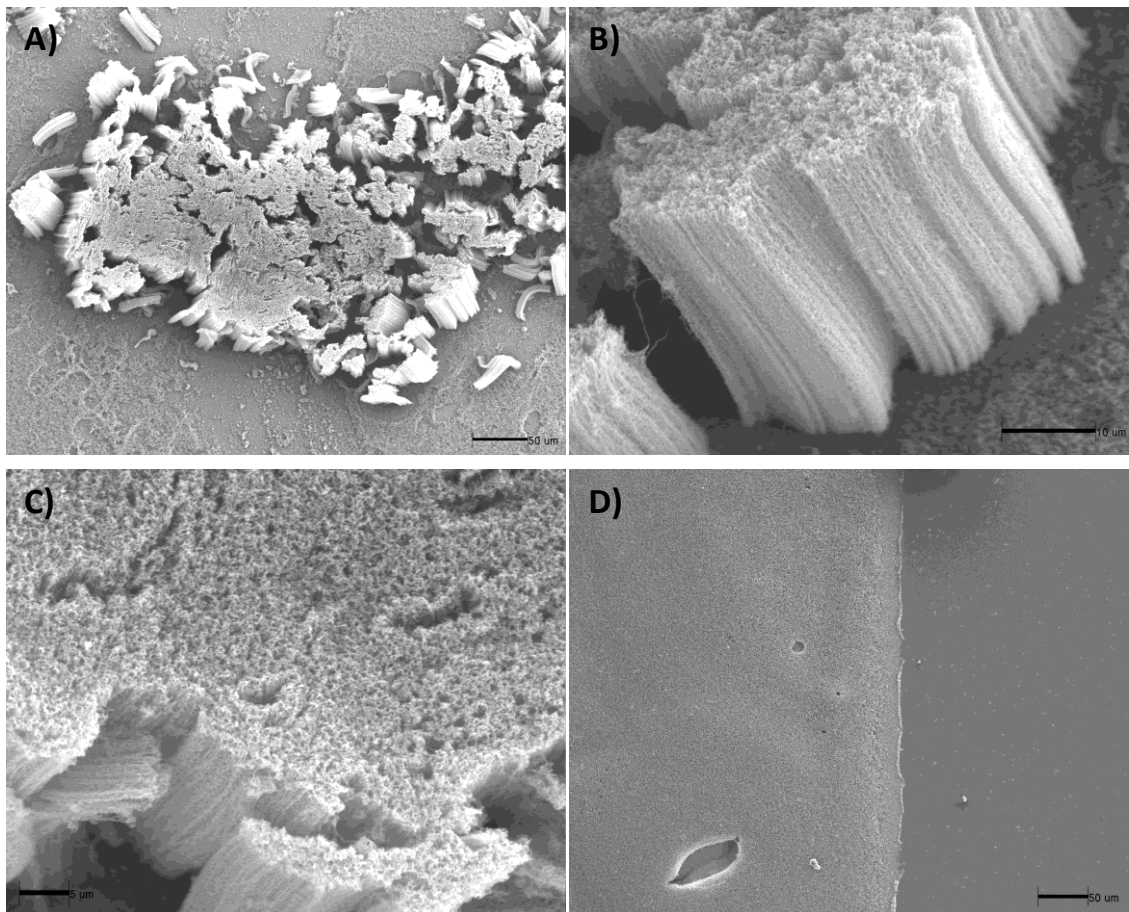


Figure 5.1: SEM images of tCVD grown CNT array on silicon.

By modifying the growth parameters the effect on the resultant CNT array can be observed. Figure 5.2 shows the resultant arrays produced by replacing the iron catalyst with nickel, which has previously been shown to be a nanotube growth catalyst.<sup>181-183</sup> Clearly the produced nanotubes are highly disordered lacking the density and alignment seen when using the iron catalyst. This disorder has been observed previously in the literature<sup>183</sup> and to achieve alignment etching of the nickel particles to form uniform crystal facets was found to be required.<sup>181</sup> Instead of the aligned array seen using the iron catalyst long highly curved and coil like structures are formed on the surface, this lack of density and alignment would be detrimental for any further applications and because of this iron was chosen as the catalyst for all further experiments.

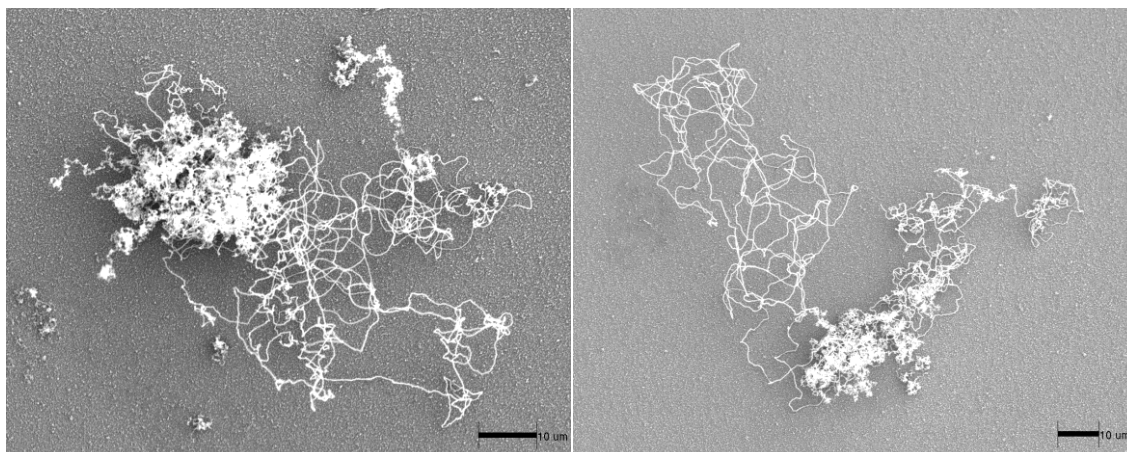
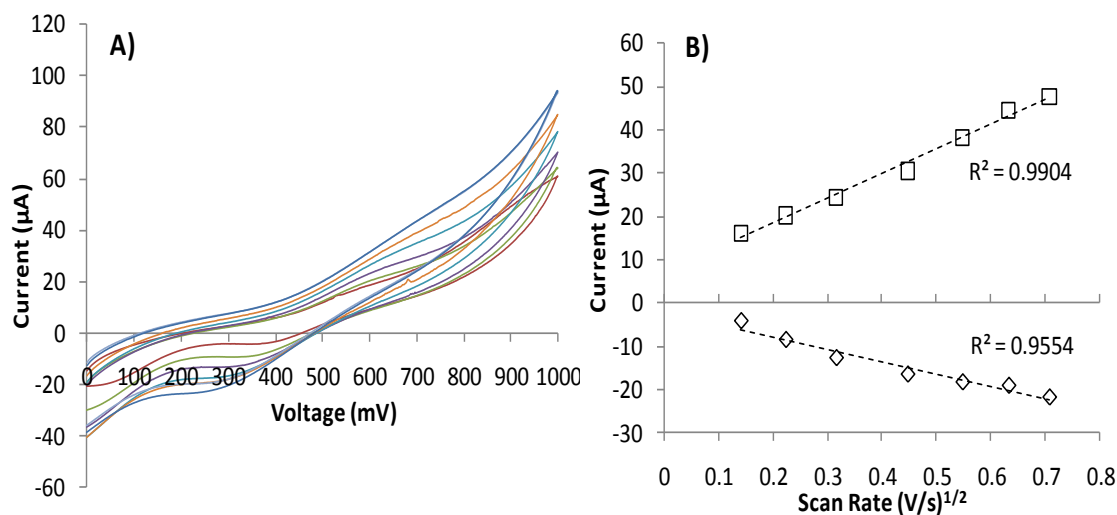


Figure 5.2: tCVD CNTs grown with a nickel catalyst.

### 5.1.2 Electrochemical Characterisation of CVD Grown CNT Arrays

As was done previously for the other CNT electrodes the electron transfer characteristics were analysed using electrochemistry. To act as a point of comparison the electron transfer properties of the bare unmodified silicon wafer was determined. The CV traces with increasing scan rates is shown in Figure 5.3A, whilst the relationship between peak height and the square root of the scan rate is shown in Figure 5.3B. Noticeably the peak heights are quite low and this is to be expected because the silicon wafer forms a passivating native oxide ( $\text{SiO}_2$ ), which is highly insulating.



**Figure 5.3:** CV plots for ferrocene in solution with bare silicon working electrode. (A) Graph showing relationship between peak current and square root of scan rate. (B)

The CV plots for the tCVD modified silicon surface are seen in Figure 5.4A, along with the linear dependence on the square root of scan rate in Figure 5.4B. This time the peaks are much higher immediately suggesting the electrode performance has increased. This increased conductivity is due to two factors; firstly the passivating  $\text{SiO}_2$  layer is thinned by the reducing atmosphere in the pre-treatment step, and secondly the greatly increased active surface area produced by the highly conductive CNT array.

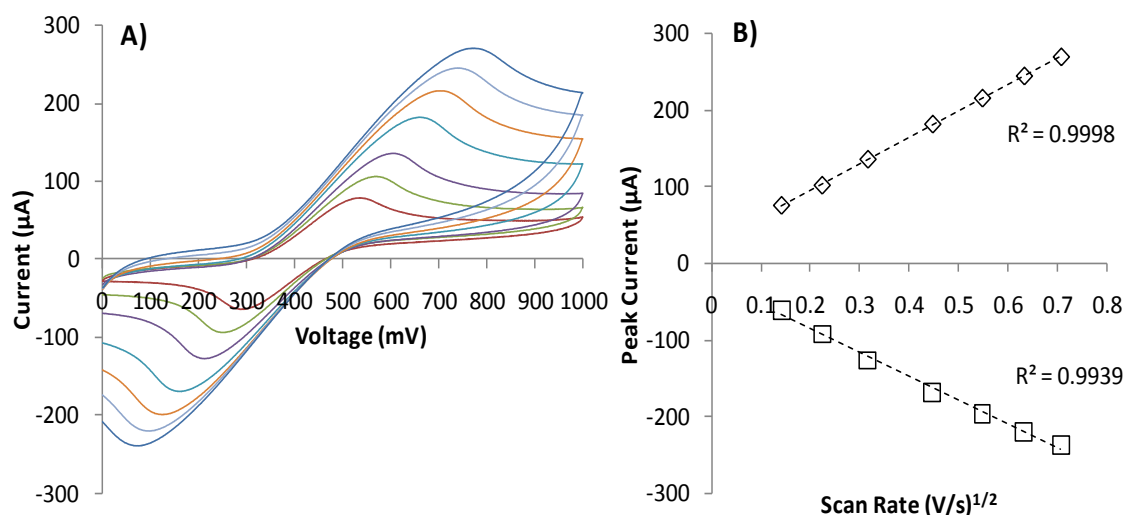


**Figure 5.4:** CV plots for ferrocene in solution with tCVD functionalised working electrode. (A) Graph showing relationship between peak current and square root of scan rate. (B)

Figure 5.5 allows for a direct comparison of the CV traces at the same scan rate ( $100\text{mV}\cdot\text{s}^{-1}$ ) between the bare silicon and the tCVD grown MWCNT surface. As mentioned the tCVD modification provides a vast improvement over the insulating silicon.

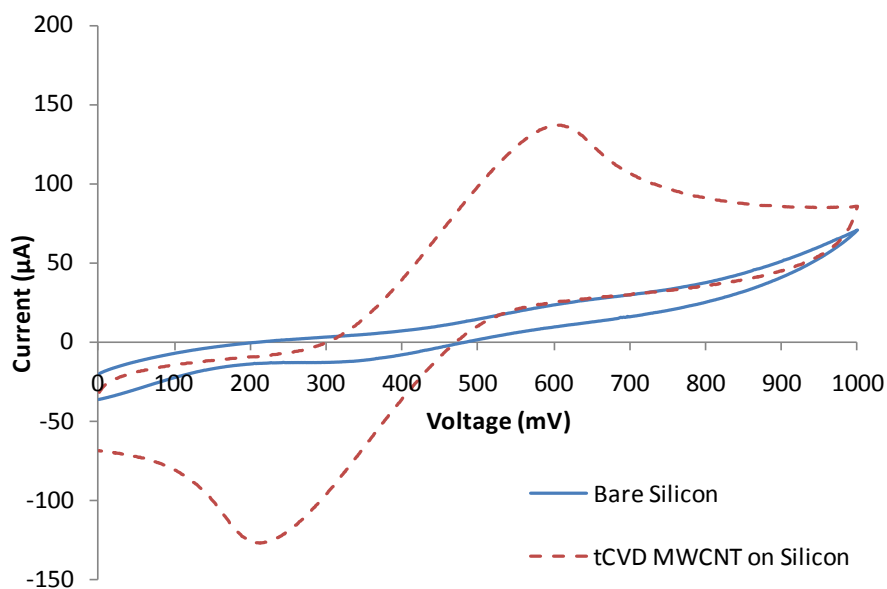


**Figure 5.5: Comparison of CV plots for bare silicon and tCVD grown CNT on silicon at an identical scan rate ( $100\text{mV}\cdot\text{s}^{-1}$ ).**

The heterogeneous electron transfer co-efficient can then be calculated from the plot of peak position versus the natural log of scan rate, shown in Figure 5.6. The calculated  $k_s$  value is  $0.088 \pm 0.01\text{cm}\cdot\text{s}^{-1}$  and this is slightly higher than the transfer co-efficient calculated for the chemically attached SWCNT and MWCNTs at  $0.071 \pm 0.014\text{cm}\cdot\text{s}^{-1}$  and  $0.076 \pm 0.014\text{cm}\cdot\text{s}^{-1}$  respectively. This is most likely due to the greatly increased surface area, with an array height of  $\sim 20\mu\text{m}$  for the grown MWCNT and  $0.1\text{-}0.5\mu\text{m}$  for the chemically attached arrays. In fact due to the vast difference in array surface area, but comparable transfer co-efficient it can be said that the chemical attachment allows for much a more efficient electrode.

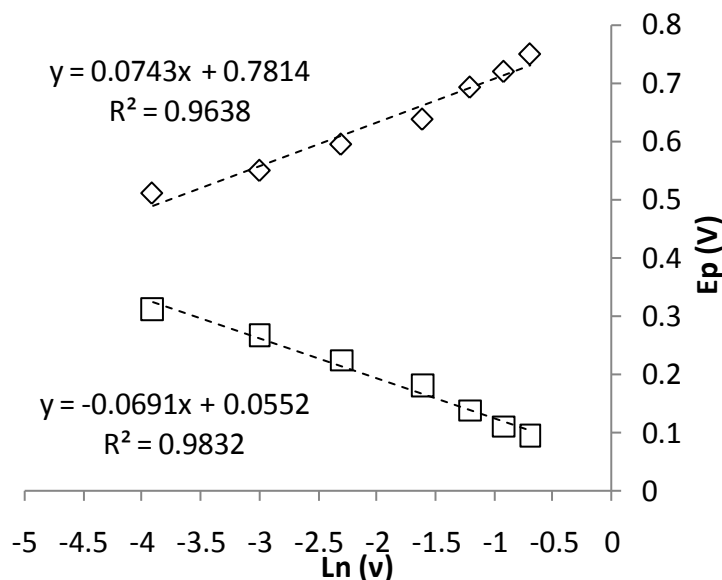


Figure 5.6: Plot of anodic and cathodic peak potential ( $E_p$ ) versus the natural logarithm of scan rate ( $v$ ) for the tCVD functionalised working electrode.

### 5.1.3 Raman Characterisation of CVD Grown CNT Arrays

To identify the produced CNT array as indeed MWCNT the Raman spectroscopy was used. As has been discussed previously the Raman spectrum of MWCNT would be expected to have a high D/G ratio, no RBM peak and no  $G^{+/-}$  peak splitting. The spectrum of the tCVD grown CNT array is compared to the purchased MWCNT in Figure 5.7. The D/G ratio is 1.2 and there is no RBM peak or splitting of the G band; all evidence of MWCNT. This is in agreement with the SEM that suggested the presence of large diameter MWCNT. Noticeably the G and D band peak width is larger for the grown MWCNT compared to the purchased tubes; this is caused by the wide distribution of nanotube diameters and presence of residual amorphous carbon produced by the CVD growth, whilst the purchased MWCNT tubes have been chemically treated prior to attachment on the surface reducing the amorphous carbon content and narrowing the distribution of diameters.

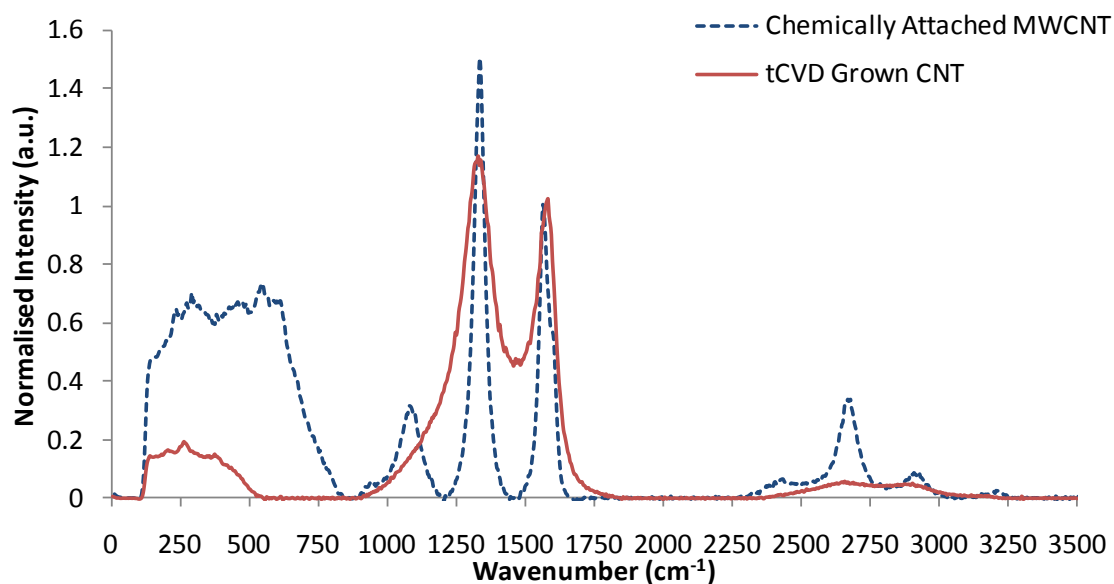
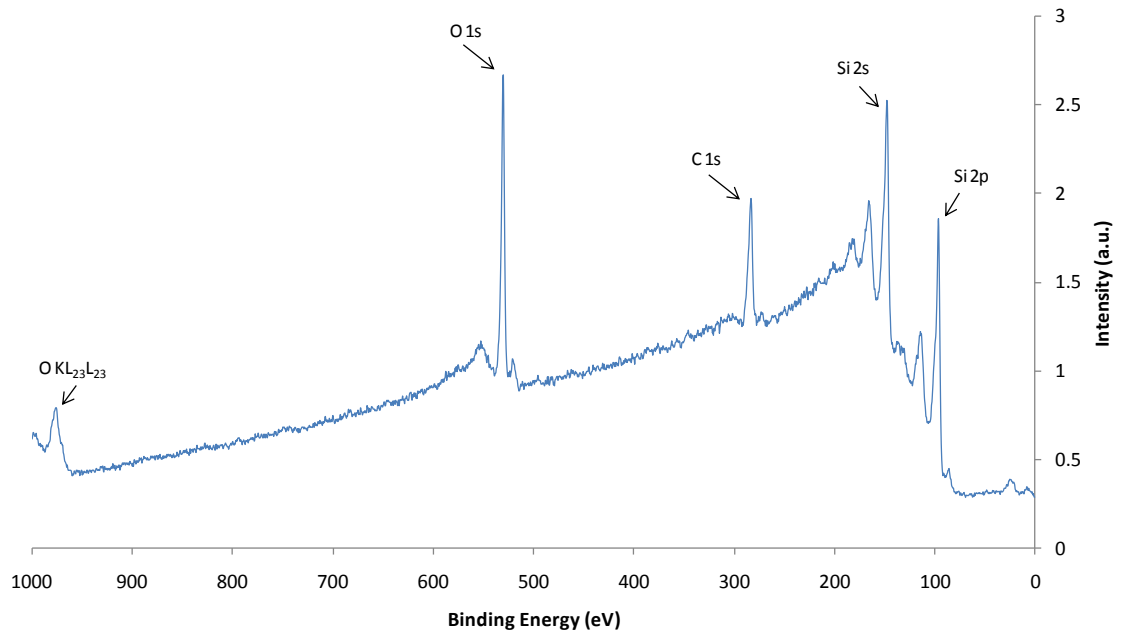


Figure 5.7: Comparison between tCVD grown SWCNT arrays and purchased MWCNT arrays chemically attached to FTO glass.

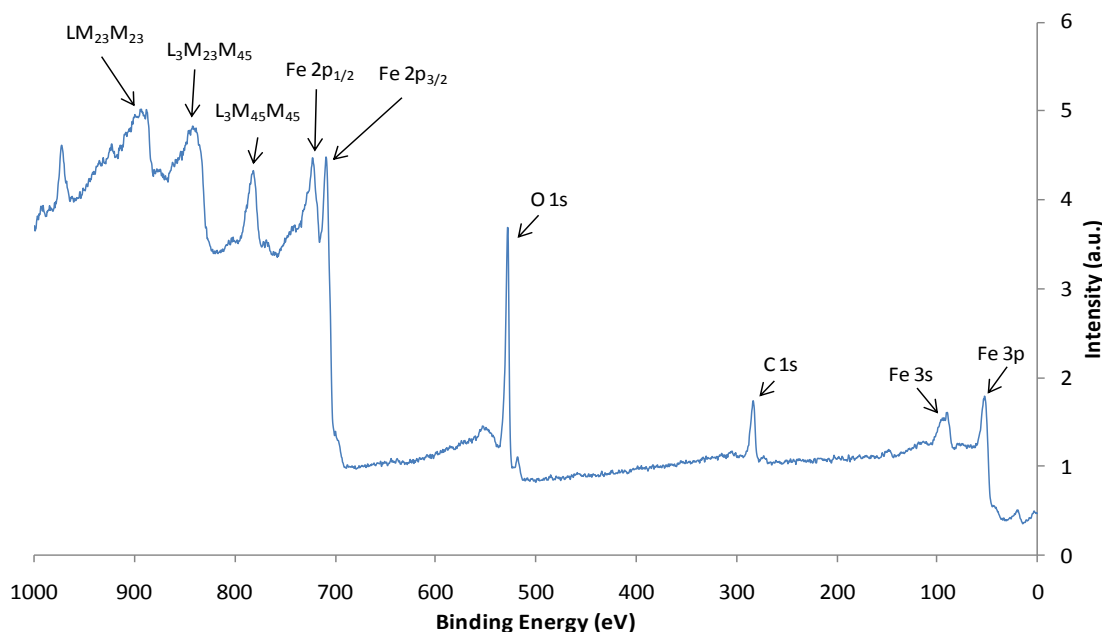
#### 5.1.4 XPS Characterisation of CVD Grown CNT Arrays

X-ray photoelectron spectroscopy was used to analyse the substrate surface during each step of growth. To act as a point of comparison an XPS spectrum was taken of the bare silicon and is shown in Figure 5.8. The most intense peaks have been labelled and these are the Si2p peaks, from the substrate, the oxygen O1s peak from the passivating SiO<sub>2</sub> layer present on the surface and finally a carbon C1s peak from adventitious or atmospheric carbon contaminants. These are all as expected and allow comparison with the spectra taken after each step.



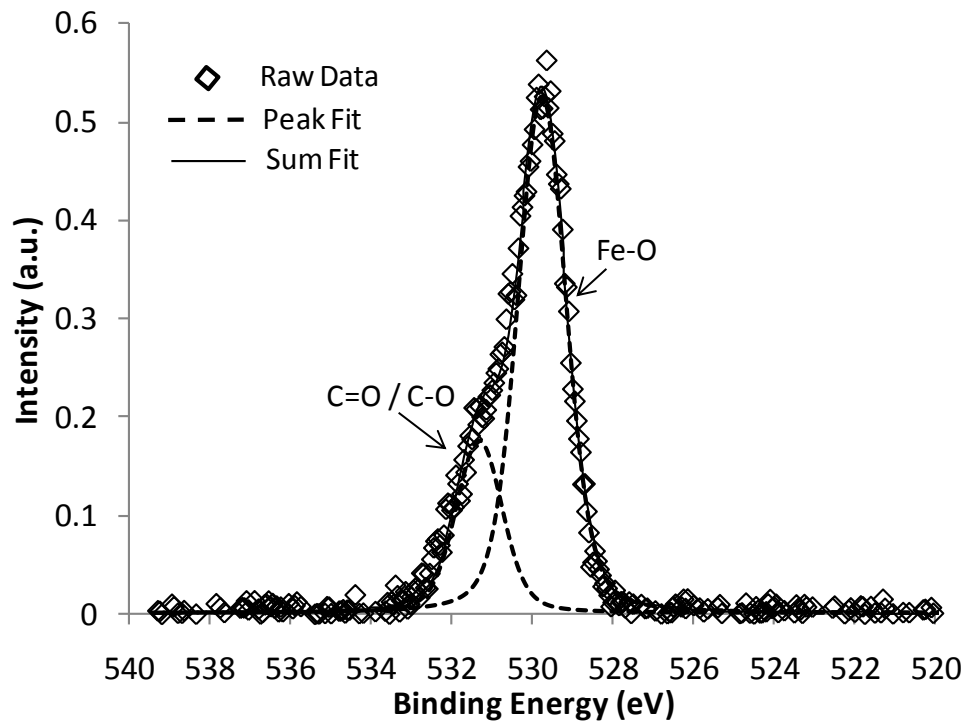
**Figure 5.8: XPS survey spectrum of bare silicon.**

After the bare silicon had been analysed the 5nm thick layer of iron was sputtered on and the sample analysed again, with the spectrum seen in Figure 5.9. This time the silicon peaks are not noticeable and instead, as would be expected, the most intense peaks are all from the iron. There is a series of peaks labelled  $L_xM_xM_x$  and these are caused by Auger electrons, instead of photoelectrons. Auger electrons are caused by an electron falling into a vacancy left behind by an emitted photoelectron releasing energy, this energy is then absorbed by a neighbouring electron which is emitted and detected. Interestingly though there is still a large oxygen peak present and some adventitious carbon and these are believed to be caused during the sample transfer from the sputter chamber to the XPS chamber which involves exposing the sample to atmospheric conditions for approximately 1 minute.



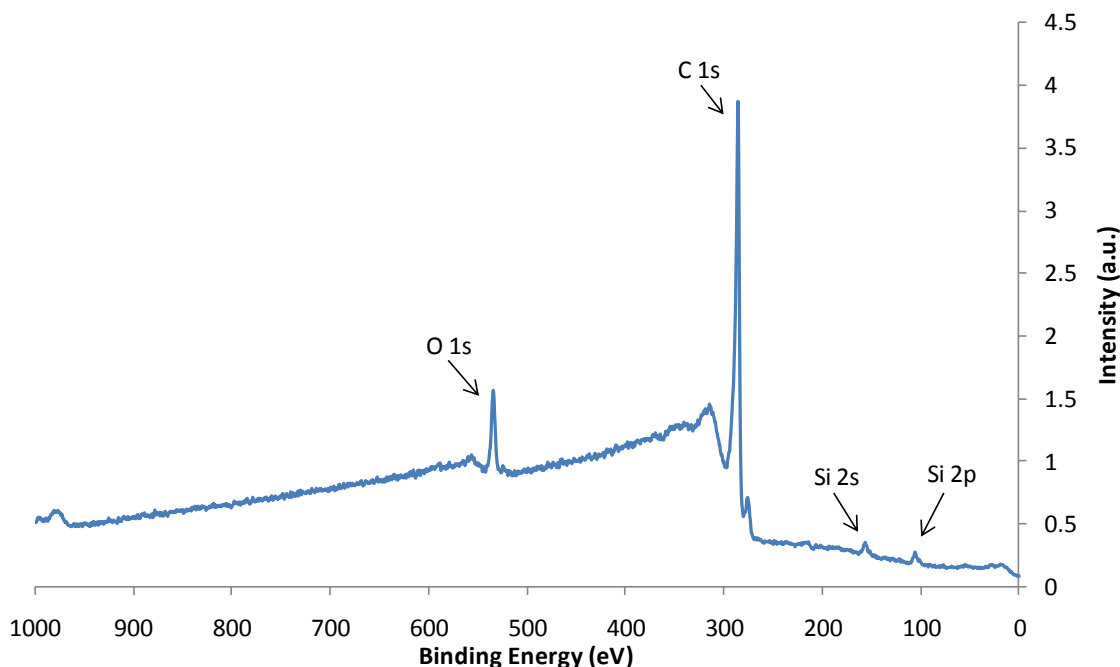
**Figure 5.9: XPS survey spectrum of silicon after 5nm iron deposition.**

To further investigate the oxygen peak a high resolution spectrum was taken of the O1s binding region, shown in Figure 5.10. The O1s peak is made up of two different contributions the most intense centred at 529.7eV is attributed to iron oxide (Fe-O)<sup>155</sup> whilst the lower intensity peak at 531.2eV is from carbon-oxygen groups within the adventitious carbon present on the surface. This indicates that surface contamination and oxidation of the iron catalyst layer happens very quickly and would suggest the need to maintain vacuum between production and analysis. The reducing hydrogen atmosphere during growth would be expected to produce metallic iron and thus the nanoparticles can still retain their catalytic properties.



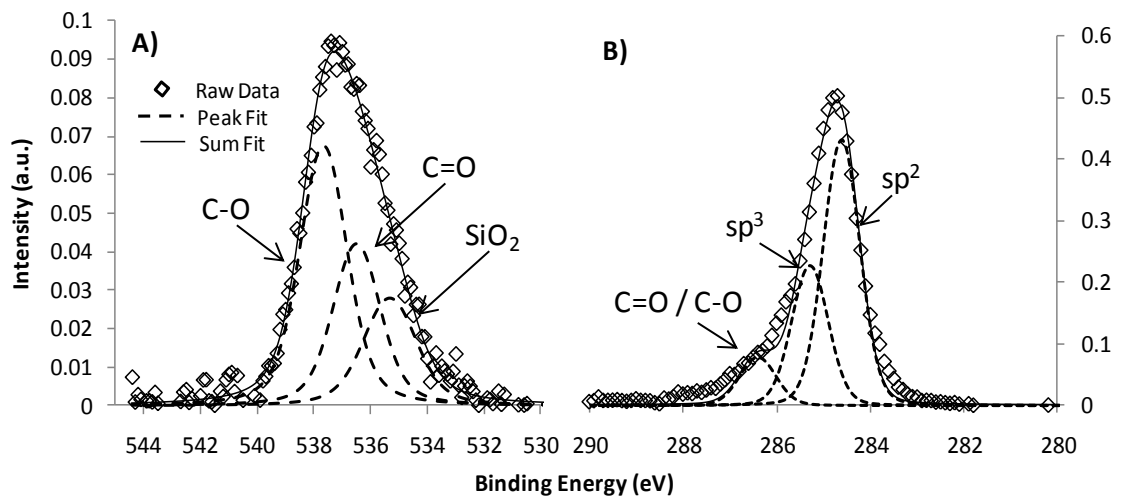
**Figure 5.10:** High resolution XPS spectrum of oxygen 1s binding region for silicon after iron catalyst layer deposition.

Figure 5.11 shows the XPS spectrum for the silicon surface after the chemical vapour deposition step has been completed. Immediately noticeable is the disappearance of the iron peaks. This is important because there is some debate about the location of the catalyst particle during CVD growth. If the so called ‘tip-growth’ occurred, that is the iron nanoparticle was on the end of the nanotube, then we would expect to still see some signal from the iron, but as we do not it can be ascertained that ‘base-growth’, or growth where the catalyst particle remains on the surface, has occurred. Clearly the predominant peak in the spectrum is the large carbon peak, but there is also a small amount of oxygen present as well as small silicon peaks. The presence of these silicon peaks suggests that the density of the nanotubes must not be complete and that some small areas of the underlying substrate may be exposed.



**Figure 5.11: Survey XPS spectrum of tCVD MWCNT surface.**

To investigate the chemical environment of both the oxygen and carbon high resolution XPS spectra were taken and peak deconvolution performed and this can be seen in Figure 5.12. The oxygen binding region, Figure 5.12A, is distinctly different from the previous XPS spectra of CNTs on surfaces due to the increased number of nanotubes providing increased signal intensity from the carbon-oxygen component. The most intense peak is located at 537.5eV followed by one at 536.2eV and finally 534.8eV, these are attributed to C-O, C=O and SiO<sub>2</sub> respectively. The carbon peak, shown in Figure 5.12B, also has three components with the most intense at 284.5eV from sp<sup>2</sup> carbon followed by 285.2eV for sp<sup>3</sup> carbon and finally 286.5eV for carbonyl and other carbon oxygen groups.<sup>156</sup> These match what would be expected for carbon nanotubes. The presence of the carboxylic acid groups on the nanotubes does not in this case come from acid treatment but instead from oxidation of defects sites during the growth process, made possible by the availability of water vapour during the growth.



**Figure 5.12:** High resolution XPS spectra of O1s binding region (A) and C1s binding region (B) for the tCVD MWCNT surface.

Figure 5.13 compares the XPS survey spectra for each step of the growth process. Firstly there is the bare silicon showing only the expected silicon peaks, then after iron deposition the silicon signal is completely buried and a layer of iron oxide is formed, finally after growth has occurred a large carbon signal with a minor oxygen component is achieved. The lack of any residual iron signal indicates that ‘base-growth’ is the predominant process occurring. Also the presence of oxygen indicates that some of the nanotubes side-walls are likely to have oxidised defect sites.

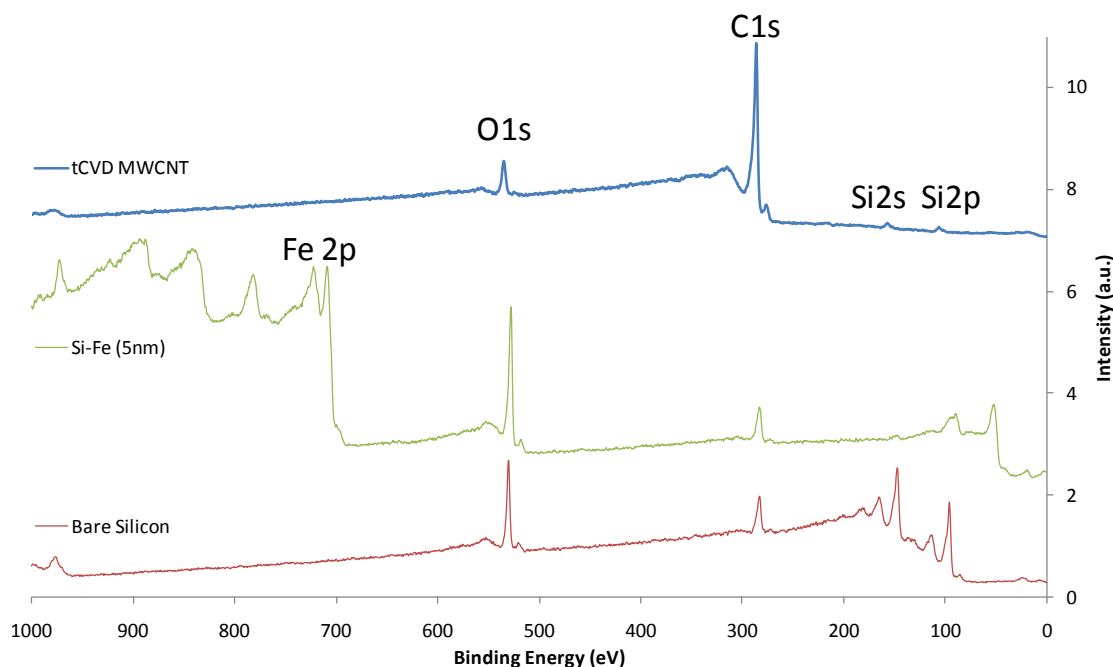


Figure 5.13: XPS spectra comparing each step of tCVD CNT growth.

### 5.1.5 Photovoltaic Properties of CVD Grown CNT Arrays

Figure 5.14 compares the J-V curves for the chemically attached MWCNT as discussed in Chapter 3.3 and the tCVD grown MWCNT. Immediately noticeable is the much lower response of the tCVD array, despite the SEM showing a much larger amount of MWCNTs on the surface. The maximum current produced by the tCVD MWCNT electrode is only  $0.8\mu\text{A}\cdot\text{cm}^{-2}$  and a voltage of 1.04mV to give a maximum power of only  $0.24\text{nW}\cdot\text{cm}^{-2}$ , this compares to  $92.96\text{nW}\cdot\text{cm}^{-2}$  for the chemically attached MWCNT. This large difference in photoresponse, despite the tCVD having considerably more nanotube present on the surface, is attributed to two factors. Firstly, the chemical attachment provides a much more efficient conduction pathway between the nanotubes and the underlying substrate and this will assist charge separation. Secondly the attached MWCNT have been oxidised during the attachment process introducing defects into their structure. These defects can begin to convert some nanotubes from metallic into semi-conductors. An important conclusion from this result is support for the idea that chemical attachment, despite having lower nanotube density, is a superior electrode modification. It also suggests that the semi-

conducting properties of CNTs are required to perform efficiently in photovoltaic devices as evidenced by superior photovoltaic performance and Raman spectroscopy.

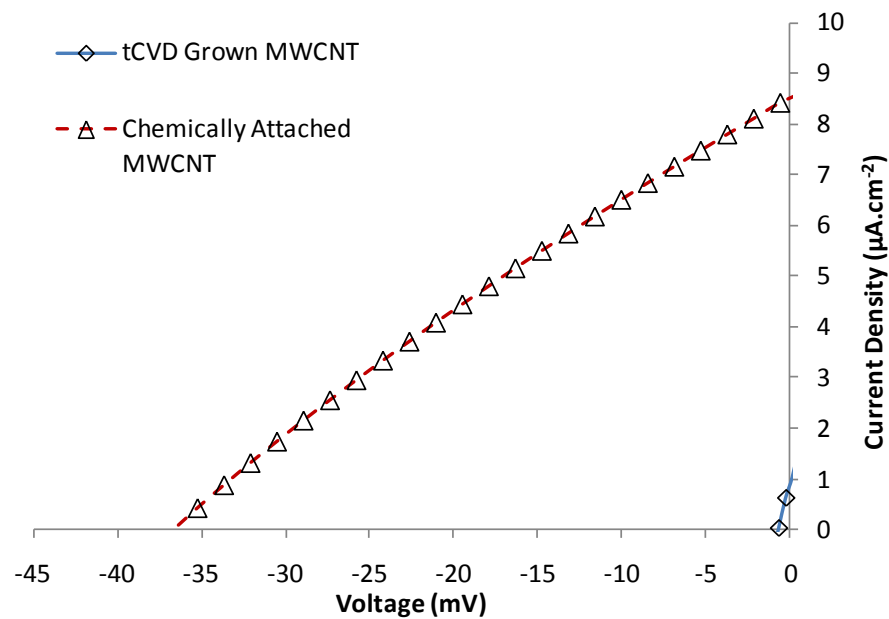


Figure 5.14: J-V curve for tCVD grown and chemically attached MWCNT. Light intensity  $100\text{mW.cm}^{-2}$ .

## 5.2 Thermal Chemical Vapour Deposition Growth of CNT Arrays on Indium Tin Oxide Coated Quartz

For applications in light harvesting the desire to grow carbon nanotubes on optically transparent substrate is of obvious advantage. However, typical optically transparent and conductive substrates such as FTO and ITO are thin coatings on soda lime glass, which lacks the thermal stability needed for CVD growth. Therefore a transparent, high thermal stability and conductive substrate had to be found and ITO coated quartz slides were chosen. The quartz allows for very high thermal stability, up to approximately  $1700^{\circ}\text{C}$ , whilst maintaining excellent transparency across a wide range of wavelengths.

### 5.2.1 Scanning Electron Microscopy of CVD Grown CNT on ITO Coated Quartz

As mentioned previously the quartz underlying substrate is known to have high thermal stability, however the ITO coating may not. To determine the effect of heating on the slides they were placed in a tube furnace under an inert atmosphere and

heated to 750°C and left for 10 minutes before leaving to cool to room temperature, after which they were checked for conductivity using a multimeter. The as received ITO slides have a conductivity of 8-12Ω/square and after heat treatment this rose to the MΩ range indicating conductivity had been negatively affected by the heating process. By analysing the heated and as received slides using SEM a distinct morphological change was noticed, seen in Figure 5.15, which show a featureless surface for the as received in Figure 5.15A whilst large domains separated by cracks are seen in Figure 5.15B after heating. This cracking is believed to be due to a difference in thermal expansion, although the ITO layer itself is not damaged by the heating process the quartz and the ITO have different rates of expansion and contraction during the heating and cooling cycles leading to stress on the thin ITO layer. Once separated into these discrete domains there is severely diminished electrical contact across the surface, leading to the increased resistance.

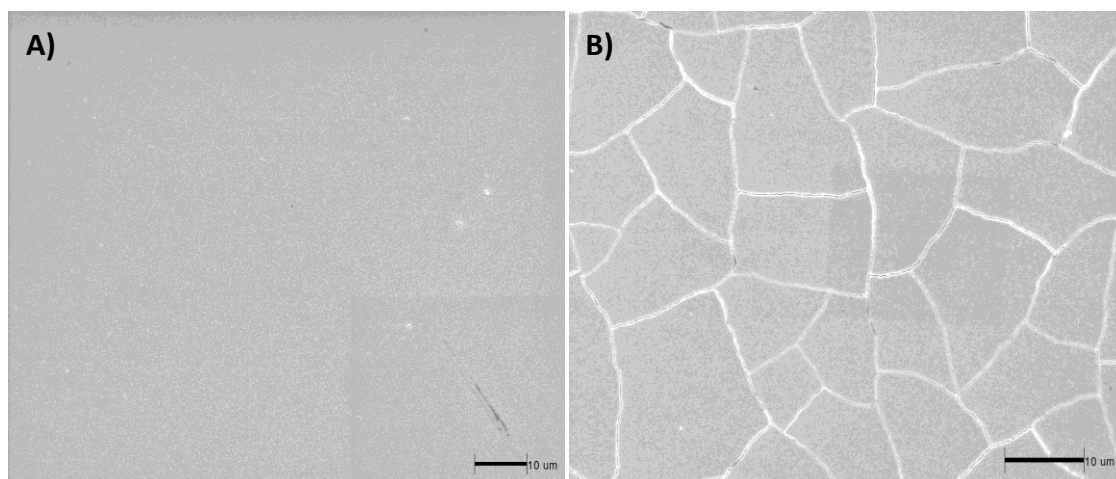


**Figure 5.15: SEM images of ITO coated quartz slides. A) As received and B) after 750°C for 10 mins.**

It was believed, however, that the presence of the iron layer coupled with a reduced rate of heating and cooling might make it possible to overcome this cracking effect and CVD growth was attempted using identical conditions as was used for the silicon substrate. The resulting surface was analysed under SEM and the image of the catalyst layer interface is shown in Figure 5.16. Immediately noticeable in Figure 5.16A, which shows the angled SEM image, is the presence of many spherical objects on the surface. In Figure 5.16B the increased magnification of a single sphere is shown, and the resultant structure is shown to be very uniform whilst the zoom of the sphere on

the catalyst side (Figure 5.16C) shows a similar sphere but this time covered in nanotube structures.

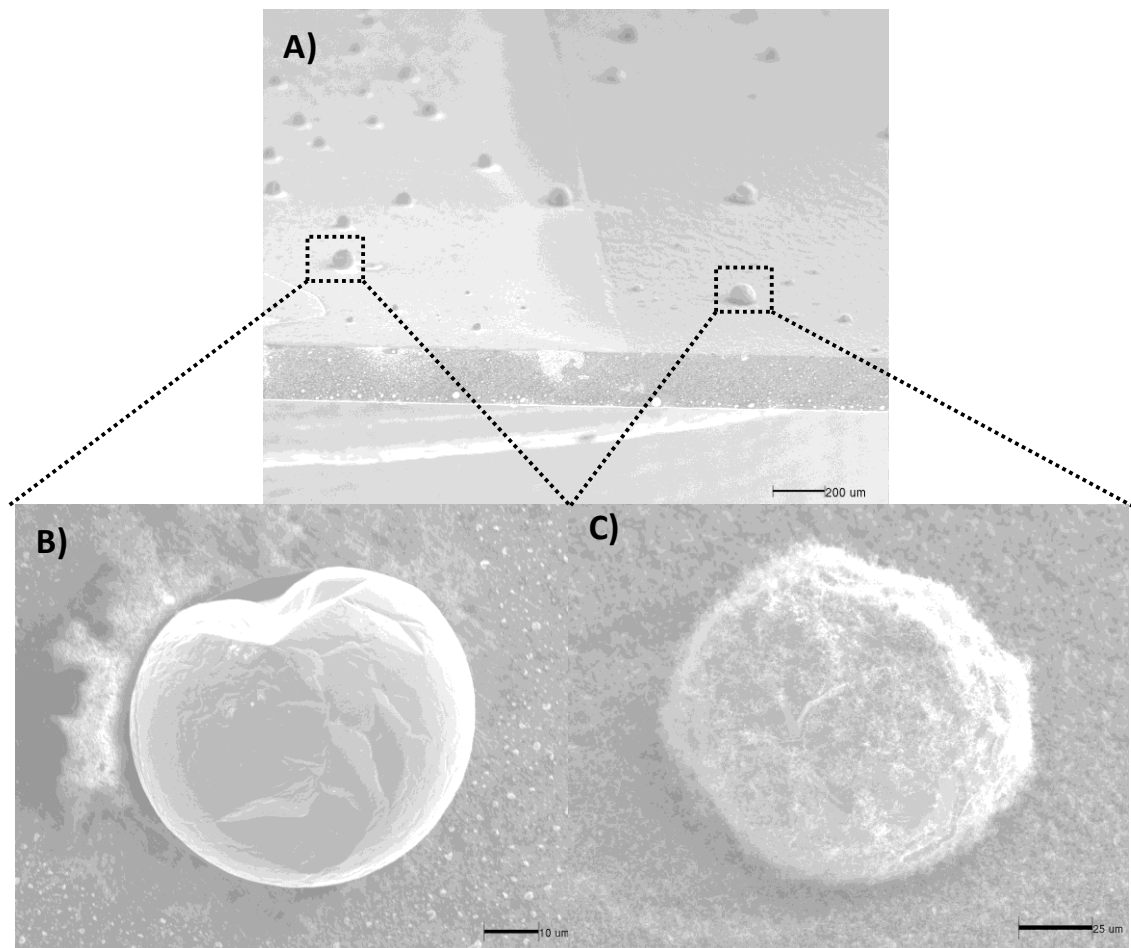


**Figure 5.16:** Angled SEM image of tCVD Modified ITO-quartz slide showing iron-no iron interface. (A) Zoom of single sphere on no iron side. (B) Zoom of single sphere on iron side. (C)

To determine the elemental make up of the spheres present on the surface energy dispersive X-ray analysis (EDX) was used. EDX allows for a spectrum to be generated from a localised area of choice on a substrate by directing the electron beam. An EDX spectrum of a sphere is shown in Figure 5.17 and upon analysis of the peak locations the spheres are identified as tin. The tin oxide present on the surface is reduced to metallic tin under the reducing atmosphere of hydrogen, which at 750°C becomes liquid and forms tin spheres.

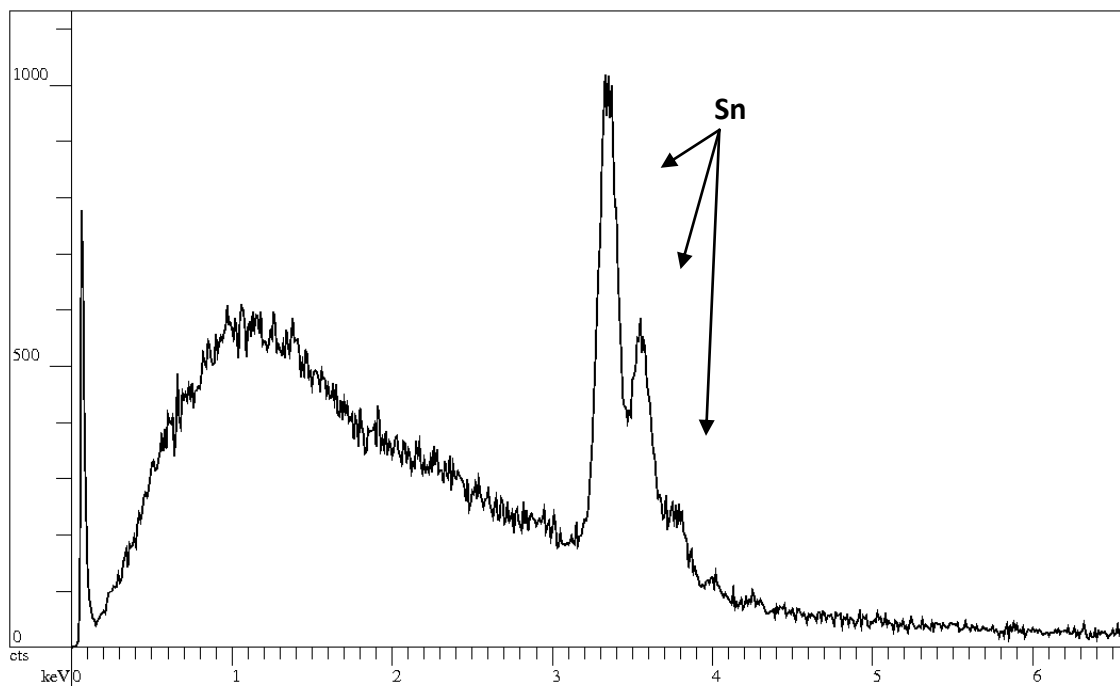


**Figure 5.17: EDX spectrum of spheres seen on ITO surface.**

To determine if any alignment had occurred and also to ascertain the height of the nanotubes present on the surface one sample was broken in half and the edge analysed under SEM, seen in Figure 5.18. From Figure 5.18 the height of the array is approximately  $5\mu\text{m}$ , significantly less than the  $\sim 20\mu\text{m}$  when grown on silicon and there is no discernible alignment or organised structure.

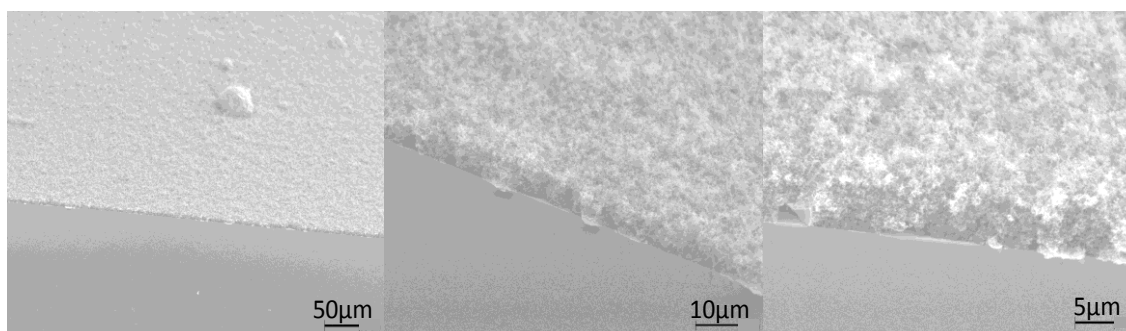


**Figure 5.18: Side-on view of CNTs grown on ITO-quartz.**

Due to the detrimental effect of hydrogen on the underlying ITO substrate growth was undertaken without the presence of hydrogen, which is normally necessary for continued reduction of the iron nanoparticles. The resultant surface is shown in Figure 5.19 and show a messy web like mix of tubes with no alignment. Larger coiled nanofibres with diameters of several hundred nanometres are also visible

and this indicates that without the hydrogen to reduce the iron to smaller diameter nanoparticles the subsequent structures are of a much larger diameter. This result indicates that hydrogen is necessary both during growth and during the pre-treatment stage to produce clean aligned arrays of nanotubes.

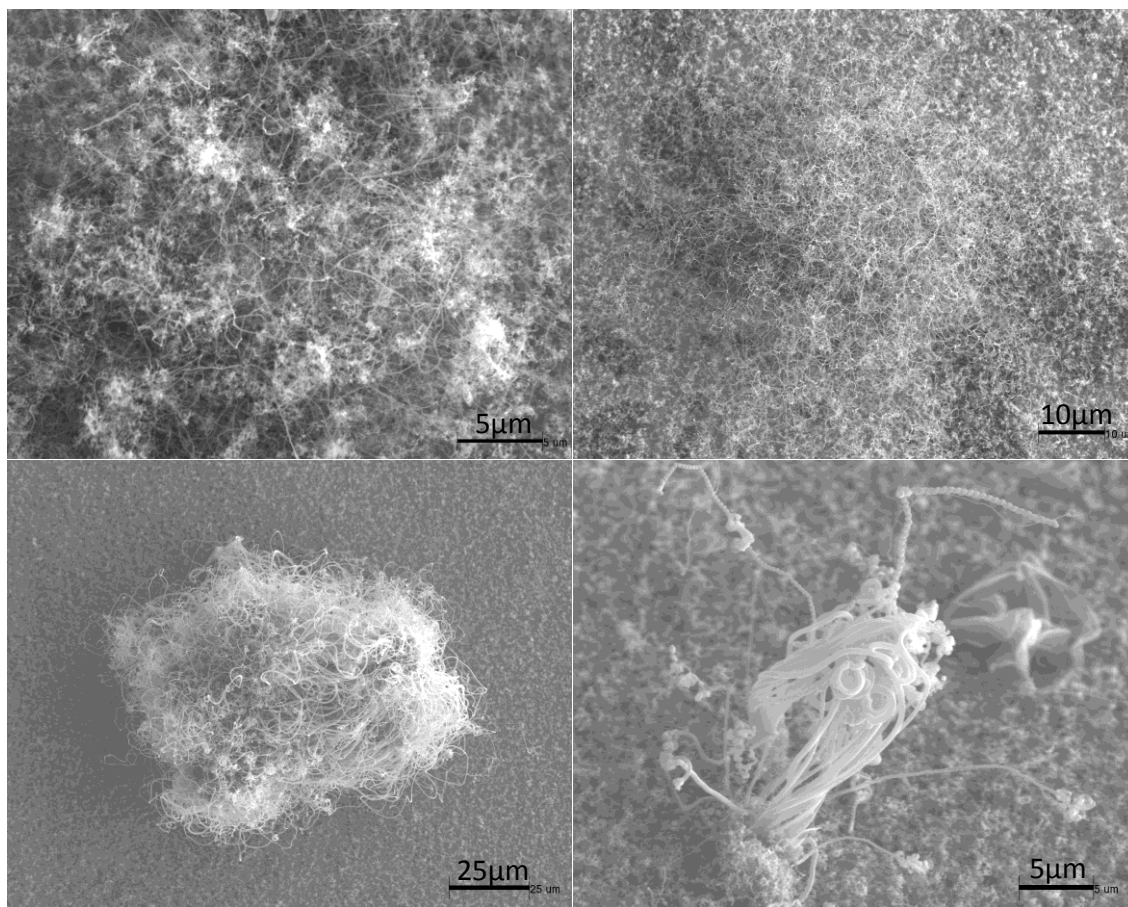


**Figure 5.19: SEM images of CNTs grown on ITO without hydrogen.**

### 5.2.2 Raman Characterisation of tCVD Grown CNT On ITO Coated Quartz

To analyse the tCVD modified ITO surfaces confocal Raman spectroscopy was also used. Figure 5.20 shows the G band map (Figure 5.20A) of one of the tin spheres coated in CNTs along with an SEM image of a similar sphere (Figure 5.20B). The Raman map shows that the entire surface of the sphere is coated in CNTs. The increased intensity compared to the CNTs on the underlying substrate is due to the difference in focal plane. The presence of nanotubes on the sphere itself also suggests that some of

the pre-deposited iron catalyst has remained on the surface or possibly alloyed with the tin to catalyse growth.

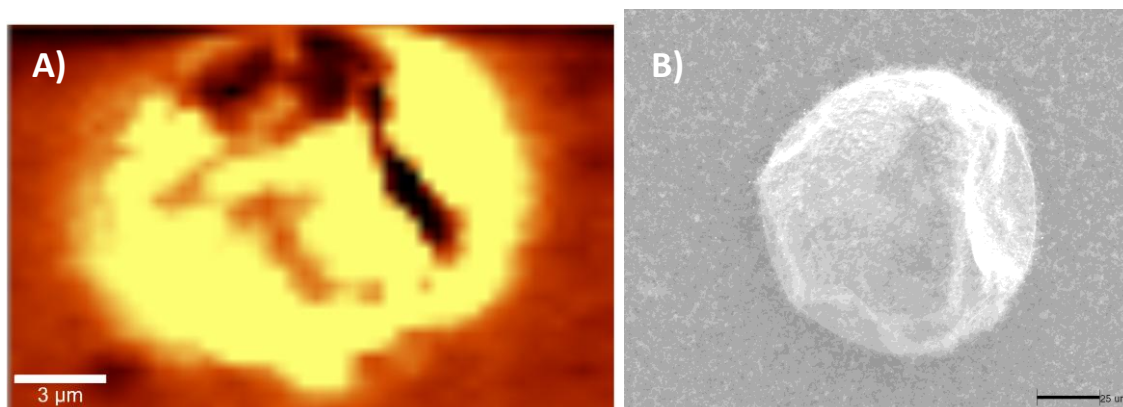


**Figure 5.20: Raman image (G-Band) of CNT covered sphere. (A) SEM image of a similar CNT covered sphere. (B)**

Upon examination of an average of several individual spectra from differing areas on the surface it can be seen (Figure 5.21) that the CNTs are multi-walled, due to the D/G ratio and lack of  $G^{+/-}$  splitting. However, also shown in Figure 5.21 is one of several spectra which show the presence of a radial breathing mode peak (RBM), the presence of which would normally indicate single-walled nanotube growth. The rarity of these RBM containing spectra and the high D/G ratio might indicate that indeed some SWCNTs have been formed but are promptly buried beneath amorphous carbon, causing an apparent rise in the D/G peaks. However due to the apparent diameter and size of the tubes from SEM along with the average spectrum it can be concluded that, as expected, nanotubes formed are predominantly multi-walled.

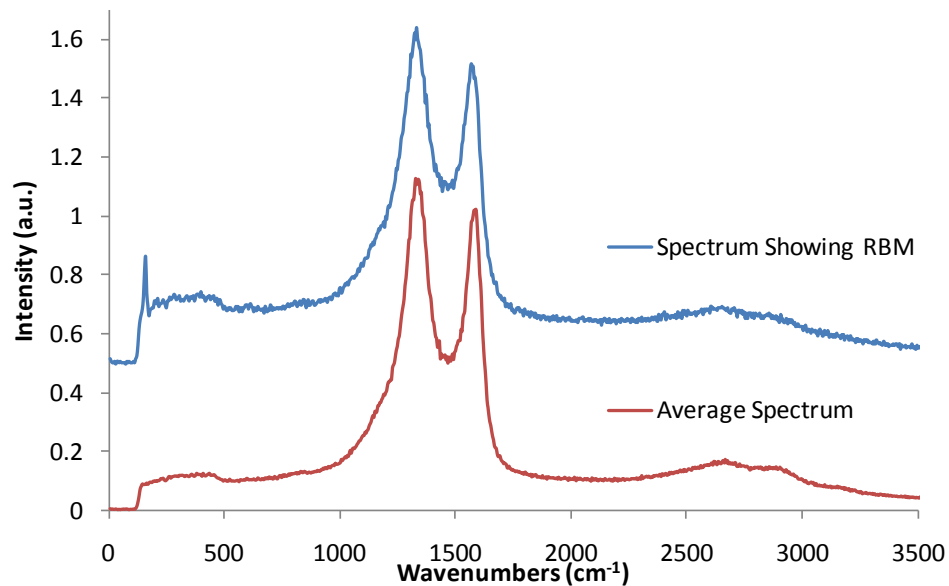


Figure 5.21: Raman spectra of the tCVD CNTs grown on ITO-quartz.

Due to the lack of conductivity after CVD had been completed photovoltaic testing was not undertaken. The clear disorder of the surface combined with Raman spectroscopy indicating the surface is predominantly MWCNT would suggest that the surface would be a very poor photovoltaic electrode.

### 5.3 Plasma Enhanced Chemical Vapour Deposition for Growth of Carbon Nanotube Arrays

In an attempt to produce predominantly SWCNT plasma enhanced chemical vapour deposition (PECVD) was used. Like tCVD PECVD produces nanotubes on a surface that has had a metal catalyst deposited and is then heated under vacuum and exposed to a plasma.<sup>84, 85</sup> However, PECVD offers several advantages over thermal CVD such as the use of low pressure environments, aiding cleanliness and meaning that much lower concentrations of reactants can be used, whilst the plasma state aids dissociation of the feedstock gas affording lower temperature processes to be used, leading to a more controlled growth process.<sup>85, 184, 185</sup> Whilst the plasma typically contains a carbon feedstock gas such as methane or acetylene, it also often consists of a reducing gas such as hydrogen or ammonia. In the case of hydrogen this has been found to aid in the carbon feedstock dissociation and also affect the catalyst activity.<sup>78,</sup>

<sup>186</sup> The use of a vacuum system also reduces the atmospheric contamination giving a cleaner growth process and fewer defects in the resultant CNTs. Despite these advantages the growth of CNTs by PECVD has remained difficult due to the need for specialised growth chambers, and difficulty in tailoring the growth procedure to obtain the required nanotubes, either single-walled (SWCNT) or multi-walled (MWCNT). Specifically the production of SWCNTs remains more difficult to achieve than MWCNT.<sup>84, 85, 187</sup> It has been shown previously that the CNTs produced can be tailored by altering growth conditions such as the catalyst material and thickness, plasma composition and power and the growth temperature.<sup>85, 188</sup>

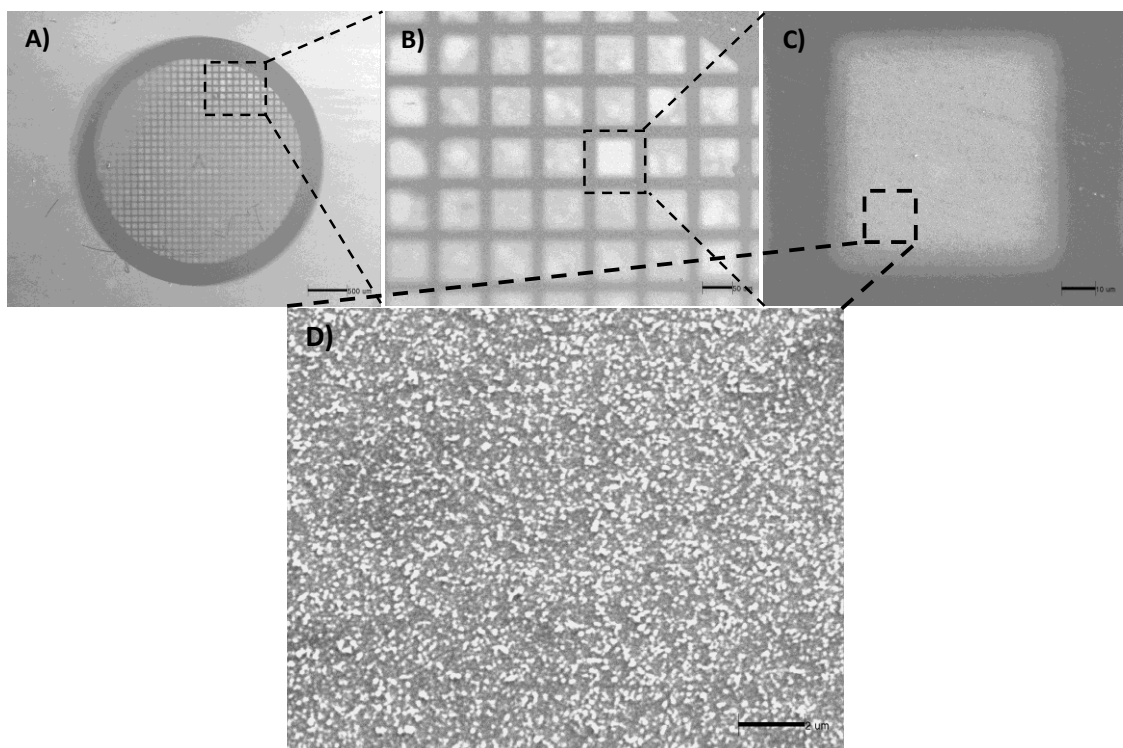
Silicon wafers were chosen as substrates to provide excellent thermal stability and the native oxide present on the surface ( $\text{SiO}_2$ ) also assists in CNT growth by inhibiting the diffusion of catalyst atoms into the substrate.<sup>189</sup> Typically to produce high quality SWCNT an oxidised aluminium layer is deposited prior to the iron catalyst layer.<sup>190</sup> This step was found to not be necessary in this procedure. In fact the opposite effect was found in that the presence of the alumina layer produced MWCNT instead of SWCNT. The carbon feedstock gas used was high purity methane, it has been shown previously that pure methane needs to be diluted to achieve CNT growth.<sup>191</sup> Neutrals such as nitrogen and argon plasma help to remove any amorphous carbon produced during growth, leading to a high purity and homogenous CNT array.<sup>85, 191, 192</sup> As mentioned previously typically hydrogen is added into the growth mixture, however, in this work this was found to not be necessary and this is believed to be due to the large number of dissociation products available from a methane plasma, listed in Table 5.1, which show that molecular hydrogen can be supplied by the methane itself.

**Table 5.1: Methane dissociation reactions. From Mao *et al.*<sup>83</sup>**

$e^- + \text{CH}_4 \rightarrow \text{CH}_3 + \text{H} + e^-$
$e^- + \text{CH}_4 \rightarrow \text{CH}_2 + \text{H}_2 + e^-$
$e^- + \text{CH}_4 \rightarrow \text{CH} + \text{H}_2 + \text{H} + e^-$
$e^- + \text{CH}_4 \rightarrow \text{C} + 2\text{H}_2 + e^-$

### 5.3.1 Scanning Electron Microscopy

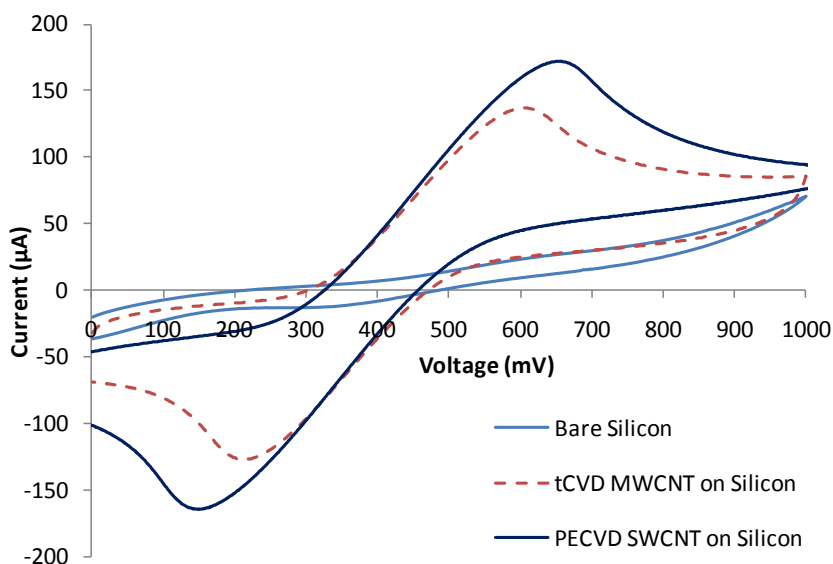
Figure 5.22 presents scanning electron microscopy (SEM) images of the substrate at three different magnifications when the growth is undertaken for 10 minutes at a temperature of 650°C to illustrate the production of patterned surfaces. Patterning was achieved by using a copper TEM grid as a negative mask during the catalyst deposition stage. By masking areas of the substrate it is possible to investigate the difference between areas where catalyst has been deposited and the masked areas of bare substrate. This technique of shadow masking provides a very simple and low cost method of producing patterned surfaces, in a similar manner to work on sol-gel CNT growth by Pan et al.<sup>193, 194</sup> Clearly there is a difference in the patterned and unpatterned areas, however, the production of CNTs is not immediately evident from the SEM due to the lack of discernible tube like structures and this was later verified using Raman spectroscopy.



**Figure 5.22:** Scanning electron microscopy images of the patterned substrate after CNT growth at different magnifications. The scale bars are 500 $\mu\text{m}$  (A), 50 $\mu\text{m}$  (B), 10 $\mu\text{m}$  (C) and 2 $\mu\text{m}$  (D).

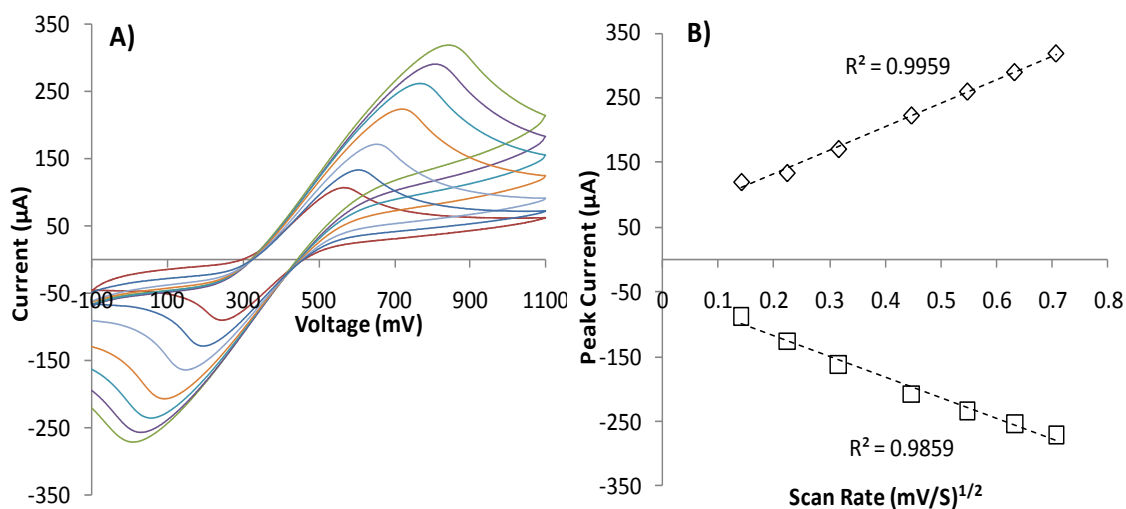
### 5.3.2 Electrochemical Characterisation of PECVD Grown CNT Arrays

Cyclic voltammetry was again used to compare the electron transfer characteristics of the PECVD grown SWCNT arrays, when growth is undertaken for 10 minutes at a temperature of 650°C. Figure 5.23 shows the CV plots for a solution of ferrocene with bare silicon working electrode, tCVD MWCNT electrode (both shown previously in section 5.1.2) and the PECVD SWCNT working electrode. Immediately noticeable is the increased peak height from the PECVD surface indicating an increased conductivity over the MWCNT and far increased over the bare silicon. The peak separation of the PECVD surface does increase slightly when compared to the tCVD surface and this is caused by the incomplete coverage of SWCNTs on the surface leaving some of the insulating silicon substrate exposed. Thus when taking into account the fewer SWCNTs present on the surface the PECVD sample is the more efficient electrode as it produces a greater magnitude current with far less nanotubes.



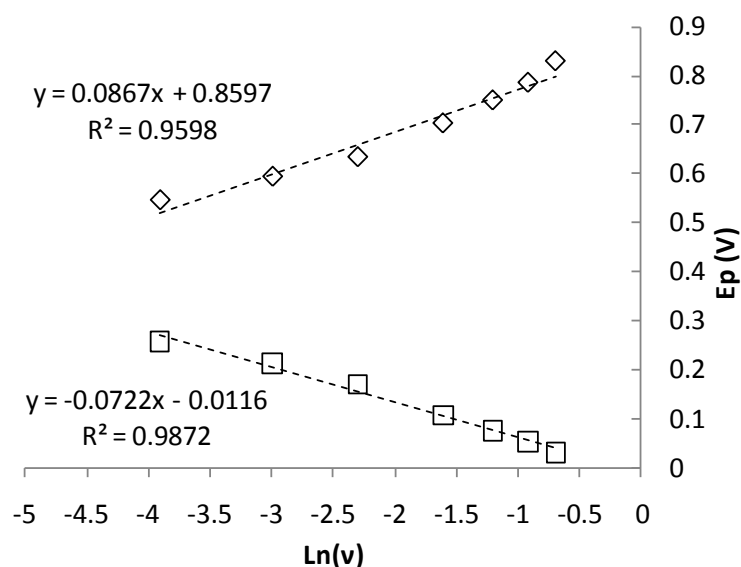
**Figure 5.23: Comparison of CV plots for bare silicon, tCVD and PECVD grown CNT on silicon at identical scan rates ( $100\text{mV}\cdot\text{s}^{-1}$ ).**

Figure 5.24 shows the CV plots with increasing scan rate (Figure 5.24A) and linear dependence on peak height with the square root of scan rate (Figure 5.24B) confirming the redox active molecule is indeed in solution.



**Figure 5.24:** CV plots for ferrocene in solution with PECVD functionalised working electrode. (A) Graph showing relationship between peak current and square root of scan rate. (B)

The shift in redox peak position is then used to determine the electron transfer co-efficient as discussed previously. The plot of peak position versus the natural log of scan rate (Figure 5.25) gives a  $k_s$  value of  $0.052 \pm 0.017 \text{cm.s}^{-1}$ , compared to the chemically attached SWCNT which had a  $k_s$  value of  $0.071 \pm 0.014 \text{cm.s}^{-1}$  indicates that again chemical attachment provides a superior electrode.



**Figure 5.25:** Plot of anodic and cathodic peak potential ( $E_p$ ) versus the natural logarithm of scan rate ( $v$ ) for the PECVD functionalised working electrode.

### 5.3.3 Raman Characterisation of PECVD Grown CNT Arrays

To confirm the presence of CNTs, when growth is undertaken for 10 minutes at a temperature of 650°C, and characterise them confocal Raman microscopy and spectroscopy were used. In the Figure 5.26 inset the Raman image (100x100µm) of the G (or graphitic) band at 1590cm<sup>-1</sup> clearly shows the boundary between the masked, where no catalyst exists, and unmasked areas, where SWCNTs are clearly present. This corresponds well with the SEM image of a similar square, indicating that SWCNT growth has occurred only in the designated areas. Figure 5.26 also compares the Raman spectra of the bare silicon region (dashed line) to the CNT growth region (solid line). The presence of the narrow G band at 1590cm<sup>-1</sup> is indicative of high purity sp<sup>2</sup> hybridised carbon. The single sharp peak at 173cm<sup>-1</sup>, the RBM, is well-known to be caused by circumferential expansions that are only present in carbon nanotubes.<sup>69</sup> Due to only a single sharp RBM peak being seen, despite the spot size of the Raman sampling an area of approximately 300nm in diameter, there must be exceptional homogeneity of the nanotube diameters across the surface. The G peak also exhibits the G<sup>+/-</sup> splitting that its specific to SWCNTs.<sup>69</sup> The very narrow peak width and high intensity of both the RBM and G band combined with the low intensity of the D peak indicate that high purity tubes with few defects have been produced. The intensity of the D and G bands provide a quantitative measure of the level of defects or functionalisation present in the SWCNT.<sup>82, 188</sup> The average D/G ratio of 0.17 agrees well with other ratios found for high purity SWCNTs. As mentioned previously the RBM is a circumferentially dependent peak, thus its Raman frequency can be used to determine the diameter of the produced nanotubes,<sup>69</sup> the average nanotube diameter across the 50µm<sup>2</sup> area was found to be 1.47±0.03nm. The very narrow peak width and high intensity of both the RBM and G band combined with the low intensity of the D peak indicate that high purity tubes with few defects have been produced. The diameter of the CNT is dependent on the catalyst nanoparticle diameter,<sup>195</sup> so it can be inferred that the heating under vacuum has resulted in an iron nanoparticle size of ~1.5nm.

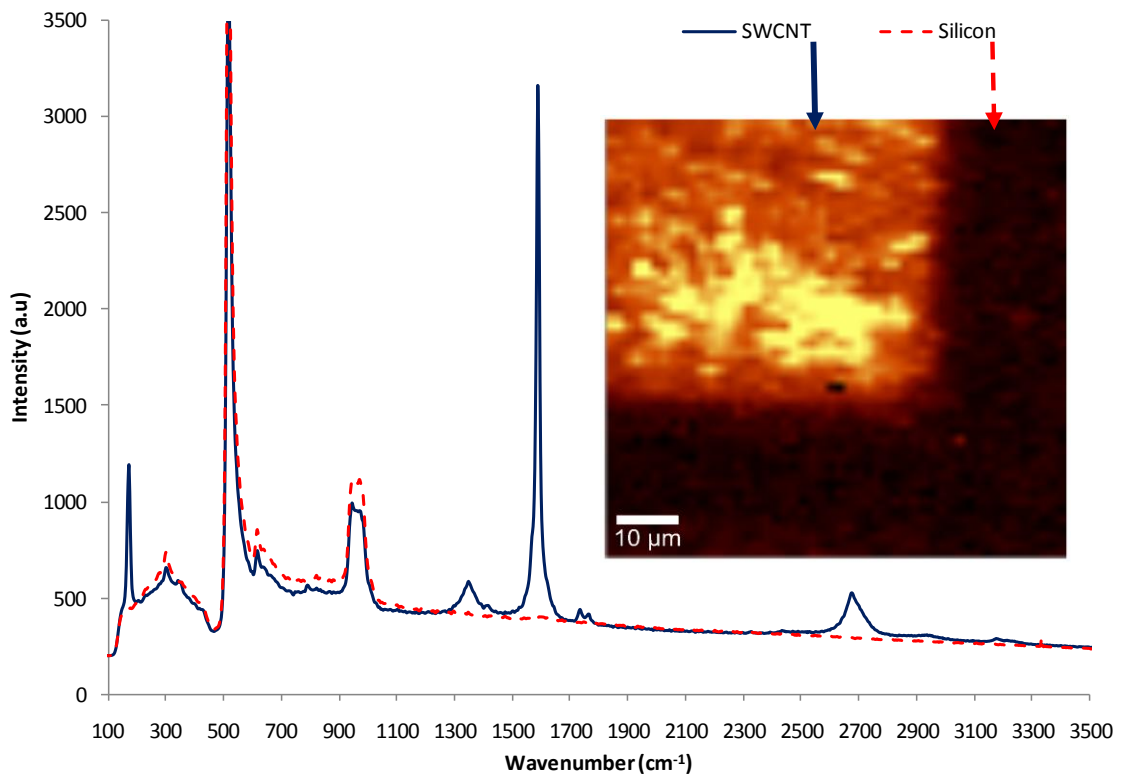


**Figure 5.26:** Raman spectra corresponding to the patterned area (SWCNT) and unpatterned area (Silicon). Inset is a 100x100 μm image plotting the intensity of the G band at 1590 cm<sup>-1</sup> showing the boundary between where the masked areas.

The G peak for the patterned SWCNT also exhibits some further fine structure when enlarged, seen in Figure 5.27, where the G peak exists as both a G<sup>-</sup> peak at 1570 cm<sup>-1</sup> and a G<sup>+</sup> peak at 1590 cm<sup>-1</sup> which is characteristic of SWCNTs.<sup>69</sup> Also the relative intensities of these G<sup>+/-</sup> peaks provides an indication of whether the SWCNTs are semi-conducting or metallic, with a more intense G<sup>+</sup> peak, as seen in the produced SWCNTs, indicating that semi-conducting SWCNTs have been produced.<sup>145</sup> This may be expected as it has been shown previously that metallic SWCNT undergo selective etching during PECVD, specifically in the presence of methane, leading to preferential semi-conducting nanotube growth.<sup>196</sup> This would be of benefit for applications such as photovoltaics which have shown that semi-conducting nanotubes are needed whilst metallic nanotubes are detrimental to performance.<sup>60, 160, 197, 198</sup>

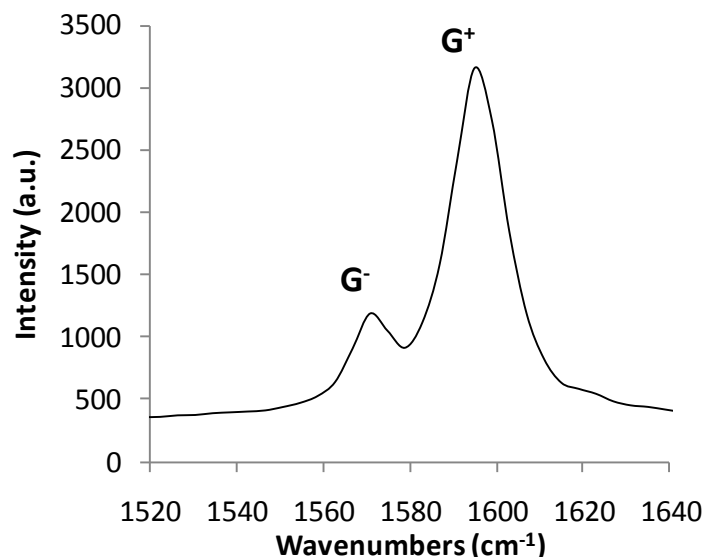


**Figure 5.27:** Enlargement of Raman G Band region showing G<sup>-</sup> peak at 1570cm<sup>-1</sup> and G<sup>+</sup> peak at 1590cm<sup>-1</sup>, characteristic of semi-conducting SWCNT.

After establishing that SWCNT can be produced and patterned into defined areas, the growth conditions were then altered to produce different species of nanotube. Figure 5.28 shows the Raman spectra for changing the growth time and the growth temperature. In Figure 5.28A we see the Raman spectra with changing growth time. As discussed previously 10 minutes of growth produces a characteristic SWCNT spectrum, with a clear RBM ( $d_t = 1.47\text{nm}$ ), low D/G ratio and G<sup>+/-</sup> peak splitting. If the length of time exposed to the plasma is extended to 30 minutes the spectrum still has SWCNT specific peaks such as the RBM and G<sup>+/-</sup> splitting; however the RBM is shifted to a lower frequency of 149cm<sup>-1</sup> indicating that the tube diameter has increased to 1.66nm. As the growth time is further extended to 60 minutes the spectrum changes significantly, producing no RBM and a D/G ratio of approximately 1, indicating that MWCNTs have been produced. A similar non-linear growth behavior has been observed previously for the production of nanotubes using a cobalt catalyst in the presence of hydrogen and has been attributed to an initial growth of SWCNT followed by a decrease in the catalytic activity, due to amorphous carbon deposition, of the nanoparticles leading to MWCNT formation.<sup>199</sup> Additionally the SWCNT are quite fragile and over prolonged time can be preferentially etched away by the plasma.<sup>192</sup> However, MWCNT are more resistant to plasma etching and so after a prolonged growth exposure only MWCNT remain. Short growth time also tends to produce a

small distribution of nanotube lengths and diameters, as opposed to long growth times that produce large distributions of lengths and diameters, again increasing the chance of MWCNT being present.<sup>200</sup>

A similar trend is observed in Figure 5.28B with changing growth temperature. Previously it has been shown that higher temperatures tend to preferentially produce SWCNT and a similar trend is observed here.<sup>82</sup> The 650°C spectrum is again clearly SWCNT. Lowering the temperature to 550°C lowers the D/G ratio slightly, but still maintains the SWCNT specific peaks. However, upon lowering the temperature to 450°C the spectrum clearly changes, again now showing a D/G ratio of  $\approx 1$ , and no RBM was observed. The increased noise in the 450°C spectrum is due to the low intensity of the G peaks against which the spectra have been normalised. Also due the relative intensity of the silicon peaks compared to the D and G band we can say that the overall nanotube coverage is much lower than for the higher temperatures. When comparing the growth temperatures the effect of plasma heating also has to be considered. It has been observed previously that CNT growth can be undertaken without any external heating by the inherent plasma heating of the substrate.<sup>201</sup> However, to achieve the required growth temperature a high plasma density and a DC plasma power of 200W was required. In this work the use of a much lower plasma density and lower RF power of 10W would tend to indicate that the effect of plasma heating would be negligible. Indeed if growth is attempted without external heating no carbon nanostructures are achieved. Figure 5.28 demonstrates how by simply changing one growth variable the resultant CNTs produced can be altered to suit the desired application without the need for large experimental changes.

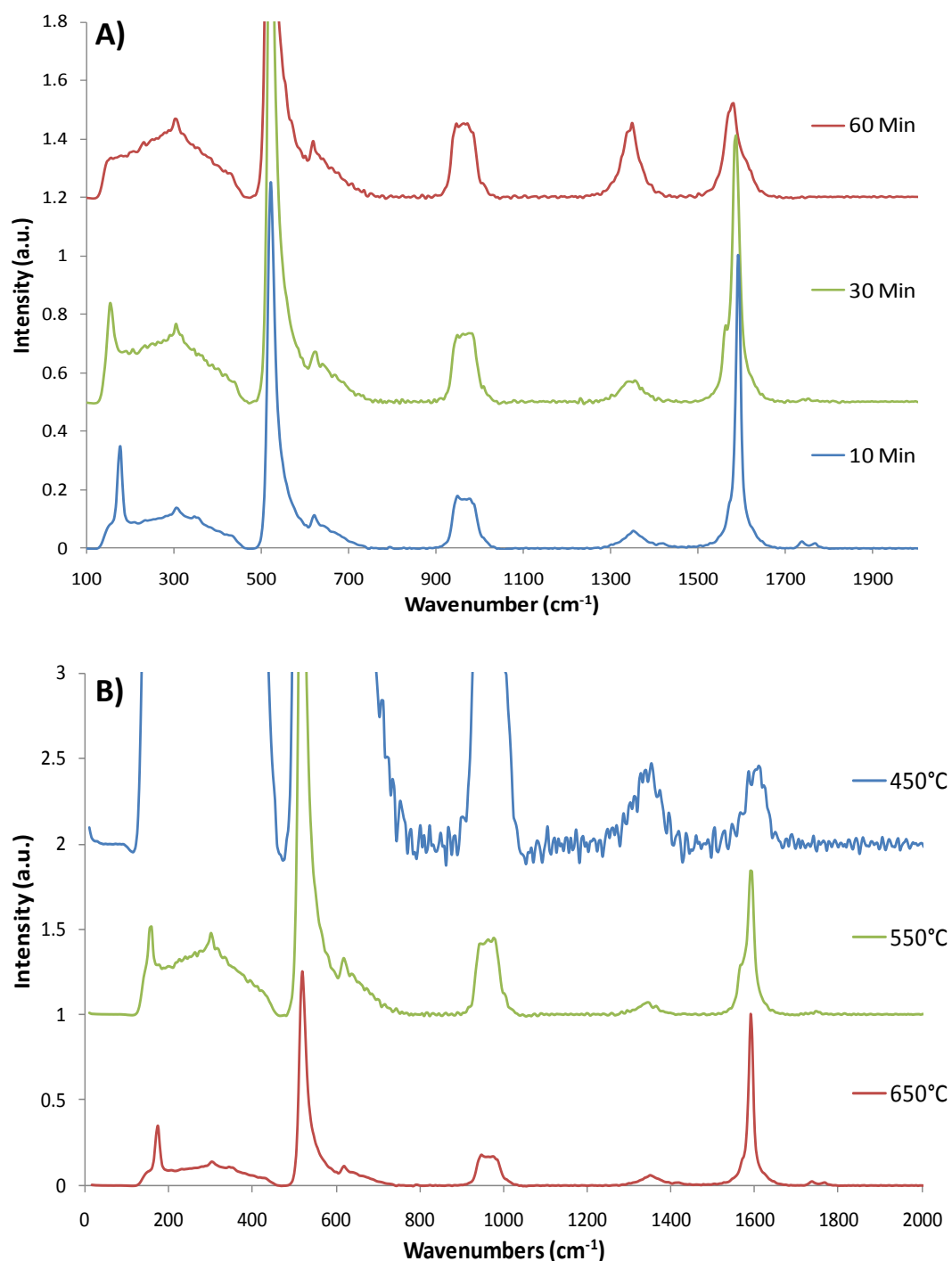


**Figure 5.28: Raman spectra with changing growth time (A) and growth temperature (B).**

Figure 5.29 shows the Raman spectra for CNTs produced with various catalyst conditions. By simply changing the catalyst material but keeping all other variables constant we can analyse the effect a different catalyst would have on the nanotube structure. Figure 5.29A shows the D and G band region (1200cm<sup>-1</sup>-1700cm<sup>-1</sup>) for CNTs grown with a nickel catalyst and an iron catalyst. As discussed previously the D/G ratio

can be used to identify the nanotubes present and in the case of Figure 5.29A the nickel catalyst has a D/G ratio of  $\approx 1$ , with no G band splitting identifying them as MWCNTs. This is significantly different from the iron catalyst spectra which has a D/G band ratio of 0.07 and clear  $G^{+/-}$  band splitting. This illustrates how simply replacing the catalyst layer has drastically altered the nanotube structure. Figure 5.29B compares the Raman spectra when an aluminium layer is deposited prior to the iron and when just iron is deposited. Typically it is reported that an aluminium oxide (alumina) layer helps prevent iron diffusion into the catalyst and is necessary to produce SWCNT.<sup>190</sup> In this work however, the opposite was observed. By first depositing an aluminium layer and allowing it to oxidise in air to produce alumina, followed by iron deposition and growth with identical conditions the resultant Raman spectra is clearly MWCNT, with no RBM present and a D/G ratio of  $\approx 1$ . This is in contrast to the iron deposited straight onto the silicon which has all of the characteristic SWCNT peaks, indicating that the alumina layer actually impedes growth of SWCNT. It also demonstrates how the structure of the produced CNTs can be tuned by altering the catalyst layer.

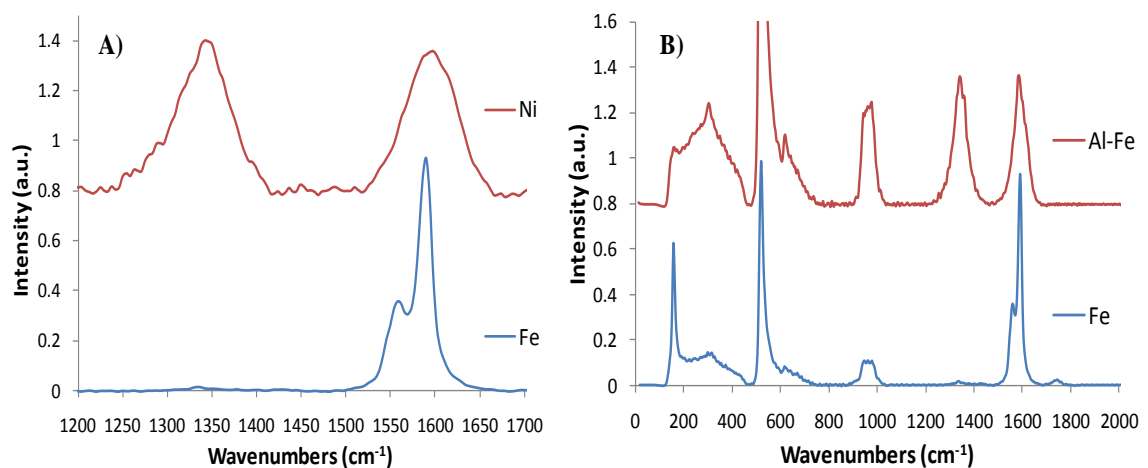


**Figure 5.29: Raman spectra for nickel and iron catalysts showing D and G Bands (A). Spectra for aluminium underlayer present and no aluminium layer. (B)**

### 5.3.4 XPS Characterisation of PECVD Grown CNT Arrays

To complement the Raman data and electrochemistry, XPS was performed to analyse the surface of the SWCNT sample. As was done for the tCVD grown tubes Figure 5.30 shows the XPS spectra of successive steps during growth. Starting with the bare silicon substrate followed by deposition of the 5nm of iron and finally after growth has occurred. Interestingly after growth has been undertaken some iron signal is still present and this may be due to either catalyst particles present on the end of the nanotubes, the so called 'tip-growth' process, or more likely is simply due to the incomplete coverage of the substrate leaving areas of the iron coated silicon exposed. There is also a small amount of silicon still detectable and this again indicates that the coverage of the surface is not complete. There is a small peak located at 115eV in between the silicon 2s and 2p peaks and this is caused by the presence of aluminium. This was at first unexplainable and thought to possibly be a contaminant in the silicon, however after several control experiments it was discovered that the heating mantle used in the PECVD growth, which contains an alumina ceramic mantle, was in fact causing contamination of the surface.

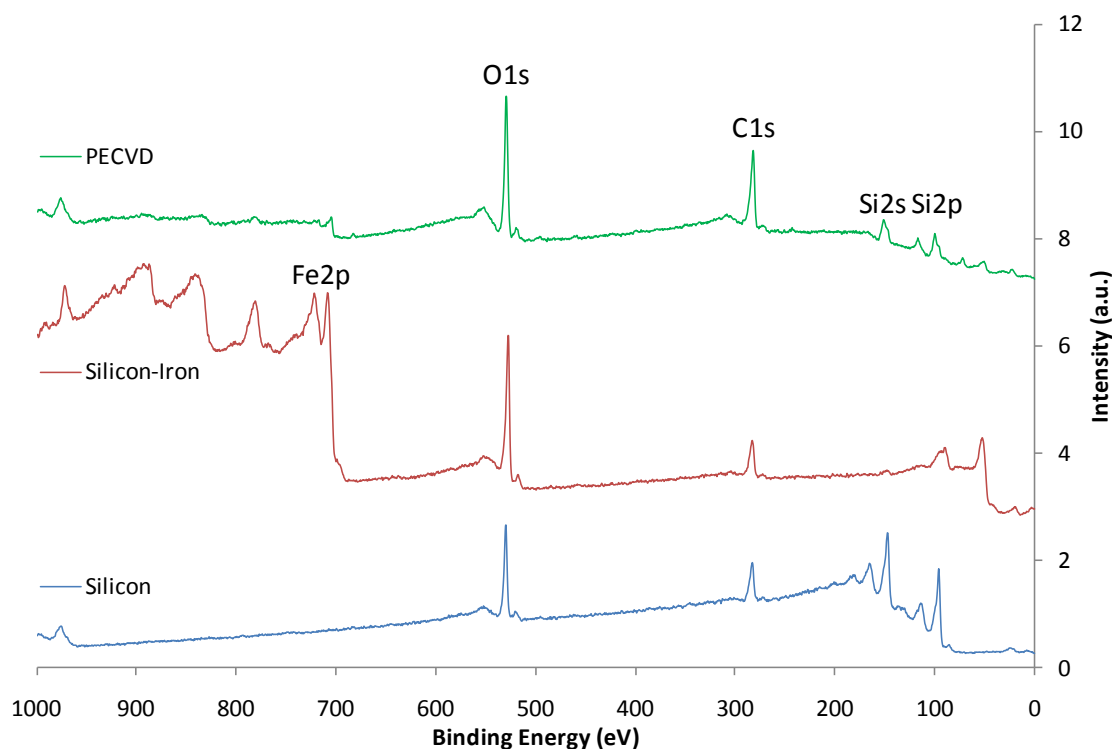


Figure 5.30: XPS survey spectra for bare silicon, silicon after iron deposition and finally after PECVD growth has occurred.

If the carbon deposited on the surface was amorphous in nature or if the CNTs contained defects in their walls as functional groups, then XPS can determine the extent of any functionality and if so, the specific chemical functionalities present. Figure 5.31 shows the high resolution scan of the C1s region on a sample of grown SWCNTs. The spectrum has been fitted with three components; one at 284.4eV attributed to  $sp^2$  hybridised carbon, a second peak at 285.2 attributed to  $sp^3$  carbon,<sup>78</sup> and finally a peak at 286.8eV encompassing oxides of carbon such as carboxyl and carbonyl moieties.<sup>202</sup> The XPS data shows predominantly graphitic carbon is present on the surface, in agreement with the Raman data presented earlier. There is a small amount amorphous or  $sp^3$  hybridised carbon present on the surface, possibly from adventitious carbon or defect sites along the CNT walls and end groups. The low amounts of this defective amorphous carbon agree with the D/G ratio seen in the Raman data, indicating high purity.

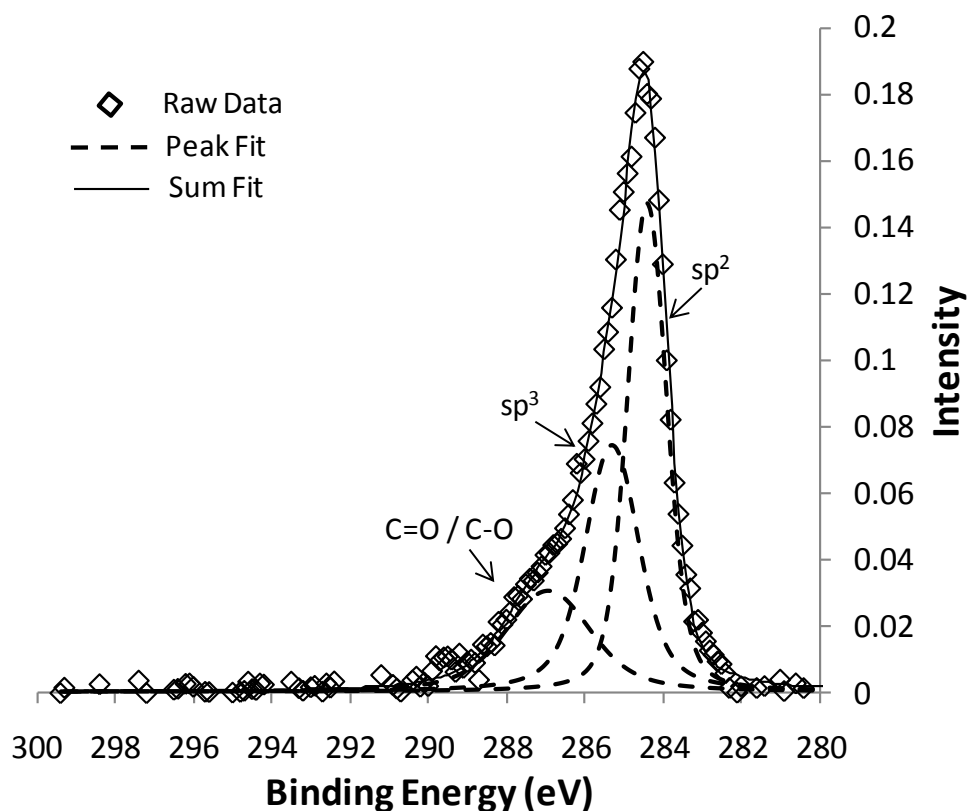


Figure 5.31: High resolution XPS spectrum of C1s binding region.

### 5.3.5 Photovoltaic Properties of PECVD Grown CNT Arrays

Finally, electrochemical solar cells were constructed from the PECVD grown arrays and photovoltaic testing performed. Figure 5.32 compares the J-V curves for the PECVD array, which produces a modest response of only  $0.5\mu\text{A}\cdot\text{cm}^{-2}$  and 22mV. This is very low when compared to the chemically attached array also shown in Figure 5.32. This again confirms that chemical attachment provides a superior electrode for photovoltaic applications. The response of the PECVD array may however be able to be increased significantly by increasing the height of the SWCNTs. As shown previously there is proportionality between the photoresponse and number of tubes present on the surface and the SEM indicates that the PECVD produced SWCNTs are short. By increasing the array height and also investigating alignment this response may be possible to increase.

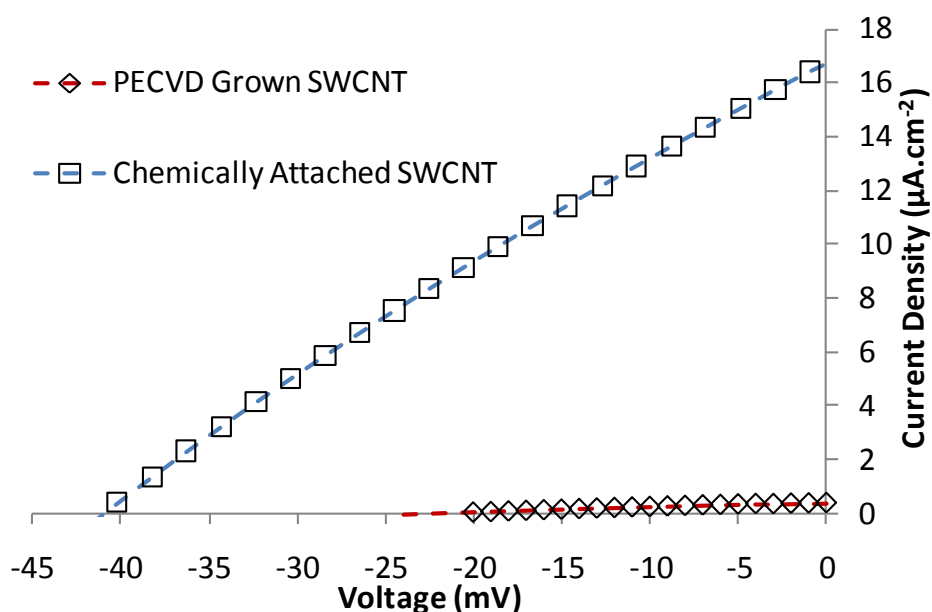


Figure 5.32: J-V curves for PECVD grown SWCNT electrode and chemically attached SWCNT electrode. Light intensity  $100\text{mW}\cdot\text{cm}^{-2}$ .

Although the PECVD SWCNT response is low when compared to the chemically attached array, when compared to the tCVD grown array (Shown in Figure 5.33) it is significantly superior. The voltage of less than 1mV for the tCVD array indicates severe back reactions are reducing any meaningful power ( $0.24\text{nW}\cdot\text{cm}^{-2}$ ) from being produced, whilst the PECVD array can produce  $3.3\text{nW}\cdot\text{cm}^{-2}$  approximately 14 times greater for a

fraction of the nanotubes. This supports that semi-conducting SWCNT, even in lower numbers, are necessary for photovoltaic applications.

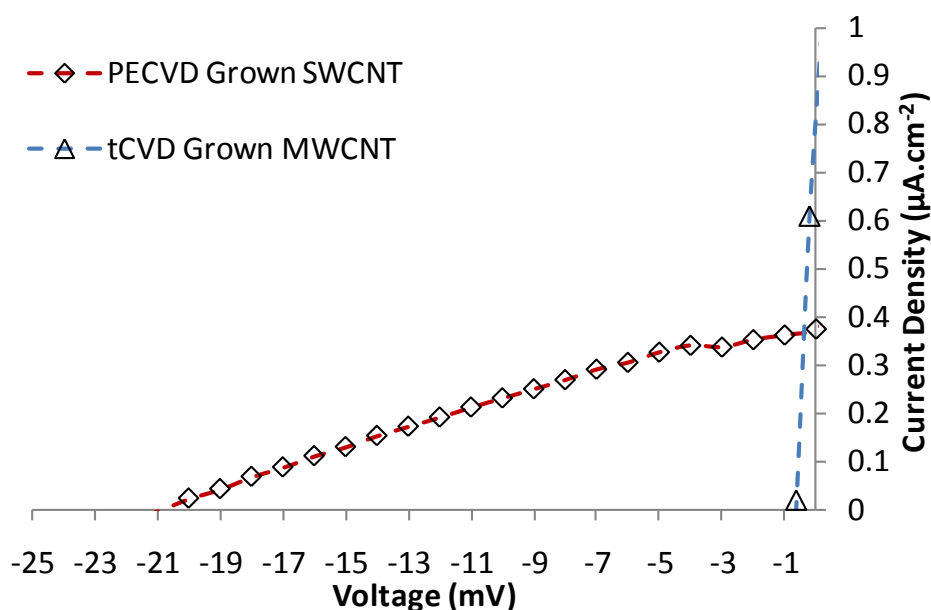


Figure 5.33: J-V curves for PECVD grown SWCNT electrode and tCVD MWCNT electrode. Light intensity  $100\text{mW.cm}^{-2}$ .

## 5.4 Chapter Conclusions

Carbon nanotubes, both single and multi-walled have been synthesised using chemical vapour deposition. The use of tCVD was found to produce predominantly MWCNT in large vertically aligned arrays; however, although these arrays behaved adequately as electrochemical electrodes their performance in photovoltaics was minimal. This is because for nanotube photovoltaics it was found that semi-conducting tubes are necessary, and thus SWCNT are required. SWCNT were successfully produced by plasma enhanced CVD, these were characterised by electrochemistry, Raman spectroscopy and XPS. It was found that despite a lower density of tubes on the surface the grown SWCNT were more efficient at electron transfer. The photovoltaic performance of the grown SWCNT was also far superior to the grown MWCNT, as the SWCNT can exist as semi-conductors. However, it was also apparent that the chemical attachment of the CNTs to the surface prior to any light harvesting applications provided a far greater efficiency. From this chapter it can be concluded that SWCNT are superior to MWCNT for photovoltaic applications and that chemically attached arrays are superior to CVD grown arrays.

---

## **6. Conclusion & Future Work**

---

## 6.1 Conclusions

In the work presented in this thesis it has been shown that carbon nanotubes have many varied applications to photovoltaics. In chapter 3 it was demonstrated that vertically aligned SWCNT arrays are capable of producing a photocurrent of  $13.13\mu\text{A}\cdot\text{cm}^{-2}$  and voltage of 40mV when exposed to visible light with prompt response time of less than 200ms, yet due to the low amount of material (thickness  $\approx 100\text{nm}$ ) these arrays can remain transparent. This photocurrent response was found to be linearly related to incident light power and the resultant response was able to be modified by altering the cutting and attachment time of the nanotubes, which in turn modified the amount of SWCNTs present on the surface and their electronic structure. As a result the direct proportionality between the number of nanotubes present on the surface and the produced photocurrent was found along with the benefit from acid cutting leading to an increased semi-conducting proportion of nanotubes. Multi-walled carbon nanotubes were also used to create arrays in an identical fashion to that of the SWCNTs. The ability to directly compare the performance of multi and single-walled nanotubes will also help steer future work. As was predicted by theory SWCNT were far superior to MWCNT, which in this particular cell geometry produced 45% less power, due to the difference in electronic structure with SWCNT behaving as semi-conductors and MWCNT as metallic conductors. The superior performance of SWCNT at first appears counterintuitive as the MWCNT substrates have an increased number of nanotubes on the surface. However, due to their semi-conducting electronic structure the SWCNT are superior despite lower coverage. The novel application of SWCNT as the light harvesting element within the traditional DSSC design provides a starting point for a new solar cell architecture based on purely carbon nanostructures. This new cell design, of note due to the small amount of material needed to generate power yet stable and reproducible, provides excellent promise for future applications in transparent light harvesting by replacing windows with solar cell arrays for home and office buildings.

In chapter 4 the chemical modification of these SWCNT arrays was shown to produce an increased performance which could be tailored depending on the specific application desired, with the rapid electron transfer through the arrays and high

surface area showing the benefits of integrating carbon nanotubes into electronic devices. The ability to chemically functionalise the nanotube arrays shows promise for other applications as well as photovoltaics such as electrochemical sensing. The direct comparison between the performance of a ruthenium based dye (N3) and a similar ruthenium based porphyrin (RuTPP) showed that the dye was far superior at light harvesting. The N3 modified arrays produced  $16.38\mu\text{A}\cdot\text{cm}^{-2}$ , however had a reduced voltage of 25mV whilst the RuTPP modified array produced  $7.37\mu\text{A}\cdot\text{cm}^{-2}$  and also 25mV, indicating that there is a compromise in overall power. This has been supported by other work in the literature which states that porphyrins have several disadvantages when used in photovoltaics, such as a lack of sensitivity to the infra-red regions. The growth of PAMAM-type dendrons directly from surface bound vertically aligned SWCNT arrays had not previously been demonstrated and as well as applications in photovoltaics the growth of dendrons that can be functionalised for a multitude of applications will open up many future possibilities. The optimal photoresponse of the dendron modified arrays was found to occur at generation 2 and produced an overall power increase of 60% over the unmodified nanotube array. The combination of the dye and PAMAM-type dendron modifications showed an even greater performance increase than either by itself, with an increased photocurrent of  $15\mu\text{A}\cdot\text{cm}^{-2}$  whilst still retaining a voltage of 45mV occurring at G-1.5-N3.

Chapter 5 saw the production of carbon nanotube arrays directly onto the working electrode. This allowed for a direct comparison between chemically attached arrays, as discussed in chapter 3, and physisorbed arrays grown by chemical vapour deposition with the covalent attachment of the nanotube shown to be the superior electrode. This is despite lower carbon nanotube densities. A combination of Raman spectroscopy, XPS and SEM imaging was used to characterise the CVD grown arrays as either SWCNT or MWCNT. Photovoltaic comparisons between grown MWCNT and SWCNT also agreed with the data from the chemisorbed arrays, with the PECVD grown SWCNT exhibiting a superior response to the much denser grown MWCNT array. Patterning of these grown arrays was also demonstrated as well as the conversion between SWCNT and MWCNT in PECVD, which will be of importance for any procedure where SWCNT are required in sufficient purity.

## 6.2 Future Work

There are still many avenues of interesting research to further the work presented in this thesis. As was shown the ability to produce for electrically sorted SWCNTs, which is separating semi-conducting and metallic, would be of enormous benefit for applications in photovoltaics, and work towards this goal is currently underway. Other future directions for this work already underway include the attachment of nanotube arrays to FTO surfaces by the use of 'click' chemistry which could provide advantageous electron transport and ease of synthesis. Modification of the electrolyte solutions within the solar cells is also underway to further optimise the energy levels present to better match the energy levels of the nanotubes and the application of a blocking layer to the working electrode surface to lower back reactions and increase voltage, increasing the overall cell efficiency. There also exists many opportunities for further work in chemical functionalisation of the nanotube arrays such as the growth of other dendrons. There have been several studies on the production of porphyrin and dye based dendron structures that could provide enhanced photovoltaic performance.<sup>95, 203</sup> The work presented here suggests that a high degree of aromaticity would be beneficial for such structures, both in terms of conductivity and light harvesting.<sup>105, 204</sup> The benefits of covalent attachment of the nanotubes to the substrate shown in this work can also help guide future work in the production of nanotube based solar cells.

However, perhaps the area with most possible improvement remaining is the growth of carbon nanotubes directly onto electrode surfaces. The ability to grow dense ordered arrays of semi-conducting single-walled carbon nanotubes would still be of great interest for applications in light harvesting. By increasing the density and height of the nanotube arrays the amount of light that could interact with the nanotubes can be increased, hopefully leading to significantly increased efficiencies. The ability to create non-reflective coatings from nanotube arrays would also increase the chance of photon absorption and exciton creation. However, from the results presented here this technique should also ideally be based on a covalent attachment between the nanotube and the underlying substrate. Ideally the substrate should also be highly conductive whilst remaining transparent. Work is currently being undertaken to

produce semi-conducting SWCNT by PECVD from solutions of ethanol, which can provide both the carbon source, reducing behaviour of hydrogen and the oxidising behaviour of oxygen, in effect mimicking the successful water assisted super-growth technique used for thermal CVD. Other avenues of interest would be the post-plasma treatment of grown arrays by other materials. For example doping of carbon nanotubes with nitrogen or fluorine can be undertaken in situ during growth by introducing controlled amounts of contaminant gases. These doped nanotube arrays can then be applied electronics applications and have their band structures altered to suit. Work is also currently underway on applications of carbon nanotubes into other photovoltaic designs such as deposition of p-doped SWCNT onto n-type silicon to act as an n-p heterojunction.<sup>58</sup>

New research into materials such as graphene offer great promise to provide transparent conductive layers replacing conductive oxides such as ITO and FTO.<sup>205-207</sup> This can be further expanded upon by chemical functionalisation, based on the work discussed here, of these graphene structures with other photoactive molecules. Also work has been done showing that photoluminescent graphene oxide can produce a photocurrent and this shows promise for further investigation.<sup>208</sup> There are significant experimental difficulties yet to be overcome and the work presented here provides answers to some fundamental questions governing the future directions of carbon based solar cells.

---

## **7. References**

---

1. Brunekreeft, G.; Neuhoff, K.; Newbery, D., Electricity transmission: An overview of the current debate. *Utilities Policy* **2005**, *13* (2), 73-93.
2. Smalley, R. E., Future global energy prosperity: The terawatt challenge. *MRS Bull.* **2005**, *30* (6), 412-417.
3. Becquerel, A., Mémoire sur les effets électriques produits sous l'influence des rayons solaires. *CR* **1839**, *9*, 561-567.
4. Riordan, M.; Hoddeson, L., The origins of the pn junction. *IEEE Spectrum* **1997**, *34* (6), 46-51.
5. Sze, S. M.; Ng, K. K., *Physics of Semiconductor Devices*. 3rd ed.; John Wiley & Sons, Inc: Hoboken, New Jersey, 2007.
6. Bird, R. E.; Hulstrom, R. L.; Lewis, L. J., Terrestrial solar spectral data sets. *Sol. Energy* **1983**, *30* (6), 563-573.
7. Cui, Y.; Duan, X. F.; Hu, J. T.; Lieber, C. M., Doping and electrical transport in silicon nanowires. *J. Phys. Chem. B.* **2000**, *104* (22), 5213-5216.
8. Amisola, G. B.; Behrensmeier, R.; Galligan, J. M.; Otter, F. A.; Namavar, F.; Kalkoran, N. M., Scanning Probe Microscopy and Scanning Tunneling Spectroscopy of Porous Silicon. *Appl. Phys. Lett.* **1992**, *61* (21), 2595-2597.
9. Street, R. A., Doping and the Fermi Energy in Amorphous Silicon. *Phys. Rev. Lett.* **1982**, *49* (16), 1187.
10. Tripanagnostopoulos, Y.; Souliotis, M.; Battisti, R.; Corrado, A., Energy, cost and LCA results of PV and hybrid PV/T solar systems. *Progress in Photovoltaics: Research and Applications* **2005**, *13* (3), 235-250.
11. Tsakalakos, L., Nanostructures for photovoltaics. *Mater. Sci. Eng. R-Rep* **2008**, *62* (6), 175-189.
12. O'Regan, B.; Grätzel, M., A Low-Cost, High-Efficiency Solar Cell Based on Dye-Sensitized Colloidal TiO<sub>2</sub> Films. *Nature* **1991**, *353* (6346), 737-740.

13. Calandra, P.; Calogero, G.; Sinopoli, A.; Gucciardi, P. G., Metal Nanoparticles and Carbon-Based Nanostructures as Advanced Materials for Cathode Application in Dye-Sensitized Solar Cells. *Int. J. Photoenergy* **2010**, Article ID 109495, 15 Pages.
- 13a. Grätzel, M., Photoelectrochemical cells. *Nature* **2001**, 414 (6861), 338-344.
14. Grätzel, M., Conversion of sunlight to electric power by nanocrystalline dye-sensitized solar cells. *J. Photoch. Photobio. A* **2004**, 164 (1-3), 3-14.
15. Nazeeruddin, M. K.; Kay, A.; Rodicio, I.; Humphrybaker, R.; Muller, E.; Liska, P.; Vlachopoulos, N.; Grätzel, M., Conversion of Light to Electricity by *cis*-X<sub>2</sub>Bis(2,2'-bipyridyl-4,4'-dicarboxylate)ruthenium(II) Charge-Transfer Sensitizers (X = Cl-, Br-, I-, CN-, and SCN-) on Nanocrystalline TiO<sub>2</sub> Electrodes. *J. Am. Chem. Soc.* **1993**, 115 (14), 6382-6390.
16. Zakeeruddin, S. M.; Nazeeruddin, M. K.; Humphry-Baker, R.; Pechy, P.; Quagliotto, P.; Barolo, C.; Viscardi, G.; Grätzel, M., Design, synthesis, and application of amphiphilic ruthenium polypyridyl photosensitizers in solar cells based on nanocrystalline TiO<sub>2</sub> films. *Langmuir* **2002**, 18 (3), 952-954.
17. Horiuchi, T.; Miura, H.; Uchida, S., Highly-efficient metal-free organic dyes for dye-sensitized solar cells. *Chem. Commun.* **2003**, (24), 3036-3037.
18. Jasieniak, J.; Johnston, M.; Waclawik, E. R., Characterization of a porphyrin-containing dye-sensitized solar cell. *J. Phys. Chem. B.* **2004**, 108 (34), 12962-12971.
19. Seok, W. K.; Gupta, A. K.; Roh, S. J.; Lee, W.; Han, S. H., Synthesis and application of new Ru(II) complexes for dye-sensitized nanocrystalline TiO<sub>2</sub> solar cells. *B. Kor. Chem. Soc.* **2007**, 28 (8), 1311-1316.
20. Meyer, G. J., The 2010 Millennium Technology Grand Prize: Dye-Sensitized Solar Cells. *ACS Nano* **2010**, 4 (8), 4337-4343.
21. Kim, S.; Lee, J. K.; Kang, S. O.; Ko, J.; Yum, J. H.; Fantacci, S.; De Angelis, F.; Di Censo, D.; Nazeeruddin, M. K.; Grätzel, M., Molecular engineering of organic sensitizers for solar cell applications. *J. Am. Chem. Soc.* **2006**, 128 (51), 16701-16707.
22. Kusama, H.; Arakawa, H., Influence of benzimidazole additives in electrolytic solution on dye-sensitized solar cell performance. *J. Photoch. Photobio. A* **2004**, 162 (2-3), 441-448.

23. Usui, H.; Matsui, H.; Tanabe, N.; Yanagida, S., Improved dye-sensitized solar cells using ionic nanocomposite gel electrolytes. *J. Photoch. Photobio. A* **2004**, *164* (1-3), 97-101.
24. Fabregat-Santiago, F.; Bisquert, J.; Garcia-Belmonte, G.; Boschloo, G.; Hagfeldt, A., Influence of electrolyte in transport and recombination in dye-sensitized solar cells studied by impedance spectroscopy. *Sol. Energ. Mat. Sol. C* **2005**, *87* (1-4), 117-131.
25. Boschloo, G.; Haggman, L.; Hagfeldt, A., Quantification of the Effect of 4-tert-Butylpyridine Addition to I-/I<sup>3-</sup>- Redox Electrolytes in Dye-Sensitized Nanostructured TiO<sub>2</sub> Solar Cells. *J. Phys. Chem. B* **2006**, *110* (26), 13144-13150.
26. Kim, S.; Kim, D.; Choi, H.; Kang, M. S.; Song, K.; Kang, S. O.; Ko, J., Enhanced photovoltaic performance and long-term stability of quasi-solid-state dye-sensitized solar cells via molecular engineering. *Chem. Commun.* **2008**, (40), 4951-4953.
27. Boschloo, G.; Hagfeldt, A., Characteristics of the Iodide/Triiodide Redox Mediator in Dye-Sensitized Solar Cells. *Accounts Chem. Res.* **2009**, *42* (11), 1819-1826.
28. Hattori, S.; Wada, Y.; Yanagida, S.; Fukuzumi, S., Blue Copper Model Complexes with Distorted Tetragonal Geometry Acting as Effective Electron-Transfer Mediators in Dye-Sensitized Solar Cells. *J. Am. Chem. Soc.* **2005**, *127* (26), 9648-9654.
29. Oskam, G.; Bergeron, B. V.; Meyer, G. J.; Searson, P. C., Pseudohalogens for Dye-Sensitized TiO<sub>2</sub> Photoelectrochemical Cells. *J. Phys. Chem. B* **2001**, *105* (29), 6867-6873.
30. Wang, P.; Zakeeruddin, S. M.; Moser, J.-E.; Humphry-Baker, R.; Grätzel, M., A Solvent-Free, SeCN<sup>-</sup>/(SeCN)<sub>3</sub><sup>-</sup> Based Ionic Liquid Electrolyte for High-Efficiency Dye-Sensitized Nanocrystalline Solar Cells. *J. Am. Chem. Soc.* **2004**, *126* (23), 7164-7165.
31. Suzuki, K.; Yamaguchi, M.; Kumagai, M.; Yanagida, S., Application of Carbon Nanotubes to Counter Electrodes of Dye-sensitized Solar Cells. *Chem. Lett.* **2003**, *32* (1), 28-29.
32. Hino, T.; Ogawa, Y.; Kuramoto, N., Dye-sensitized solar cell with single-walled carbon nanotube thin film prepared by an electrolytic micelle disruption method as the counterelectrode. *Fuller. Nanotub. Car. N.* **2006**, *14* (4), 607-619.

33. Hino, T.; Ogawa, Y.; Kuramoto, N., Preparation of functionalized and non-functionalized fullerene thin films on ITO glasses and the application to a counter electrode in a dye-sensitized solar cell. *Carbon* **2006**, *44* (5), 880-887.
34. Huang, Z.; Liu, X.; Li, K.; Li, D.; Luo, Y.; Li, H.; Song, W.; Chen, L.; Meng, Q., Application of carbon materials as counter electrodes of dye-sensitized solar cells. *Electrochem. Commun.* **2007**, *9* (4), 596-598.
35. Ramasamy, E.; Lee, W. J.; Lee, D. Y.; Song, J. S., Nanocarbon counterelectrode for dye sensitized solar cells. *Appl. Phys. Lett.* **2007**, *90* (17), 173103-3.
36. Ramasamy, E.; Lee, W. J.; Lee, D. Y.; Song, J. S., Spray coated multi-wall carbon nanotube counter electrode for tri-iodide reduction in dye-sensitized solar cells. *Electrochem. Commun.* **2008**, *10* (7), 1087-1089.
37. Chen, J.; Li, K.; Luo, Y.; Guo, X.; Li, D.; Deng, M.; Huang, S.; Meng, Q., A flexible carbon counter electrode for dye-sensitized solar cells. *Carbon* **2009**, *47* (11), 2704-2708.
38. Chou, C.-S.; Yang, R.-Y.; Weng, M.-H.; Huang, C.-I., The applicability of SWCNT on the counter electrode for the dye-sensitized solar cell. *Adv. Powder Technol.* **2009**, *20* (4), 310-317.
39. Li, P.; Wu, J.; Lin, J.; Huang, M.; Huang, Y.; Li, Q., High-performance and low platinum loading Pt/Carbon black counter electrode for dye-sensitized solar cells. *Sol. Energy* **2009**, *83* (6), 845-849.
40. Liu, J.; Kuo, Y.-T.; Klabunde, K. J.; Rochford, C.; Wu, J.; Li, J., Novel Dye-Sensitized Solar Cell Architecture Using TiO<sub>2</sub>-Coated Vertically Aligned Carbon Nanofiber Arrays. *ACS Appl. Mater. Interfaces* **2009**, *1* (8), 1645-1649.
41. Wang, Y. Q.; Hu, G. Q.; Duan, X. F.; Sun, H. L.; Xue, Q. K., Microstructure and formation mechanism of titanium dioxide nanotubes. *Chem. Phys. Lett.* **2002**, *365* (5-6), 427-431.
42. Zhao, J. L.; Wang, X. H.; Chen, R. Z.; Li, L. T., Fabrication of titanium oxide nanotube arrays by anodic oxidation. *Solid State Commun.* **2005**, *134* (10), 705-710.
43. Law, M.; Greene, L. E.; Johnson, J. C.; Saykally, R.; Yang, P. D., Nanowire dye-sensitized solar cells. *Nat. Mater.* **2005**, *4* (6), 455-459.

44. Jung, K. H.; Hong, J. S.; Vittal, R.; Kim, K. J., Enhanced photocurrent of dye-sensitized solar cells by modification of TiO<sub>2</sub> with carbon nanotubes. *Chem. Lett.* **2002**, (8), 864-865.
45. Sun, J.; Iwasa, M.; Gao, L.; Zhang, Q., Single-walled carbon nanotubes coated with titania nanoparticles. *Carbon* **2004**, 42 (4), 895-899.
46. Jung, K. H.; Jang, S. R.; Vittal, R.; Kim, V. D.; Kim, K. J., Photocurrent improvement by incorporation of single-wall carbon nanotubes in TiO<sub>2</sub> film of dye-sensitized solar cells. *B. Kor. Chem. Soc.* **2003**, 24 (10), 1501-1504.
47. Ferrere, S.; Zaban, A.; Gregg, B. A., Dye Sensitization of Nanocrystalline Tin Oxide by Perylene Derivatives. *J. Phys. Chem. B* **1997**, 101 (23), 4490-4493.
48. Nusbaumer, H.; Moser, J.-E.; Zakeeruddin, S. M.; Nazeeruddin, M. K.; Grätzel, M., CoII(dbbip)<sub>2</sub><sup>2+</sup> Complex Rivals Tri-iodide/Iodide Redox Mediator in Dye-Sensitized Photovoltaic Cells. *J. Phys. Chem. B* **2001**, 105 (43), 10461-10464.
49. Barazzouk, S.; Hotchandani, S.; Vinodgopal, K.; Kamat, P. V., Single-Wall Carbon Nanotube Films for Photocurrent Generation. A Prompt Response to Visible-Light Irradiation. *J. Phys. Chem. B.* **2004**, 108 (44), 17015-17018.
50. Lee, J. U., Photovoltaic effect in ideal carbon nanotube diodes. *Appl. Phys. Lett.* **2005**, 87 (7), 073101.
51. Castrucci, P.; Tombolini, F.; Scarselli, M.; Speiser, E.; Gobbo, S. D.; Richter, W.; Crescenzi, M. D.; Diociaiuti, M.; Gatto, E.; Venanzi, M., Large photocurrent generation in multiwall carbon nanotubes. *Appl. Phys. Lett.* **2006**, 89 (25), 253107.
52. Kamat, P. V., Harvesting photons with carbon nanotubes. *Nano Today* **2006**, 1 (4), 20-27.
53. Kongkanand, A.; Martinez Dominguez, R.; Kamat, P. V., Single Wall Carbon Nanotube Scaffolds for Photoelectrochemical Solar Cells. Capture and Transport of Photogenerated Electrons. *Nano Lett.* **2007**, 7 (3), 676-680.
54. Liu, G.; Liu, Z.; Zhao, Y.; Zheng, K.; Huang, H.; Ma, W.; Gu, C.; Sun, L.; Xie, S., Large photocurrent generated by a camera flash in single-walled carbon nanotubes. *J. Phys. D Appl. Phys.* **2007**, 40 (22), 6898-6901.

55. Umeyama, T.; Fujita, M.; Tezuka, N.; Kadota, N.; Matano, Y.; Yoshida, K.; Isoda, S.; Imahori, H., Electrophoretic Deposition of Single-Walled Carbon Nanotubes Covalently Modified with Bulky Porphyrins on Nanostructured SnO<sub>2</sub> Electrodes for Photoelectrochemical Devices. *J. Phys. Chem. C* **2007**, *111* (30), 11484-11493.
56. Wei, J.; Jia, Y.; Shu, Q.; Gu, Z.; Wang, K.; Zhuang, D.; Zhang, G.; Wang, Z.; Luo, J.; Cao, A.; Wu, D., Double-Walled Carbon Nanotube Solar Cells. *Nano Lett.* **2007**, *7* (8), 2317-2321.
57. Shi, Y.; Fu, D.; Marsh, D. H.; Rance, G. A.; Khlobystov, A. N.; Li, L.-J., Photoresponse in Self-Assembled Films of Carbon Nanotubes. *J. Phys. Chem. C* **2008**, *112* (33), 13004-13009.
58. Li, Z.; Kunets, V. P.; Saini, V.; Xu, Y.; Dervishi, E.; Salamo, G. J.; Biris, A. R.; Biris, A. S., Light-Harvesting Using High Density p-type Single Wall Carbon Nanotube/n-type Silicon Heterojunctions. *ACS Nano* **2009**, *3* (6), 1407-1414.
59. Zhu, H.; Wei, J.; Wang, K.; Wu, D., Applications of carbon materials in photovoltaic solar cells. *Sol. Energ. Mat. Sol. C.* **2009**, *93* (9), 1461-1470.
60. Bissett, M. A.; Shapter, J. G., Photocurrent Response from Vertically Aligned Single-Walled Carbon Nanotube Arrays. *J. Phys. Chem. C* **2010**, *114* (14), 6778-6783.
61. Tune, D. D.; Flavel, B. S.; Quinton, J. S.; Ellis, A. V.; Shapter, J. G., Single walled carbon nanotube network electrodes for dye solar cells. *Sol. Energ. Mat. Sol. C.* **2010**, *94* (10), 1665-1672.
62. Iijima, S., Helical microtubules of graphitic carbon. *Nature* **1991**, *354* (6348), 56-58.
63. Hong, S.; Myung, S., Nanotube Electronics: A flexible approach to mobility. *Nat Nano* **2007**, *2* (4), 207-208.
64. Martel, R.; Schmidt, T.; Shea, H. R.; Hertel, T.; Ph, A., Single- and multi-wall carbon nanotube field-effect transistors. *Appl. Phys. Lett.* **1998**, *73* (17), 2447-2449.
65. Postma, H. W. C.; Teepen, T.; Yao, Z.; Grifoni, M.; Dekker, C., Carbon nanotube single-electron transistors at room temperature. *Science* **2001**, *293* (5527), 76-79.
66. Saito, R.; Dresselhaus, G.; Dresselhaus, M. S., *Physical Properties of Carbon Nanotubes*. Imperial College Press: London, 1998.

67. Zhang, M.; Fang, S. L.; Zakhidov, A. A.; Lee, S. B.; Aliev, A. E.; Williams, C. D.; Atkinson, K. R.; Baughman, R. H., Strong, transparent, multifunctional, carbon nanotube sheets. *Science* **2005**, *309* (5738), 1215-1219.
68. Dekker, C., Carbon nanotubes as molecular quantum wires. *Physics Today* **1999**, *52* (5), 22-28.
69. Dresselhaus, M. S.; Dresselhaus, G.; Saito, R.; Jorio, A., Raman spectroscopy of carbon nanotubes. *Phys. Rep.* **2005**, *409* (2), 47-99.
70. Ebbesen, T. W.; Ajayan, P. M., Large-scale synthesis of carbon nanotubes. *Nature* **1992**, *358* (6383), 220-222.
71. Guo, T.; Nikolaev, P.; Thess, A.; Colbert, D. T.; Smalley, R. E., Catalytic growth of single-walled nanotubes by laser vaporization. *Chem. Phys. Lett.* **1995**, *243* (1-2), 49-54.
72. Hata, K.; Futaba, D. N.; Mizuno, K.; Namai, T.; Yumura, M.; Iijima, S., Water-Assisted Highly Efficient Synthesis of Impurity-Free Single-Walled Carbon Nanotubes. *Science* **2004**, *306* (5700), 1362-1364.
73. Ostrikov, K.; Yoon, H.-J.; Rider, A. E.; Vladimirov, S. V., Two-Dimensional Simulation of Nanoassembly Precursor Species in Ar+H<sub>2</sub>+C<sub>2</sub>H<sub>2</sub> Reactive Plasmas. *Plasma Process. Polym.* **2007**, *4* (1), 27-40.
74. Cui, H.; Zhou, O.; Stoner, B. R., Deposition of aligned bamboo-like carbon nanotubes via microwave plasma enhanced chemical vapor deposition. *J. Appl. Phys.* **2000**, *88* (10), 6072-6074.
75. Bower, C.; Zhu, W.; Jin, S.; Zhou, O., Plasma-induced alignment of carbon nanotubes. *Appl. Phys. Lett.* **2000**, *77* (6), 830-832.
76. Hofmann, S.; Ducati, C.; Robertson, J.; Kleinsorge, B., Low-temperature growth of carbon nanotubes by plasma-enhanced chemical vapor deposition. *Appl. Phys. Lett.* **2003**, *83* (1), 135-137.
77. Bell, M. S.; Lacerda, R. G.; Teo, K. B. K.; Rupesinghe, N. L.; Amaratunga, G. A. J.; Milne, W. I.; Chhowalla, M., Plasma composition during plasma-enhanced chemical vapor deposition of carbon nanotubes. *Appl. Phys. Lett.* **2004**, *85* (7), 1137-1139.

78. Okita, A.; Suda, Y.; Oda, A.; Nakamura, J.; Ozeki, A.; Bhattacharyya, K.; Sugawara, H.; Sakai, Y., Effects of hydrogen on carbon nanotube formation in CH<sub>4</sub>/H<sub>2</sub> plasmas. *Carbon* **2007**, *45* (7), 1518-1526.
79. Hiramatsu, M.; Shiji, K.; Amano, H.; Hori, M., Fabrication of vertically aligned carbon nanowalls using capacitively coupled plasma-enhanced chemical vapor deposition assisted by hydrogen radical injection. *Appl. Phys. Lett.* **2004**, *84* (23), 4708-4710.
80. Delzeit, L.; McAninch, I.; Cruden, B. A.; Hash, D.; Chen, B.; Han, J.; Meyyappan, M., Growth of multiwall carbon nanotubes in an inductively coupled plasma reactor. *J. Appl. Phys.* **2002**, *91* (9), 6027-6033.
81. Denysenko, I. B.; Xu, S.; Long, J. D.; Rutkevych, P. P.; Azarenkov, N. A.; Ostrikov, K., Inductively coupled Ar/CH<sub>4</sub>/H<sub>2</sub> plasmas for low-temperature deposition of ordered carbon nanostructures. *J. Appl. Phys.* **2004**, *95* (5), 2713-2724.
82. Weng, C. H.; Yang, C. S.; Lin, H.; Tsai, C. H.; Leou, K. C., Low Temperature Synthesis of Single-Walled Carbon Nanotubes in an Inductively Coupled Plasma Chemical Vapor Deposition System. *J. Nanosci. Nanotechnol.* **2008**, *8*, 2526-2533.
83. Mao, M.; Bogaerts, A., Investigating the plasma chemistry for the synthesis of carbon nanotubes/nanofibres in an inductively coupled plasma enhanced CVD system: the effect of different gas mixtures. *J. Phys. D Appl. Phys.* **2010**, *43* (20), 205201.
84. Meyyappan, M.; Delzeit, L.; Cassell, A.; Hash, D., Carbon nanotube growth by PECVD: a review. *Plasma Sources Sci. T.* **2003**, *12* (2), 205.
85. Meyyappan, M., A review of plasma enhanced chemical vapour deposition of carbon nanotubes. *J. Phys. D Appl. Phys.* **2009**, *42* (21), 213001.
86. Jang, S. R.; Vittal, R.; Kim, K. J., Incorporation of functionalized single-wall carbon nanotubes in dye-sensitized TiO<sub>2</sub> solar cells. *Langmuir* **2004**, *20* (22), 9807-9810.
87. Zhang, Y.; Iijima, S., Elastic Response of Carbon Nanotube Bundles to Visible Light. *Phys. Rev. Lett.* **1999**, *82* (17), 3472.
88. Mele, E. J.; Král, P.; Tománek, D., Coherent control of photocurrents in graphene and carbon nanotubes. *Phys. Rev. B* **2000**, *61* (11), 7669.

89. Freitag, M.; Martin, Y.; Misewich, J. A.; Martel, R.; Avouris, P., Photoconductivity of Single Carbon Nanotubes. *Nano Lett.* **2003**, *3* (8), 1067-1071.
90. Khakani, M. A. E.; Borgne, V. L.; Aissa, B.; Rosei, F.; Scilletta, C.; Speiser, E.; Scarselli, M.; Castrucci, P.; Crescenzi, M. D., Photocurrent generation in random networks of multiwall-carbon-nanotubes grown by an "all-laser" process. *Appl. Phys. Lett.* **2009**, *95* (8), 083114.
91. Dissanayake, N. M.; Zhong, Z., Unexpected Hole Transfer Leads to High Efficiency Single-Walled Carbon Nanotube Hybrid Photovoltaic. *Nano Lett.* **2011**, *11* (1), 286-290.
92. Hasobe, T.; Fukuzumi, S.; Kamat, P. V., Organized assemblies of single wall carbon nanotubes and porphyrin for photochemical solar cells: Charge injection from excited porphyrin into single-walled carbon nanotubes. *J. Phys. Chem. B.* **2006**, *110* (50), 25477-25484.
93. Ren, D. M.; Guo, Z.; Du, F.; Zheng, J. Y.; Chen, Y. S., Nanohybrid material of SWNTs covalently functionalized with porphyrin for light harvesting antenna: Synthesis and photophysical properties. *J. Nanosci. Nanotechno.* **2007**, *7* (4-5), 1539-1545.
94. Yu, J.; Mathew, S.; Flavel, B. S.; Johnston, M. R.; Shapter, J. G., Ruthenium Porphyrin Functionalized Single-Walled Carbon Nanotube Arrays; A Step Toward Light Harvesting Antenna and Multibit Information Storage. *J. Am. Chem. Soc.* **2008**, *130* (27), 8788-8796.
95. Palacin, T.; Khanh, H. L.; Joussetme, B.; Jegou, P.; Filoramo, A.; Ehli, C.; Guldi, D. M.; Campidelli, S. p., Efficient Functionalization of Carbon Nanotubes with Porphyrin Dendrons via Click Chemistry. *J. Am. Chem. Soc.* **2009**, *131* (42), 15394-15402.
96. Bissett, M. A.; Shapter, J. G., Electrochemistry and Photocurrent Response from Vertically-Aligned Chemically-Functionalized Single-Walled Carbon Nanotube Arrays. *J. Electrochem. Soc.* **2011**, *158* (3), K53-K57.
97. Valentini, L.; Armentano, I.; Ricco, L.; Alongi, J.; Pennelli, G.; Mariani, A.; Russo, S.; Kenny, J. M., Selective interaction of single-walled carbon nanotubes with conducting dendrimer. *Diam. Relat. Mater.* **2006**, *15* (1), 95-99.
98. Pan, B. F.; Cui, D. X.; Gao, F.; He, R., Growth of multi-amine terminated poly(amidoamine) dendrimers on the surface of carbon nanotubes. *Nanotechnology* **2006**, *17* (10), 2483-2489.

99. Jiang, G.; Wang, L.; Chen, C.; Dong, X.; Chen, T.; Yu, H., Study on attachment of highly branched molecules onto multiwalled carbon nanotubes. *Mater. Lett.* **2005**, *59* (16), 2085-2089.
100. Nantalaksakul, A.; Reddy, D.; Bardeen, C.; Thayumanavan, S., Light Harvesting Dendrimers. *Photosynth. Res.* **2006**, *87* (1), 133-150.
101. Adronov, A.; Frechet, J. M. J., Light-harvesting dendrimers. *Chem. Commun.* **2000**, (18), 1701-1710.
102. Satoh, N.; Nakashima, T.; Yamamoto, K., Metal-Assembling Dendrimers with a Triarylamine Core and Their Application to a Dye-Sensitized Solar Cell. *J. Am. Chem. Soc.* **2005**, *127* (37), 13030-13038.
103. Lu, J.; Xia, P. F.; Lo, P. K.; Tao, Y.; Wong, M. S., Synthesis and Properties of Multi-Triarylamine-Substituted Carbazole-Based Dendrimers with an Oligothiophene Core for Potential Applications in Organic Solar Cells and Light-Emitting Diodes. *Chem. Mater.* **2006**, *18* (26), 6194-6203.
104. Peng, Z.; Melinger, J.; Kleiman, V., Light Harvesting Unsymmetrical Conjugated Dendrimers as Photosynthetic Mimics. *Photosynth. Res.* **2006**, *87* (1), 115-131.
105. Satoh, N.; Takashima, T.; Albrecht, K.; Yamamoto, K., Dye-sensitized Solar Cell using pi-Conjugated Dendrimer. *J. Photopolym. Sci. Tec.* **2006**, *19* (2), 141-142.
106. Sun, J.-T.; Hong, C.-Y.; Pan, C.-Y., Surface modification of carbon nanotubes with dendrimers or hyperbranched polymers. *Polymer Chemistry* **2011**, *2* (5), 998-1007.
107. Martin, I. K.; Twyman, L. J., The synthesis of unsymmetrical PAMAM dendrimers using a divergent/divergent approach. *Tetrahedron Lett.* **2001**, *42* (6), 1119-1121.
108. Hobson, L. J.; Feast, W. J., Poly(amidoamine) hyperbranched systems: synthesis, structure and characterization. *Polymer* **1999**, *40* (5), 1279-1297.
109. Tomalia, D. A.; Baker, H.; Dewald, J.; Hall, M.; Kallos, G.; Martin, S.; Roeck, J.; Ryder, J.; Smith, P., A New Class of Polymers: Starburst-Dendritic Macromolecules. *Polym. J.* **1985**, *17* (1), 117-132.

110. Storrier, G. D.; Takada, K.; Abruna, H. D., Synthesis, Characterization, Electrochemistry, and EQCM Studies of Polyamidoamine Dendrimers Surface-Functionalized with Polypyridyl Metal Complexes. *Langmuir* **1999**, *15* (3), 872-884.
111. Frechet, J. M. J.; Tomalia, D. A., *Dendrimers and other Dendritic Polymers*. John Wiley & Sons, Ltd.: Chichester, 2001.
112. Michael, A., Ueber die Addition von Natriumacetessig- und Natriummalonsäureäthern zu den Aethern ungesättigter Säuren. *Journal für Praktische Chemie* **1887**, *35* (1), 349-356.
113. Nakashima, T.; Satoh, N.; Albrecht, K.; Yamamoto, K., Interface Modification on TiO<sub>2</sub> Electrode Using Dendrimers in Dye-Sensitized Solar Cells. *Chem. Mater.* **2008**, *20* (7), 2538-2543.
114. Siegers, C.; Olàh, B.; Würfel, U.; Hohl-Ebinger, J.; Hinsch, A.; Haag, R., Donor-acceptor-functionalized polymers for efficient light harvesting in the dye solar cell. *Sol. Energ. Mat. Sol. C.* **2009**, *93* (5), 552-563.
115. Marshall, M. W.; Popa-Nita, S.; Shapter, J. G., Measurement of functionalised carbon nanotube carboxylic acid groups using a simple chemical process. *Carbon* **2006**, *44* (7), 1137-1141.
116. Yu, J. X.; Losic, D.; Marshall, M.; Bocking, T.; Gooding, J. J.; Shapter, J. G., Preparation and characterisation of an aligned carbon nanotube array on the silicon (100) surface. *Soft Matter* **2006**, *2* (12), 1081-1088.
117. Gooding, J. J.; Wibowo, R.; Liu, J.; Yang, W.; Losic, D.; Orbons, S.; Mearns, F. J.; Shapter, J. G.; Hibbert, D. B., Protein Electrochemistry Using Aligned Carbon Nanotube Arrays. *J. Am. Chem. Soc.* **2003**, *125* (30), 9006-9007.
118. Liu, J.; Rinzler, A. G.; Dai, H.; Hafner, J. H.; Bradley, R. K.; Boul, P. J.; Lu, A.; Iverson, T.; Shelimov, K.; Huffman, C. B.; Rodriguez-Macias, F.; Shon, Y.-S.; Lee, T. R.; Colbert, D. T.; Smalley, R. E., Fullerene Pipes. *Science* **1998**, *280* (5367), 1253-1256.
119. Liu, Z.; Shen, Z.; Zhu, T.; Hou, S.; Ying, L.; Shi, Z.; Gu, Z., Organizing Single-Walled Carbon Nanotubes on Gold Using a Wet Chemical Self-Assembling Technique. *Langmuir* **2000**, *16* (8), 3569-3573.

120. Flavel, B. S.; Yu, J.; Shapter, J. G.; Quinton, J. S., Patterned attachment of carbon nanotubes to silane modified silicon. *Carbon* **2007**, *45* (13), 2551-2558.
121. Yu, J. X.; Shapter, J. G.; Quinton, J. S.; Johnston, M. R.; Beattie, D. A., Direct attachment of well-aligned single-walled carbon nanotube architectures to silicon (100) surfaces: a simple approach for device assembly. *Phys. Chem. Chem. Phys.* **2007**, *9* (4), 510-520.
122. Flavel, B. S.; Yu, J. X.; Shapter, J. G.; Quinton, J. S., Patterned ferrocenemethanol modified carbon nanotube electrodes on silane modified silicon. *J. Mater. Chem.* **2007**, *17* (45), 4757-4761.
123. Yu, J.; Shapter, J. G.; Johnston, M. R.; Quinton, J. S.; Gooding, J. J., Electron-transfer characteristics of ferrocene attached to single-walled carbon nanotubes (SWCNT) arrays directly anchored to silicon(1 0 0). *Electrochim. Acta* **2007**, *52* (21), 6206-6211.
124. Yu, J.; Flavel, B. S.; Shapter, J. G., Optical and electrochemical properties of single-walled carbon nanotube arrays attached to silicon(100) surfaces. *Fuller. Nanotub. Car. N.* **2008**, *16* (1), 18-29.
125. Constantopoulos, K. T.; Shearer, C. J.; Ellis, A. V.; Voelcker, N. H.; Shapter, J. G., Carbon Nanotubes Anchored to Silicon for Device Fabrication. *Adv. Mater.* **2010**, *22* (5), 557-571.
126. Lu, Q.; Liu, K.; Zhang, H.; Du, Z.; Wang, X.; Wang, F., From Tunneling to Hopping: A Comprehensive Investigation of Charge Transport Mechanism in Molecular Junctions Based on Oligo(p-phenylene ethynylene)s. *ACS Nano* **2009**, *3* (12), 3861-3868.
127. Yamada, T.; Maigne, A.; Yudasaka, M.; Mizuno, K.; Futaba, D. N.; Yumura, M.; Iijima, S.; Hata, K., Revealing the Secret of Water-Assisted Carbon Nanotube Synthesis by Microscopic Observation of the Interaction of Water on the Catalysts. *Nano Lett.* **2008**, *8* (12), 4288-4292.
128. Amama, P. B.; Pint, C. L.; McJilton, L.; Kim, S. M.; Stach, E. A.; Murray, P. T.; Hauge, R. H.; Maruyama, B., Role of Water in Super Growth of Single-Walled Carbon Nanotube Carpets. *Nano Lett.* **2008**, *9* (1), 44-49.
129. Laviron, E., The use of linear potential sweep voltammetry and of a.c. voltammetry for the study of the surface electrochemical reaction of strongly adsorbed systems and of redox modified electrodes. *J. Electroanal. Chem.* **1979**, *100* (1-2), 263-270.

130. Laviron, E., Adsorption, autoinhibition and autocatalysis in polarography and in linear potential sweep voltammetry. *J. Electroanal. Chem.* **1974**, *52* (3), 355-393.
131. Laviron, E., General expression of the linear potential sweep voltammogram in the case of diffusionless electrochemical systems. *J. Electroanal. Chem.* **1979**, *101* (1), 19-28.
132. Flavel, B. S.; Yu, J. X.; Ellis, A. V.; Shapter, J. G., Electroless plated gold as a support for carbon nanotube electrodes. *Electrochimica Acta* **2009**, *54* (11), 3191-3198.
133. Ye, B. X., The study of electrochemical characteristics of methotrexate. *Journal of the Chinese Chemical Society* **2005**, *52* (6), 1111-1116.
134. Barsoukov, E.; Macdonald, J. R., *Impedance Spectroscopy: Theory, Experiment, and Applications*. 2nd ed.; Wiley: Hoboken, New Jersey, 2005.
135. Hauch, A.; Georg, A., Diffusion in the electrolyte and charge-transfer reaction at the platinum electrode in dye-sensitized solar cells. *Electrochim. Acta* **2001**, *46* (22), 3457-3466.
136. Kern, R.; Sastrawan, R.; Ferber, J.; Stangl, R.; Luther, J., Modeling and interpretation of electrical impedance spectra of dye solar cells operated under open-circuit conditions. *Electrochim. Acta* **2002**, *47* (26), 4213-4225.
137. Longo, C.; Nogueira, A. F.; De Paoli, M. A.; Cachet, H., Solid-State and Flexible Dye-Sensitized TiO<sub>2</sub> Solar Cells: a Study by Electrochemical Impedance Spectroscopy. *J. Phys. Chem. B.* **2002**, *106* (23), 5925-5930.
138. Wang, Q.; Moser, J. E.; Grätzel, M., Electrochemical Impedance Spectroscopic Analysis of Dye-Sensitized Solar Cells. *J. Phys. Chem. B.* **2005**, *109* (31), 14945-14953.
139. Koo, B.-K.; Lee, D.-Y.; Kim, H.-J.; Lee, W.-J.; Song, J.-S.; Kim, H.-J., Seasoning effect of dye-sensitized solar cells with different counter electrodes. *J. Electroceram.* **2006**, *17* (1), 79-82.
140. Liberatore, M.; Decker, F.; Burtone, L.; Zardetto, V.; Brown, T.; Reale, A.; Di Carlo, A., Using EIS for diagnosis of dye-sensitized solar cells performance. *J. Appl. Electrochem.* **2009**, *39* (11), 2291-2295.
141. Raman, C. V.; Krishnan, K. S., A New Type of Secondary Radiation. *Nature* **1928**, *121*, 501-502.

142. Dresselhaus, M. S.; Dresselhaus, G.; Jorio, A.; Souza Filho, A. G.; Pimenta, M. A.; Saito, R., Single Nanotube Raman Spectroscopy. *Accounts Chem. Res.* **2002**, *35* (12), 1070-1078.
143. Dresselhaus, M. S.; Dresselhaus, G.; Jorio, A.; Souza Filho, A. G.; Saito, R., Raman spectroscopy on isolated single wall carbon nanotubes. *Carbon* **2002**, *40* (12), 2043-2061.
144. Filho, A. G. S.; Jorio, A.; Samsonidze, G. G.; Dresselhaus, G.; Saito, R.; Dresselhaus, M. S., Raman spectroscopy for probing chemically/physically induced phenomena in carbon nanotubes. *Nanotechnology* **2003**, *14* (10), 1130-1139.
145. Jorio, A.; Pimenta, M. A.; Filho, A. G. S.; Saito, R.; Dresselhaus, G.; Dresselhaus, M. S., Characterizing carbon nanotube samples with resonance Raman scattering. *New J. Phys.* **2003**, *5*, 139-139.
146. Dresselhaus, M. S.; Dresselhaus, G.; Hofmann, M., The big picture of Raman scattering in carbon nanotubes. *Vib. Spectrosc.* **2007**, *45* (2), 71-81.
147. Chou, S. G.; Son, H.; Kong, J.; Jorio, A.; Saito, R.; Zheng, M.; Dresselhaus, G.; Dresselhaus, M. S., Length characterization of DNA-wrapped carbon nanotubes using Raman spectroscopy. *Appl. Phys. Lett.* **2007**, *90* (13), 131109-3.
148. Merchant, C. A.; Marković, N., The photoresponse of spray-coated and free-standing carbon nanotube films with Schottky contacts. *Nanotechnology* **2009**, *20* (17), 175202.
149. Li, C.-Z.; Choi, W.-B.; Chuang, C.-H., Size effects on the photoelectrochemical activities of single wall carbon nanotubes. *Electrochim. Acta* **2008**, *54* (2), 821-828.
150. Balasubramanian, K.; Fan, Y.; Burghard, M.; Kern, K.; Friedrich, M.; Wannek, U.; Mews, A., Photoelectronic transport imaging of individual semiconducting carbon nanotubes. *Appl. Phys. Lett.* **2004**, *84* (13), 2400-2402.
151. Gooding, J. J., Nanostructuring electrodes with carbon nanotubes: A review on electrochemistry and applications for sensing. *Electrochim. Acta* **2005**, *50* (15), 3049-3060.
152. Flavel, B. S.; Garrett, D. J.; Lehr, J.; Shapter, J. G.; Downard, A. J., Chemically immobilised carbon nanotubes on silicon: Stable surfaces for aqueous electrochemistry. *Electrochim. Acta* **2010**, *55* (12), 3995-4001.

153. Gooding, J. J.; Chou, A.; Liu, J.; Losic, D.; Shapter, J. G.; Hibbert, D. B., The effects of the lengths and orientations of single-walled carbon nanotubes on the electrochemistry of nanotube-modified electrodes. *Electrochem. Commun.* **2007**, *9* (7), 1677-1683.
154. Diao, P.; Liu, Z., Vertically Aligned Single-Walled Carbon Nanotubes by Chemical Assembly – Methodology, Properties, and Applications. *Adv. Mater.* **2010**, *22* (13), 1430-1449.
155. Moulder, J. F.; Stickle, W. F.; Sobol, P. E.; Bomben, K. D., *Handbook of X-Ray Photoelectron Spectroscopy*. Physical Electronics, Inc.: Eden Prairie, 1995.
156. Okpalugo, T. I. T.; Papakonstantinou, P.; Murphy, H.; McLaughlin, J.; Brown, N. M. D., High resolution XPS characterization of chemical functionalised MWCNTs and SWCNTs. *Carbon* **2005**, *43* (1), 153-161.
157. Fan, B.; Mei, X.; Sun, K.; Ouyang, J., Conducting polymer/carbon nanotube composite as counter electrode of dye-sensitized solar cells. *Appl. Phys. Lett.* **2008**, *93* (14), 143103-3.
158. Murakami, T. N.; Grätzel, M., Counter electrodes for DSC: Application of functional materials as catalysts. *Inorg. Chim. Acta* **2008**, *361* (3), 572-580.
159. Trancik, J. E.; Barton, S. C.; Hone, J., Transparent and Catalytic Carbon Nanotube Films. *Nano Lett.* **2008**, *8* (4), 982-987.
160. Dang, X.; Yi, H.; Ham, M.-H.; Qi, J.; Yun, D. S.; Ladewski, R.; Strano, M. S.; Hammond, P. T.; Belcher, A. M., Virus-templated self-assembled single-walled carbon nanotubes for highly efficient electron collection in photovoltaic devices. *Nat. Nanotechnol.* **2011**, *6* (6), 377-384.
- 160a. Jang, S. R.; Vittal, R.; Lee, J. W.; Jeong, N.; Kim, K. J., Linkage of N3 dye to N3 dye on nanocrystalline TiO<sub>2</sub> through trans-1,2-bis(4-pyridyl) ethylene for enhancement of photocurrent of dye-sensitized solar cells. *Chem. Commun.* **2006**, (1), 103-105.
161. Klingler, R. J.; Kochi, J. K., Electron-transfer kinetics from cyclic voltammetry. Quantitative description of electrochemical reversibility. *J. Phys. Chem.* **1981**, *85* (12), 1731-1741.
162. Tu, W.; Lei, J.; Ju, H., Noncovalent nanoassembly of porphyrin on single-walled carbon nanotubes for electrocatalytic reduction of nitric oxide and oxygen. *Electrochem. Commun.* **2008**, *10* (5), 766-769.

163. Umeyama, T.; Imahori, H., Carbon nanotube-modified electrodes for solar energy conversion. *Energ. Environ. Sci.* **2008**, *1* (1), 120-133.
164. Brown, P.; Takechi, K.; Kamat, P. V., Single-Walled Carbon Nanotube Scaffolds for Dye-Sensitized Solar Cells. *J. Phys. Chem. C* **2008**, *112* (12), 4776-4782.
165. Stulz, E.; Sanders, J. K. M.; Montalti, M.; Prodi, L.; Zaccheroni, N.; Fabrizi de Biani, F.; Grigiotti, E.; Zanello, P., Phosphine and Phosphonite Complexes of a Ru(II) Porphyrin. 2. Photophysical and Electrochemical Studies. *Inorg. Chem.* **2002**, *41* (20), 5269-5275.
166. Mu, X. H.; Kadish, K. M., Applications of thin-layer FTIR, UV-vis, and ESR spectroelectrochemistry for evaluating carbonyltetraphenylporphyrinruthenium redox reactions in nonaqueous media. *Langmuir* **1990**, *6* (1), 51-56.
167. Brown, G. M.; Hopf, F. R.; Ferguson, J. A.; Meyer, T. J.; Whitten, D. G., Metalloporphyrin redox chemistry. Effect of extraplanar ligands on the site of oxidation in ruthenium porphyrins. *J. Am. Chem. Soc.* **1973**, *95* (18), 5939-5942.
168. Mu, X. H.; Kadish, K. M., Applications of Thin-Layer FTIR, UV-vis, and ESR Spectroelectrochemistry for Evaluating (TPP)Ru(CO) Redox Reactions in Nonaqueous Media. *Langmuir* **1990**, *6* (1), 51-56.
169. Kadish, K. M.; Hu, Y.; Tagliatesta, P.; Boschi, T., Synthesis and electrochemical characterization of ruthenium porphyrins containing a bound PF<sub>3</sub> axial ligand. *J. Chem. Soc., Dalton Trans.* **1993**, 1167-1172.
170. Malinski, T.; Chang, D.; Bottomley, L. A.; Kadish, K. M., Substituent effects on the redox reactions of para-substituted tetraphenylporphyrin complexes of ruthenium(II). *Inorg. Chem.* **1982**, *21* (12), 4248-4253.
171. Kadish, K. M.; Chang, D., Solvent-binding and solvation effects on the electrode reactions of tetraphenylporphyrin carbonyl complexes of ruthenium(II). *Inorg. Chem.* **1982**, *21* (10), 3614-3618.
172. Kadish, K. M.; Leggett, D. J.; Chang, D., Investigation of the electrochemical reactivity and axial ligand binding reactions of tetraphenylporphyrin carbonyl complexes of ruthenium(II). *Inorg. Chem.* **1982**, *21* (10), 3618-3622.

173. Davis, A. P.; Ma, G.; Allen, H. C., Surface vibrational sum frequency and Raman studies of PAMAM G0, G1 and acylated PAMAM G0 dendrimers. *Anal. Chim. Acta* **2003**, *496* (1-2), 117-131.
174. Lee, J. W.; Kim, J. H.; Kim, H. J.; Han, S. C.; Kim, J. H.; Shin, W. S.; Jin, S.-H., Synthesis of Symmetrical and Unsymmetrical PAMAM Dendrimers by Fusion between Azide- and Alkyne-Functionalized PAMAM Dendrons. *Bioconjugate Chem.* **2007**, *18* (2), 579-584.
175. Hammerich, O.; Hansen, T.; Thorvildsen, A.; Christensen, J. B., Electrochemical One-Electron Oxidation of Low-Generation Polyamidoamine-Type Dendrimers with a 1,4-Phenylenediamine Core. *ChemPhysChem* **2009**, *10* (11), 1805-1824.
176. Chung, Y. C.; Su, Y. O., Effects of Phenyl- and Methyl-Substituents on p-Phenylenediamine, an Electrochemical and Spectral Study. *J. Chin. Chem. Soc-Taipei* **2009**, *56* (3), 493-503.
177. Cardona, C. M.; McCarley, T. D.; Kaifer, A. E., Synthesis, Electrochemistry, and Interactions with  $\beta$ -Cyclodextrin of Dendrimers Containing a Single Ferrocene Subunit Located "Off-Center". *J. Org. Chem.* **2000**, *65* (6), 1857-1864.
178. Cardona, C. M.; Kaifer, A. E., Asymmetric Redox-Active Dendrimers Containing a Ferrocene Subunit. Preparation, Characterization, and Electrochemistry. *J. Am. Chem. Soc.* **1998**, *120* (16), 4023-4024.
179. Appoh, F. E.; Thomas, D. S., Chirality and Encapsulation Properties of Disubstituted Ferrocene-Peptide Dendrimers. *Macromolecules* **2006**, *39* (17), 5629-5638.
180. Han, L.; Koide, N.; Chiba, Y.; Mitate, T., Modeling of an equivalent circuit for dye-sensitized solar cells. *Appl. Phys. Lett.* **2004**, *84* (13), 2433-2435.
181. Ren, Z. F.; Huang, Z. P.; Xu, J. W.; Wang, J. H.; Bush, P.; Siegal, M. P.; Provencio, P. N., Synthesis of Large Arrays of Well-Aligned Carbon Nanotubes on Glass. *Science* **1998**, *282* (5391), 1105-1107.
182. Huang, Z. P.; Wang, D. Z.; Wen, J. G.; Sennett, M.; Gibson, H.; Ren, Z. F., Effect of nickel, iron and cobalt on growth of aligned carbon nanotubes. *Appl. Phys. A-Mater.* **2002**, *74* (3), 387-391.

183. Mo, Y. H.; Kibria, A. K. M. F.; Nahm, K. S., The growth mechanism of carbon nanotubes from thermal cracking of acetylene over nickel catalyst supported on alumina. *Synth. Metals* **2001**, *122* (2), 443-447.
184. Chhowalla, M.; Teo, K. B. K.; Ducati, C.; Rupesinghe, N. L.; Amaratunga, G. A. J.; Ferrari, A. C.; Roy, D.; Robertson, J.; Milne, W. I., Growth process conditions of vertically aligned carbon nanotubes using plasma enhanced chemical vapor deposition. *J. Appl. Phys.* **2001**, *90* (10), 5308-5317.
185. Hatakeyama, R.; et al., Plasma-synthesized single-walled carbon nanotubes and their applications. *J. Phys. D Appl. Phys.* **2011**, *44* (17), 174004.
186. Zhang, G.; Mann, D.; Zhang, L.; Javey, A.; Li, Y.; Yenilmez, E.; Wang, Q.; McVittie, J. P.; Nishi, Y.; Gibbons, J.; Dai, H., Ultra-high-yield growth of vertical single-walled carbon nanotubes: Hidden roles of hydrogen and oxygen. *P. Natl. Acad. Sci. USA* **2005**, *102* (45), 16141-16145.
187. Lim, S.; Luo, Z.; Shen, Z.; Lin, J., Plasma-Assisted Synthesis of Carbon Nanotubes. *Nanoscale Res. Lett.* **2010**, *5* (9), 1377-1386.
188. Bae, E. J.; Min, Y.-S.; Kang, D.; Ko, J.-H.; Park, W., Low-Temperature Growth of Single-Walled Carbon Nanotubes by Plasma Enhanced Chemical Vapor Deposition. *Chem. Mater.* **2005**, *17* (20), 5141-5145.
189. Jung, Y. J.; Wei; Vajtai, R.; Ajayan, P. M.; Homma, Y.; Prabhakaran, K.; Ogino, T., Mechanism of Selective Growth of Carbon Nanotubes on SiO<sub>2</sub>/Si Patterns. *Nano Lett.* **2003**, *3* (4), 561-564.
190. Amama, P. B.; Pint, C. L.; Kim, S. M.; McJilton, L.; Eyink, K. G.; Stach, E. A.; Hauge, R. H.; Maruyama, B., Influence of Alumina Type on the Evolution and Activity of Alumina-Supported Fe Catalysts in Single-Walled Carbon Nanotube Carpet Growth. *ACS Nano* **2010**, *4* (2), 895-904.
191. Valentini, L.; Kenny, J. M.; Lozzi, L.; Santucci, S., Formation of carbon nanotubes by plasma enhanced chemical vapor deposition: Role of nitrogen and catalyst layer thickness. *J. Appl. Phys.* **2002**, *92* (10), 6188-6194.

192. Gohier, A.; Minea, T. M.; Djouadi, M. A.; Granier, A., Impact of the etching gas on vertically oriented single wall and few walled carbon nanotubes by plasma enhanced chemical vapor deposition. *J. Appl. Phys.* **2007**, *101* (5), 054317.
193. Pan, Z.-W.; Zhu, H.; Zhang, Z.; Im, H.-j.; Dai, S.; Beach, D. B.; Lowndes, D. H., Patterned Growth of Vertically Aligned Carbon Nanotubes on Pre-patterned Iron/Silica Substrates Prepared by Sol-Gel and Shadow Masking. *J. Phys. Chem. B.* **2003**, *107* (6), 1338-1344.
194. Pan, Z.-W.; Zhu, H.-G.; Zhang, Z.-T.; Im, H.-J.; Dai, S.; Beach, D. B.; Lowndes, D. H., Hierarchically ordered carbon tubes. *Chem. Phys. Lett.* **2003**, *371* (3-4), 433-437.
195. Li, Y.; Kim, W.; Zhang, Y.; Rolandi, M.; Wang, D.; Dai, H., Growth of Single-Walled Carbon Nanotubes from Discrete Catalytic Nanoparticles of Various Sizes. *J. Phys. Chem. B.* **2001**, *105* (46), 11424-11431.
196. Zhang, G.; Qi, P.; Wang, X.; Lu, Y.; Li, X.; Tu, R.; Bangsaruntip, S.; Mann, D.; Zhang, L.; Dai, H., Selective Etching of Metallic Carbon Nanotubes by Gas-Phase Reaction. *Science* **2006**, *314* (5801), 974-977.
197. Schuettfort, T.; Nish, A.; Nicholas, R. J., Observation of a Type II Heterojunction in a Highly Ordered Polymer-Carbon Nanotube Nanohybrid Structure. *Nano Lett.* **2009**, *9* (11), 3871-3876.
198. Pasquier, A. D.; Unalan, H. E.; Kanwal, A.; Miller, S.; Chhowalla, M., Conducting and transparent single-wall carbon nanotube electrodes for polymer-fullerene solar cells. *Appl. Phys. Lett.* **2005**, *87* (20), 203511.
199. Gohier, A.; Minea, T. M.; Djouadi, A. M.; Granier, A.; Dubosc, M., Limits of the PECVD process for single wall carbon nanotubes growth. *Chem. Phys. Lett.* **2006**, *421* (1-3), 242-245.
200. Kato, T.; Hatakeyama, R., Direct Growth of Short Single-Walled Carbon Nanotubes with Narrow-Chirality Distribution by Time-Programmed Plasma Chemical Vapor Deposition. *ACS Nano* **2010**, *4* (12), 7395-7400.
201. Teo, K. B. K.; Hash, D. B.; Lacerda, R. G.; Rupesinghe, N. L.; Bell, M. S.; Dalal, S. H.; Bose, D.; Govindan, T. R.; Cruden, B. A.; Chhowalla, M.; Amaratunga, G. A. J.; Meyyappan, M.; Milne, W. I., The Significance of Plasma Heating in Carbon Nanotube and Nanofiber Growth. *Nano Lett.* **2004**, *4* (5), 921-926.

202. Marcoux, P. R.; Schreiber, J.; Batail, P.; Lefrant, S.; Renouard, J.; Jacob, G.; Albertini, D.; Mevellec, J.-Y., A spectroscopic study of the fluorination and defluorination reactions on single-walled carbon nanotubes. *Phys. Chem. Chem. Phys.* **2002**, *4* (11), 2278-2285.
203. Li, W.-S.; Aida, T., Dendrimer Porphyrins and Phthalocyanines. *Chem. Rev.* **2009**.
204. Nantalaksakul, A.; Mueller, A.; Klaikherd, A.; Bardeen, C. J.; Thayumanavan, S., Dendritic and Linear Macromolecular Architectures for Photovoltaics: A Photoinduced Charge Transfer Investigation. *J. Am. Chem. Soc.* **2009**, *131* (7), 2727-2738.
205. Kamat, P. V., Graphene-Based Nanoassemblies for Energy Conversion. *The Journal of Physical Chemistry Letters* **2011**, *2* (3), 242-251.
206. Kavan, L.; Yum, J. H.; Grätzel, M., Optically Transparent Cathode for Dye-Sensitized Solar Cells Based on Graphene Nanoplatelets. *ACS Nano* **2011**, *5* (1), 165-172.
207. Wang, X.; Zhi, L.; Mullen, K., Transparent, Conductive Graphene Electrodes for Dye-Sensitized Solar Cells. *Nano Lett.* **2007**, *8* (1), 323-327.
208. Vogt, A. P.; Gibson, C. T.; Tune, D. D.; Bissett, M. A.; Voelcker, N. H.; Shapter, J. G.; Ellis, A. V., High-order graphene oxide nanoarchitectures. *Nanoscale* **2011**, *3*, 3076-3079.